Institut für Erd- & Umweltwissenschaften
Mathematisch-Naturwissenschaftliche Fakultät
Universität Potsdam

Neotectonics & Cooling History of the Southern Patagonian Andes:

Assessing the Role of Ridge Collision and Slab Window Formation inboard of the Chile Triple Junction (46-47°S)

D I S S E R T A T I O N

von
Dipl.-Geol. Viktoria Georgieva

zur Erlangung des akademischen Grades

doctor rerum naturalium
»Dr. rer. nat.«
in der Wissenschaftsdisziplin Geologie

eingereicht an der
Mathematisch-Naturwissenschaftlichen Fakultät
der Universität Potsdam

Potsdam, den 5. Oktober, 2016

Published online at the
Institutional Repository of the University of Potsdam:
URN urn:nbn:de:kobv:517-opus4-104185
http://nbn-resolving.de/urn:nbn:de:kobv:517-opus4-104185

Allgemeine Zusammenfassung

Die Anden von Südamerika sind ein einzigartiger Gebirgszug, der durch die Subduktion von ozeanischer unter kontinentale Lithosphäre über einen Zeitraum von mehreren Millionen Jahre entstanden ist. Über eine Länge von 7000 km erstreckt sich dieses tektonisch aktive Gebirge von den feuchten Tropen im Norden bis zu den gletscherbedeckten Patagonischen Anden im Süden und durchquert dabei unterschiedliche Wind- und Niederschlagsgürtel. Entlang dieser Plattengrenze ändern sich auch bedingt durch unterschiedliche Subduktionswinkel und die Subduktion von Ozeanbodentopographie die tektonischen und vulkanischen Prozesse in der Südamerikanischen Platte. Diese Bedingungen und die hohen topographischen und klimatischen Gradienten machen dieses Gebirge zu einem idealen natürlichen Labor, tektonische und klimatische Prozesse und deren gekoppelte Wechselwirkungen bei der Gebirgsbildung zu analysieren.

Die Subduktion bathymetrischer Anomalien in Südpatagonien, in diesem Fall das ozeanische Spreizungszentrum Chile-Rise, hat die geologische und topographische Entwicklung der übergelagerten kontinentalen Platte deutlich beeinflusst und Spuren hinterlassen. Diese Region ist somit ein außergewöhnliches Beispiel für eine aktive ozeanische Rückenkollision, die über mehrere Millionen Jahre hinweg aufrechterhalten wurde. Die Landschaftsentwicklung sowie die verschiedenen geologischen Merkmale dieses Gebiets wurden in der jüngeren Vergangenheit in diesem Kontext bereits kontrovers diskutiert. Vor allem spielen dabei entweder klimatisch oder tektonisch beeinflusste Endgliedermodelle eine Rolle. Eine insbesondere kontrovers diskutierte Frage in diesem Gebiet betrifft die Interpretation sogenannter thermochronometrischer Datensätze, welche über die Bildung temperaturabhängiger Spaltspuren oder (U-Th)/He-Datierungen im Mineral Apatit die jüngste Abkühlung der Erdkruste und die damit verbundene Landschaftsentwicklung in Südpatagonien dokumentieren können. Diese Abkühlgeschichte kann theoretisch zeitliche und/oder räumliche Variationen im Grad der Erosion bedingt durch Oberflächen- oder tektonische Prozesse und der daraus resultierenden jüngsten Exhumation (Abkühlung) nachweisen oder sie spiegeln auch überlagerte thermische Effekte wieder, die durch Prozesse im Erdmantel gesteuert werden können.

Diese Doktorarbeit fokussiert auf zwei wesentlichen Aspekten dieser Problematik und befasst sich erstens mit der Erkennung bisher kaum erforschter Manifestationen junger (neotektonischer) Deformation in der Erdkruste, die unmittelbar mit der Rückenkollision in Verbindung steht. Diese Deformation hat nachweislich die Topographie und die thermochronometrisch dokumentierte Abkühlgeschichte der Patagonischen Anden in direkter Nachbarschaft der Kollision mitbeeinflusst. Der zweite Forschungsfokus liegt auf der Erweiterung einer quantitativen Modellierung und Interpretation eines Teils des thermochronometrischen Datensatzes von Südpatagonien. Es wurden daher neue numerische Modellierungen durchgeführt mit dem Ziel, die thermische Geschichte solcher Proben, die am besten die beobachteten Daten reproduzieren können, zu definieren und die Bedeutung geodynamischer und oberflächennaher, klimagesteuerter Prozesse (Vergletscherung und glaziale Erosion) bei der großregionalen Exhumation abzuschätzen.

Junge tektonischer Krustenversätze, die unmittelbar auf die Kollision des ozeanischen Rückens zurückzuführen sind, liefern dabei wichtige Erkenntnisse über die Kontrollmechanismen der Krustendynamik, die für die Bildung von Topographie in Patagonien und anderen Regionen verantwortlich sind. Die Ergänzung und Neuinterpretation des thermochronometrischen Datensatzes aus Südpatagonien bietet somit die Möglichkeit für eine objektive Analyse und Darstellung der Exhumationsgeschichte der Südpatagonischen Anden, stellt damit die Landschaftsgeschichte in Zusammenhang mit der tektonisch und klimatisch gesteuerten Prozessdynamik und bietet erstmalig eine solide Basis für ähnliche Ansätze zur Bewertung tektonisch-klimatischer Dynamik von Prozessen bei der Gebirgsbildung.

Abstract

The collision of bathymetric anomalies, such as oceanic spreading centers, at convergent plate margins can profoundly affect subduction dynamics, magmatism, and the structural and geomorphic evolution of the overriding plate. The Southern Patagonian Andes of South America are a prime example for sustained oceanic ridge collision and the successive formation and widening of an extensive asthenospheric slab window since the Middle Miocene. Several of the predicted upper-plate geologic manifestations of such deep-seated geodynamic processes have been studied in this region, but many topics remain highly debated. One of the main controversial topics is the interpretation of the regional low-temperature thermochronology exhumational record and its relationship with tectonic and/or climate-driven processes, ultimately manifested and recorded in the landscape evolution of the Patagonian Andes. The prominent along-strike variance in the topographic characteristics of the Andes, combined with coupled trends in low-temperature thermochronometer cooling ages have been interpreted in very contrasting ways, considering either purely climatic (i.e. glacial erosion) or geodynamic (slab-window related) controlling factors.

This thesis focuses on two main aspects of these controversial topics. First, based on field observations and bedrock low-temperature thermochronology data, the thesis addresses an existing research gap with respect to the neotectonic activity of the upper plate in response to ridge collision - a mechanism that has been shown to affect upper-plate topography and exhumational patterns in similar tectonic settings. Secondly, the qualitative interpretation of my new and existing thermochronological data from this region is extended by inverse thermal modelling to define thermal histories recorded in the data and evaluate the relative importance of surface vs. geodynamic factors and their possible relationship with the regional cooling record.

My research is centered on the Northern Patagonian Icefield (NPI) region of the Southern Patagonian Andes. This site is located inboard of the present-day location of the Chile Triple Junction - the juncture between the colliding Chile Rise spreading center and the Nazca and Antarctic Plates along the South American convergent margin. As such this study area represents the region of most recent oceanic-ridge collision and associated slab window formation. Importantly, this location also coincides with the abrupt rise in summit elevations and relief characteristics in the Southern Patagonian Andes. Field observations, based on geological, structural and geomorphic mapping, are combined with bedrock apatite (U-Th)/He and apatite fission track (AHe and AFT) cooling ages sampled along elevation transects across the orogen. This new data reveals the existence of hitherto unrecognized neotectonic deformation along the flanks of the range capped by the NPI.

This deformation is associated with the closely spaced oblique collision of successive oceanic-ridge segments in this region over the past 6 Ma. I interpret that this has caused a crustal-scale partitioning of deformation and the decoupling, margin-parallel migration, and localized uplift of a large crustal sliver (the NPI block) along the subduction margin. The location of this uplift coincides with a major increase of summit elevati-

ons and relief at the northern edge of the NPI massif. This mechanism is compatible with possible extensional processes along the topographically subdued trailing edge of the NPI block as documented by very recent and possibly still active normal faulting. Taken together, these findings suggest a major structural control on short-wavelength variations in topography in the Southern Patagonian Andes - the region affected by ridge collision and slab window formation.

The second research topic addressed here focuses on using my new and existing bedrock low-temperature cooling ages in forward and inverse thermal modeling. The data was implemented in the HeFTy and QTQt modeling platforms to constrain the late Cenozoic thermal history of the Southern Patagonian Andes in the region of the most recent upper-plate sectors of ridge collision. The data set combines AHe and AFT data from three elevation transects in the region of the Northern Patagonian Icefield. Previous similar studies claimed far-reaching thermal effects of the approaching ridge collision and slab window to affect patterns of Late Miocene reheating in the modelled thermal histories. In contrast, my results show that the currently available data can be explained with a simpler thermal history than previously proposed. Accordingly, a reheating event is not needed to reproduce the observations. Instead, the analyzed ensemble of modelled thermal histories defines a Late Miocene protracted cooling and Pliocene-to-recent stepwise exhumation. These findings agree with the geological record of this region. Specifically, this record indicates an Early Miocene phase of active mountain building associated with surface uplift and an active fold-and-thrust belt, followed by a period of stagnating deformation, peneplanation, and lack of synorogenic deposition in the Patagonian foreland. The subsequent period of stepwise exhumation likely resulted from a combination of pulsed glacial erosion and coeval neotectonic activity. The differences between the present and previously published interpretation of the cooling record can be reconciled with important inconsistencies of previously used model setup. These include mainly the insufficient convergence of the models and improper assumptions regarding the geothermal conditions in the region. This analysis puts a methodological emphasis on the prime importance of the model setup and the need for its thorough examination to evaluate the robustness of the final outcome.

Zusammenfassung

Die Kollision ozeanischer Rückensysteme entlang aktiver Subduktionszonen kann eine nachhaltige Wirkung auf die geodynamische, magmatische, strukturelle und geomorphologische Entwicklung der Oberplatte ausüben. Die Südpatagonischen Anden repräsentieren ein außergewöhnliches Beispiel für eine aktive ozeanische Rückenkollision mit einem Kontinentalrand, die über mehrere Millionen Jahre hinweg aufrechterhalten wurde. Dieser Prozess wurde begleitet von großräumigen Mantelprozessen mit der gleichzeitigen Bildung eines asthenosphärischen Fensters unter Südpatagonien – eine weiträumige Öffnung zwischen den divergierenden ozeanischen Platten unter der Oberplatte, die den Kontakt des asthenosphärischen Mantels mit der kontinentalen Lithosphäre ermöglicht hat. Auch wenn die daraus resultierenden geologischen Erscheinungsformen der Oberplatte bereits in unterschiedlichen Regionen studiert wurden, bleiben viele Fragen hinsichtlich der assoziierten Exhumations- Abkühlungs- und Deformationsprozesse noch offen. Eine kontroverse Frage in diesem Zusammenhang bezieht sich auf die Interpretation von Niedrigtemperatur-Thermochronologiedaten, welche die jüngste Abkühlungs- und Deformationsgeschichte der Erdkruste und die Landschaftsentwicklung in Südpatagonien dokumentieren. Diese Abkühlgeschichte kann theoretisch zeitliche und/oder räumliche Variationen im Erosionspotential von Oberflächenprozessen und der daraus resultierenden jüngsten Exhumation beleuchten oder auch den Einfluss überlagerter thermischer Effekte des hochliegenden Mantels widerspiegeln. Die ausgeprägten topographischen Änderungen entlang des Streichens der Patagonischen Anden, die offenbar auch an Trends in den thermochronometrischen Daten gekoppelt sind, wurden in der Vergangenheit bereits äußerst kontrovers interpretiert. Endglieder dieser Diskussion sind entweder klimatisch gesteuerte Prozessmodelle und eine damit verbundene räumliche Variabilität in der Exhumation (glaziale Erosion) oder geodynamischen Prozesse, die insbesondere eine regional begrenzte Deformation und Hebung mit der Kollision des ozeanischen Chile-Rückens in Verbindung bringen.

Diese Dissertation ist daher auf zwei wesentliche Aspekten dieser Problematik fokussiert. Sie befasst sich einerseits mit der soweit kaum erforschten Existenz junger (neotektonischer) Deformationsphänomene, die unmittelbar mit der Rückenkollision in Verbindung steht und das Potenzial hat, die Topographie und die thermochronometrisch dokumentierte Abkühlgeschichte des Patagonischen Gebirgszuges mitbeeinflusst zu haben. Ein weiterer Forschungsfokus liegt auf der erweiterten Interpretation eines Teils der im Rahmen dieser Arbeit erstellten sowie von vorhandenen thermochronometrischen Datensätzen durch inverse numerische Modellierungen. Diese Modellierungen hatten das Ziel, die thermische Geschichte der Proben, die am besten die beobachteten Daten reproduzieren kann, zu definieren und die relative Bedeutung geodynamischer und oberflächennaher Prozesse abzuschätzen.

Das Untersuchungsgebiet liegt in dem Gebirgsmassiv des Nordpatagonischen Eisfeldes von Südostpatagonien. Dieser Teil der Südpatagonischen Anden liegt in der Region, wo die derzeitig aktive Kollision des Chile-Rückens seit 6 Millionen Jahren im Gange ist. Der Nordrand des Gebirgsmassivs fällt zusammen mit der abrupten

Zunahme der Topographie am Übergang von den Nord- in den Südpatagonischen Anden - das Gebiet, das von ozeanischer Rückenkollision betroffen wurde und durch die Bildung des asthenosphärischen Fensters gekennzeichnet ist. Diverse Feldbeobachtungen, kombiniert mit neuen thermochronometrischen Daten ((U-Th)/He- und Spaltspurendatierungen an Apatiten von Festgesteinsproben, AHe und AFT), dokumentieren die bisher unbekannte Existenz junger tektonischer Bewegungen entlang der Flanken dieses erhöhten Gebirgszuges, welche die topographischen, geomorphologischen und thermochronometrischen Charakteristika der Region deutlich beeinflusst haben. Diese Deformation wurde ausgelöst durch die schräge Kollision von Segmenten des Chile-Rückens, die eine Partitionierung in der Krustendeformation in Komponenten die jeweils parallel und orthogonal zum konvergenten Plattenrand orientiert sind, nach sich zog. Dieser hierbei entstandene Krustenblock des Nordpatagonischen Eisfeldes wurde entlang der Plattengrenze entkoppelt und nordwärts bewegt. Diese Kinematik führte zur lokalen Hebung und Extension (Absenkung) jeweils entsprechend am Nord- und Südrand des Krustenblocks. Die resultierende differentielle Hebung und Extension dieses Krustenblocks korreliert sehr gut mit Muster der räumlichen Verteilung der Topographie und den regionalen thermochronometrischen Daten und legt somit eine direkte Beziehung zwischen geodynamischen Randbedingungen, tektonischer Deformation, Exhumation und Landschaftsentwicklung nahe.

Der zweite Forschungsfokus liegt auf der Implementierung meiner neuen sowie bereits publizierter thermochronometrischer Daten in Vorwärts- und inversen numerischen Modellierungen. Es wurden die frei verfügbaren Modellierungsplattformen HeFTy und QTQt benutzt, um die Abkühlungsgeschichte der Südpatagonischen Anden im Gebiet der jüngsten ozeanischen Rückenkollision zu definieren. Der Datensatz kombiniert AHe und AFT Abkühlalter aus drei Höhenprofilen in der Region des Nordpatagonischen Eisfeldes. Kürzlich publizierte Studien, die auf identischen Datierungsmethoden und numerischen Ansätzen beruhen, postulieren, dass ein signifikanter und räumlich weitreichender thermischer Effekt, , sich bereits während des Obermiozäns in den thermochronometrischen Daten manifestiert und auf die Bildung des asthenosphärischen Fensters zurückzuführen ist. Im Unterschied dazu zeigen meine Ergebnisse, dass die verfügbaren thermochronometrischen Daten mit einem einfacheren thermischen Szenario erklärt werden können und ein thermischer Puls nicht notwendig ist, um die Abkühlalter in der vorliegenden Form zu reproduzieren. Das kumulative Ergebnis der Modellierungen dokumentiert eine alternative Möglichkeit mit einer langsamen und/oder stagnierenden Abkühlung im Obermiozän, auf die dann im Pliozän eine schnelle und ausgeprägt schrittweise Abkühlung stattfand. Diese Ergebnisse sind kompatibel mit der geologischen Geschichte der Region. So wurde in diesem Gebiet eine Phase aktiver Einengung, Hebung und Exhumation im Unteren Miozän nachgewiesen. Dieser Episode folgte eine Phase der Ruhe in der Deformation, eine großräumige Einebnung der Deformationsfront durch fluviatile Prozesse und eine drastische Abnahme synorogener Ablagerungen. Die darauffolgende Phase schrittweiser Abkühlung resultierte aus einer Kombination von einerseits rekurrenten weiträumigen Vergletscherungen und damit einhergehender glazialer Erosion und andererseits von gleichzeitigen lokalen tektonischen Vertikalbewegungen durch Störungen, die im plattentektonischen Kontext aktiver ozeanischer Rückenkolli-

sion entstanden. Die signifikanten Unterschiede zwischen bereits publizierten und den hier präsentierten Ergebnissen beruhen auf der Erkenntnis wichtiger Nachteile der früher benutzten Modellannahmen. Diese beinhalten z.B. die unzureichende Konvergenz (unzureichende Anzahl an Iterationen) und Vorgaben bezüglich der regionalen geothermischen Bedingungen. Diese kritische Betrachtung zeigt, dass methodische Schwerpunkte und Annahmen dieser Modellierungen gründlich geprüft werden müssen, um eine objektive Abschatzung der Ergebnisse zu erzielen.

Zusammenfassend kann festgestellt werden, dass der Impakt bisher unbekannter neotektonischer Strukturen entlang des konvergenten Plattenrandes von Südpatagonien sehr weitreichende Folgen hat. Diese Strukturen stehen räumlich und zeitlich in direkter Beziehung zur seit dem Obermiozän andauernden Subduktion verschiedener Segmente des Chile-Spreizungszentrums; sie unterstreichen die fundamentale Bedeutung der Subduktion bathymetrischer Anomalien für die tektonische und geomorphologische Entwicklung der Oberplatte, besonders in Regionen mit ausgeprägten Erosionsprozessen. Die hier dokumentierten Ergebnisse aus der inversen numerischen Modellierung thermochronometrischer Daten stellen bereits publizierte Befunde aus Studien infrage, die auf ähnlichen Ansätzen beruhen und welche den regionalen thermischen Effekt des asthenosphärischen Fensters in Südpatagonien hervorheben. Meine Ergebnisse dokumentieren stattdessen eine Abkühlungsgeschichte, die durch eine synergistische, klimatisch und tektonisch bedingte schrittweise Exhumation definiert ist. Eine abschließende synoptische Betrachtung der gesamten thermochronometrischen Daten in Südpatagonien belegt das Fehlen von Mustern in der regionalen Verteilung von Abkühlaltern entlang des Streichens des Orogens. Die Existenz eines solchen Trends wurde früher postuliert und im Rahmen eines transienten Pulses dynamischer Topographie und Exhumation interpretiert, der mit der Bildung und Migration des asthenosphärischen Fensters assoziiert wurde. Meine neue Zusammenstellung und Interpretation der Thermochronometrie zeigt stattdessen, dass die regionale Verteilung von Abkühlaltern in Südpatagonien vor allem durch die langfristig wirksame räumliche Verteilung glazialer Erosionsprozesse bestimmt wird, die u.a. zu einer tieferen Exhumation im Zentrum des Orogens geführt hat. Dieses regionale Exhumationsmuster wird allerdings lokal durch differentielle Hebung von Krustenblöcken modifiziert, die mit den neotektonischen Bewegungen im Rahmen der Kollision des Kontinentalrandes mit dem ozeanischen Chile-Rücken und der Partitionierung der Deformation in Zusammenhang stehen.

Acknowledgements

First of all I want to thank my supervisor Manfred Strecker for his continuous support in every possible way over all these years. He made me understand what the nice german word *"Doktorvater"* truly means and I couldn't imagine a better guidance from the beginning towards the fulfilment of this project. I deeply appreciate the freedom he gave me to direct my work and his confidence in my ideas and encouragement to keep going. I am looking forward for many more years of collaboration and friendship. And after all, Manfred, I might finally make my way to the Argentinean Andes!

I am endlessly grateful to Daniel Melnick, my husband, whose ideas gave birth to the Patagonian project and his willingness to let *me* develop it and explore the Patagonian Icefields. I am grateful for the long discussions, collaboration and his constant optimism about the final outcome of this work that formed one of the main pillars of this project. And of course, for our two side projects that turned out in-between and transformed our lives!

I would like to thank Taylor Schildgen, who was a continuous and extremely helpful mentor for me since the very beginning. Thank you, Taylor, for joining the project, for always listening and helping me when I needed it and for your confidence and assurance that were crucial to get back my motivation in some difficult moments.

Yves Lagabrielle was in the very core of my dedication to Patagonian geology and I feel fortunate for the time spent together in the field. Thank you, Yves for all the knowledge, for sharing your vision about the history of this exciting region and most of all for the life lesson I learned from you. I greatly appreciate your friendship and hope to stay connected in the future.

Special thanks to Todd Ehlers, my mentor and co-supervisor in this project, for his willingness to join the project, for his crucial help to design the research proposal, for his continuous guidance and financial support of the analytical work, and for the many scientific discussions from which I learned a lot. I am looking forward for continuous collaboration in the future.

Over the years, I sought advise from many more people that shared their knowledge giving rise to fruitful discussions. Ed Sobel, Heiko Pingel, Kerry Gallagher, Eva Enkelmann, Konstanze Stübner, Paolo Ballato, Artur Sobczyk, Amaury Pourteau, Veronica Torres, Iris van der Veen, Bernd Hoffmann, Mauricio Parra, Javier Quinteros and many more are all thanked for having been available to discuss and help me out on difficult topics.

Fieldwork in the Patagonian Andes would not have been possible without the essential support and hard work of Pascual Diaz, the Berrocal-brothers (Qto and Lapo), Jonathan Leidich, Hector Soto, Gringo, and Noel Vidal. Thanks for guiding me, helping me carry all these rocks and sharing your culture and amazing land with me! I also want to thank my family in Chile for their love and support and for being such wonderful grandparents without whom fieldwork would not have been possible either!!

I couldn't imagine a nicer working environment than our group at the Institute for Earth and Environmental Sciences at the University of Potsdam. The constellation of

people has been changing over all these years I spent at the institute and I have found many many good friends and colleagues. Thanks for all the nice times together!

Finally, I am deeply grateful for having my family in Bulgaria, whose love, support and faith in me have always been a pillar in my life and helped me fulfil this project.

Contents

List of figures

Chapter 1

Thesis organization

This thesis constitutes one peer-reviewed, published article, a chapter that will soon be submitted as a manuscript for review to a scientificc journal and a general synthesis, review and re-evaluation of work done by others, which are relevant for the final conclusions drawn here. The overarching goal of this thesis is to better understand and constrain the effects of oceanic ridge collision and slab window opening on the structural and thermal evolution of the upper crust of the overriding plate as reflected by the exhumational and topographic patterns of the region inboard of the triple junction. The project was initially started within the framework of the DFG-Leibniz Center for Surface Process and Climate Studies, funded by the Leibniz awards of Deutsche Forschungsgemeinschaft (DFG) to M. Strecker and G. Haug, with the aim to link studies of tectonics, climate, and surface processes on geologic to annual timescales. Furthermore, the study was supported by the European Research Council (ERC), Consolidator Grant. *"EXTREME: EXtreme Tectonics and Rapid Erosion in Mountain Environments"*, granted to T. Ehlers (University of Tübingen). These two centers provided the platform for a pilot and feasibility study that ultimately resulted in a DFG research joint proposal, titled *"Quantifying Tectonic and Glacial Controls on Topography: Patagonia, South America"*, funded to T. Ehlers (University of Tübingen) and M. Strecker (University of Potsdam). My thesis represents an integral part of this proposal, which had three main goals: (1) Characterising new, hitherto unrecognised, active faults in the high-elevation region inboard the Chile Triple Junction, where closely spaced collision of three subsequent oceanic ridge segments occurred over the last 6 Myr; (2) providing a dense low-temperature thermochronology data set including various thermochronometers from this region to decipher the late Miocene-to-recent exhumational patterns and their interference with recent tectonic uplift; and (3) to perform thermal modelling of the new and published low-temperature thermochronology data in order to constrain the general thermal history of the upper crust in this region since the late Miocene, and

particularly to re-evaluate the thermal effects of oceanic ridge collision and slab window opening on the thermal histories. The following paragraphs present a brief summary of the contents of each chapter.

Chapter 2 – *Introduction.* This chapter provides a brief introduction to the topics of oceanic ridge collision and slab window formation and lays out the rationale and motivation of the dissertation.

Chapter 3 – *Tectonic control on rock uplift, exhumation and topography above an oceanic-ridge collision – Southern Patagonian Andes (47°S), Chile.* This chapter describes newly discovered fault structures along the flanks of the Northern Patagonian Icefield - an elevated massive located inboard of the Chile Triple Junction. Based on field observations and apatite (U-Th)/He data it discusses their relation to oceanic ridge collision and proposes a neotectonic model that is consistent with topographic and exhumational patterns in this region. This chapter has been published as *Georgieva, V., Melnick D., Schildgen, T.F., Ehlers, T.A., Lagabrielle, Y., Enkelmann, E. and Strecker, M.R., 2016. Tectonic control on rock uplift, exhumation and topography above an oceanic-ridge collision – Southern Patagonian Andes (47°S), Chile, Tectonics, doi: 10.1002/2016TC004120.*. VG carried out all fieldwork, including geological and structural mapping, fault-kinematic measurements, and sampling for low-temperature thermochronology dating methods. VG carried out mineral separation and apatite picking under the guidance of TFS, EE and TAE. EE performed isotope measurements and corrections at Universiy of Tübingen. DM and YL provided introduction to the field area and regional geology and supported fieldwork and logistics. All illustrations are the responsibility of VG. All authors participated in discussing the results and interpretations, and critically read the manuscript.

Chapter 4 – *Late Cenozoic Cooling History of the Southern Patagonian Andes at 47°S - Insights from Inverse thermal modelling.* This chapter discusses the late Cenozoic thermal history recorded in samples from the Northern Patagonian Icefield region as constrained by inverse thermal modeling of single- and multiple-sample thermal histories using Hefty and QTQt modeling platforms. The multiple-sample approach was applied to elevation transects with apatite (U-Th)/He data presented by Georgieva *et al.* (2016) combined with new apatite fission track data presented here. Furthermore, a re-evaluation of single- and multi-sample modelling results from Guillaume *et al.* (2013) and

Blisniuk *et al.* (2006) has been performed and considered for the final conclusions drawn here. A shortened version of this chapter is currently in preparation for submission to the peer-review scientific journal *Earth and Planetary Science Letters* as Georgieva, V., Gallagher, K., Sobczyk, A., Sobel, E., Schildgen, T.F. , Ehlers, T.A., Strecker, M.R. *Late Cenozoic Cooling History of the Southern Patagonian Andes at 47°S - Insights from Inverse Thermal Modelling.*

Chapter 5 – *Discussion and conclusions.* This chapter summarises the principal results from Chapter 3 and Chapter 4 and discusses the main conclusions in a more regional geodynamic and tectonic context. It furthermore includes an interpretation of the large-scale patterns and trends of low-temperature bedrock cooling ages in Southern Patagonia against the background of previously proposed controlling factors and new results presented here.

Chapter 2

Introduction

A simple glance at the Earth's surface and the morphology of the ocean floor and its fragmented crust reveals that the convergence of tectonic plates inevitably results in the intersection of oceanic relief with active plate margins. Many of these high-topography sectors on the oceanic crust represent active oceanic spreading centres and fracture zones characterised by thickened and very buoyant crust that constitute major topographic and thermal anomalies across the oceanic basins (e.g. Thorkelson, 1996; Groome & Thorkelson, 2009). Oceanic basins are being borne along oceanic spreading centres and consumed along active subduction margins. The variability of spreading and convergence rates and directions results in the collision and consumption of oceanic ridges along subduction margins forming trench-ridge-trench triple junctions. Furthermore, the collision of active oceanic ridges separating plates that continue to diverge after subduction leads to the formation of a slab window - a gap in the subducting lithosphere that abruptly generates a pathway for hot asthenospheric mantle that will interact with the overriding lithosphere. Both effects, the continuing collision of buoyant topographic features and the evolving asthenospheric slab window are expected to significantly affect the tectono-magmatic evolution of the margin of the overriding plate (e.g. Thorkelson, 1996; Groome & Thorkelson, 2009; Sisson *et al.*, 2003a).

Whereas the nature and magnitude of these effects largely depend on the ridge-trench geometry (obliquity of collision) and the convergence velocities (Thorkelson, 1996), some common geologic characteristics have been assigned to these processes including, for example, anomalous high-T metamorphism and mafic magmatism in the fore-arc (DeLong *et al.*, 1979; Underwood *et al.*, 1993; Sisson & Pavlis, 1993; Brown, 1998), cessation of subduction-related volcanism in the magmatic arc due to the missing slab and hydration of the mantle wedge(Abratis & Wörner, 2011; Kay *et al.*, 1993) , differences in deformation style along strike of the convergent margin and particularly across the triple junction(Cembrano *et al.*, 2002; Haeussler *et al.*, 2003; Georgieva *et al.*, 2016), and

transient pulses of dynamic uplift above the evolving slab window (Buiter *et al.*, 2002; Rogers *et al.*, 2002; Guillaume *et al.*, 2013; Braun *et al.*, 2013; Gutscher *et al.*, 1999). These effects have been mainly inferred to be associated with the replacement of the cold, dense subducting lithosphere by hot, buoyant asthenospheric mantle in the slab window. The upper-plate response to ridge collision and slab window formation have been studied in several regions around the globe characterised by ongoing ridge collision and/or slab window formation, such as Southern Patagonia (Murdie *et al.*, 1993; Forsythe & Nelson, 1985; Lagabrielle *et al.*, 1994; Cembrano *et al.*, 2002; Guillaume *et al.*, 2013; Georgieva *et al.*, 2016), the Antarctic Peninsula(Guenthner *et al.*, 2010), the Central North American Cordillera(Merritts & Bull, 1989), or by the fossil record of these processes from the past, e.g. in Southern Alaska or Japan (e.g. Haeussler *et al.*, 1995, 2003; Underwood *et al.*, 1993; Sisson *et al.*, 2003a).

From these examples the geodynamic framework of Southern Patagonia certainly represents a showcase setting, where 16 Ma of protracted, but episodically migrating ridge collision has left its mark along the subduction margin(Breitsprecher & Thorkelson, 2009). Today, active ridge collision in Southern Patagonia is still ongoing. Numerous studies over the past 30 years have furnished insights to characterise the deep-seated geodynamic processes and geometries related to the oblique and northwards-migrating collision of the Chile Rise spreading center with the South American continent and the opening of the Patagonian slab window.

New approaches have added a different perspective based on considerations of the geomorphic and cooling history record in Southern Patagonia, highlighting the peculiar landscape evolution and present-day topographic characteristics of the Patagonian Andes along the margin (Ramos, 2005; Thomson *et al.*, 2010; Braun *et al.*, 2013; Guillaume *et al.*, 2013). Interestingly, the substantial along-strike variability of topography in the Patagonian Andes appears as a particularly controversial topic and has been interpreted in either a purely deeply-seated geodynamic (Guillaume *et al.*, 2010, 2013) or exclusively surface-processes related climatic (Thomson *et al.*, 2010) context. Furthermore, very little work has been done on studying localised crustal deformation related to ridge collision that might have potentially affected the topographic and exhumational record in this environment, even if such effects have been described in similar settings elsewhere.

It is intriguing that many of the controversial studies on this topic are entirely or at least to some extent based on the same regional data set of low-temperature bedrock cooling ages that has been interpreted in very different ways. Low-temperature ther-

mochronological data has the potential to record the relatively recent cooling and exhumational history of the crust and may thus provide important insight into the forcing mechanisms that ultimately drive crustal cooling(e.g. Reiners & Brandon, 2006; Ehlers & Farley, 2003). The Southern Patagonian Andes have been subjected to repeated and extensive glaciations since the Late Miocene (Mercer & Sutter, 1982; Lagabrielle *et al.*, 2010). Simultaneously this region of the Andean orogen was affected by ridge collision and slab window formation (Breitsprecher & Thorkelson, 2009). Hence, both processes have the potential both in space and time to influence the most recent cooling history evolution of the crust.

Given the temporal overlap of the geodynamic and climatic controlling factors, it appears surprising that the topographic characteristics and exhumational record of the Patagonian Andes have been repeatedly interpreted in a rather unidimensional way by considering either one or the other driving mechanisms. The main motivation for this thesis was to adopt a more integrative approach and to address the cooling record and the evolution of topography in the Patagonian Andes inboard and immediately south of the Chile Triple Junction, where ridge collision and slab window formation have had the most recent impact.

My research approach combines field-based structural and geomorphic mapping and strategically oriented sampling for low-temperature bedrock thermochronology along elevational transects from the orogen's interior aimed at closing crucial gaps for the interpretation of the existing data sets that were mainly generated from samples collected at low elevations in the orogen's fore- and back-arc regions. Furthermore, different approaches of inverse thermal modelling have been adopted in order to better constrain the most recent thermal history recorded in the data and to re-evaluate previously proposed scenarios. Finally, a thorough review and evaluation of the regional low-temperature data set from the entire Patagonian Andes is presented and discussed in the context of the complex geodynamic, tectonic and climatic conditions in this region.

The thesis has a threefold structure. The first research chapter (Chapter 3) is focused on the analysis of neotectonic activity inboard of the Chile Triple Junction as constrained by field work and apatite (U-Th)/He bedrock cooling ages. The second research chapter (Chapter 4) focuses on the reconstruction of the thermal history constrained by apatite (U-Th)/He and fission track data from samples along elevational transects from a more extended region at the same latitudes, applying inverse thermal modelling with the modelling platforms HeFTy and QTQt. This chapter also contains a thorough re-evaluation of previously published scenarios and modelling approaches, with

a methodological emphasis on the model setup. The final chapter (Chapter 5, General Discussion) offers a brief summary of results from this thesis and an extensive discussion based on a compilation of the entire available low-temperature bedrock cooling record in Southern Patagonia.

Chapter 3

Tectonic control on rock uplift, exhumation and topography above an oceanic ridge collision – Southern Patagonian Andes (47°S), Chile[†]

Georgieva, V.[1], Melnick, D.[1, 6], , Schildgen, T. F.[1, 2], Ehlers, T. A.[3], Lagabrielle, Y.[4], Enkelmann, E.[5], Strecker, M. R.[1]

[1]*Institute of Earth and Environmental Science, University of Potsdam, Karl-Liebknecht-Str. 24-25, 14476 Potsdam-Golm, Germany*

[2]*Helmholtz-Zentrum Potsdam, Deutsches GeoForschungsZentrum GFZ, Telegrafenberg, 14473 Potsdam, Germany*

[3]*Department of Geosciences, University of übingen, Wilhelmstr. 56, 72074 Tübingen, Germany*

[4]*Geosciences Rennes UMR 6118, Université de Rennes 1, Campus de Beaulieu, 35042 Rennes Cedex, France*

[5]*Department of Geology, University of Cincinnati, 500 Geology Physics Building P.O. Box 210013, Cincinnati, OH 45221-0013, Cincinnati, US*

[6]*Facultad de Ciencias, Escuela de Geología, Universidad Austral de Chile, Casilla 567, Valdivia, Chile*

Abstract

The subduction of bathymetric anomalies at convergent margins can profoundly affect subduction dynamics, magmatism, and the structural and geomorphic evolution of the overriding plate. The Northern Patagonian Icefield (NPI) is located east of the Chile Triple Junction at 47°S, where the Chile Rise spreading center collides with South America. This region is characterized by an abrupt increase in summit elevations and relief that has been controversially debated in the context of geodynamic vs. glacial erosion effects on topography. Here, we present geomorphic, thermochronological, and structural data that document neotectonic activity along hitherto unrecognized faults along the flanks of the NPI.

[†]*published in Tectonics, doi: 10.1002/2016TC004120*

New apatite (U-Th)/He bedrock cooling ages suggest faulting since 2-3 Ma. We infer the northward translation of a 140-km-long forearc sliver – the NPI block – results from enhanced partitioning of oblique plate convergence due to the closely spaced collision of three successive segments of the Chile Rise. In this model, greater uplift occurs in the hanging wall of the Exploradores thrust at the northern leading edge of the NPI block, whereas the Cachet and Liquiñe-Ofqui dextral faults decouple the NPI block along its eastern and western flanks, respectively. Localized extension possibly occurs at its southern trailing edge along normal faults associated with margin-parallel extension, tectonic subsidence, and lower elevations along the Andean crest line. Our neotectonic model provides a novel explanation for the abrupt topographic variations inland of the Chile Triple Junction and emphasizes the fundamental effects of local tectonics on exhumation and topographic patterns in this glaciated landscape.

3.1 Introduction

The collision of oceanic-ridge segments at subduction margins can significantly affect the structural, magmatic, and topographic evolution of the overriding plate (Scholz & Small, 1997; Gräfe *et al.*, 2002; Taylor *et al.*, 2005; Groome & Thorkelson, 2009). Upper-plate responses to ridge collision include an increase in interplate coupling and subduction erosion (Maksymowicz *et al.*, 2012), near-trench magmatism (Bourgois *et al.*, 1996; Lagabrielle *et al.*, 2000), forearc uplift and deformation (Taylor *et al.*, 1987; Hsu, 1992; Gardner *et al.*, 1992; Collins *et al.*, 1995; Sak *et al.*, 2009; Margirier *et al.*, 2015), as well as decoupling and motion of large forearc slivers (Forsythe & Nelson, 1985; Cembrano *et al.*, 2002; Witt *et al.*, 2006; Michaud *et al.*, 2009; Melnick *et al.*, 2009a). Furthermore, the collision of an active oceanic spreading center leads to the formation of a slab window below the overriding plate, where hot asthenospheric mantle rises through the gap created between the two diverging plates and thus modifies the thermal structure and buoyancy state of the upper plate (Thorkelson, 1996; Breitsprecher & Thorkelson, 2009; Groome & Thorkelson, 2009; Guenthner *et al.*, 2010; Guillaume *et al.*, 2013). The formation of a slab window has been specifically associated with modifications of upper-mantle structure and asthenospheric flow (Murdie *et al.*, 1993; Groome & Thorkelson, 2009; Guillaume *et al.*, 2010; Russo *et al.*, 2010a), a gap in arc volcanism (Ramos & Kay, 1992; Gorring *et al.*, 1997), back-arc extension (Lagabrielle *et al.*, 2007; Scalabrino *et al.*, 2010, 2011), and volcanism with an asthenospheric signature (Gorring *et al.*, 1997; Guivel *et al.*, 2006; Boutonnet *et al.*, 2010). Finally, an areally extensive region of upper-plate dynamic uplift creating up to a few hundred meters of transient dynamic topography has been modeled in slab window settings (Groome & Thorkelson, 2009; Braun, 2010;

Guillaume *et al.*, 2009, 2013). Such a long-wavelength pulse of dynamic uplift and ensuing exhumation has been proposed for the Antarctic Peninsula above the colliding Antarctic-Phoenix spreading center (Guenthner *et al.*, 2010) and for Southern Patagonia above the Patagonian slab window (Guillaume *et al.*, 2009, 2010, 2013; Jeandet, 2014; Braun *et al.*, 2013).

In the Patagonian Andes, an abrupt and major increase of both summit elevations and local relief along the orogenic crest occurs immediately inland of the Chile Triple Junction (CTJ) - where the Chile Rise collides with the South American continent (Figure 3.1). Collision has resulted in opening of an areally extensive slab window below Southern Patagonia (Cande & Leslie, 1986; Cande *et al.*, 1987; Murdie *et al.*, 1993; Breitsprecher & Thorkelson, 2009; Russo *et al.*, 2010b). Recent studies have proposed dynamic support of high topography above the Patagonian slab window as a plausible explanation for the sudden increase in summit elevations and relief, corresponding to some extent to the predictions of analog (Guillaume *et al.*, 2010) and numerical models (e.g. Braun *et al.*, 2013; Guillaume *et al.*, 2013), as well as thermochronological data from the eastern foreland (Haschke *et al.*, 2006; Thomson *et al.*, 2010; Guillaume *et al.*, 2013). In an alternative interpretation, based on a thermochronology data set spanning the entire Patagonian Andes, Thomson et al. [2010] linked increased summit elevations in Southern Patagonia with latitudinal climate gradients and changes in the efficiency of glacial erosion, leading to protection of high topography from erosion and promotion of orogenic growth.

While appealing in various aspects, neither of these hypotheses specifically accounts for the role of crustal tectonics along the continental margin, which has experienced oblique subduction, strain partitioning, and oceanic ridge collision since the middle Miocene (Breitsprecher & Thorkelson, 2009). The oblique collision of the Chile Rise has been considered to be a major driver of transpressional deformation along the continental margin (Forsythe & Nelson, 1985; Murdie *et al.*, 1993; Nelson *et al.*, 1994), causing the detachment and northward translation of a large (>1,000 km) crustal sliver – the Chiloé block (Forsythe & Nelson, 1985; Nelson *et al.*, 1994; Cembrano *et al.*, 2002; Rosenau *et al.*, 2006; Melnick *et al.*, 2009b). Ramos (1989) suggested that ridge collision enhanced shortening in the Andean fold-and thrust belt, resulting in uplift and higher topography south of the CTJ. However, field data show that shortening perpendicular to the margin in this sector of the Andes ceased before the onset of ridge collision (Coutand *et al.*, 1999; Suarez *et al.*, 2000; Lagabrielle *et al.*, 2004; Blisniuk *et al.*, 2005; Scalabrino *et al.*,

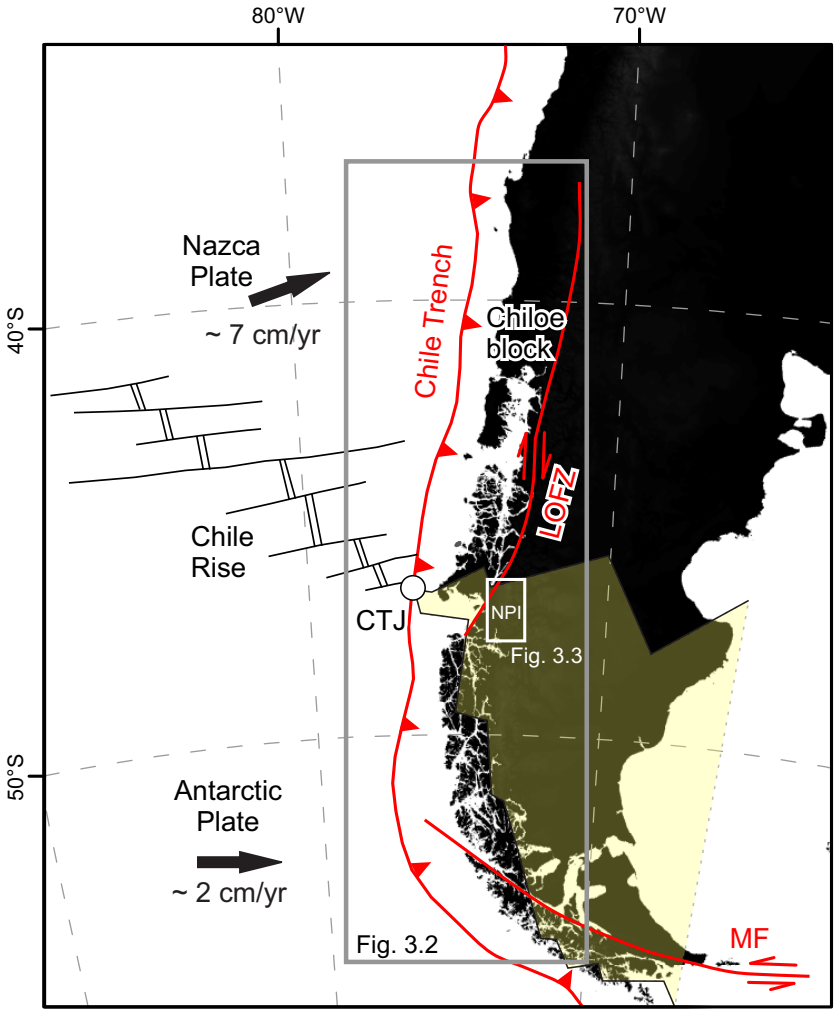

Figure 3.1 – Tectonic setting and location of study area. Grey rectangle (Figure 3.2) spans the Patagonian Andes along the subduction margin of South America. White rectangle (Figure 3.3) marks location of the Northern Patagonian Icefield (NPI). Yellow-shaded area outlines the present extent of the Patagonian slab window. CTJ: Chile Triple Junction; LOFZ: Liquiñe Ofqui Fault Zone; MF: Magallanes Fault.

2011). Thus, the link between topographic growth and possible neotectonic activity inland of the CTJ has not been fully explored.

We aim to address this lacuna and focus on the hypothesis that ridge collision triggered tectonic activity inland from the CTJ, with topographic impacts that were superimposed on those associated with other regional processes, such as glacial erosion and slab window-related dynamic uplift. Our investigation is based on geomorphological, geological, and structural observations from the Northern Patagonian Icefield (NPI) - the elevated area that marks the pronounced increase of summit elevations and relief immediately inland of the CTJ (46°30' S, Figure 3.2). Furthermore, we use low-temperature thermochronology (apatite (U-Th)/He dating) on bedrock samples to track exhumation patterns in the study area over the last several million years, and assess those data in the context of mapped faults, glacial erosion processes, and the spatiotemporal evolution of ridge collision. Finally, we propose a tectonic model for the structural evolution of the margin that provides an alternative explanation for the topographic evolution inland from the CTJ.

3.2 Methods

3.2.1 Geomorphic and Structural Mapping

We surveyed geomorphic features and performed structural and geological mapping along the flanks of the Northern Patagonian Icefield (NPI). We used the SRTM-1 30-m resolution DEM as well as Google Earth and ASTER satellite imagery for mapping faults at the macroscale (103-104 m) and for morphometric analysis of displaced glacial landforms. At the outcrop meso- and microscale (10-1-102 m), we mapped faults and collected structural data of fault planes and lineations with fault-kinematic indicators such as mineral-growth fabrics of slickensides to infer the sense of displacement. Data collection at outcrop scale was hampered by challenging access conditions and dense vegetation in this remote and glaciated region. The available outcrop-scale kinematic data is presented using the Stereonet 9 fault-analysis software by R. Allmendinger (http://www.geo.cornell.edu/geology/faculty/RWA/).

3.2.2 Sample Preparation and Analytical Methods

We collected 30 bedrock samples along the eastern and northern foothills of the NPI Appendix A and applied low-temperature thermochronology dating methods to assess the exhumation history of bedrock samples as they pass through the upper 1-5 km of the crust (Wolf *et al.*, 1996; Ehlers & Farley, 2003). After standard mineral separation

procedures (jaw crushing, sieving, magnetic separation, heavy liquids) we performed apatite (U-Th)/He (AHe) and fission track (AFT) analyses.

For AHe analysis clear, euhedral apatite grains mostly with diameters 70 µm and without visible inclusions were selected using a binocular microscope. The grain dimensions were measured for the calculation of the alpha-correction factor (Farley *et al.*, 1996). Subsequently, single grains were packed in Nb-tubes for (U-Th)/He analysis. We measured 3 to 5 aliquots per sample using the Patterson Helium-extraction line at University of Tübingen. The analytical errors of the mass-spectrometer measurements are generally very low and do not exceed 2%. In contrast, the reproducibility of the sample aliquots constitutes a much larger range. We therefore report the mean AHe age and the standard deviation of the measured aliquots as the sample error.

3.3 Regional setting

3.3.1 General Tectonic and Geodynamic Setting

The forearc of the southern Andes comprises the Chile Triple Junction (CTJ), which joins the Nazca, Antarctic, and South American plates (Figure 3.2). North of the CTJ, the Nazca plate has been subducting in a northeasterly direction since the early Miocene (20 Ma) (Pardo-Casas & Molnar, 1987; Kendrick *et al.*, 2003) at a rate of 7 cm/yr (Angermann *et al.*, 1999; Kendrick *et al.*, 2003; Wang *et al.*, 2007; DeMets *et al.*, 2010). Oblique plate convergence in addition to collision of several oceanic ridge segments has resulted in the structural decoupling of the Chiloé block from the rest of the orogen along the Liquiñe-Ofqui Fault Zone (LOFZ, Figure 3.1, Figure 3.2A) (Cembrano *et al.*, 1996; Rosenau *et al.*, 2006; Melnick *et al.*, 2009a). The LOFZ constitutes a crustal-scale, intra-arc, dextral-transpressional fault system extending >1000 km north of the CTJ that accommodates the margin-parallel component of oblique plate convergence (Cembrano *et al.*, 2002; Thomson, 2002; Rosenau *et al.*, 2006; Hernandez Moreno *et al.*, 2014). The LOFZ is seismically active (Lange *et al.*, 2008; Agurto-Detzel *et al.*, 2012) and has been associated with recent crustal earthquakes, volcanic activity, rock uplift, exhumation, and enhanced cooling that initiated between 16 and 10 Ma (Thomson, 2002; Cembrano *et al.*, 2002; Rosenau *et al.*, 2006). The LOFZ is aligned with the Southern Volcanic Zone located 250-300 km inland of the trench, comprising volcanic units of Pliocene to Quaternary age that overlie the Northern Patagonian Batholith, an exhumed Jurassic-Miocene magmatic arc segment (Pankhurst *et al.*, 1992; Seifert *et al.*, 2005).

South of the CTJ, subduction of the Antarctic plate initiated at 16 Ma with collision of the Chile Rise with South America at 54°S (Figure 3.2A) (Breitsprecher & Thorkelson, 2009). The oblique collision geometry resulted in the northward migration of the CTJ as subsequent trench-parallel ridge segments collided. Since about 6 Ma, the CTJ has remained close to its present-day location due to the closely spaced collision of three relatively short ridge segments at 6 Ma, 3 Ma, and 0.3 Ma in the Golfo de Penas region. Ridge collision has resulted in the opening of an asthenospheric slab window beneath southern Patagonia, which is rapidly widening due to the differences in convergence velocity between the Nazca and Antarctic plates relative to South America (e.g. Forsythe & Nelson, 1985; Breitsprecher & Thorkelson, 2009). At present, the Antarctic Plate is subducting orthogonally below South America with a convergence rate of 2 cm/yr (Wang *et al.*, 2007).

3.3.2 Geomorphology and Geology of the Northern Patagonian Icefield

The Patagonian Andes extend over 2000 km, from 38°S to 53°S, parallel to the Andean subduction margin (Figure 3.2B). Since approximately 7 Ma, the orogen has been subjected to repeated, extensive glaciations (e.g. Mercer & Sutter, 1982; Ton-That *et al.*, 1999; Singer *et al.*, 2004; Hein *et al.*, 2009; Lagabrielle *et al.*, 2010) that have shaped the mountain belt. h topography of the Patagonian Andes reveals distinct variations along strike. North of 46°30'S (current location of the CTJ), maximum and mean elevations approach 2000 and 1000 m, respectively. Maximum relief (including the bathymetry of glacial fjords) is uniform, averaging 2000 m, with local fluctuations of several hundred meters associated with isolated volcanic summits or deep glacial fjords (Figure 3.2B). South of the CTJ, topography abruptly rises towards the peak summits of the NPI, with maximum elevations between 3000 and 4000 m, whereas mean elevations increase by several hundred meters and become more variable. Maximum relief doubles, becomes highly variable, and locally exceeds 5000 m where the highest peaks are adjacent to deep glacial fjords (Figure 3.2B). The NPI caps a high massif bounded by steep flanks. The 3000-m-high northern edge of the icefield includes Mt. San Valentin (4058 m), Patagonia's highest peak. From the northern edge, the ice plateau is gently inclined towards the south and punctuated by several high summits aligned along sigmoidal ridges (Figure 3.3A). In the southern foothills of the NPI surrounding Caleta Tortel, the rugged terrain and high summits abruptly change to a relatively subdued morphology, where mean and summit elevations drop below 500 and 1500 m, respectively. In this region, numerous fjords traverse the orogen reaching the eastern foreland, and reflecting the

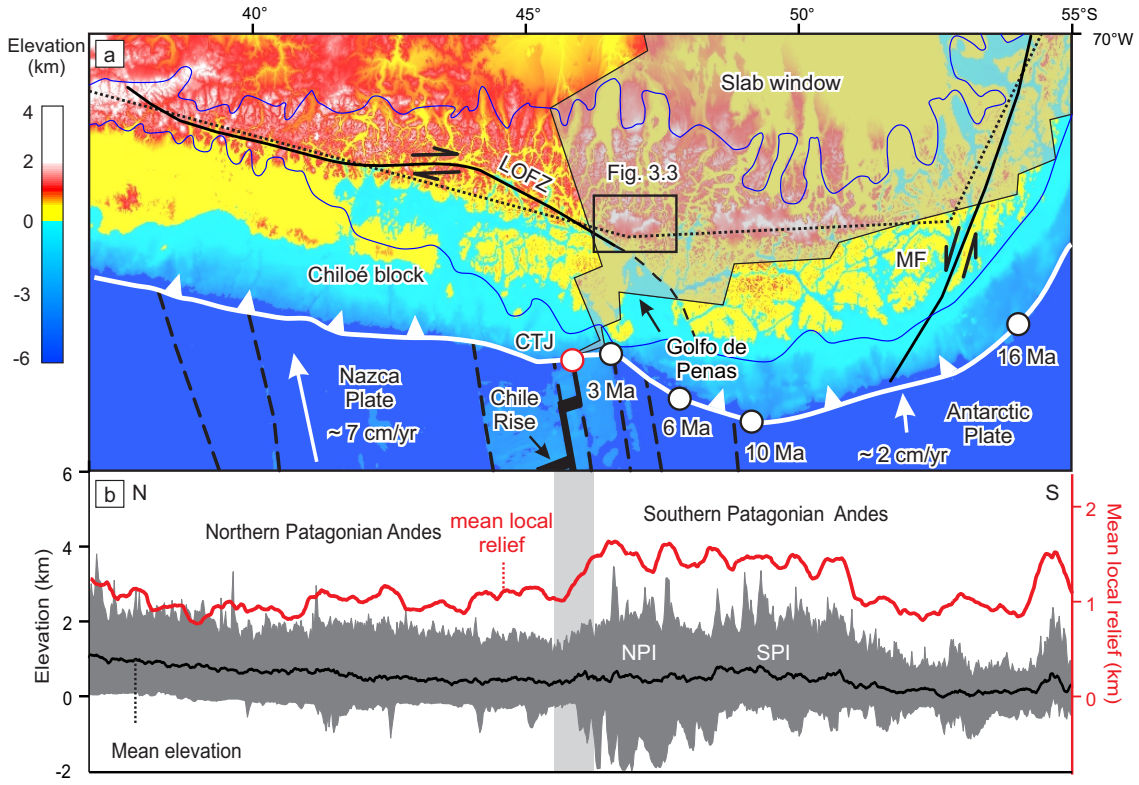

Figure 3.2 – (A) Topography and tectonic setting of the Patagonian Andes. Shaded area outlines the present extent of the Patagonian slab window (Breitsprecher & Thorkelson, 2009). White circles and ages indicate the spatiotemporal path and present position of the Chile Triple Junction (Breitsprecher & Thorkelson, 2009). Dotted black line shows location of the latitudinal swath profile along the orogenic divide presented in (B). White arrows indicate plate convergence. Black rectangle locates Figure 3.3. Blue line corresponds to glacial extent during the Last Glacial Maximum. CTJ: Chile Triple Junction; LOFZ: Liquiñe-Ofqui Fault Zone; MF: Magallanes Fault (b) Latitudinal swath profile (4-longitudinal-degrees width) including bathymetry. Red line represents swath profile of mean local relief calculated for 10 km-radius moving window across the swath area. The grey shaded stripe indicates the abrupt increase in relief and summit elevations at the latitude of the Chile Triple Junction. NPI/SPI: Northern/Southern Patagonian Icefield.

deep incision of former outlet glaciers, which connected with the NPI with the Southern Patagonian Icefield located further south (Figure 3.2).

The bedrock underlying the NPI comprises Paleozoic metamorphic rocks intruded by Jurassic to Miocene plutons of the Patagonian Batholith [Hervé et al., 2007] (Figure 3.3B). To the east of the NPI, Jurassic to Oligocene volcanic rocks and marine sedimentary units and Miocene synorogenic deposits record episodic shortening and uplift during the Late Cretaceous to Middle Miocene (22 to 14 Ma) (Coutand *et al.*, 1999; Suarez *et al.*, 2000; Lagabrielle *et al.*, 2004; Blisniuk *et al.*, 2005; Scalabrino *et al.*, 2011). Most shortening occurred during deposition of Early Miocene synorogenic sediments (Ramos, 1989; Lagabrielle *et al.*, 2004; Blisniuk *et al.*, 2005). At 14 Ma, sedimentation rates dramatically decreased, as reflected by the limited thickness and extent of younger deposits (Blisniuk *et al.*, 2005). These sedimentary units (younger than 14 Ma) were not affected by shortening (Suarez *et al.*, 2000). Since 12 Ma, extensive plateau basalts with geochemical signatures of asthenospheric mantle likely associated with the evolving Patagonian slab window (Gorring *et al.*, 1997; Guivel *et al.*, 2006; Boutonnet *et al.*, 2010), were emplaced in the eastern foreland on a gently eastward-sloping surface, sealing the eastern thrust front of the Southern Patagonian Andes (Ramos, 1989; Lagabrielle *et al.*, 2004). Coutand *et al.* (1999) reported similar observations to the south at 49°S, where undeformed early Pliocene basalts unconformably overlie older shortened units. After 14 Ma, only minor Pliocene-to-recent extensional deformation has been documented within the former Patagonian fold-and-thrust belt (Suarez *et al.*, 2000; Lagabrielle *et al.*, 2007; Scalabrino *et al.*, 2011). Together, these observations suggest that lateral orogenic growth associated with an active fold-and-thrust belt terminated synchronously with the onset of ridge collision and slab-window opening in Southern Patagonia (Suarez *et al.*, 2000; Lagabrielle *et al.*, 2007; Breitsprecher & Thorkelson, 2009; Scalabrino *et al.*, 2011).

3.4 Geomorphic & Structural Observations

In this study we characterize neotectonic activity along the hitherto unrecognized Cachet, Exploradores, and El Salton faults, located respectively in the eastern, northern, and southeastern foothills of the NPI (Figure 3.3A).

3.4.1 Cachet Fault

The Cachet Fault is a N-S striking, dextral strike-slip fault spanning the eastern foothills of the NPI for at least 60 km (Figure 3.3A, Figure 3.4). It follows a low-elevation corridor that defines a major axial drainage in the eastern foothills of the NPI, which is perpendicular to the west-to-east regional drainage direction. A continuous segment of

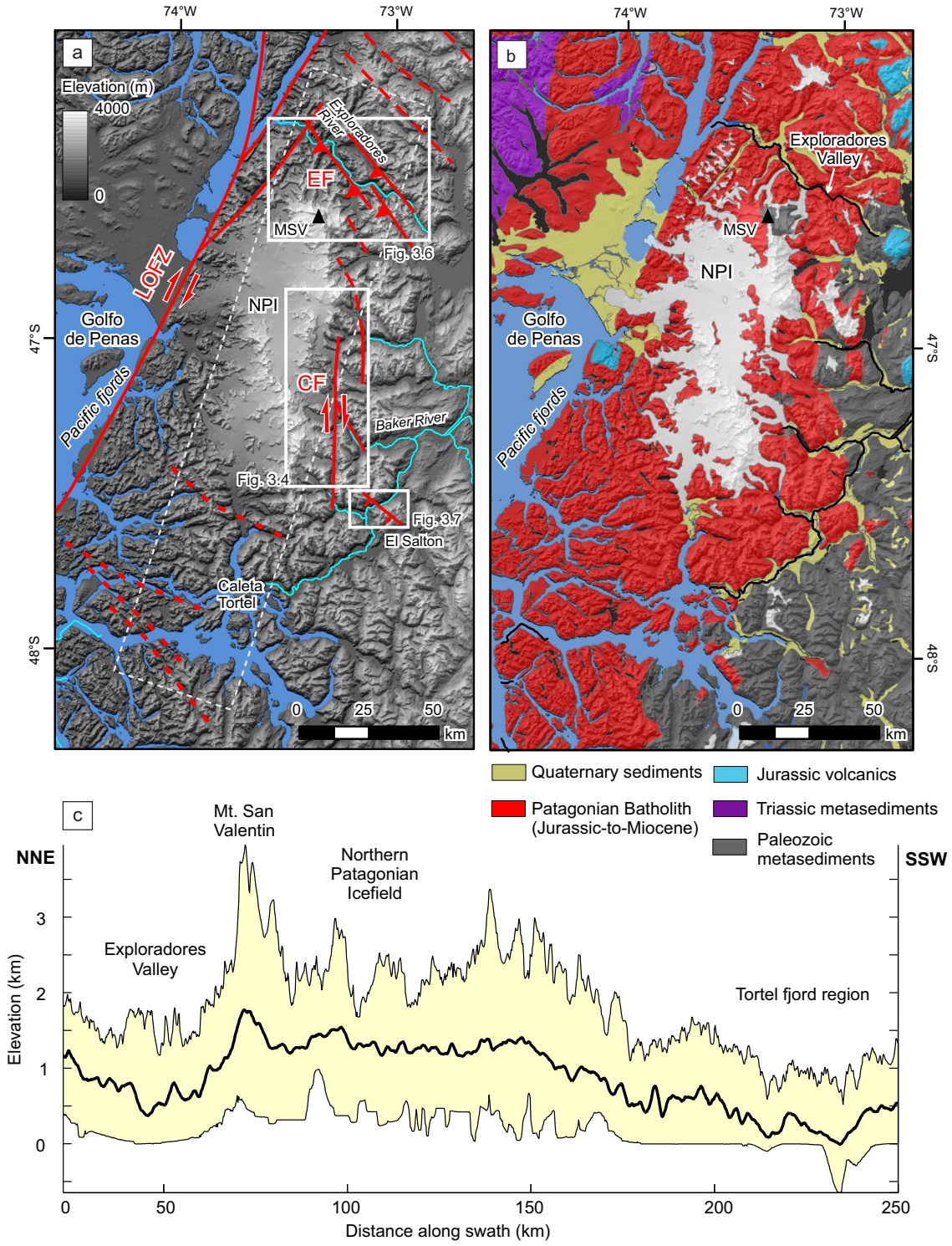

Figure 3.3 – Study areas at the Northern Patagonian Icefield. (A) Topography (SRTM-1 30-m resolution) and tectonic structures (red lines) in the study area; LOFZ: Liquiñe-Ofqui Fault Zone; EF: Exploradores Fault Zone; CF: Cachet Fault; NPI: Northern Patagonian Icefield; MSV: Mount San Valentin. White rectangles indicate location of Figures 3.4, 3.5, and 3.7. Stippled white rectangle indicates the area of the swath profile presented in (C). (B) Geological map of the Northern Patagonian Icefield modified after SERNAGEOMIN (2000) 1:1 Mio. Geological Map of Chile. (C) Swath profile along strike of the Northern Patagonian Icefield (white rectangle in (A)). Vertical exaggeration factor 26.

the fault extends between the Pared Norte and Soler glaciers (Figure 3.4B), sporadically represented by brittle faults observed at outcrop scale. Unfortunately, well-exposed fault planes and slickensides with clear kinematic indicators are rare. Nonetheless, mafic, pegmatitic, and aplitic dikes are displaced along the fault between the Soler and Nef glaciers and east of the Colonia glacier. The few observed sub-meter displacements record a right-lateral sense of motion along steep (60 to 90° dipping) faults striking between N10W and N10E with subhorizontal lineations (inset in Figure 3.4B), see dataset in Figure A.7 in Appendix A3). North of the Soler glacier, the Cachet Fault loses continuity. Based on satellite imagery, we infer that it transitions into several NNW-SSE striking, right-stepping en échelon faults that merge into the Exploradores Fault Zone farther north (Figure 3.3A).

The Cachet Fault crosscuts the three main eastward-draining glacial outlet streams - the Nef, Colonia, and Pared Norte glaciers (Figure 3.4A). A pronounced dextral deflection of the main glacial valleys and glaciers occurs at the fault crossing. Furthermore, three smaller glaciers and glacial cirques west of the fault can be consistently correlated with beheaded valleys east of the fault (red lines in Figure 3.4B), confirming the dextral offset pattern. The upper ends of the three eastward-draining beheaded valleys east of the Cachet Fault are exposed along the three main glacier valleys (Figure 3.4A, B, Figure 3.5A). The truncated valley floors lie between 300 and 450 m above the main trunk valleys. They form narrow (< 1-km-wide), headward-open cirques containing small lakes. The most conspicuous case of valley beheading occurs where fluvial or glacial valleys have been completely truncated by faults and disconnected from upstream areas (Brocard *et al.*, 2011; Simon *et al.*, 2013). Beheading by lateral erosion of the trunk glacier is possible [Bishop, 1995], but in this case unlikely, given the consistency of truncation and the correlation with valleys west of the main fault. Beheading by strike-slip faults occurs where the rate of horizontal displacement is significantly larger than the rate of lateral migration of the river or glacier crossing the fault (e.g. Sieh & Jahns, 1984; Lindvall *et al.*, 1989; Simon *et al.*, 2013). The smaller glaciers were probably not able to keep pace with rates of horizontal offset and lost continuity with their lower valley sectors, which were then disconnected from the corresponding accumulation areas.

To provide a first-order approximation for the amount of dextral slip along the Cachet Fault, we selected three pinpoints (two ridgelines and the valley bottom) for each displaced valley on either side of the fault trace (Figure 3.4B) and measured their displacements across the fault. The variability within each set of six pinpoints (representing 1 displaced valley) is recorded in the error bars for each measured offset. The Pared

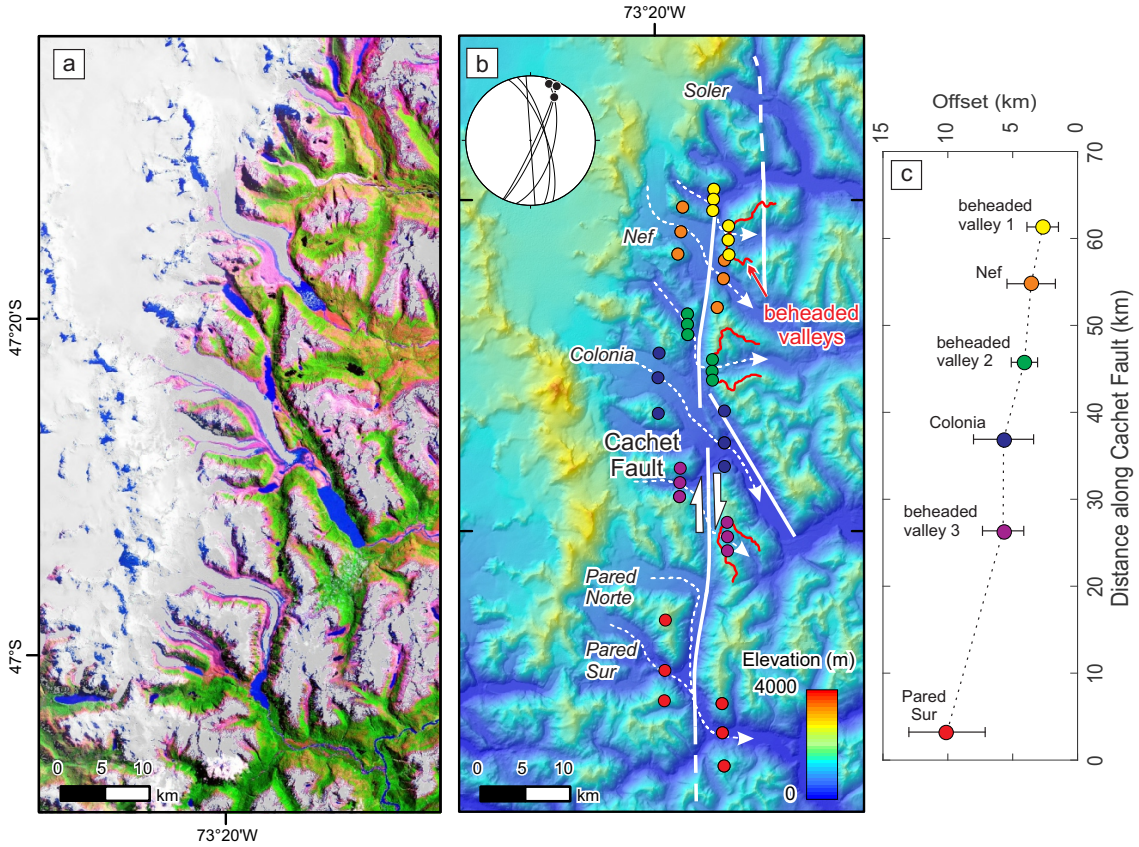

Figure 3.4 – Cachet Fault (A) Satellite image (ASTER imagery, USGS) of the eastern flank of the Northern Patagonian Icefield spanning the Cachet Fault (CF). Note the pronounced right-lateral deflection of the Nef, Colonia and Pared Norte outlet glaciers at their intersection with the Cachet Fault. (B) Topography (SRTM-1 30 m) and fault structures (white lines) related to the Cachet Fault. Red lines indicate beheaded valleys along the main fault trace. Note that all three beheaded valleys drain towards the east. Inset shows stereoplot of fault planes an lineations along main fault trace. White dashed arrow lines indicate the correlation of displaced glacial and beheaded valleys across the fault trace. Colored circles correspond to pinpoints (3 per displaces valley) used for displacement estimates and calculation of error bars in (C). See text for explanation. (C) Displacement-distance plot along the Cachet Fault. Symbols are color-coded according to (b).

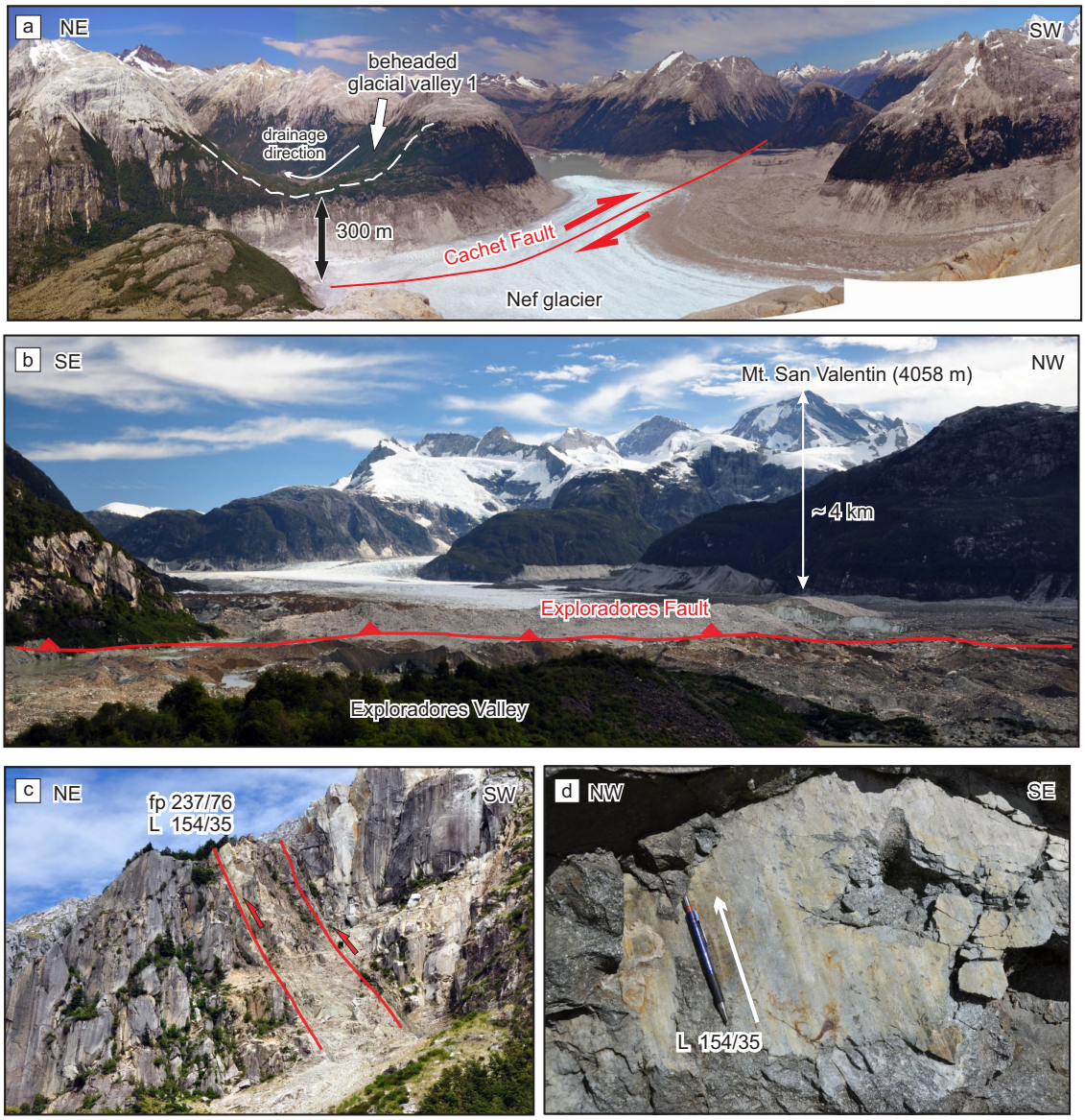

Figure 3.5 – (A) Field view of the deflected Nef glacier and the northernmost beheaded glacial valley along the trace of the Cachet Fault. The white stippled line indicates the ridgeline along the truncated valley head. Note the low-elevation corridor towards the south in the continuation of the Cachet Fault. (B) View of the northern flank of the Northern Patagonian Icefield where summit elevations and relief abruptly increase from the bottom of the Exploradores Valley to the top of Mt. San Valentin. (C) and (D) Steep reverse, top to NNW fault structures along the Exploradores Valley.

Norte and Pared Sur glaciers (southernmost site along the Cachet Fault) appear to have flowed together into the wider corresponding valley on the eastern side of the Cachet Fault. In this case, we tested for the maximum and minimum offsets by independently correlating these two glacial valleys from the western fault block with the trunk valley east of the fault (Figure A.3 in Appendix A3). For the present discussion we prefer a more conservative approach and favor the lower estimate in order to avoid an over-interpretation of the offset trend.

The displacement along the Cachet Fault varies between 3 and 10 km. It appears to decrease northward along the main fault strand between the Pared Sur and Soler glaciers (Figure 3.4C), although this pattern is ambiguous because of the large uncertainties of the method. To the north, the Cachet Fault changes to discontinuous, NNW-SSE striking faults with a right-stepping en échelon geometry, whereas south of the Pared Sur glacier, it appears to die out abruptly close to the intersection with El Salton normal fault (Figure 3.3A, Section 3.4.3).

3.4.2 Exploradores Fault Zone

The Exploradores Fault Zone spans the northern foothills of the NPI (Figure 3.3, Figure 3.6), and consists of N120E-striking, moderate–to-steeply southwestward dipping (50-80°) reverse faults with a minor strike-slip component. It coincides with the course of the Exploradores Valley, which marks the almost 4 km drop in relief at the northern flank of the NPI (Figure 3.2B, and Figure 3.5B). The valley traverses the orogen obliquely at low elevations (< 350 m) between Lake General Carreras in the east and the Pacific fjords in the west (Figure 3.6A). In the southeastern Exploradores Valley, metamorphic basement of siliciclastic metasediments with abundant intercalations of marble is exposed(Herve *et al.*, 1999), which constitutes the host rock for the Patagonian Batholith (Figure 3.3B). Passing the transition into the granitoids towards the northwest, the valley narrows and slopes become steeper; metamorphic basement is exposed only at the summit of Mt. San Valentin and its northern face. In this part of the valley, the general NW-SE oriented course of Rio Exploradores is interrupted by several sharp turns (Figure 3.6B), which are associated with pronounced N120E-striking lineaments that intersect the valley at a high angle, suggesting a possible structural control on the river course. In the field, these lineaments coincide with 10- to 15-m-wide fault zones characterized by closely spaced brittle faults (Figure 3.5C, D) The fault planes dip steeply toward the SW (fault plane 237/76, dip direction/dip), and the SE-plunging lineations indicate oblique reverse faulting with a minor lateral component (lineation 154/35, dip direction/plunge, Figure 3.5D). Along the Exploradores Valley, numerous road cuts expose similar faults.

The structural data from the Exploradores Valley are presented in two groups corresponding to outcrops from the northwestern and southeastern parts of the valley (Figure 3.6B, side panel). Outcrops are scarce and difficult to access, which limited the number of structural measurements collected, thus precluding a more quantitative interpretation of the data. The northwestern data set (upper stereoplot in Figure 3.6B) reveals two main preferred orientations: A NW-SE striking set of fault planes, which are moderately to steeply dipping to the SW (N30W, 60-80°) and are parallel to the strike of the Exploradores Valley, with N90W-N140W plunging lineations consistently showing reverse shear sense. Another NNE-SSW striking set of fault planes dips steeply or vertical (N20E-N40E, 60-80°) with a similar orientation with respect to the LOFZ. The structural data from this part of the valley likely reflect an interference pattern resulting at the intersection of the Exploradores Fault Zone with the eastern strands of the LOFZ (Figure 3.6B, Figure 3.3B). The few measurements from the southeastern part of the valley (lower stereoplot in Figure 3.6b) still reflect the NW-SE orientation of the Exploradores Fault Zone, although the overall pattern is less systematic. The geometry of macro- and meso-scale structures and the analysis of fault-kinematic indicators suggests oblique reverse faulting along the Exploradores Fault Zone.

3.4.3 El Salton Fault

Recent extensional deformation was observed at the El Salton Fault located in the southeastern foothills of the NPI near the southern termination of the Cachet Fault (Figure 3.3A). The NW-SE striking El Salton Fault is oriented at a high angle to the Rio Baker, which flows along the eastern flank of the icefield, draining the eastward-flowing glacial outlets and Lake General Carreras into the Pacific Ocean. Near the southern termination of the Cachet Fault, Rio Baker follows a pronounced gorge with steep walls bounding a floodplain up to 1 km wide (Figure 3.7). The area locally known as “El Salton” (“the Big Jump” in Spanish) is characterized by an abrupt, 600-m-long narrow segment of Rio Baker (down to only 20 m width) associated with a 15-m-high abrupt drop in elevation forming a distinct knickpoint (Figure 3.7A). Based on published maps and field observations, we found no evidence for a more resistant lithology that might control the location of the knickpoint. The pronounced knickpoint and channel narrowing at El Salton are unique along the entire course of the Rio Baker, which is otherwise characterized by a wide, gently meandering channel. The Rio Baker valley has been free of ice since at least 13 ky (Turner *et al.*, 2005). Subsequent fluvial erosion appears to have obliterated subglacially formed knickpoints, which could be potentially mistaken for those associated with active faulting.

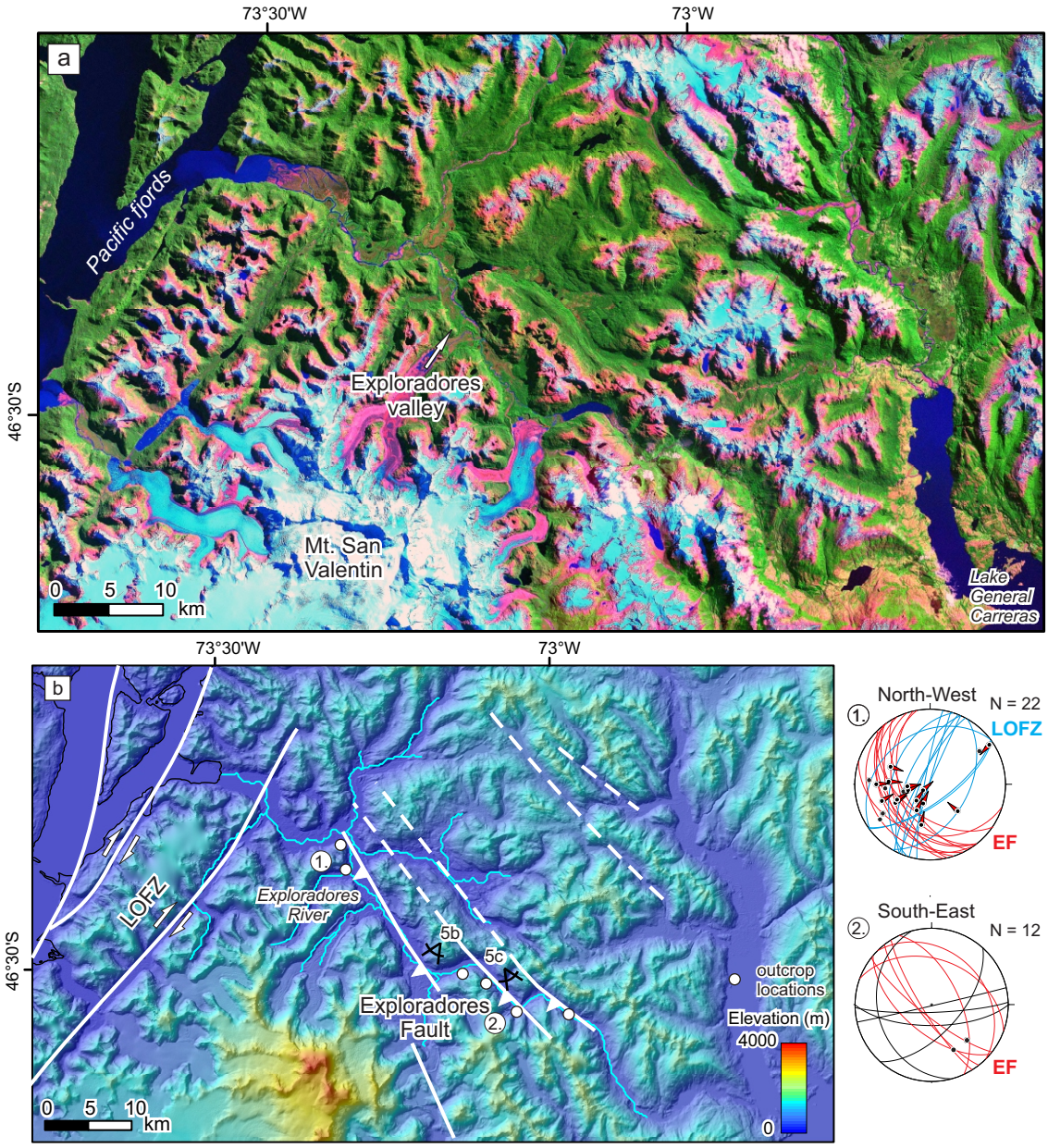

Figure 3.6 – Exploradores Fault Zone (S) Satellite image (LANDSAT, data available from the U.S. Geological Survey) of the NW-SE oriented Exploradores Valley spanning the northern foothills of the NPI. Note the sharp NW-SE striking landscape lineaments parallel to the mapped fault structures in (B). (B) Topography (SRTM-1 30 m) and main fault structures (white lines) along the Exploradores Valley. Note sharp turns in the course of the upper Exploradores Valley coinciding with fault structures related to the Exploradores Fault Zone. Stereoplots summarize structural measurements (fault planes and striations with shear sense where measured) from outcrops (white circles on map) in the NW (plot 1) and SE (plot 2) part of the valley. Red and blue fault planes highlight orientation of structures related to the Exploradores Fault Zone (EF) and LOFZ, respectively. The black great circles in the lower stereoplot correspond to likely older fault planes with differing orientation originating from the metamorphic basement (cf. Figure 3.3B).

Immediately adjacent to the El Salton knickpoint, two 3-km-long, N120E-oriented and SW-facing scarps are found northwest of Rio Baker, forming a staircase morphology clearly visible on a DEM generated from 1-m topographic contours (surveyed by a local mapping agency) (Figure 3.7B). The scarps cross the river and farther to the southeast bend toward a more westerly direction (N90E-N100E) where they lose continuity and geomorphic expression as the valley walls become steeper. Field observations confirmed that the scarps are related to N120E–N90E-striking and SSW-dipping faults with moderate-to-steep (50-80°) SSW-plunging lineations and kinematic indicators of dip-slip, normal displacement (Figure 3.7B, inset). Rio Baker is the river with the highest discharge in Chile (Escobar, 1992) and thus knickpoints that are not associated with active faults would be expected to retreat rapidly as a result of rigorous fluvial erosion. The persistence of a pronounced river knickpoint in this major glacial valley coincident with the sharp disruption of the smooth glacial landforms by the faults suggests active deformation by extensional processes. Given that the Rio Baker valley has been ice-free since at least 13 ky (Turner *et al.*, 2005) and assuming that tectonic offset predating this time was somehow balanced by glacial erosion, this interpretation implies a maximum vertical fault slip rate of 1.2 mm/yr since 13 ky to produce the observed 15 m of vertical offset.

3.5 Results from Apatite (U-Th)/He Thermochronometry

We sampled bedrock for apatite (U-Th)/He (AHe) thermochronology with two main objectives: (1) to decipher Late Cenozoic apparent exhumation rates from age-elevation relationships (AERs) of bedrock samples, which represent the first elevation transects documenting cooling histories from the glaciated region of the orogen's interior south of the CTJ; and (2) to detect differences in the level of exhumation between the two main sampling regions (Nef and Leones catchments), which could constrain relative deformation as well as the timing and magnitude of movement along the Exploradores Fault Zone.

We obtained AHe cooling ages from 30 bedrock samples (Figure 3.8A). All samples are from Late Jurassic to Cretaceous granites and granodiorites of the Patagonian Batholith. Twenty-three of the dated samples were taken along two elevation transects in the Leones and Nef glacial catchments, which lie 30 km apart at the eastern flank of the NPI (Figure 3.8A, B). Of the remaining samples, one originates from the lower parts of the Leones valley (200 m a.s.l.), one from the valley bottom of the Exploradores Valley (35 m a.s.l.), and three other samples come from the Colonia valley, east of the Cachet Fault

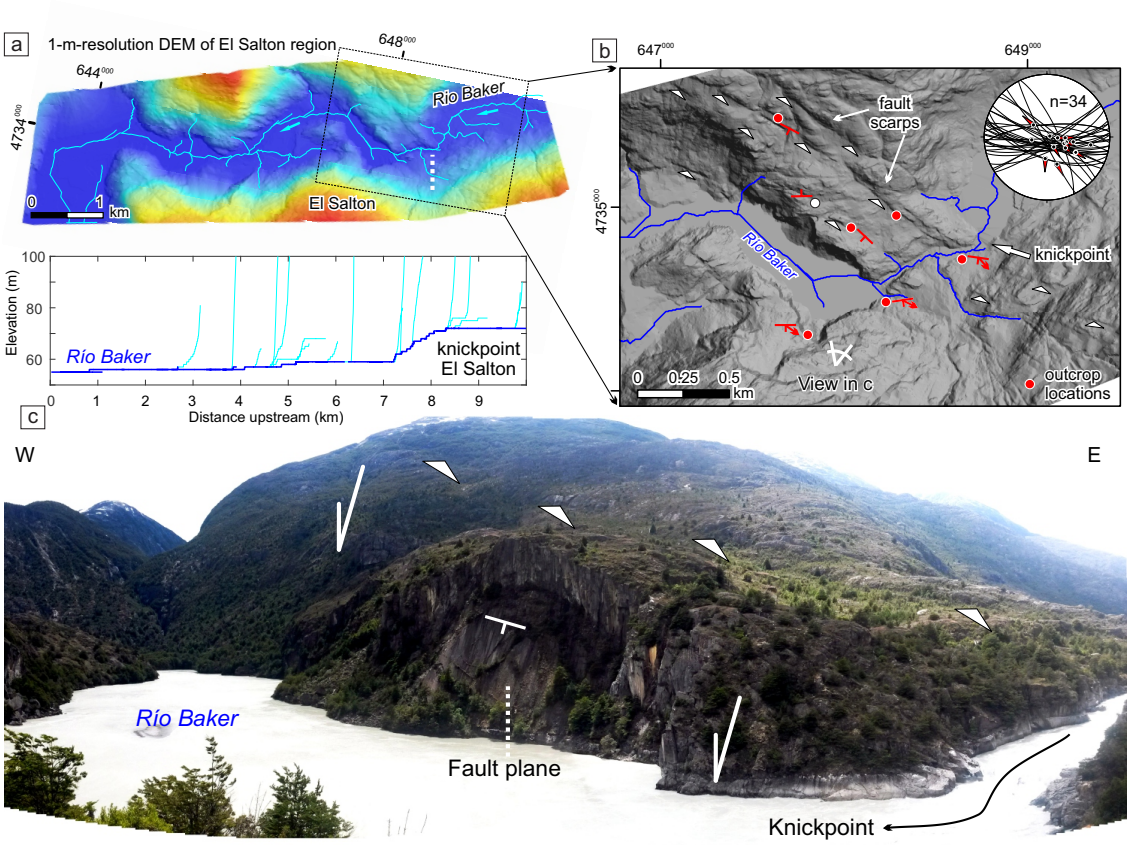

Figure 3.7 – El Salton Fault. (A) High-resolution topography (based on 1-m contour lines) of the El Salton region along the Rio Baker at the southeastern tip of the Northern Patagonian Icefield (cf. Figure 3.3A). Note the river knickpoint associated with the location of the El Salton Fault. (B) Hill-shaded relief of the El Salton region. White triangles indicate the trace of pronounces landscape scarps likely associated with fault structures. Inset in the upper right corner shows measured fault planes (n=34, black lines) and lineations (n=15) with shear sense indicators (red arrows). The stereoplot is a composite projection of measurements collected at outcrops indicated by red circles. (C) Field view of the Baker River at the exit from the narrow channel known as El Salton. Note the exposed fault planes aligning with the knickpoint of the river in the lower part of the channel. More degraded landscape escarpments towards the north form staircase morphology and correspond to the clear lineaments visible in the hill-shade topography in (B).

at elevations between 300 and 880 m. Two dated samples were excluded from the AER-regressions due to high age-dispersion in the single aliquots that lack correlation with variations in U-content or grain size (see Appendix B).

The Leones profile in the north encompasses 16 samples between 300 and 2100 m a.s.l. over a horizontal distance of 18 km, reaching the accumulation zone of the Leones Glacier above the ice plateau. The Nef profile in the south encompasses 7 samples between 230 and 1450 m over a horizontal distance of 13 km in the upper catchment of the Nef Glacier, also slightly exceeding the local level of the ice plateau. The quality of the obtained apatite grains is mostly very good, but it decreases with elevation in both profiles. It was not possible to obtain good-quality apatites from samples collected at more than 300 m above the local level of the ice plateau. Also, dispersion in single-grain ages within individual samples increases with elevation, which is reflected in the larger age uncertainties for the highest samples. Mean ages were calculated for three to five single-grain aliquots per sample.

Mean ages range from 4.6 ± 1.1 Ma to 8.1 ± 0.3 Ma for the Nef profile, and from 2 ± 0.5 Ma to 6.8 ± 1.1 Ma for the Leones profile (Figure 3.8B). The three samples from the Colonia Valley yield mean ages between 5.3 ± 0.4 and 6.6 ± 0.9 Ma and sample VG12-EX11 from the Exploradores Valley has a mean age of 4.2 ± 0.4.

3.6 Interpretation of Apatite (U-Th)/He Data

The AHe cooling ages are positively correlated with elevation in both the Leones and Nef elevation transects (Figure 3.8B). Sample LE08-02 (4.3 ± 0.7 Ma, not shown in Figure 3.8B) from the lower Leones Valley has not been included in the age-elevation regression analysis because it is located 10 km downstream from the steep elevation transect (Figure 3.8B). This sample shows an incipient trend toward older ages downstream, although there are not enough data to confirm this. Similarly, a low-elevation sample from the downstream Nef region yields relatively older ages (AG08-08, not shown in Figure 3.8B); this sample was not included in the regression analysis due to a large spread of single-grain ages (between 8 and 19 Ma, see dataset in Figure A.1 in Appendix A2). The samples from the Nef region were collected across the northern tip of the Cachet Fault. Samples from similar elevations on either side of the fault yield similar ages, indicating that there is no significant vertical offset, at least within the resolution of the data. This result is in line with our field-based interpretation of dominant lateral movement along the Cachet Fault.

The slope calculated from a linear regression of mean ages (bootstrap analysis with 1000 samples) averages 0.5 ± 0.1 mm/yr in both Nef (r2 = 0.85) and Leones (r2 = 0.68) age-elevation relationships (AERs) (Figure 3.8B, c). There is no evident break in slope in the AERs, suggesting uniform apparent exhumation rates between 6 and 2 Ma for the Leones catchment and between 8 and 4 Ma for the Nef catchment.

A notable feature in the AER plot is the prominent offset in cooling ages between the two regression lines (Figure 3.8B). Both single-grain and mean ages from the Leones catchment (blue symbols in Figure 3.8B) are consistently younger than the cooling ages of corresponding samples at similar elevations from the Nef catchment (red symbols in Figure 3.8B). The offset between the two AERs averages 2 Ma and is distinct at the 1σ confidence level (dashed blue and red lines in Figure 3.8B). The observed offset between the two regression lines is equivalent to a vertical offset of about 1 km, as can be inferred from the mean difference in the zero-age intercepts of the linear regressions (bootstrap analysis with 1000 iterations) (Figure 3.8D).

The observed offset between the AERs could result from a differing depth of the AHe closure isotherm below both regions. In this case, because there is no prominent break-in-slope in the AERs, the difference in isotherm depth must have been established and stayed stable since at least 6-8 Ma, which is the time when the highest (oldest) samples from both AERs crossed the AHe closure isotherm. If the closure isotherm were shallower in the north (Leones catchment), the exhumation paths above it would be consistently shorter and the samples would yield younger cooling ages. In this case, assuming a background exhumation rate of 0.5 mm/yr (Figure 3.8B, C), approximately 1 km of deflection of the closure isotherm would be required to explain the 2-Ma age difference between the two catchments. Localized warping of shallow isotherms could result from the existence of a long-lived fault between the elevation transects [e.g. Ehlers and Farley, 2003]; however, there is no field evidence for any active or inherited faults between them. Alternatively, spatial differences in the thermal structure of the crust could arise in slab-window environments (Thorkelson, 1996; Groome & Thorkelson, 2009). A northward migration of crustal heating related to slab-window opening has been proposed for this region based on cooling ages from the eastern foreland (Guillaume *et al.*, 2013). This heating wave was detected over large distances (250 km) and proposed at 15 Ma for the latitudes of Leones and Nef regions (47°S), and at 5 Ma for the Coyhaique region 200 km to the north (45.5°S). Given the short distance between the Leones and Nef regions (30 km) relative to the spatial extent of the slab window (several hundreds of km), it is likely that both regions would be equally and nearly synchronously affected by

crustal thermal perturbations, likely well before the samples from both AERs crossed the closure isotherm. Moreover, the thermal impact of the migrating slab window is a dynamic signal (Groome & Thorkelson, 2009; Guillaume *et al.*, 2010), which is unlikely to have remained stable for 6 to 8 m.y. Based on these arguments, we conclude that a differing depth of the closure isotherm is not a likely scenario.

Alternatively, if the closure isotherm beneath both regions were located at a similar depth (Figure 3.9), systematically younger ages from the Leones region in the north would reflect deeper levels of exhumation. Because both AERs have the same slope within error, we assume similar exhumation rates for the time frame constrained by AHe cooling ages - between 8 and 4 Ma in the Nef region and between 6 and 2 Ma in the Leones region. Hence, the differential pulse of exhumation responsible for the 2 Ma-offset in cooling ages between samples from similar elevations, which corresponds to 1 km of differential exhumation, must have occurred after closure of the AHe system for the youngest (lowest elevation) samples, i.e., 2-3 Ma (Figure 3.8B). A process inducing differential rock uplift is necessary, because deeper erosion alone (Figure 3.9A) could not account for the consistent offset in cooling ages between the AERs at similar elevations. Differential uplift could result from: 1) an isostatic response to differential erosion (with more effective erosion in the Leones region compared to the Nef region; Figure 3.9B); 2) differential (e.g. tectonic) rock uplift (with a higher magnitude of tectonic uplift in the Leones region; Figure 3.9C); or 3) a combination of both.

Assuming a range of geothermal gradients between 35 and 45°C/km, the calculated apparent exhumation rate of 0.5 mm/yr yields a cooling rate of 17-22°C/Ma. For such relatively fast cooling rates, together with the relatively young AHe bedrock cooling ages, we can assume that the effect of radiation damage on He diffusion (i.e., on closure temperature) (Flowers *et al.*, 2009; Gautheron *et al.*, 2009) is negligible and that the commonly used closure temperature for He diffusion in apatite of 70°C is a reasonable assumption (Shuster *et al.*, 2006). A range of geothermal gradients between 35 and 45°C/km results in an expected closure depth between 2 and 1.5 km.

We explored probable erosion rates and depths to the closure-temperature environment using Willett & Brandon (2013)'s MATLAB script AGE2EDOT, which provides a steady-state solution of 1D- erosion rates from a single thermochronometric age (Willett & Brandon, 2013). Assuming typical thermal properties of the crust and a modern geothermal gradient between 35 and 45 °C/km, the youngest apatites from the Leones region (2 Ma at an elevation of 300 m) require exhumation rates between 0.6 and 0.9 mm/yr, equivalent to 1.2 to 1.8 km of eroded material since 2 Ma. For the Nef

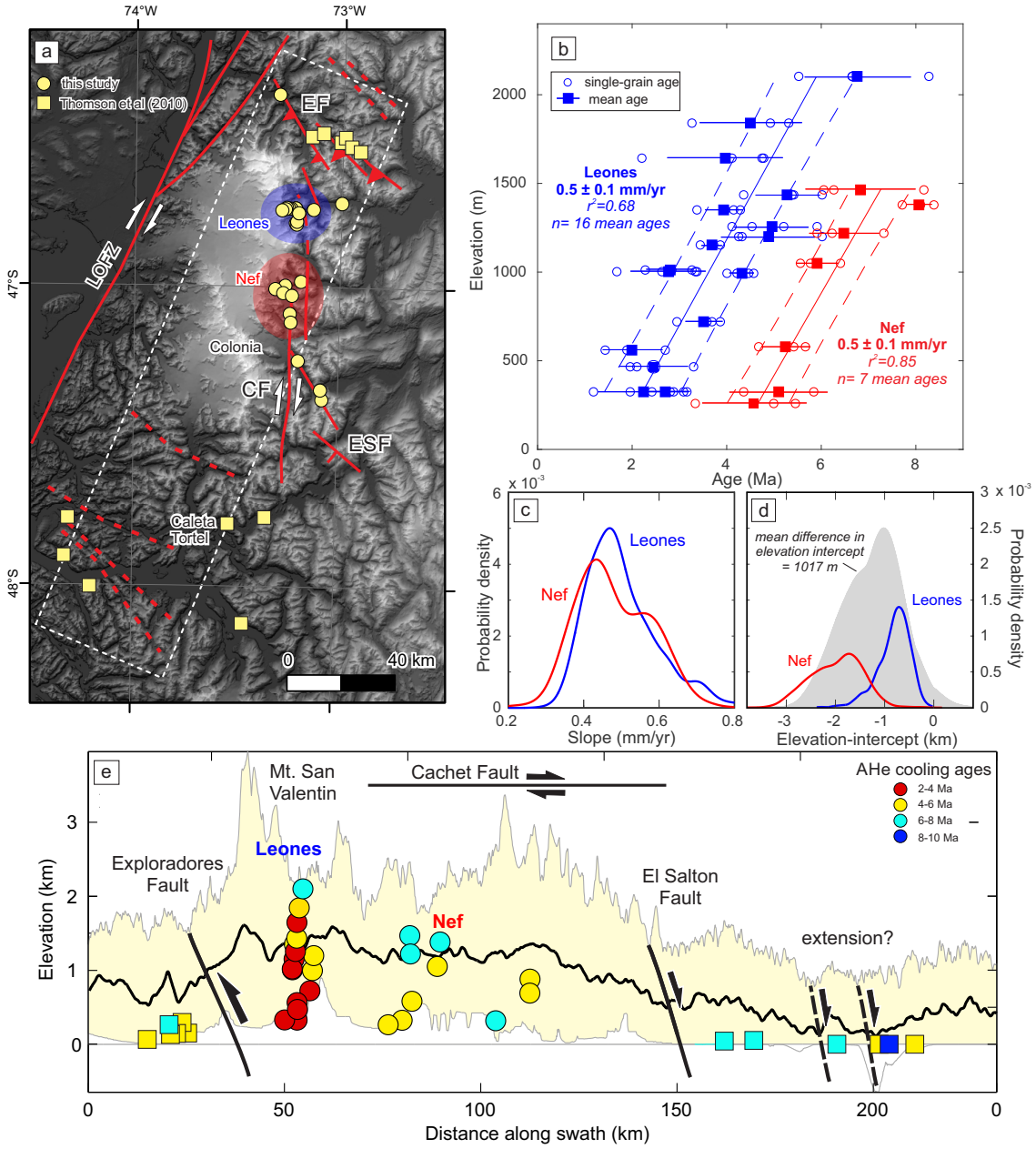

Figure 3.8 – (A) Topography (SRTM-1 30 m) of the Northern Patagonian Icefield region with main fault structures and location of bedrock samples used for apatite (U-Th)/He (AHe) dating. Circles are samples presented in this study; squares correspond to AHe data from Thomson *et al.* (2010). Dashed white rectangle indicates area for swath profile in (E). EF/CF/ESF: Exploradores/Cachet/El Salton faults. (B) Age-elevation relationships with single (hollow circles) and mean (filled circles) ages from the Nef (red) and Leones (blue) catchments. Dashed lines indicate the 1σ confidence interval for the linear regression of mean ages. Note the equal slope (C) and the difference in zero-age elevation intercept between both AERs of about 1 km (D) as inferred from the mean of the difference in probability density functions of the intercepts obtained from a bootstrap analysis of the linear regressions. (E) AHe data color-coded by mean ages and projected with sample elevation along the swath profile from the area indicated in (A). Black lines indicate the approximate location of the Exploradores and Cachet faults at the flanks of the NPI, as well as possible extension in the Tortel fjord region. Vertical exaggeration factor 15.

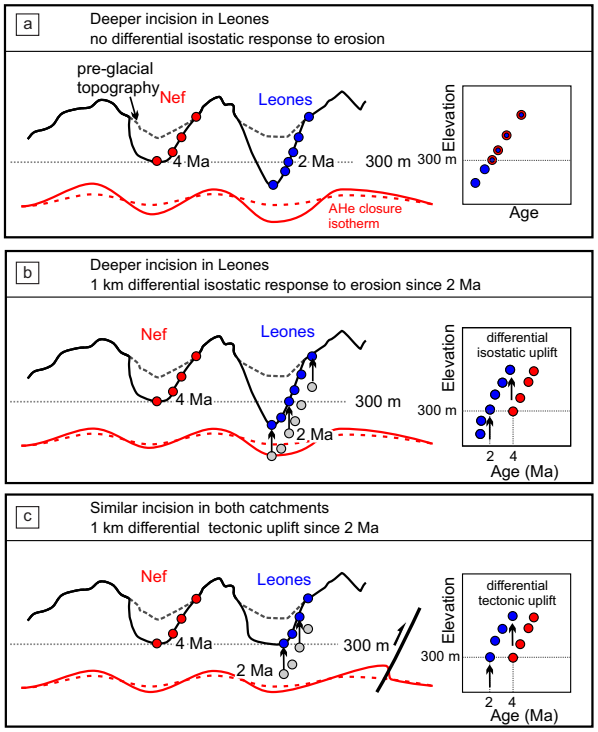

Figure 3.9 – Schematic representation of different scenarios for landscape evolution and sample history with corresponding plots of age vs. elevation for Nef (red symbols) and Leones (blue symbols) regions. The samples at 300 m elevation with AHe cooling ages of 2 Ma (Leones) and 4 Ma (Nef) represent a reference level from the original data set. Red stippled and continuous lines sketch AHe closure isotherm before and after incision, respectively. (A) Deeper incision in the Leones region after 2 Ma without differential isostatic response to erosion. (B) Deeper incision in the Leones region and differential isostatic response after 2 Ma with higher magnitude in Leones. (C) Similar incision in both regions with superposed differential tectonic uplift after 2 Ma with higher magnitude in Leones (located closer to the fault). This scenario represents best the observed topography (similar catchment morphology) and thermochronological data (AERs, see Figure 3.8B).

region, the same calculation for the youngest samples (4 Ma at an elevation of 300 m) results in exhumation rates between 0.2 and 0.4 mm/yr, equivalent to 0.8 to 1.6 km of eroded material since 4 Ma (see Figure A.4 and A.5 in Appendix A3). Compared to the exhumation rates between 6 and 2 Ma for the Leones region (0.5 mm/yr), the above calculation implies an increase in exhumation rate of between 0.1 and 0.4 mm/yr averaged over the last 2 Ma. For the Nef region, no increase in exhumation rate after 4 Ma can be detected. Given that the extent of Plio-to-Pleistocene glaciations in Patagonia was similar to previous advances (Mercer & Sutter, 1982; Singer *et al.*, 2004; Lagabrielle *et al.*, 2010), and that glacial erosion was likely a major controlling factor of regional exhumation during this time period, we consider a decrease in exhumation rate down to 0.2 mm/yr after 4 Ma unlikely (lower estimate in the Nef region based on higher geothermal gradient). Therefore, we rather favor the assumption of a lower geothermal gradient around 35°C/km and the higher estimates for exhumation rates after 2 and 4 Ma in the Leones and Nef regions, respectively.

The first possibility for differential uplift (differential erosion) requires a higher magnitude of erosional exhumation in the Leones region compared to the Nef region since

2 Ma (youngest/lowest elevation samples, Figure 3.8B). The Patagonian Andes have been glaciated since 5-7 Ma (Mercer & Sutter, 1982; Lagabrielle *et al.*, 2010) and were repeatedly subjected to extensive glacial advances during glacial maxima (Singer *et al.*, 2004; Kaplan *et al.*, 2005). Moreover, glaciation intensified during the Quaternary (Haug *et al.*, 1999; Ravelo *et al.*, 2004; Clark *et al.*, 2006), which may have impacted erosion, as inferred from several thermochronometric studies elsewhere, such as in British Columbia (Shuster *et al.*, 2005; Ehlers *et al.*, 2006) and the European Alps (Valla *et al.*, 2011b; Herman *et al.*, 2013). More intense regional glacial erosion might have contributed to the accelerated exhumation after 2 Ma (steepening of both AERs), but erosional exhumation must have been more efficient in the Leones relative to the Nef region to explain the observed shift in ages between the sample transects.

Ice dynamics comprise non-linear processes (Cuffey & Paterson, 2010; Herman *et al.*, 2015), and glacial erosion is proportional to ice sliding velocity (Hallet, 1979; Humphrey & Raymond, 1994; MacGregor *et al.*, 2009; Iverson, 2012) or ice flux (Anderson *et al.*, 2006). Erosional processes are therefore very sensitive to changes in topography or ice accumulation. It is questionable whether the analysis of modern catchment hypsometries and glacial characteristics is representative of the erosional potential averaged over several million years, but they could be used to provide first-order assessments of major differences in glacial erosion efficiency (Brocklehurst & Whipple, 2004; Anderson *et al.*, 2006; Sternai *et al.*, 2011; Yanites & Ehlers, 2012).

The neighbouring Leones and Nef catchments host two of the principal eastward-draining glacial outlets of the NPI, the Leones and Nef glaciers. Both glacial catchments are located on the same flank of the icefield and therefore have been exposed to analogous climatic conditions affecting the dynamics and thermal state of the ice, which are in turn linked to erosion (Hallet, 1979; MacGregor *et al.*, 2009; Iverson, 2012). Both catchments have very similar topographic characteristics as indicated by hypsometric integrals (0.463 for Nef, 0.387 for Leones) and catchment-surface areas (230 km^2 for Nef, 208 km^2 for Leones, see Figure A.6 in Appendix A3). The ice-surface and ice-accumulation areas of the Nef glacier are 126 km^2 and 79 km^2, respectively, and are nearly twice the corresponding areas in the Leones catchment (66 km^2 and 47 km^2). Both catchments feature similar overdeepenings of the valleys close to the glacier termini, reaching sea level and below. In the Leones region, where glacier retreat has been more significant, the overdeepened sector is occupied by a proglacial lake (Lake Leones). In the Nef region, the overdeepened section is still covered by ice, but has been inferred from a ground-penetrating airborne radar system (Centro de Estudios Cientificos, 2012;

Rivera *et al.*, 2014). In summary, neither catchment nor glacial characteristics in these regions support more efficient erosional exhumation in the Leones catchment compared to the Nef catchment. Hence, differential glacial erosion and isostatic rebound cannot be responsible for the 1-km-greater rock uplift in Leones since 2-3 Ma compared to Nef. We argue here that another process must have not only created the observed difference in uplift/exhumation, but also compensated for potentially greater glacial erosion and isostatic rebound in the Nef catchment.

A second hypothesis for differential exhumation invokes a superimposed pulse of tectonic rock uplift that affected the Leones region, but not (or less so) the Nef region (Figure 3.9C). Again, such a pulse must have occurred after 2-3 Ma, uplifting the samples from the Leones AER after all samples had already crossed the AHe closure isotherm. The southernmost strands of the N120E-striking Exploradores Fault Zone are located approximately 30 and 60 km north of the Leones and Nef catchments, respectively (Figure 3.8A). These are steeply dipping reverse faults that may represent inherited, steeply dipping basement structures, linked to the long-term structural evolution of the margin and likely reaching deeper crustal levels. Reactivation of these structures in recent times could account for a gradual increase of rock uplift and exhumation in the hanging wall approaching the faults, and therefore be responsible for deeper levels of exhumation in the Leones catchment. We therefore favor the interpretation of the shift in cooling ages between the AERs resulting from an increasing depth of exhumation related to differential tectonic rock uplift along the Exploradores Fault Zone (Figure 3.9C). The absolute magnitude of the increase in exhumation rate (0.1-0.4 mm/yr for Leones, Figure A.4 in Appendix A3) likely reflects the combined effects of locally superimposed tectonic uplift along the Exploradores Fault Zone and of possibly more intense glacial erosion over the Quaternary. However, because there is no detectable increase in exhumation rates for the Nef catchment during the Quaternary, the effect of Quaternary glaciations on exhumation patterns is probably similar to that of earlier glaciations. Based on the previous arguments, we conclude that 2-3 Ma (youngest samples in Leones) is the maximum timing for the onset of motion along the Exploradores Fault Zone.

3.7 Discussion

3.7.1 The Controversy on Patagonian Topography

Several hypotheses have been put forward to explain the abrupt rise in summit elevations and relief from the Northern to the Southern Patagonian Andes at 46°S (Ramos & Kay, 1992; Ramos, 2005; Lagabrielle *et al.*, 2007; Thomson *et al.*, 2010; Guillaume

et al., 2010, 2013). Thomson *et al.* (2010) explained the higher elevations in Southern Patagonia with a first-order influence of climatically controlled processes on internal dynamics of mountain building (Whipple & Meade, 2006; Tomkin & Roe, 2007). In their interpretation, less erosive glaciers associated with the cooler climate of the Southern Patagonian Andes were inferred to have armored the mountains, inhibited erosion, and ultimately promoted topographic growth. The authors based their conclusion on an extensive low-temperature thermochronometry data set (AHe and apatite fission track). However, their observed trend towards older ages to the south are likely an artefact of spatially biased sampling (Thomson *et al.*, 2010, their Figure 1). For example, younger cooling ages from the Northern Patagonian Andes (north of the CTJ) are from the intra-arc region of the orogen and mainly along the active transpressive LOFZ (Cembrano *et al.*, 1996; Thomson, 2002; Adriasola *et al.*, 2006; Rosenau *et al.*, 2006; Lange *et al.*, 2008), where active faulting is responsible for rock uplift and faster exhumation rates, resulting in younger cooling ages (Thomson, 2002; Adriasola *et al.*, 2006). South of the CTJ, older cooling ages from their data set correspond mainly to samples located along the shoulders of deep glacial fjords in the forearc, where regional exhumation is less pronounced due to very localized erosion along distal glacial outlets. We therefore suggest that certain aspects of the model of Thomson *et al.* (2010) need to be reconsidered to reconcile their interpretation with our new data.

The thermochronological data set presented here reveals the exhumation history of the glaciated interior of the Southern Patagonian Andes, south of the CTJ. The well-constrained AERs from the Leones and Nef glacial catchments record moderate background exhumation rates of 0.5 mm/yr between 8 and 2 Ma, likely reflecting the pace of glacial erosion over this time period(Adriasola *et al.*, 2006; Thomson, 2002). Guillaume *et al.* (2013) reported a similar range of AHe data from a comparable elevation transect located 80 km southeast of our study area. Likewise, Fosdick *et al.* (2013) reported AHe data from the proximate retroarc region at 51°S documenting similarly young ages ($<$ 10 Ma, and mostly between 6 and 4 Ma), which they interpreted to indicate significant Late Miocene and Pliocene denudation by fluvioglacial erosion.

Notably, the data sets of Guillaume *et al.* (2013) and Fosdick *et al.* (2013) are rather similar to the Nef AER, i.e., they are 2 Ma older at equivalent elevations compared to the Leones AER. Hence, these data and the Nef AER likely reflect the regional exhumational patterns governed by glacio-fluvial erosional exhumation, whereas the Leones AER reflects the same regional erosion signal and an additional locally superimposed

effect, which we relate to tectonic uplift after 2-3 Ma. The Nef region might have been tectonically uplifted as well, but by a magnitude that is below the resolution of our data.

All together, the range of AHe ages matches cooling ages and predicted exhumation rates from the interior of the Northern Patagonian Andes (north of the CTJ), where Thomson *et al.* (2010) argued for efficient glacial erosion (see Figure 3.3 and Figure 4 from Thomson *et al.* (2010)). Notably, the magnitude of glacial erosion, as estimated from AERs of AHe and apatite fission-track data in Thomson *et al.* (2010)'s study, might be somewhat overestimated, considering that many of the $<$ 2-Ma AHe and $<$ 5-Ma AFT cooling ages north of the CTJ originate from the immediate vicinity of the active transpressive LOFZ (Thomson, 2002; Adriasola *et al.*, 2006; Thomson *et al.*, 2010). Taken together, our results combined with the data from

The spatial coincidence of the CTJ with the increase in summit elevations and relief suggests potential feedbacks between oceanic-ridge collision, upper-plate deformation, and relief evolution in Southern Patagonia. Modelling approaches combined with thermochronology data (Guillaume *et al.*, 2010; Braun *et al.*, 2013; Guillaume *et al.*, 2013) have highlighted how mantle flow through the slab window and related dynamic topography may be linked to the cooling history and relief evolution in Southern Patagonia. Mantle convection results in uplift or lowering of Earth's crust, with an amplitude reaching a few hundred meters and wavelengths exceeding 100 km (Hager *et al.*, 1985; Mitrovica *et al.*, 1989; Ricard *et al.*, 1993; Braun, 2010; Braun *et al.*, 2013; Faccenna *et al.*, 2014). In the Patagonian foreland, areally extensive and transient uplift is documented by uplifted Pleistocene marine terraces along the Atlantic coast reaching 180 m a.s.l. (Darwin, 1846; Pedoja *et al.*, 2011) and tilted river terraces (Guillaume *et al.*, 2009). These effects have been inferred to reflect the dynamic response of the continental lithosphere to the opening of the slab window (Guillaume *et al.*, 2009, 2010; Pedoja *et al.*, 2011). Furthermore, AHe and apatite fission-track data east of the main divide spanning 200 km along strike of the former fold-and-thrust belt have been inferred to show a northward trend towards younger ages, probably reflecting a pulse of dynamic uplift, progressive heating, and/or erosional exhumation associated with slab-window formation (Braun *et al.*, 2013; Guillaume *et al.*, 2013).

However, explaining all aspects of high topography in the Southern Patagonian Andes with deep, dynamic mechanisms is difficult. Although Guillaume *et al.* (2013) and Guillaume *et al.* (2010) proposed that the high summits of the Patagonian Andes could be explained with a transient and northward-migrating pulse of dynamic uplift, the modelled location of both the maximum dynamic uplift since 4 Ma and the cumulative

dynamic uplift since 8 Ma is in the low-elevation fjords south of the NPI (Guillaume *et al.*, 2013, their Figure 5). Furthermore, the abrupt increase in relief and summit elevations at the northern edge of the NPI and the similarly sudden drop in topography south of it occur over distances that are too short to be explained by dynamic topography. In summary, while dynamic uplift likely played an important role in the long-wavelength topographic evolution of Southern Patagonia (Guillaume *et al.*, 2009; Jeandet, 2014) and might have influenced the regional cooling signal in the eastern foreland (Braun *et al.*, 2013; Guillaume *et al.*, 2013), we emphasize the need for alternative mechanisms to explain the short-wavelength topographic variations, structural and geomorphic observations, and thermochronological data in the NPI region.

3.7.2 Neotectonics of the Northern Patagonian Icefield

The structural, geomorphic, and thermochronological data presented in this study document Late Pliocene to Quaternary fault activity at the northern and eastern flanks of the NPI. The geomorphic signature of displaced landforms along the dextral Cachet Fault suggests active lateral translation. Although the timing of the onset of motion along this structure is difficult to assess due to the lack of sedimentary deposits or unambiguous, datable markers, the displacement of previously carved large glacial landforms implies that accrued dextral offset began some time after the onset of glaciation in this region 5-7 Ma ago (Mercer & Sutter, 1982; Ton-That *et al.*, 1999; Lagabrielle *et al.*, 2010). Recent studies from the foreland at these latitudes suggest the main incision and glacial overprint of the landscape occurred as recently as 3 Myr ago and was accompanied by the reactivation of tectonic structures and disruption of the foreland in the course of oceanic-ridge collision and slab-window opening (Lagabrielle *et al.*, 2010; Scalabrino *et al.*, 2011). A time window around 3 Ma might furnish a maximum constraint for the onset of faulting along the Cachet Fault, although this is speculative. Considering the lateral offsets of glacial valleys between 3 and 10 km, a first-order estimate for a slip rate between 1 and 3 mm/yr may be inferred for the Cachet Fault.

The AHe data from the Leones and Nef regions presented here further support the onset of tectonic exhumation along the Exploradores Fault Zone at around 2-3 Ma. We infer the anomalous course of the Exploradores Valley to be at least partly structurally controlled, cross-cutting the entire Andean orogen at a high angle from the eastern foreland to the Pacific fjords (Figure 3.6). Faults with N120E strikes and steep dip angles are common farther north along the trace of the LOFZ, and have been mostly interpreted as inherited basement structures that were reactivated and kinematically linked to the LOFZ during the Quaternary (Adriasola *et al.*, 2006; Rosenau *et al.*, 2006;

Glodny *et al.*, 2008; Lange *et al.*, 2008; Melnick *et al.*, 2009a). The Exploradores Fault Zone mimics this structural expression in the basement and likely represents an inherited set of structures that have been reactivated due to their favorable orientation in the course of strain partitioning and margin-parallel shortening triggered by closely-spaced oblique ridge collision in this region.

The inferred neotectonic activity at the NPI is reflected in an along-strike projection of the entire data set of cooling ages from the Exploradores Valley in the north to the fjord region around Caleta Tortel to the south (Figure 3.8E). Over the 150-km-long zone from Caleta Tortel towards the Exploradores Fault Zone, a northward trend of increasing elevations for samples with similar cooling ages can be observed. At Caleta Tortel, samples with 6-8 Ma AHe mean cooling ages are located at sea level, whereas in the Nef and Leones catchments, similar ages are characteristic for elevations around 1000 and 2000 m, respectively (Figure 3.8E). The Tortel region is located between the Northern and Southern Patagonian icefields and is characterized by numerous linked glacial fjords that traverse the orogen. During glacial maxima, this region was entirely covered by ice, whereas during interglacial periods, outlet glaciers from both icefields were restricted to valleys developing into future fjords (Hulton *et al.*, 2002; Hubbard *et al.*, 2005). Although this region was extensively affected by glacial erosion, the shallow levels of exhumation reflected by AHe data (Figure 3.8E) argue against efficient erosional exhumation of the landscape being solely responsible for low elevations along the orogenic divide. Based on this argument and our field observations of recent normal faulting at El Salton, we speculate that extension across the Tortel fjord region contributed to the low relief, low elevations, and relatively older ages found along the southern foothills of the NPI. Farther north, when crossing the Exploradores Fault Zone from Leones in the south (hanging wall) to the bottom of the Exploradores valley in the north (footwall), the elevation of 4-6 (yellow symbols) and 6-8 Ma (cyan symbols) samples abruptly drops by nearly 2000 m. This pattern can be explained by north-vergent thrusting along the Exploradores Fault Zone.

Overall, we interpret the latitudinal AHe cooling-age pattern along the orogenic crest in the NPI region (Figure 3.8E) to reflect the regional erosional exhumation signal that is spatially disrupted by tectonically controlled differential rock uplift accommodated by the Exploradores and Cachet faults systems, and possibly by extensional subsidence across the Tortel fjords in the south. Despite extensive glacial exhumation and modification of the landscape reflected by AHe ages between 9 and 2 Ma (Figure 3.8E), superimposed differential tectonic uplift after 2-3 Ma appears to be largely responsible

for relative elevation shifts across uplifting (Exploradores Fault Zone) or lowering (Tortel fjord region) crustal blocks.

The activity of the Cachet Fault and the Exploradores Fault Zone that we infer is further supported by the patterns of crustal microseismicity registered by a local seismic network installed between 44.6°S and 48.3°S between 2004 and 2005 (Miller *et al.*, 2005; Agurto-Detzel *et al.*, 2014) (Figure 3.10). The distribution of microseismicity occurs in clusters, notably associated with the Hudson Volcano located 80 km north of the NPI, the LOFZ, and the CTJ, and the clusters are mostly shallower than 10 km depth, where stick-slip fault behavior and intra-plate seismicity might be expected. The cluster of events at the western flank of the NPI in the area of San Quintin and San Rafael glaciers aligns well with the southern termination of the LOFZ. However, smaller clusters at the eastern and northern NPI flanks were not assigned a specific origin by these authors (Figure 3.10B). Agurto-Detzel *et al.* (2014) speculated that calving events and avalanches were possible seismogenic sources for "glacial earthquakes" based on the coincidence of terminal zones of calving glaciers. We consider this explanation unlikely, mainly because: 1) the interpretation was not supported by the necessary frequency analysis of the seismic waveforms, necessary to distinguish between tectonic and glacial sources (Ekström *et al.*, 2003; Amundson *et al.*, 2008; West *et al.*, 2010); 2) the seismic events in question occur mainly at depths between 2 and 10 km, which is not compatible with glacial triggers located at shallow depths; and 3) there are several other larger calving outlet glaciers at the NPI that do not exhibit such seismic activity. Instead, despite location uncertainties (Figure 3.10A), the seismic clusters in question coincide remarkably well with the tips of the Cachet Fault and the Exploradores Fault Zone and their intersection (Figure 3.10B) and therefore might support active faulting along the NPI flanks. Notably, these clusters represent chance findings, as the local seismic network was not initially designed to track the faulting along the flanks of the NPI. However, it is noteworthy that seismicity is fairly well resolved along known strands of the LOFZ, which are located even farther away from the seismic network. A more targeted positioning of seismic stations with such purpose would likely provide better constraints on fault geometries along the NPI flanks.

3.7.3 Tectonic Control on Topography Inland of the Chile Triple Junction

We argue that the inferred geometry, timing, and kinematics of deformation at the NPI can provide the link between processes related to oceanic-ridge collision and changes of topography at the latitude of the CTJ. We interpret margin-parallel strike-slip deformation along the Cachet Fault at the eastern flank of the elevated NPI to arise from

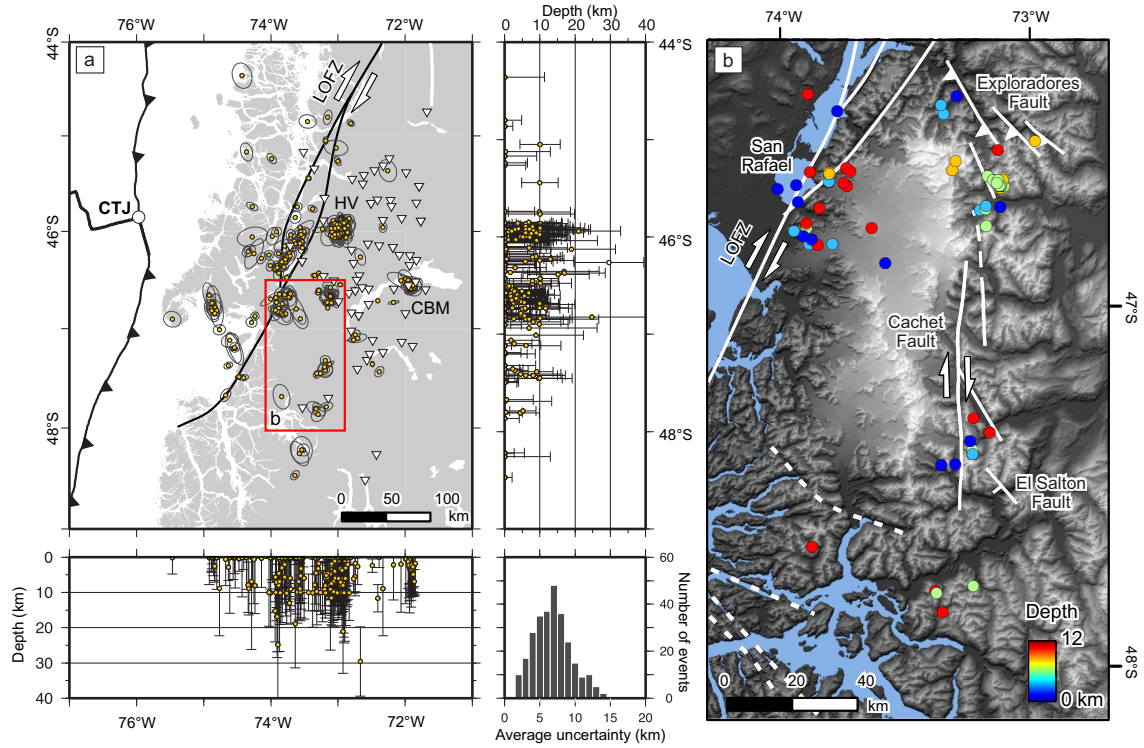

Figure 3.10 – (A) Seismicity distribution in the vicinity of the Chile Triple Junction (CTJ) with data from the study by Agurto-Detzel *et al.* (2014). Inverted white triangles indicate locations of seismic stations. Orange circles indicate locations of seismic events. Ellipses in plan view and error bars in profiles correspond to 68% confidence of location uncertainties. Histogram shown in lower right corner indicates averaged values from the three semi-axes of the uncertainty ellipsoids. Red rectangle outlines area shown in (B). HV: Hudson Volcano; CBM: Cerro Bayo Mine; LOFZ: Liquine-Ofqui Fault Zone. (B) Distribution of background local seismicity at the Northern Patagonian Icefield (Agurto-Detzel *et al.*, 2014). Circles represent single seismic events color-coded by depth. Event magnitudes range between 0.5 and 2.8 for this region.

closely spaced oblique collision of three segments of the Chile Rise at 6, 3, and 0.3 Ma between in the Golfo de Penas region (Figure 3.2, Figure 3.11). These collisions resulted in the decoupling of the NPI block from the Patagonian foreland along the LOFZ and the Cachet Fault, forming a crustal sliver. We suggest that northward translation of the NPI block results in (1) localized N-S shortening accommodated by reverse faults of the Exploradores Fault Zone system along its leading edge, and possibly (2) coeval extension accommodated by normal faults in the Tortel fjord region along its southern trailing edge (Figure 3.11B).

This tectonic model not only reasonably explains local fault kinematics, deformed geomorphic features, and cooling patterns in the NPI region, but also provides a straightforward link to the regional tectonic framework. Margin-parallel translation of crustal slivers along active subduction zones is characteristic of forearc deformation, reflecting strain partitioning due to oblique subduction (e.g. Witt *et al.*, 2006; Melnick *et al.*, 2006; Manaker *et al.*, 2008; LaFemina *et al.*, 2009; Michaud *et al.*, 2009). In Patagonia, oblique convergence since 20 Ma has induced strain partitioning, resulting in margin-normal shortening in the forearc and margin-parallel dextral shear in the intra-arc region along the LOFZ, defining a typical transpressive environment (e.g. Cembrano & Hervé, 1993; Cembrano *et al.*, 1996; Thomson, 2002; Adriasola *et al.*, 2006; Rosenau *et al.*, 2006; Lange *et al.*, 2008; Hernandez Moreno *et al.*, 2014). Besides oblique subduction, collision of the Chile Rise with the margin since 10 Ma south from the Golfo de Penas region (Breitsprecher & Thorkelson, 2009) has been considered a major driving mechanism for the activity of the LOFZ, which decouples and accommodates northward motion of the Chiloé forearc sliver relative to the South American foreland (Forsythe & Nelson, 1985; Murdie *et al.*, 1993; Thomson, 2002; Cembrano *et al.*, 2002; Adriasola *et al.*, 2006) (Figure 3.11B). This is evidenced from Pliocene-to-recent fault kinematics and paleomagnetic rotation patterns (Rosenau *et al.*, 2006; Hernandez Moreno *et al.*, 2014), seismicity (Lange *et al.*, 2008; Agurto-Detzel *et al.*, 2012) and space geodetic data (Wang *et al.*, 2007) . Northward motion of the Chiloé sliver is further accommodated by extension in the Golfo de Penas basin to the south identified in earlier studies (Forsythe & Nelson, 1985; Nelson *et al.*, 1994). Analogous margin-parallel decoupling and translation of a crustal sliver has been described along the Ecuadorian coast, where collision of the Carnegie Ridge has triggered northward translation of the North Andean Block and formation of the extensional Guayaquil basin at its trailing edge in the south (Witt *et al.*, 2006; Michaud *et al.*, 2009).

We interpret the northward motion of the NPI block to reflect progressive strain partitioning farther inboard in the overriding plate. The NPI region may be particularly prone to enhanced strain partitioning due to the closely spaced collision of three successive oceanic-ridge segments since 6 Ma (Figure 3.11A). The closely spaced oblique collision of buoyant oceanic asperities would enhance the transfer of interplate coupling and shear stresses to the overriding plate, promoting margin-parallel strike-slip faulting. The Cachet Fault and the Exploradores Fault Zone are likely genetically linked to this long-lived history of oblique subduction and ridge collision. We propose that enhanced dextral transpression and associated extension in the NPI region took advantage of the favorable orientation of pre-existing structures, accommodating part of the margin-parallel motion along the Cachet Fault (equivalent to the LOFZ, but farther inland), and uplifting the decoupled NPI block along the Exploradores Fault Zone, which acts as a backstop and crustal ramp supporting high topography at the northern edge of the icefield. Margin-parallel extension in the Tortel fjords is likely a consequence of northward motion of the NPI block and progressive margin-orthogonal subduction of the Antarctic Plate, analogous to extension in the Golfo de Penas basin at the trailing edge of the Chiloé block (Figure 3.11A). The proposed extension south of the NPI is compatible with field observations along the El Salton normal fault where right-lateral translation along the Cachet Fault transitions into the extensional domain.

It is noteworthy that the high nunataks of the NPI, which rise several hundreds of meters above the level of the ice sheet, are aligned in three pronounced ridges with sigmoidal shape and a strike similar to that of the Exploradores Fault Zone (Figure 3.8A and 3.11A). Although more field observations are needed, this geometry might suggest further internal crustal stacking and formation of a duplex-like structure within this crustal block as a consequence of induced margin-parallel shortening. Such internal deformation would also explain the apparent long wavelength of uplift inferred from thermochronological data between Tortel and the Exploradores Fault Zone (Figure 3.8E) as not only resulting from uplift along the Exploradores Fault Zone, but possibly also along as of yet unknown structures in the interior of the NPI.

The time constraints based on our AHe data suggest an onset of faulting along the flanks of the NPI after 2-3 Ma, which implies a time lag following the onset of ridge subduction in the southern Golfo de Penas at 6 Ma (Breitsprecher & Thorkelson, 2009). This lag time could be explained by initial accommodation of margin-parallel slip along the LOFZ, followed by a shift of deformation towards the Cachet Fault in the east.

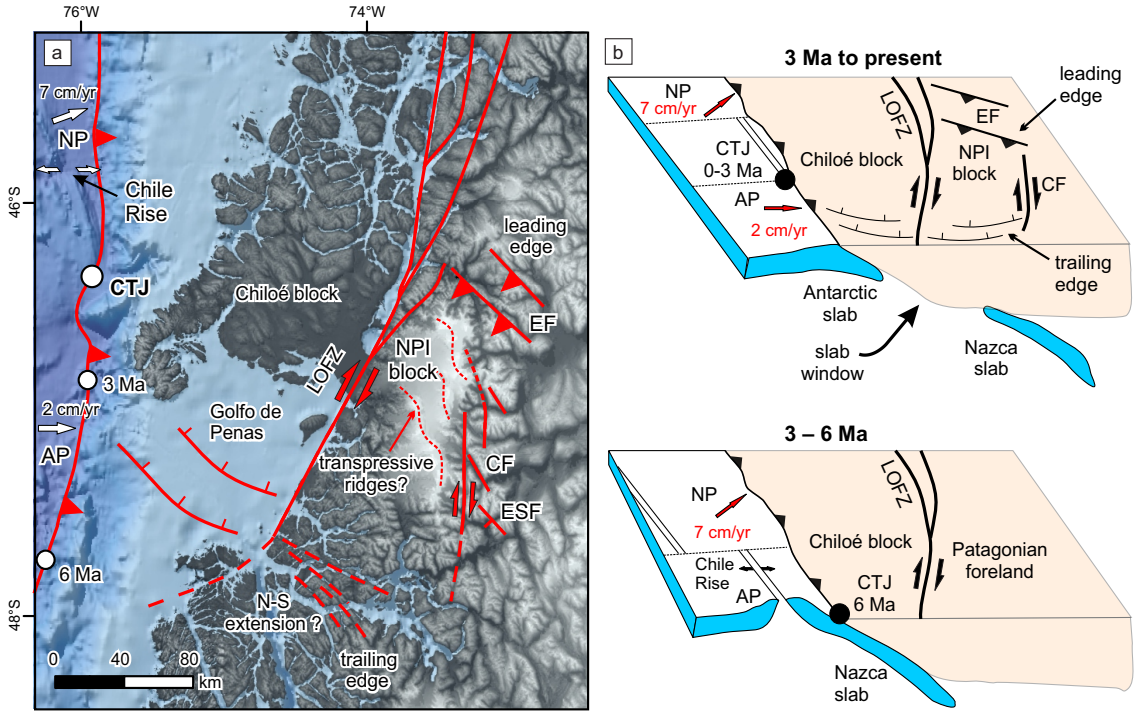

Figure 3.11 – Neotectonic model for the Northern Patagonian Icefield region inland of the Chile Triple Junction (CTJ). (A) Topography, location and kinematics of main tectonic structures. EF/CF/ESF: Exploradores/Cachet/El Salton Fault; LOFZ: Liquiñe-Ofqui Fault Zone; NP/AP: Nazca/Antarctic Plate (B) Structural evolution of the NPI region for the time intervals 3-6 Ma (lower panel) and 3-Ma-to-present (upper panel).

This new tectonic model successfully reconciles cooling patterns, structural data and geomorphic observations at the NPI. It integrates several aspects of the evolution of the tectonic framework in Southern Patagonia, particularly the development of structures related to ridge collision at the latitude of the Chile Triple Junction. Finally, the model provides an explanation for topographic differences along strike of the Patagonian Andes, complementing previous studies that have considered mechanisms of topographic evolution involving only lithospheric-scale geodynamic (dynamic topography) or climatic (glacial erosion) factors.

3.8 Conclusions

The combined geomorphic and structural field observations and apatite (U-Th)/He data presented in this study reveal neotectonic activity along the flanks of the Northern Patagonian Icefield (NPI) inland of the Chile Triple Junction during the past 2-3 m.y. Relative displacements across newly recognized fault structures with clear geomorphic markers

(displaced and beheaded valleys) disrupt the regional late Cenozoic exhumation signal as recorded by the distribution of cooling ages. We interpret margin-parallel right-lateral strike-slip deformation along the eastern flank NPI (Cachet Fault) to arise from strain partitioning enhanced by the closely spaced oblique collision of successive oceanic-ridge segments during the past 6 Ma. Faulting along the Cachet Fault triggered decoupling and northward motion of the NPI block with respect to the Patagonian foreland. Northward motion of this crustal sliver is accommodated by shortening across reverse faults of the Exploradores Fault Zone at its leading edge, which acts as a crustal ramp supporting high topography. Margin-parallel extension possibly occurs at the southern trailing edge of the NPI block across normal faults in the Tortel region, where fjord landscapes characterize anomalously low elevation regions along the axis of the mountain belt. This region is analogous to the Golfo de Penas extensional basin immediately to the west, which is associated with the trailing edge of the Chiloé block, an adjacent crustal sliver moving northward in response to oblique ridge collision and induced upper-plate strain partitioning. The neotectonic model presented here provides an alternative explanation for the abrupt variations in summit elevations and relief south of the Chile Triple Junction and emphasizes the fundamental effects of local tectonics on the evolution of topography in these glaciated mountain ranges.

Acknowledgements

Data used for Figure 3.8 is available in Appendix A2. Data from Thomson *et al.* (2010) used in Figure 3.8 is linked to the online version of the original paper at www.nature.com/nature. Data used for Figure 3.10 is available in the Supporting Information from Agurto-Detzel *et al.* (2014) online at http://dx.doi.org/10.1016/j.jsames.2013.12.011. The locations of outcrops and all structural measurements summarized in the stereoplots of Figures 3.4, 3.6 and 3.7 are presented in Figure A.7 in Appendix A3. Elevation data (SRTM-1, 30-m resolution) can be freely accessed over USGS (https://lta.cr.usgs.gov/SRTM). This study was supported by the initiative Potsdam University's Research Cluster for Georisk Analysis, Environmental Change and Sustainability (PROGRESS), funded by the German Ministry of Education and Research (M. Strecker), and the European Research Council Consolidator Grant Program (ERC 615703, T. Ehlers). We wish to thank Konstanze Stübner for supplemental laboratory support at the University of Tübingen and Pascual Diaz (Turismo Kalem, Puerto Guadal), Eugenio Berrocal, Noel Vidal (Entre Hielos, Caleta Tortel), and Jonathan Leidich (Patagonia Adventure Expeditions, Puerto Bertrand) for essential logistic support during fieldwork. We thank the Associate Editor Lindsay Schoenbohm, Andrew Meigs and one anonymous reviewer for their detailed and constructive comments.

Supplementary Material

See Appendix A.

Chapter 4

Late Cenozoic cooling history of the Southern Patagonian Andes at 47°S - insights from inverse multi-thermochronometer thermal modeling[†]

4.1 Introduction

The subduction of oceanic basins at convergent margins commonly transfers oceanic ridge-transform systems towards the deep-sea trench and in contact with the upper plate. If the oceanic ridge is actively spreading and the bounding plates continue to diverge during subduction, a slab window forms below the overriding plate (DeLong *et al.*, 1979; Dickinson & Snyder, 1979; Forsythe & Nelson, 1985; Sisson & Pavlis, 1993; Thorkelson, 1996). The slab window provides a pathway for the upwelling of relatively hot asthenospheric (sub-slab) mantle material that is expected to affect the mechanical and thermal structure of the overlying lithosphere in various ways. These thermo-mechanical effects largely depend on the geometry of the ridge-transform system (i.e. the orientation of transform faults and offset ridge segments with respect to the trench), which defines the spatial and temporal evolution of slab window formation and migration below the overriding plate (Thorkelson, 1996).

Some common geologic manifestations of slab window formation, regardless of its geometry, include anomalous high-temperature metamorphism in the fore-arc (DeLong *et al.*, 1979; Underwood *et al.*, 1993; Sisson & Pavlis, 1993; Haeussler *et al.*, 1995; Groome *et al.*, 2003); mafic near-trench magmatism (Forsythe *et al.*, 1986; Lagabrielle *et al.*, 1994; Maeda & Kagami, 1996; Bourgois *et al.*, 1996); non-arc-like volcanism (Johnston

[†] *in preparation for submission to Earth and Planetary Science Letters*

& Thorkelson, 1997; Breitsprecher *et al.*, 2003) or a gap in the volcanic arc (Cande & Leslie, 1986; Thorkelson & Taylor, 1989; Osozawa, 1997); abrupt changes in crustal deformation style across the ridge collision site (Cembrano *et al.*, 2002; Haeussler *et al.*, 2003; Georgieva *et al.*, 2016; Lagabrielle *et al.*, 2007; Scalabrino *et al.*, 2010); higher uplift rates above the slab window (Buiter *et al.*, 2002; Rogers *et al.*, 2002; Lagabrielle *et al.*, 2004; Guenthner *et al.*, 2010; Jeandet, 2014; Braun *et al.*, 2013); a transient dynamic response (uplift) in the upper plate (Guillaume *et al.*, 2009, 2010, 2013; Braun *et al.*, 2013; Jeandet, 2014). All these various effects are mainly the response to the replacement of cold and dense subducting lithosphere with hot, dry, and buoyant asthenospheric mantle through the slab window.

The formation of a slab window induces two principal changes to the mantle below the upper plate: a decrease in hydration and an increase in temperature (DeLong *et al.*, 1979; Thorkelson, 1996; Groome & Thorkelson, 2009) that result in chemical and thermal anomalies. Modeling results and field observations suggest that these effects should be particularly manifested in the forearc region, i.e. in the vicinity of ongoing ridge collision where the subducting slab is shallow and the mantle wedge is thin (Sakaguchi, 1996; Groome *et al.*, 2003; Underwood *et al.*, 1993; Brown, 1998; Sisson *et al.*, 2003b, 1989; Hudson & Plafker, 1982; Haeussler *et al.*, 1995, 2003; Dickinson & Snyder, 1979). Furthermore, analog (Funiciello *et al.*, 2004, 2006) and numerical (Piromallo *et al.*, 2006) models document the generation of complex, three-dimensional mantle flow patterns accompanying subduction and highlighted the importance of lateral (trench-parallel) sub-slab mantle flow around the edges of subducting slabs. Guillaume *et al.* (2010) extended this approach by simulating these processes for slab window settings. The results document the formation of lateral asthenospheric flow around the edges of a forming slab window and emphasised the potential for trench-parallel transport of sub-slab material and heat through advection towards much more distant parts of the subduction system, not yet directly affected by ridge collision and slab window formation.

The study of such deep-seated processes and particularly of their upper-plate geologic manifestations is an ambitious task due to the challenging reconstruction of the causal mechanisms from fossil plate-margin settings, for example in Japan or Southern Alaska (e.g. Sakaguchi, 1996; Underwood *et al.*, 1993; Brown, 1998; Sisson *et al.*, 1989; Haeussler *et al.*, 1995, 2003; Sisson *et al.*, 2003b) and the scarce occurrence of present-day or recent slab window formation, for example in the Antarctic Peninsula (Guenthner *et al.*, 2010), Southern Patagonia (e.g. Russo *et al.*, 2010b; Forsythe & Nelson, 1985), the Central and North American Pacific margin (Merritts & Bull, 1989; Johnston & Thorkelson,

1997; Zandt & Humphreys, 2008). Southern Patagonia is certainly a premier example for a subduction system with slab-window formation that has been sustained for several millions of years involving episodic ridge collision and accompanying slab window formation, where many of the geologic manifestations listed above have been studied. This setting has also been the starting point for several modeling approaches addressing the geometry of the evolving slab window (Thorkelson, 1996; Breitsprecher & Thorkelson, 2009), the thermo-mechanical effects of ridge collision and slab window formation (Groome & Thorkelson, 2009), the deep-seated mantle flow patterns (Guillaume *et al.*, 2010), and the dynamic topography effects on the upper plate (Guillaume *et al.*, 2009, 2013). The present study particularly focuses on the thermal history recorded in upper crustal levels overlying the Patagonian slab window and the re-evaluation of previously proposed models of reheating scenarios linked to progressive, northward-migrating ridge collision and slab window formation.

Sixteen million years ago the active oceanic Chile Ridge separating the Nazca and Antarctic plates began colliding with the South American subduction margin at the southernmost sector of the continent (Fig. 4.1) (Breitsprecher & Thorkelson, 2009). The trench-ridge-trench geometry resulted in a northward migration of the site of ridge collision (the Chile Triple Junction) and successive northward-directed unzipping of an extensive slab window below southern Patagonia. The spatiotemporal evolution of the slab window has been associated with a gap in the subduction-related calc-alkaline arc volcanism and has been genetically linked to the emplacement of transitional-to-alkaline main- and post-plateau basalts with variable OIB-(oceanic island basalt)-signatures in the eastern foreland (Fig. 4.1) (Kay *et al.*, 1993; Gorring *et al.*, 2003; Guivel *et al.*, 2006; Boutonnet *et al.*, 2010). Adakitic volcanism related to partial slab melting has been documented above the leading edge of the incipiently subducting Antarctic Plate forming the Austral Volcanic Zone (Stern & Kilian, 1996) .

The northward propagation of the Patagonain slab window would suggest a systematically decreasing trend in the along-strike distribution of the (emplacement) ages of associated plateau basalts in the Patagonian foreland. However, compilations of crystallisation ages from the entire volcanic backarc of southern Patagonia lack such correlation (Guivel *et al.*, 2006; Guillaume *et al.*, 2013). Interestingly, many emplacement ages predate the arrival of the leading edge of the slab window, to which they are geochemically related. Two principal mechanisms that do not exclude each other have been proposed for the generation of alkaline volcanism in the Patagonian backarc ahead of the arrival and widening of the slab window. Guivel *et al.* (2006) proposed the generation

and northward propagation of a horizontal (trench-parallel) tear in the downgoing Nazca slab that could potentially provide the necessary pathway for sub-slab asthenospheric mantle and the generation of alkaline magmatism in the upper plate preceding arrival of the slab window (illustrated in Figure 4.1A). Alternatively, Guillaume *et al.* (2013) proposed that low-temperature bedrock cooling ages from a broad region in the Andean orogen located immediately above and ahead (north) of the present-day extent of the Patagonian slab-window records a significant heat wave propagating northward from the evolving slab window since the mid Miocene that systematically affected the thermal structure and volcanism of distal crustal regions. This conclusion is mainly based on inverse thermal modeling of low-temperature bedrock cooling ages and supported by analog models showing the generation of lateral asthenospheric mantle flow around the subducting slab edges that could be responsible for margin-parallel heat transport. The scenario proposed by Guillaume *et al.* (2013) is also in agreement with the study of Blisniuk *et al.* (2006) that documents a pulse of Late Miocene reheating in the same region based on inverse thermal modeling of AFT data.

The models of Guillaume *et al.* (2013) and Blisniuk *et al.* (2006) account for the criticism that a single trench-parallel tear in the Nazca slab at 15 Ma, as proposed by Guivel *et al.* (2006), should have been rapidly transferred eastward (> 1000km east from the trench) in the course of ongoing subduction and fast (7 cm/yr) plate convergence, and therefore could account for the spatially consistent generation of alkaline volcanism in the backarc (250-300 km east from the trench). However, these reheating scenarios are somehow inconsistent with the overall understanding that the thermal pulse originating from ridge collision and slab window formation should be mainly detected in the fore-arc and not in the upper 4-5 km (as recorded by low-temperature thermochronometers such as apatite (U-Th)/He and fission track data) of the arc region.

In this study I reassess the thermal history of the orogen's interior at the latitude of the CTJ by re-evaluating the modeling procedures applied by Guillaume *et al.* (2013) and Blisniuk *et al.* (2006) and present new inverse thermal modeling results from an extended dataset. I use a combination of new and previously published (Blisniuk *et al.*, 2006; Guillaume *et al.*, 2013; Georgieva *et al.*, 2016) AHe and AFT data from three elevation transects and perform inverse thermal modeling with single- and multiple-sample simulations with the modeling plattforms HeFTy (Ketcham, 2005a) and QTQt (Gallagher, 2012). Particular methodological emphasis is put on a detailed discussion of the different model setups and examples how such factors might significantly influence the output and resulting geological and geodynamic interpretations.

4.2 Regional Setting and Location of Samples

4.2.1 Regional Setting

The general plate tectonic setting of the southern Andes has been outlined in Section 3.3 of the previous chapter. The late Cenozoic tectonic history of the Southern Patagonian Andes (south from the CTJ) is marked by the collision of the Chile Ridge, an active oceanic spreading center, with the South American continent, forming the Chile Triple Junction (CTJ), presently located at 46°S (Breitsprecher & Thorkelson, 2009, Figure 3.1 and 4.1) . Since 16 Ma, the CTJ has migrated northward from 54°S, as ridge segments subparallel to the trench collided with the subduction margin. Oceanic ridge collision resulted in the successive northward opening of an asthenospheric slab window beneath southern Patagonia, which has changed mantle flow patterns and impacted large-scale upper plate deformation (Guillaume *et al.*, 2009, 2013; Scalabrino *et al.*, 2011; Russo *et al.*, 2010b; Georgieva *et al.*, 2016). Since ~ 6 Ma, the CTJ has remained close to its present-day location (46°S) due to the closely spaced collision and subduction of three short ridge segments in the Golfo de Penas region (Breitsprecher & Thorkelson, 2009). This closely spaced oblique ridge collision resulted in enhanced strain partitioning along the margin and triggered neotectonic activity in the upper plate (Georgieva *et al.*, 2016, Chapter 3).

South from the CTJ the main orogenic arc comprises Paleozoic metamorphic rocks intruded by Jurassic to Miocene plutons of the Patagonian Batholith (e.g. Hervé *et al.*, 2007, Fig. 4.2). To the east, Jurassic to Oligocene volcano-sedimentary units and Miocene coarse-grained synorogenic clastic deposits record episodic shortening and uplift during the Late Cretaceous to Middle Miocene (22 to 14 Ma) (Coutand *et al.*, 1999; Suarez *et al.*, 2000; Lagabrielle *et al.*, 2004; Blisniuk *et al.*, 2005). Indeed, most shortening occurred during the deposition of the synorogenic sediments (Santa Cruz/Rio Zeballos Formations) and ended with a major phase of thrusting juxtaposing the pre-Cenozoic rocks of the Cordillera over the synorogenic deposits marking the easternmost and latest active location of the deformation front (Suarez *et al.*, 2000; Lagabrielle *et al.*, 2004).

Between 12 and 3 Ma, extensive plateau basalts (main plateau) were emplaced in the eastern foreland (e.g. Gorring *et al.*, 2003, 1997; Guivel *et al.*, 2006; Espinoza *et al.*, 2005, 2010; Boutonnet *et al.*, 2010) on a gently eastward-sloping erosional surface, sealing the eastern thrust front of the Southern Patagonian Andes (Lagabrielle *et al.*, 2004; Suárez & De la Cruz, 2001). These volcanic rocks display a geochemical signature

with variable OIB (oceanic island basalt)-like character that has been related to the input of hot asthenospheric mantle underlying the subducting slab below the continental lithosphere of the South American Plate. In the context of ridge collision in southern South America the generation of these volcanic rocks has been commonly associated with the formation and northward migration of the Patagonian slab window where sub-slab upwelling asthenospheric mantle has come progressively in contact with the overlying continental lithosphere (e.g. Gorring *et al.*, 2003, 1997; Guivel *et al.*, 2006; Espinoza *et al.*, 2005, 2010; Boutonnet *et al.*, 2010).

The generation of OIB-like main-plateau basalts (12-3 Ma) north from (i.e. predating) the arrival of the northern edge of the approaching slab window (Figure 4.1) has been explained by the formation of one or several tears in the Nazca slab subparallel to the ridge segments (Guivel *et al.*, 2006, illustrated in Figure 4.1A). Alternatively, Guillaume *et al.* (2013) proposed a mechanism of lateral (trench-parallel) asthenospheric flow generated at the edges of the the opening slab window that might transport heat through advection and trigger magmatism hundreds of kilometres to the north.

Starting at 3 Ma alkaline post-plateau lavas with a strong OIB-like geochemical signature began to be emplaced in the backarc at 47°S. The geochemical signature of the post-plateau lavas has been interpreted as a consequence of their direct derivation from an OIB-source in the deep asthenospheric mantle (Gorring *et al.*, 2003; Guivel *et al.*, 2006; Boutonnet *et al.*, 2010), consistent with the Patagonian slab window that opened below this region beginning at ~ 4 Ma (Figure 4.1C,D).

The data presented in this study originates from the region of the Northern Patagonian Icefield (NPI, 47°S) that caps a high mountain massif in the orogen located directly between the subduction margin and the present-day location of the CTJ in the west and the volcanic backarc region in the eastern foreland (Figure 4.2). This region is mainly characterized by Jurassic and Cretaceous granitoids of the Southern Patagonian Batholith.

4.2.2 Sample Locations

I used analytical data from a total of 35 samples grouped into three elevation transects spanning ~ 1000-2000 m. The Leones (17 samples, ~ 2000 m elevation range) and Nef (7 samples, 1000 m elevation range) elevation transects are located along the steep eastern flank of the Northern Patagonian Icefield massif and originate from the granitoid rocks in the central part of the Patagonian Batholith 3.3. The third elevation transect is located at the flanks of Cerro Barrancos (11 samples, 1000 m elevation range) - a massif located about 50 km to the southeast of the NPI. The lithology comprises the

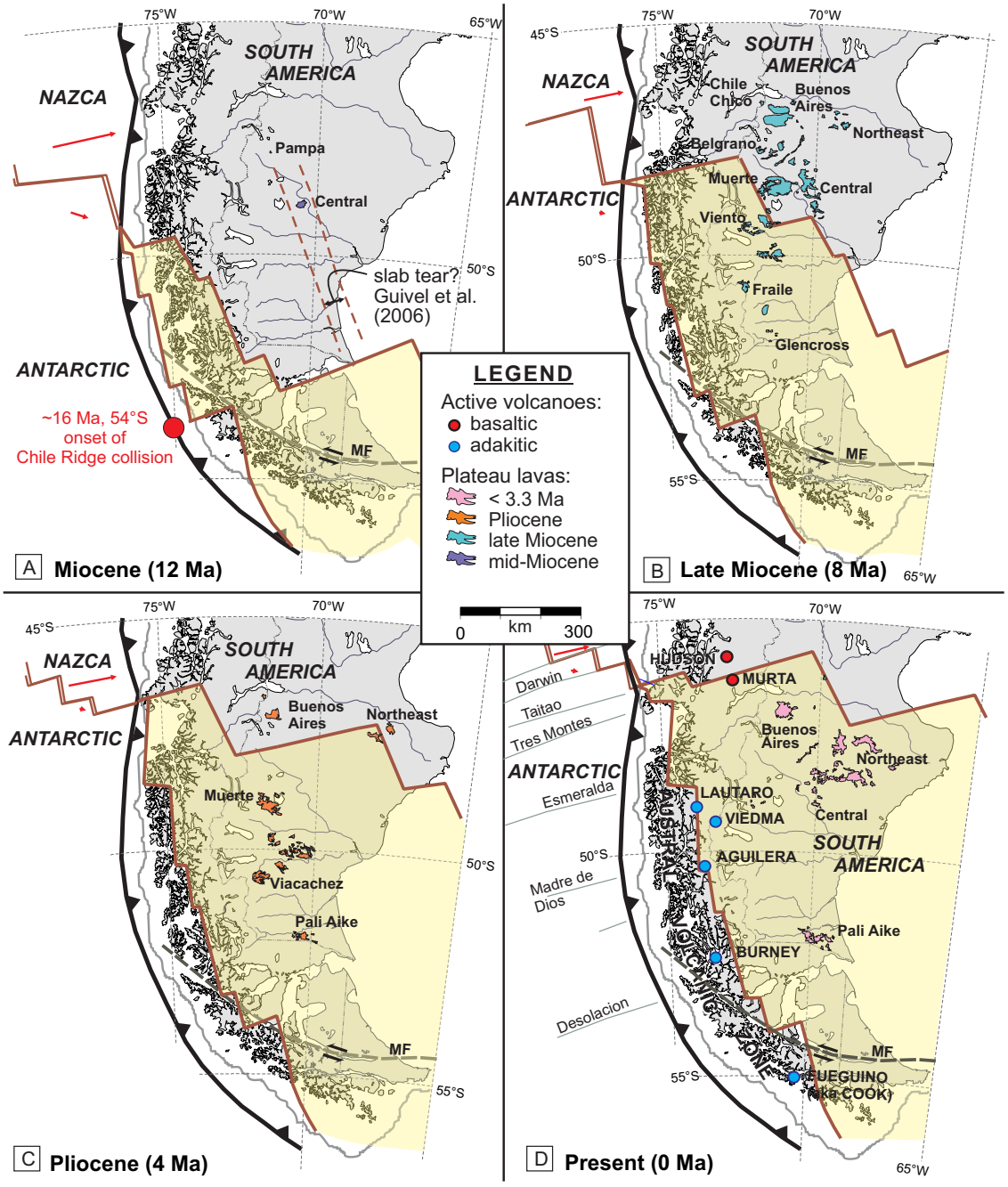

Figure 4.1 – Maximum extent of the Patagonia slab window through the Neogene. (A) Middle–Late Miocene (12 Ma); (B) Latest Miocene (8 Ma); (C) Pliocene (4 Ma); (D) Recent (0 Ma). The heavy brown lines are the kinematically-defined slab edges. Red arrows indicate the relative displacement of each subducting plate, per Ma, at the time shown for each figure panel, relative to a fixed position of South America. Figure from Breitsprecher & Thorkelson (2009).

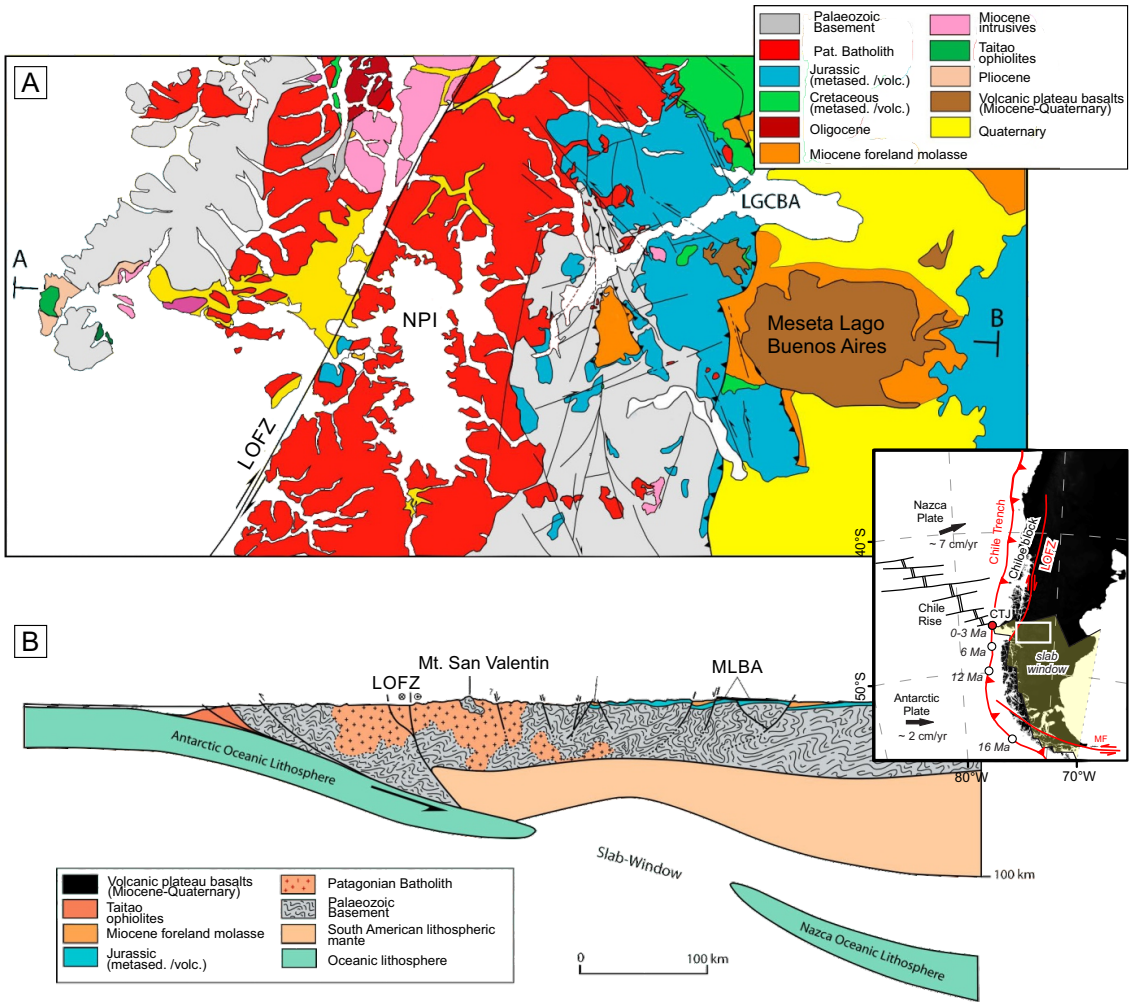

Figure 4.2 – (A) Simplified geological map of the Southern Patagonian Andes at the latitude of the Chile Triple Junction. LGCBA: Lago General Carreras Buenos Aires; LOFZ: Liquiñe-Ofqui Fault Zone; NPI: Northern Patagonian Icefield. (B) Schematic lithospheric-scale cross section A–B across the Patagonian Andes at the latitude of the Chile Triple Junction, inferred from surface geology. Section without vertical exaggeration. MLBA, Meseta del Lago Buenos Aires. Figure from Scalabrino *et al.* (2010).

Cerro Barancoso monzogranite, which is an Early Cretaceous intrusive body (Pankhurst *et al.*, 1999) associated with the Patagonian Batholith and located at its contact to the Palaeozoic metamorphic host rock.

4.3 Methods

4.3.1 General Approach

Low-temperature cooling ages (apatite (U-Th)/He and apatite fission-track dating; AHe, AFT) of bedrock samples provide approximate time-temperature constraints on the time-temperature paths of single or a group of samples from an elevation transect (e.g. Reiners & Brandon, 2006) and are used as an input for inverse thermal modeling techniques. The goal of this approach is to use information stored in the raw analytical data together with its uncertainties (AHe and AFT cooling ages, fission track length distributions, kinetic parameters such as Dpar) as an input for a statistical search of the multi-dimensional parameter space and evaluation of possible thermal histories with respect to their fit to the observed data and geological plausibility. I use in a complimentary way two commonly used, but regarding their functionality, fundamentally different modeling softwares, HeFTy (Ketcham, 2005a; Ketcham *et al.*, 2009) and QTQt (Gallagher *et al.*, 2009; Gallagher, 2012). I compare the combined modeling outputs with previously published conclusions about the low-temperature thermochronology thermal history record in this region and discuss their significance in the regional geological context.

4.3.2 Analytical Methods

4.3.2.1 Analytical Background

Thermochronological data typically assess rock cooling histories on relatively long time scales of several million years. The AHe and AFT track dating methods are two of the main thermochronologic techniques in use today that allow constraining thermal histories at temperatures below 120°C (e.g. Reiners & Brandon, 2006; Gallagher *et al.*, 1998; Gautheron *et al.*, 2009; Ehlers & Farley, 2003). Both methods are based on the production of an isotope (^{4}He) or radiation damage (fission tracks) by nuclear decay and the thermally controlled retention of these decay products.

The AHe thermochronometer is sensitive to the passing and cooling of samples below a zone of partial retention (PRZ) of the ^{4}He isotopes in apatite crystals, which is estimated between 40-70°C (Farley *et al.*, 1996; Farley, 2000; Reiners & Brandon, 2006). A closure temperature for the (U-Th/He) system around 70°C has been inferred by Wolf *et al.*

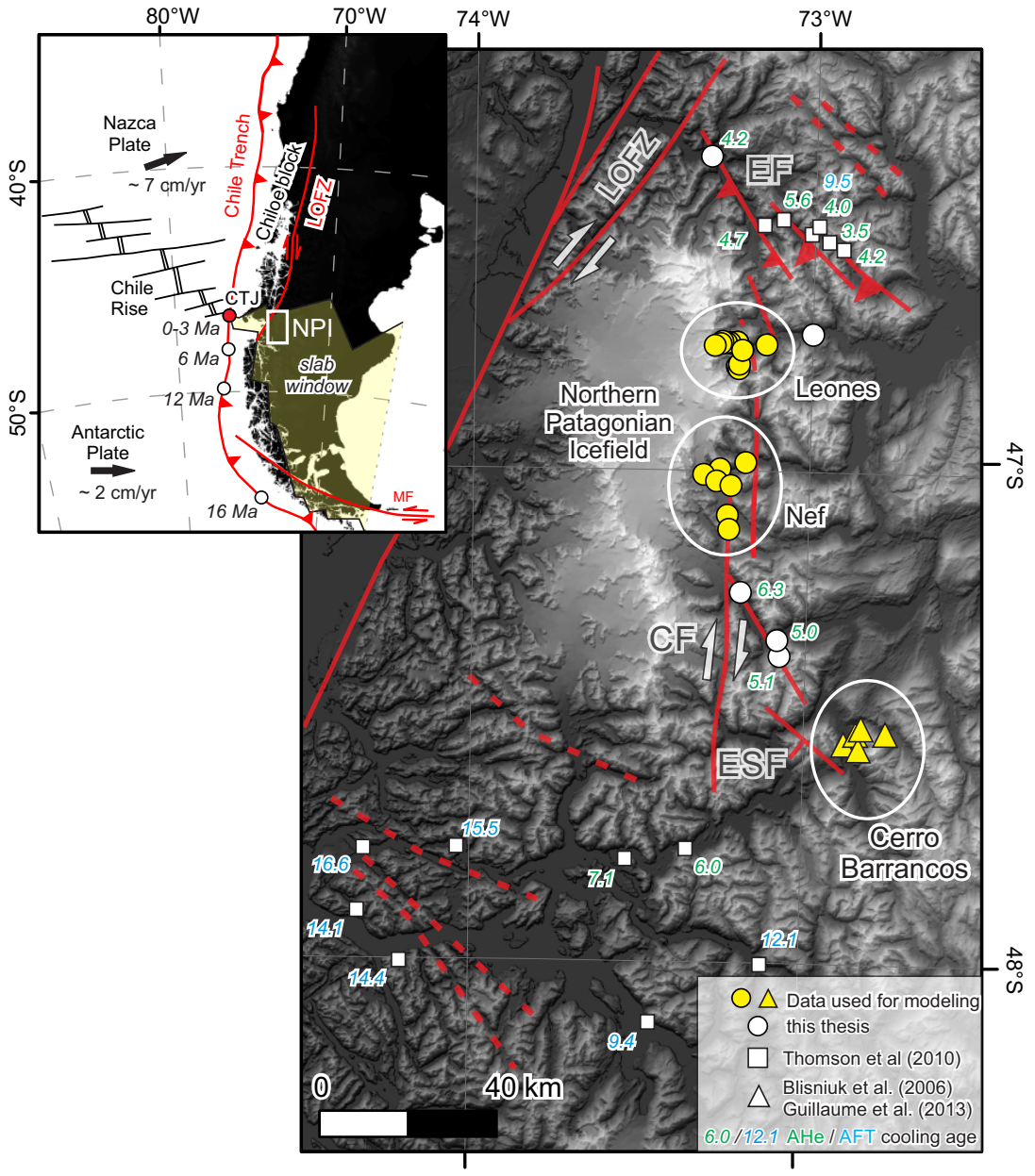

Figure 4.3 – Regional tectonic setting and location of samples. Inset indicates the regional tectonic setting of the study area in the Northern Patagonian Icefield region (NPI). Past (white) and present (red) position of the Chile Triple Junction (CTJ) are indicated along the Chile trench (Breitsprecher & Thorkelson, 2009). Yellow symbols correspond to samples with data used as input for numerical modeling. White symbols and coloured labels correspond to other AHe (green) and AFT (blue) data from this region (Thomson *et al.*, 2001, 2010; Guillaume *et al.*, 2013; Georgieva *et al.*, 2016). Red lines indicate main tectonic structures.

(1996, 1998) for a cooling rate of 10 °C/Ma and a crystal size with 60 µm radius. More sophisticated models for the closure temperatures of the AHe thermochronometer have been proposed that take into account the effects of radiation damage on He-diffusion in apatite (Gautheron *et al.*, 2009; Flowers *et al.*, 2009), which is necessary to account for in certain cases (e.g. slowly cooled terrains, high-U samples).

The AFT thermochronometer is in turn sensitive to the passing of rocks through and below a zone of partial annealing (PAZ) of damage (fission tracks) in the crystal lattice produced by fission decay of ^{238}U. The PAZ for fission tracks in apatite is estimated between 60 and 120°C and can vary depending on e.g. the chemical composition of the apatite crystals or the cooling rate (Ketcham *et al.*, 1999; Carlson *et al.*, 1999; Reiners & Brandon, 2006). Fission tracks form continuously over time at a rate dependent upon the concentration of uranium in the grain. The fission track age of a sample depends on the number of tracks counted in individual grains and the grain chemistry. Earlier-formed fission tracks are then shorter than later-formed tracks, as they will have had more time to anneal, and may have experienced higher temperatures (Green & Durrani, 1977; Green *et al.*, 1986; Gleadow *et al.*, 1986). The observed distribution of fission-track lengths in a sample represents all tracks formed and annealed during its residence below the total annealing temperature (~ 120°C). Hence, track length distributions provide an additional measure for the integrated thermal history of a sample, making this thermochronometer a uniquely powerful tool for thermal history reconstruction.

The combined application of different thermochronometers covering a wide temperature range with the elevation dependance of cooling ages provide reliable constraints on the thermal history of the sampled crustal section, which can be used as an input for a variety of numerical approaches (e.g. Van Der Beek *et al.*, 2010; Valla *et al.*, 2010; Gallagher *et al.*, 2009; Gallagher, 2012).

4.3.2.2 Analytical Procedure

AHe dating for this study has been conducted at University of Tübingen (^{4}Helium measurements) and the University of Arizona (U-Th-Sm measurements). For details on the AHe dating procedure related to the AHe data presented in this thesis see Chapter 3.2.2 and Appendix A.

AFT samples from this study have been analysed at University of Potsdam. Twelve samples from the Leones and Nef transects yielded enough apatite grains and were mounted for fission track analysis following standard procedures for sample preparation. For fission track dating of apatite I adopted the external detector method (Gleadow, 1981), zeta calibration approach (Hurford & Green, 1983) and etching protocol of

Donelick *et al.* (1999) (5.5 M HNO_3 for 20 sec at 21°C). Samples were irradiated at to produce induced fission tracks. To reconstruct thermal history, as many horizontal confined tracks-in-tracks (TINTs) as possible were measured. Measurements have been performed both for standard- and heavy-ion-irradiated slides, made to increase the number of all recorded horizontal tracks-in-tracks. AFT ages were calculated by TrackKey 4.2 g software (Dunkl, 2002). Annealing kinetics of apatite for thermal history modeling was assessed by Dpar values (Burtner *et al.*, 1994).

All details of sample preparation and analytical procedures for new AFT data from the Leones and Nef transects are given in Appendix B3. Summary of the AFT data results is provided in Appendix B4. The analytical procedures related to AFT and AHe dating on samples from the Cerro Barrancos transect are provided by Blisniuk *et al.* (2006) and Guillaume *et al.* (2013), respectively. The datasets from these studies are provided in Appendix B1 and B2.

4.3.3 Inverse Thermal Modeling Background

In this study thermal history inversions for single samples and multiple samples from elevation transects have been performed using two common modeling techniques adopted in the computer programs HeFTy (Ketcham, 2005a; Ketcham *et al.*, 2009) and QTQt (Gallagher *et al.*, 2009; Gallagher, 2012) both implementing a forward and inverse modeling platforms. This section summarises the main functionalities of HeFTy and QTQt and will be used for reference in the model setup explained below.

HeFTy (Ketcham, 2005a; Ketcham *et al.*, 2009) explores the time-temperature space with a Frequentist approach by randomly proposing a large number of thermal histories and evaluating which of these paths satisfy certain statistical criteria with "good" or "acceptable" fit to the data and rejecting the rest. The statistical criteria to define a path as "good" or acceptable" have been described in detail in the study of Ketcham *et al.* (2009). Furthermore the user is allowed to define boxes in the modeling space corresponding to time-temperature constraints through which each path tried has to pass. There are no strict rules about the number, size and location of constraint boxes. This depends largely on the modeling objective, the lack or existence of geological information and the input data. It is generally meaningful to constraint the onset of all time-temperature paths in a time period preceding the temporal information stored in the input data and at temperatures higher then the sensitivity of the used thermochronometers. Known geological events such as depositional ages, burial or reheating can also be implemented in the model as constraints; however, in the absence of such information time-temperature constraints can also be placed to increase the efficiency of the modeling by decreasing

the modeling space in regions well defined by the data. An important point for this study is that time-temperature constraints can be applied to allow for and weight out the necessity of reheating since HeFTy does not test for reheating scenarios in an unconstrained mode. HeFTy can be applied for multiple thermochronometers in single or multiple samples. In the present study only the single-sample approach has been used with HeFTy. Detailed description of the software functionality and statistical background have been presented by Ketcham (2005a), Ketcham *et al.* (2009) and in the software manual.

The QTQt software (Gallagher, 2012) implements a transdimensional Bayesian Markov Chain Monte Carlo (MCMC) algorithm (Green, 2003; Sambridge *et al.*, 2006; Gallagher *et al.*, 2009) to explore the time-temperature modeling space in a random walk along which different thermal paths are proposed, rejected or accepted, and finally ranked based on their likelihood to fit the data. The method requires the definition of a prior model space which is considered to constrain the most likely solutions (in terms of fitting the data). This is a broad general time prior encompassing a range of time and temperature defined by the information likely stored in the data (cooling ages and sensitivity of the applied thermochronometers). In the course of the search for most likely solutions the transdimensional Bayesian approach naturally discards complex models (more t-T points) in favour of simpler thermal histories given a reasonable fit to the observed data.

An important and widely used functionality of QTQt is the ability of the algorithm to model together a suite of several samples from an elevation transect, which is a common sampling technique with the objective of tracking exhumational histories. The multi-sample approach requires the set-up of an additional prior parameter which defines the temperature offset between the uppermost and lowermost samples in an elevation transect based on a range of assumed geothermal gradients. The value is selected from the input range and either kept constant or allowed to vary over time for each inverse thermal history.

QTQt requires the user to define a prior for the present-day temperature range and allows for the input of up to five additional t-T constraints, which is meaningful if there is robust geological information that needs to be considered. These t-T constraints are visually similar to the constraint boxes used in HeFTy, but their impact on the modeling output is fundamentally different: As outlined by Vermeesch & Tian (2014) QTQt cannot be used to disprove some input geological constraints based solely on the existence of modelled possible thermal paths since the Bayesian algorithm will always find some *most* likely solutions, even if there is no good fit to the data. Therefore a

torough examination of the goodness of fit (likelihood) of the modelled vs. observed data in QTQt is particularly crucial (Gallagher, 2012, 2016). Generally speaking, the incorporation of geological constraints in QTQt has to be applied rather conservatively or refrained from since the essence of the Bayesian approach is to let the data (together with their uncertainties) search for the most likely solution (Gallagher, 2012; Vermeesch & Tian, 2014). However, it could be appropriate to apply a constraint at the beginning of the model at temperatures sufficiently high to reset all input thermochronometers and at a time preceding the time period constrained by the data in order to avoid some bias from some arbitrary inherited thermal history when entering the modeling prior.

The search of the modeling space begins with an initial period of sampling ("burn-in" iterations) the result of which serves as a proxy for the posterior probability distribution conditional on the prior and the observed data. The models proposed during the burn-in period are subsequently discarded, but this step must contain sufficient number of iterations in order to provide a representative posterior probability distribution from which the final models are drawn. The latter happens in the second period of sampling ("post-burn-in") in which over a large number of iterations thermal histories are repeatedly proposed, evaluated (accepted or rejected), perturbed, evaluated etc. finally resulting in an ensemble of models ranked by their likelihood to the data in terms of posterior probability. The main goal and likewise statistical test for the performance of the MCMC sampling chain and the representativity of the final result is a desired convergence of the sampling toward a stable range of values for the likelihood to the data and the posterior probability. Such convergence is essential and indicative of sufficient exploration of the modeling space and representativity of the result. More details on the methodology and statistical background of QTQt and the Bayesican MCMC approach are given in the studies of Gallagher *et al.* (2009), Gallagher (2012) and Green (2003) with some recent examples of the application of this modeling technique to geological processes e.g. in Cogné *et al.* (2012), Cogné *et al.* (2014) and Wildman *et al.* (2016).

In their recent study Vermeesch & Tian (2014) discussed the similarities and differences between HeFTy and QTQt and highlighted some important considerations for the evaluation of modeling results. This study was motivating for our approach to combine both techniques in a complimentary way in order to make more objective interpretation of the exhumational history. As summarised by Vermeesch & Tian (2014) "HeFTy comprises all those paths, which cannot be rejected with the available evidence" (observed data) without ranking which of these "good" paths are better or more likely. On the other hand the output models from QTQt show "the most likely thermal histories, as-

suming that the observed data are good and the model assumptions are appropriate". Both modeling techniques imply objective and subjective aspects, which have to be considered when interpreting the results: In HeFTy the evaluation of proposed thermal paths is purely objective, based on a build in threshold value for the goodness of fit, whereas the placing of bounding boxes is purely subjective and the result of the user's evaluation of the significance, placement and size of constraint boxes. In QTQt the fact that the modeling space is left free of constraint boxes is rather objective, giving the data all freedom to look for the most likely solutions, whereas the geological significance of the modeling output can be only evaluated with a subjective comparison between observed data and model predictions.

The approach I adopted in this study is to perform forward and inverse modeling with HeFTy on single samples selecting the ones with the maximum data constraints (well reproducible AHe ages, AFT ages and track lengths). Next, an inverse modeling with QTQt on the same samples was performed to verify if the thermal histories proposed by HeFTy are reproduced and whether they can be ranked based on the criteria of likelihood with the observed data and preferred model simplicity. Generally speaking, modeling of individual samples can lead to over-interpretation of data patterns reflected in a increased complexity of the model (Gallagher, 2012) . In order to smooth out such possible effects I applied the multi-sample modeling approach in QTQt by combining the samples from each elevation transect in an effort to derive general thermal histories that best satisfy the observed data (and their uncertainties) and the regional geological assumptions and constraints.

4.4 Data Input and Model Setup

4.4.1 Data Input

Apatite (U-Th)/He data from the Nef and Leones transects are presented in Chapter 3.

For the **Leones transect** AHe data from all 17 samples (325 - 2250 m above sea level (a.s.l.)) have been included. Sixteen of these samples are presented in Section 3.5; AHe data from one additional sample that was dated after publication of the related manuscript was added to the dataset (sample 12-CM-02, 2254 m, see Appendix A2). Furthermore, AFT age data from seven of these samples (Section 3.6) has been included, whereas track length measurements from only two samples were considered for the data input and further interpretation. For the **Nef transect** AHe data from all seven samples (260 - 1500 m a.s.l.) has been combined with AFT age data from 3 samples.

All track length measurements from the Leones and Nef samples are used considering their c-axis projection.

For the **Cerro Barrancos transect** AFT age data and track length measurements from all five samples (130 -1960 m a.s.l.) from the study of Blisniuk *et al.* (2006) are discussed, although only four of these samples were considered in the multi-sample modeling approach (for details see Section 4.6). In the original data set the orientation of the measured track lengths with respect to the c-axis was not documented, therefore c-axis projection could not be applied here.

The AHe data from Cerro Barrancos include six samples from the study of Guillaume *et al.* (2013) spanning an elevation range from 147 to 1245 m a.s.l.. These samples were collected at the sampling locations for fission track dating by (Haschke *et al.*, 2006). As suggested by Guillaume *et al.* (2013), AHe data from their highest elevation sample (1436 m a.s.l) has not been considered, because it contains only one measured aliquot. For HeFTy modeling the mean AHe age is input with an error corresponding to the standard deviation of corrected single-grain ages from all measured aliquots. This error estimate considers the potentially large dispersion between single-grain ages, which usually represents a much larger uncertainty compared to the analytical error. For QTQt modeling data from each measured single-grain aliquot (U, Th, Sm, He) were input separately.

Figure 4.4. shows the age-elevation relationship (AER) of each dataset and slope calculation from a linear regression of mean ages (bootstrap analysis with 1000 samples). The single-grain ages in the AHe datasets are plotted for reference. All datasets, except the AFT data from Cerro Barrancos, range between 2 and 11 Ma. The calculated slopes and errors correspond to an apparent exhumation rate averaged over this time span and equal to ~ 0.5 mm/yr. The AFT data set from Cerro Barrancos averages a longer time span from 6 to 17 Ma with an average slope of 0.2 mm/yr. Apatite (U-Th)/He data from Cerro Barrancos span an elevation range of ~ 1000 m (147-1245 m a.s.l.), but show rather invariant cooling ages around 5 Ma. Only the uppermost sample located at 1245 m a.s.l. has an older mean age of 7.6 Ma; however it is averaged between 4 single-grain aliquots between 4 and 10 Ma (Guillaume *et al.*, 2013) that is not necessarily representative.

In addition it should be noted that the AFT data from the Leones and Nef transects mimic the offset observed between the AHe data from the same profiles (Section 3.6). All AFT cooling ages from the Leones profile are consistently by ~ 2 Ma younger then corresponding samples originating at similar elevations from the Nef transect. The AFT

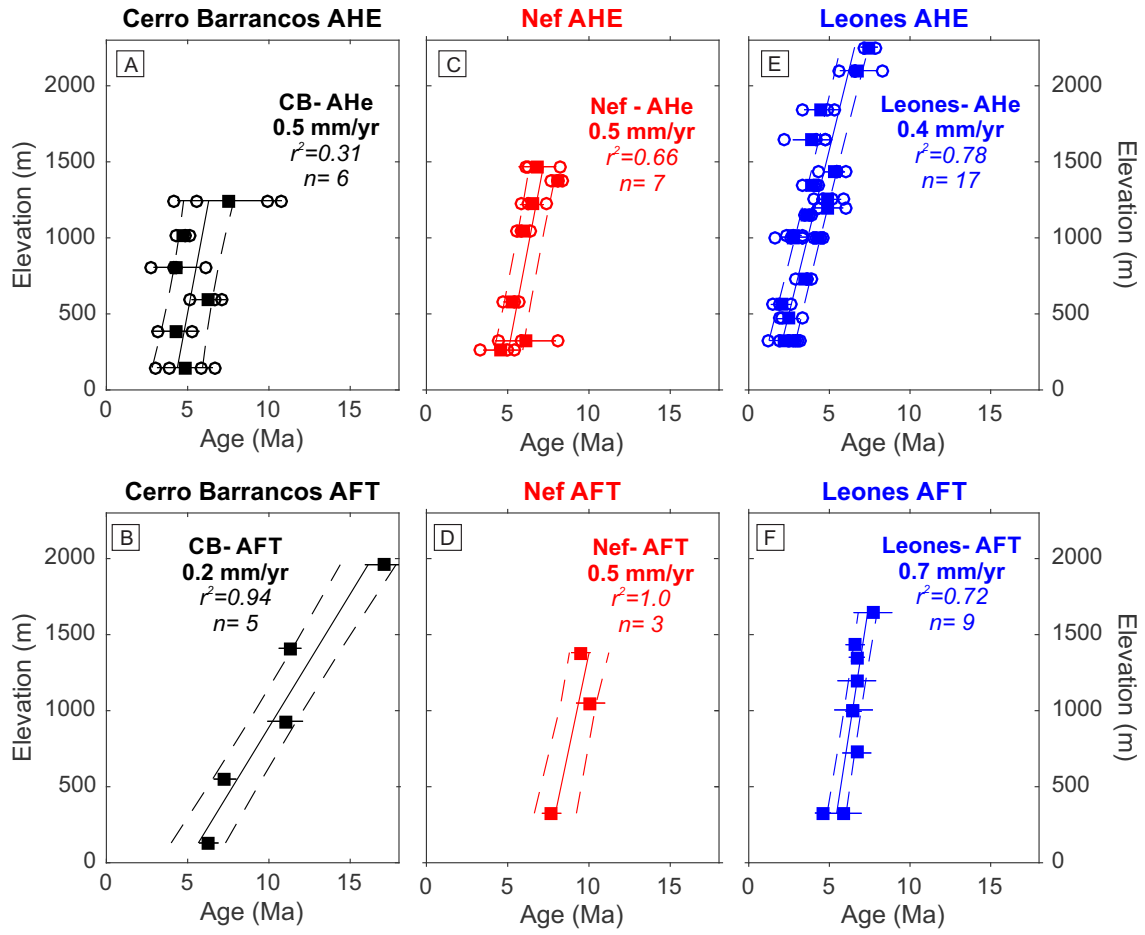

Figure 4.4 – Age-elevation relationship of input thermochronological data. AHe and AFT plotted against elevation from Cerro Barrancos (A, B), Nef (C, D), and Leones (E, F) elevation transects.

data from the Leones and Nef transects were not available at the time of publication of the study presented in Chapter 3. Importantly, the present observation strongly supports the proposed scenario for superimposed differential uplift due to fault movement along the Exploradores Fault.

All AHe data from the Leones and Nef transects are provided in Appendix A2. All AHe and AFT data from the Cerro Barrancos transect are provided in Appendix B1 and B2, respectively. All AFT data from the Leones and Nef transects are provided in Appendix B4.

4.4.2 HeFTy Model Setup

Inverse thermal modeling with HeFTy was performed on samples with sufficient fission track length measurements to back up the derived thermal histories. All five samples

from Cerro Barrancos have ~ 100 track length measurements (Blisniuk *et al.*, 2006), a number generally accepted to provide a track length distribution that is representative for the thermal history. The samples from the Leones and Nef transects proved problematic for track length analysis and only two samples from the Leones transect yielded close to 50 measurements. As a compromise and for the sake of comparison I opted for modeling the thermal histories of these two samples, although the results are interpreted with caution.

From the Leones transect forward and inverse HeFTy modeling was performed on samples 11-LL-08 (45 track lengths) and 11-LL06 (67 track lengths) located at 1005 m and 1351 m a.s.l., respectively. Both samples contain AFT and AHe age data.

From the Cerro Barrancos transect forward and inverse HeFTy modeling was performed on all five samples. AFT data from samples CB130, CB550 and CB930 (130 m, 550 m, and 930 m a.s.l, respectively) was combined with AHe data obtained from samples at similar elevations (147m, 594 m and 1019 m, respectively; cf. Guillaume *et al.* (2013)). Samples CB1410 and CB1960 were modelled with AFT data only (age data and track length measurements).

For all models I used the fission track annealing model of Ketcham *et al.* (2007b), c-axis projection where angles to the c-axis were available (Leones samples), Dpar as a kinetic parameter and heavy-ion irradiation for track length measurements (see Appendix B3. For AHe I used standard diffusion kinetics proposed by Farley (2000). For the goodness of fit (GOF) of thermal histories I adopted the default values of HeFTy of 0.5 for good paths and 0.05 for acceptable paths. Most models were run for 20 000 iterations as a reference (some for 30 000 where more freedom within the modeling space was allowed for) and the resulting number of good paths and GOFs were evaluated and compared between models. Temperature at the end of all models was fixed at 5±5°C.

The HeFTy model setup is illustrated in Figure 4.5. For all models an initial time-temperature (t-T) constraint (constraint 1) was placed at 30±2 Ma and 160±20°C.

This constraint is justified by the results from the study of Thomson *et al.* (2001) based on a regionally distributed data set of apatite and zircon fission track bedrock cooling ages at these latitudes. Results from this study imply little cooling of the entire region from the Pacific realm to the eastern foreland between 110-70 Ma and 30-10 Ma from below the closure temperature of fission tracks in zircon (~ 280°C) to below the partial annealing zone for fission tracks in apatite (~ 120°C). This t-T constrain forces total resetting of both input thermochronometers at the beginning of the model and

therefore allows for an unbiased evolution of the thermal history free from arbitrarily inherited information.

A common modeling strategy was adopted (Figure 4.5); small deviations from it for individual samples are discussed in the results section below:

1. Based on a a trial-and-error approach a forward model with good or modest fit to the input data was selected.

2. In a second step an unconstrained (except for constraint 1) model was run in order to approximately estimate the shape of the thermal history and how well it is constrained by the data. These two steps serve as a general anchor point for the t-T constraints in the final models, given the absence of other robust geological constraints for their placement. Since HeFTy performs a randomly distributed search of the entire modeling space, the placement of constraints is necessary in order to increase the efficiency of the modeling procedure and achieve final results. Another reason to place constraint boxes is to allow for the trial of reheating scenarios, which are generally not explored by the program in the unconstrained mode.

3. Based on the outcome of the forward and unconstrained inverse models a large constraint box (constraint 2) is placed encompassing the time-temperature window of the onset of final cooling. This model setup (panel A in all corresponding figures in Appendix B5) allows for a relatively simple cooling-only scenario, the plausibility of which can be evaluated based on the availability and number of good paths and their fit to the input data.

4. The episode of final cooling is generally tightly constrained by the AHe data, which are < 6 Ma for all modelled samples. However, the AFT age and particularly the track length data allow for some variability of the shape of well-fitting thermal histories preceding final cooling. All modelled samples contain shortened track lengths that could potentially record more protracted residence in the partial annealing zone and/or reheating scenarios. To test for and to evaluate between these possibilities I divided constraint 2 in two t-T constraints, from which the centre of the earlier constraint (2a) is placed at slightly lower temperature than the centre of the following constraint (2b). Importantly, I set the segment properties between these two constraints as "monotonic variable" (vs. the default "monotonic consistent") to allow for both cooling and reheating scenarios to be searched for. With

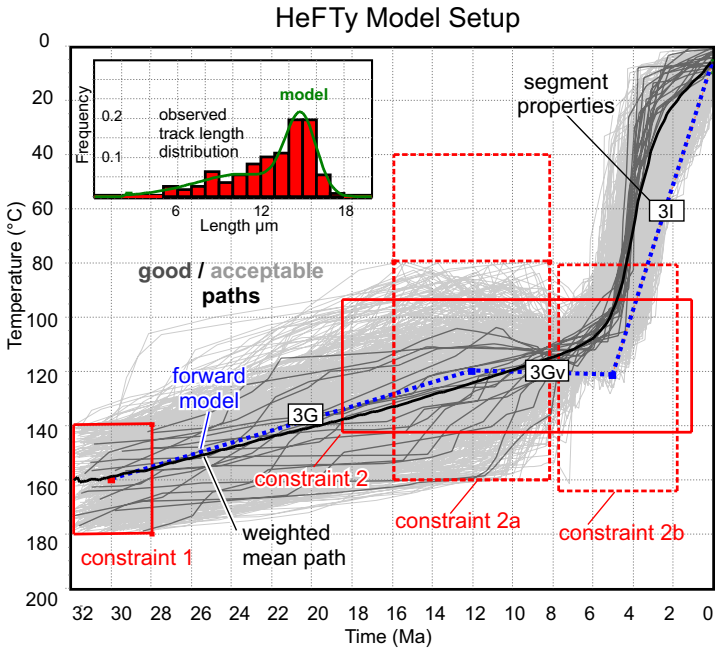

Figure 4.5 – HeFTy Model Setup

this model setup (panel B in all corresponding figures in Appendix B5) the random search of HeFTy includes scenarios with minor reheating between constraints 2a and 2b, however without forcing it (i.e. only-cooling scenarios are tried as well).

5. In the final model setup the upper bound of constraint 2a is extended towards lower temperatures allowing for a larger amount of reheating preceding final exhumation (panel C in all corresponding figures in Appendix B5).

6. The results from the HeFTy models are compared to those from the study of Blisniuk *et al.* (2006). For the sake of comparison a reference model was setup mimicking precisely the constraints used by Blisniuk *et al.* (2006) (panel D in all corresponding figures in Appendix B5).

For each HeFTy model run the number of iterations and good paths as well as the corresponding GOF values are indicated along with the observed vs. predicted track length distribution (as inset). The thick black line in each plot corresponds to the weighted mean thermal history based on all good-fitting solutions.

4.4.3 QTQt Model Setup

Input Data

Input files for QTQt were prepared over the graphical user interface of the software. Fission track age data is input as counts of induced and spontaneous tracks with corresponding Dpar measurements for each grain (averaged from 5-10 Dpar values per grain) as compositional parameter. The mean and standard deviation of all Dpar values are input as compositional proxy with corresponding error for each sample. For the Cerro Barrancos samples the original data set presented in the study of Blisniuk *et al.* (2006) documents only an averaged Dpar value per sample (data produced by Warkus (2002), unpubl. PhD thesis, University of Potsdam). If the Dpar error is set to zero, then the annealing model is chosen using the fixed value of the compositional parameter. A more realistic non-zero error input implies sampling of the compositional parameter from a normal distribution, with a mean equal to the Dpar value and a standard deviation equal to the error. This is one way QTQt allows for a reasonable uncertainty in the data and/or annealing models or their calibration. For the sake of consistency with our data (Leones and Nef) and because I consider such uncertainty a realistic and necessary assumption, a Dpar error for the Cerro Barrancos AFT data was adopted corresponding to $\sim 10\%$ of the original value and conform with Dpar variability described byWarkus (2002).

Fission track length data is input as individual length measurements, angle to the c-axis for each measurement, and Dpar value of each measured track (from slides with heavy-ion irradiation, cf. Appendix B3)). Mean track length (MTL) from original length measurements and for lengths corrected for their orientation to the c-axis are calculated by the program. C-axis projected lengths distributions were used for the Leones samples in order to account for the anisotropy of the annealing process in apatite (Green & Durrani, 1977; Laslett *et al.*, 1984).

AHe data is input as single aliquots for each sample with corresponding values for U, Th, Sm (in ppm) and He (nmol). FT correction is calculated for a sphere geometry, but generally the observed vs. modelled *uncorrected* ages were compared.

Generally the He-diffusion parameters are set according to the standard diffusion kinetics for He in apatite proposed by Farley (2000). More complex diffusion models have been proposed that consider the possible effects of radiation damage on He-diffusion in apatite (Gautheron *et al.*, 2009; Flowers *et al.*, 2009). Older AHe cooling ages, high-uranium contents, large single-grain age dispersion within samples, slow cooling or long permanence above or within the partial retention zone are all considered factors which

might hint toward potential impact of radiation damage on He-diffusion and hence cooling ages. However, U-contents of all samples presented here are normal (3-90 ppm), AHe ages are young (< 8 Ma) and slightly younger than corresponding AFT ages (< 11 Ma) suggesting rapid passage through the partial retention zone for AHe over the last couple of million years (~ 15-20°C/Ma), see Section 3.6). All samples from the Leones and Nef transects show very good reproducibility between single grain ages; The Cerro Barrancos samples (Guillaume *et al.*, 2013) also reproduce rather well with the exception of two samples (DES17 and DES22), which contain some older single-grain ages. These however are not correlated with high U-contents and could reflect tiny U- and Th-bearing inclusions providing perceivable excess-He in these relatively young samples. In summary, one can expect the effects of radiation damage to have only minor or no impact on the thermal histories derived from standard diffusion kinetics. Conversely, other authors have recently argued for an important effect of radiation damage for the Cerro Barrancos samples whose consideration is supposed to disclose a very different thermal history for this data set in particular and the regional geologic setting in general (Guillaume *et al.*, 2013). For this reason I adopted the radiation damage model of Gautheron *et al.* (2009) for some selected models with single- and multiple-sample approach in order to compare the output.

Priors

The Bayesian approach of QTQt requires the definition of a prior probability distribution in the modeling space, i.e. a broad time-temperature box that most likely contains the thermal history constrained by the data. For all models (single- or multiple-samples) the oldest age (A) (the oldest AFT age or the oldest single-grain age in this sample or suite of samples) is used as the centre of a uniform time prior with a range equal to this age (i.e. $A \pm A$) (Gallagher, 2012) (Figure 4.6). The temperature prior is centred at 100°C with a range of ± 100°C (100±100°C), which corresponds to a temperature window broadly covering the sensitivity of both input thermochronometers. For multiple-samples models an additional prior for the temperature offset between the uppermost and lowermost samples needs to be defined that implies an assumed geothermal gradient or a range of geothermal gradients. The offset parameter is selected from a given range and kept constant over time or it is alternatively allowed to vary over time within the given range. The absolute values for the temperature offset used in the models vary according to the elevation range of the input transect. Generally, I favour a scenario with a geothermal gradient between 25 and 45°C/km that is allowed to vary over time

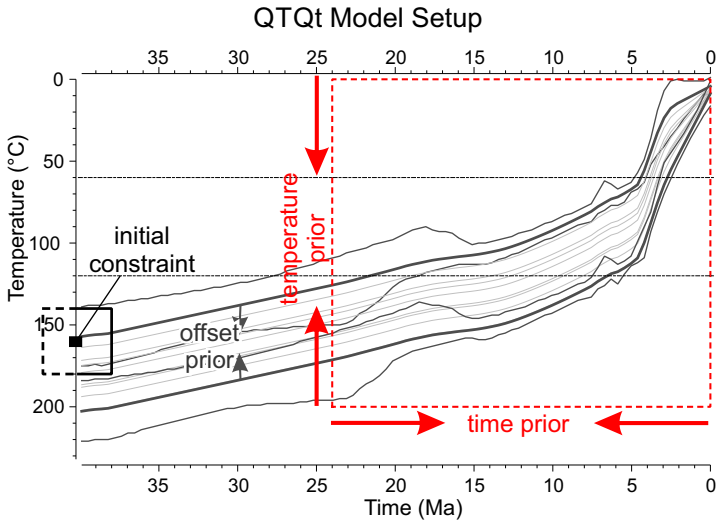

Figure 4.6 – QTQt Model Setup

within this range. For the sake of comparison and discussion some selected models were run with fixed and lower temperature offset (see Section 4.6.2).

Constraints

As outlined in the General Approach section above (Section 4.3.1) I refrain from using constraints within the time-temperature prior. This concept is compatible with the Bayesian approach of QTQt letting the data and their robustness the entire freedom to define and rank the likely solutions for the thermal history (Gallagher, 2012; Vermeesch & Tian, 2014). However, I imply an initial constraint at the beginning of all models at 30 to 50 ±2 Ma and 160± 20 Ma (consistent with the HeFTy setup described above) that ensures total resetting of both thermochronometers (Figure 4.6). The time window of the initial constraint varies between models depending on the input time prior (which depends on the oldest input age) and was generally centred at ~ 15 Ma before the upper limit of the time prior (e.g. time prior 12±12 Ma, initial constraint at 40±2 Ma and 160±20 °C, Figure 4.6). Note that all input constraints in QTQt apply to the uppermost sample in the elevation transect. For the sake of comparison and discussion some selected models were run without initial constraint. Present-day temperature for all models is set to 5±5 °C as is the present-day temperature offset between the uppermost and lowermost samples in the multi-samples models.

Model runs and output

The MCMC algorithm in the final model was run for a minimum of approximately 100 000 iterations for single-sample and 200 000 iterations for multiple-sample model

runs after discarding 50 000 iterations as "burn-in" (Gallagher, 2012). This final model run is preceded by several short model runs of approximately 20 000 iterations (10 000 as "burn-in" and 10 000 as "post burn-in", see cf.Gallagher (2012) and Wildman *et al.* (2016)) in order to tune the MCMC search parameters before performing longer runs. As suggested by Gallagher (2012) the choice of MCMC parameters is based on the value of the rate of acceptance of proposed models being ideally between 20 and 60%. This preliminary step of parameter tuning is essential for a robust modeling output because it ensures the performance of the MCMC sampling chain in terms of sufficient exploration of the modeling space and representative ranking of the proposed thermal histories. After each sampling chain the values of the acceptance rates were examined as well as the log of the likelihood function and the posterior probability. A model is considered final only after acceptance rates were within the desired range and the convergence of the sampling chain toward a stable range of values for the likelihood to the data and the posterior probability was achieved. A log summary of the performed models is provided in Appendix B7.

The output of the Bayesian approach is an ensemble of accepted thermal history models, each with an associated posterior probability. From the collection of thermal histories, a mean thermal history model (weighted by the posterior probability of each individual thermal history), termed the expected model, is produced with 95% credible intervals that provide the uncertainty of the model. The nature of the expected model is that it will retain well-constrained features (i.e., features common to many individual models) while more complex deviations observed in only a small number of viable models are averaged out. The expected model, and its associated uncertainty measures, provides the most robust, albeit conservative insight into the overall thermal history of the sample.

4.5 New Apatite Fission Track Data (Leones and Nef)

AFT analysis was performed on 9 samples from the Leones, and 3 samples from the Nef elevation transects. Horizontal confined track lengths were measured only for five samples, mainly because of highly annealed or poor quality samples. However, only two of these samples yielded an acceptable quantity of track lengths (11-LL-08, N track lengths = 45 and 11-LL-06, N track lengths = 67) and were considered for further interpretation and thermal modeling 4. Kinetic properties of individual grains were estimated with Dpar measurements. For the two track-lenghth samples 11-LL-08 and 11-LL-06 Dpar values were estimated for measured tracks on the heavy-ion irradiated slides. AFT results are summarised in Appendix B4.

AFT pooled ages range between 4.6 ± 0.5 Ma and 10.1 ± 0.9 Ma (Appendix B4). Dpar values range from 1.75 to 2.94 µm (standard irradiation) and from 2.09 to 2.95 (heavy-ion irradiation). There is no significant discrepancy in the Dpar values between the same sample mounts irradiated with different ion beams (cf. Barbarand *et al.*, 2003). Measured Dpar values are all >1.75 µm pointing to Cl- and/or OH-rich apatites that are relatively resistant to annealing (Ketcham *et al.*, 1999; Donelick *et al.*, 2005). Measured fission-track lengths varied between 9.29 ± 3.31 µm and 13.99 ± 1.27 µm. Lengths corrected for their orientation with respect to the c-axis for samples LL11-06 (n=67) and LL11-08 (n=45) resulted in mean track lengths of 14.1 ± 1.5 μm and 12.7 ± 1.5 μm, respectively. Only these two samples were used in the modeling approach.

4.6 Modeling Results

4.6.1 Inverse Thermal Modeling - HeFTy

Cerro Barrancos samples

For all samples from the Cerro Barrancos transect, except the uppermost one (CB1960, discussed below), the above modeling strategy was applied and yielded similar results. For all four samples (CB130, CB550, CB930 and CB1410) the data sets were first reasonably fitted with similar forward model paths (dark blue dotted line in all plots), entering the PAZ for AFT (~ 120°C) at some time between 14 and 10 Ma followed by a period of ~ 4-8 Myr of very slow cooling, residence or very minor reheating within the AFT-PAZ, and onset of final rapid exhumation at ~ 4-6 Ma. Figures 4.7 and 4.8 display exemplary results from samples CB130 and CB930, modeling results from all samples are presented in Appendix B5.

Inverse modeling with monotonic cooling scenarios (i.e. only-cooling allowed between constraints, panel A in Figures 4.7 and 4.8 and Figures B.6-B.9 in Appendix B5) for all four samples yields many good-fitting paths with excellent goodness of fit of the best-fit scenario (GOF) for the AFT data and acceptable (CB130, CB550) and good (CB930) fit for the AHe data. The GOFs for the AHe data in samples CB130 and CB550 are lower and modelled AHe ages in both samples show a tendency toward the lower limit of the 1-sigma standard deviation. It is noteworthy that both samples show rather large dispersion between single-grain ages (3-7 Ma for CB130 and 5-7 Ma for CB550, cf. Guillaume *et al.* (2013)) and the modeling output appears to favour the lower limit of the corresponding age range. The age dispersion does not correlate with U-contents and eU values (effective Uranium, eU = [U]+0.24×[Th]), suggesting that older ages might

be due to unrecognised tiny U- and Th-bearing inclusions that could potentially alter these relatively young samples.

Two scenarios that allow, but do not force, reheating before final exhumation were explored (panels B and C in Figures 4.7 and 4.8 and Figures B.6-B.9 in Appendix B5): One large constraint box (2a, cf. Figure 4.5) encompasses the modeling space from ~ 16-18 Ma to ~ 6-8 Ma and 80°C to 160°C and therefore covers the time window for onset of reheating proposed by previous studies (Blisniuk *et al.*, 2006; Guillaume *et al.*, 2013). The second constraint (2b, cf. Figure 4.5) is placed adjacent to constraint 2a from ~ 6-8 Ma to 2 Ma and from 80°C to 180°C. The centre of constraint 2b is placed slightly lower (at higher temperatures) then the centre of constraint 2a and the segment properties between the two are set to be monotonic-variable (see details of the model setup above). This settings are essential to setup the search algorithm of HeFTy to include cooling and reheating paths between these two constraints without forcing neither one of them. In the second reheating scenario (panel C in all corresponding figures) the temperature range of constraint 2a is larger (40°C to 160°C) allowing the testing of scenarios with larger amount of reheating before final exhumation. In all four samples (Figures 4.7 and 4.8 and Figures B.6-B.9 in Appendix B5) it is evident that monotonic cooling scenarios with protracted passing through the AFT-PAZ are preferred and constitute the majority of good-fitting paths found by HeFTy. This is also reflected by the weighted mean paths indicated by a black line in every plot. It is also evident that many reheating scenarios are acceptable and some have good fit to the data meaning that a reheating episode preceding final exhumation is supported, however not required by the data.

As noted by the original authors of the fission track data set from Cerro Barrancos (Warkus, 2002; Blisniuk *et al.*, 2006), the uppermost sample in the transect CB1960 features a notably different shape of the track length distribution (MTL 10.3±0.24 µm) and likely underwent a different thermal history. Proposed causes include the location of this particular sample on the drier, leeward (eastern) side of the Cerro Barrancos massif (Blisniuk *et al.*, 2006) or its very exposed ridge location and likely susceptibility to lightning (Warkus, 2002). Our results confirm that an only-cooling scenario that is analog to the the one tested for the other four samples (panel A in all corresponding figures) does not yield any good or even acceptable thermal histories for this sample. The data is reasonably fitted with a forward model featuring a major reheating event of ~ 60 -120°from temperatures below 40°C to the upper limit of the AFT PAZ at ~ 120°C (Figure 4.9). Constraining the modeling space more tightly (Fig. 4.9A) or broadly (Fig. 4.7B) along the path that is defined by the forward model confirms that the data is

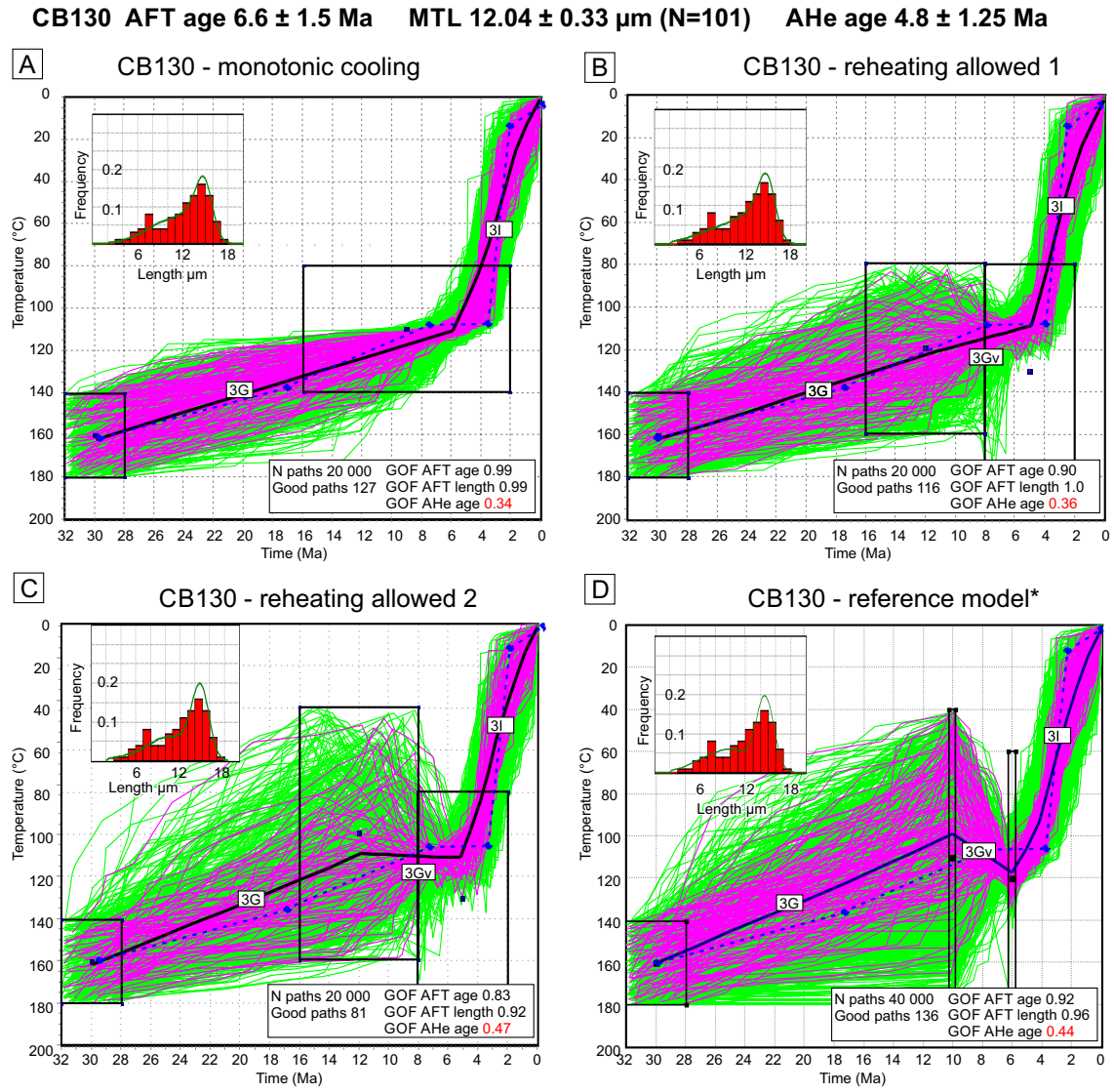

Figure 4.7 – HeFTy model of sample CB130, Cerro Barrancos with cooling-only scenario (A), minor (B) and major (B) degree of reheating allowed, and a model setup mimicking modeling conditions of Blisniuk *et al.* (2006) as a reference model (D).

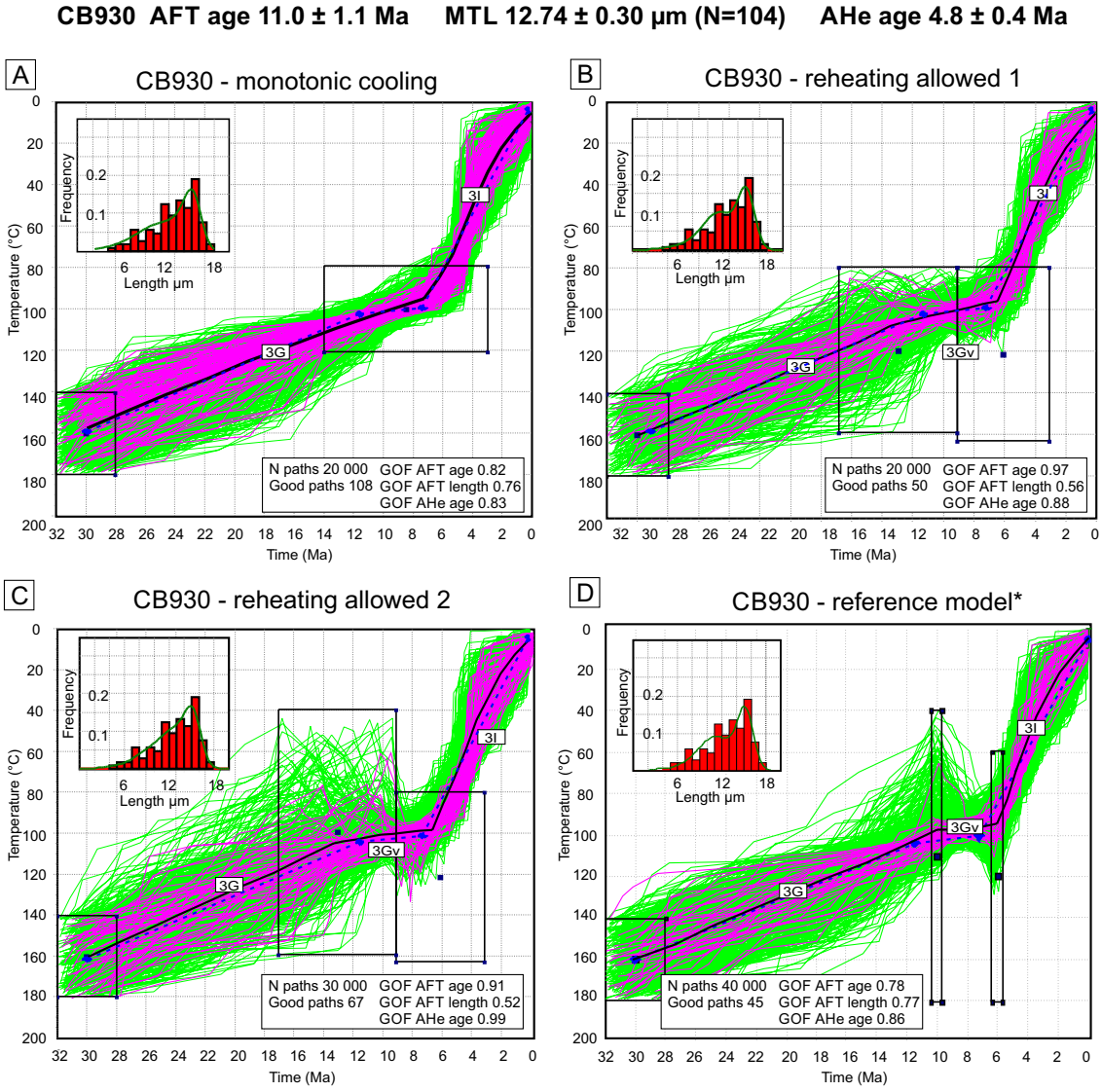

Figure 4.8 – HeFTy model of sample CB930, Cerro Barrancos with cooling-only scenario (A), minor (B) and major (B) degree of reheating allowed, and a model setup mimicking modeling conditions of Blisniuk *et al.* (2006) as a reference model (D).

best fitted by an episode of very fast and well constrained cooling from 80-120°C down to surface temperatures. This is preceded by an episode of reheating whose onset and magnitude are not well constrained. Because the second reheating scenario (Fig. 4.7B) implies very broad constraint boxes with almost the entire modeling space available for the search algorithm, I ran this simulation for a large number of iterations until 100 good-fitting thermal histories were found.

As mentioned above, Blisniuk *et al.* (2006) already explored the thermal histories of the samples from Cerro Barrancos as constrained only by the AFT data (published at the time) and using the software AFTSolve - a preceding version of HeFTy with similar functionalities (Ketcham *et al.*, 2000). Blisniuk *et al.* (2006) implied two intermediate constraints (besides initial high-temperature and final present-day constraints) that mark the possible onsets of reheating and final cooling episodes, respectively, shifting these through time to explore different temporal scenarios. In their study Blisniuk *et al.* (2006) display representative results from a scenario with constraints defining the onset of possible reheating between 10 (constraint at 10 Ma over 40-180°C) and 6 Ma (constraint at 6 Ma over 60-180°C) and followed by final cooling after 6 Ma (Figure B.27 in Appendix B6). The results presented by these authors support a constrained reheating episode between 10 and 6 Ma, i.e. all acceptable and good-fitting paths indicate reheating scenarios. These results are, however, inconsistent with ours. For the sake of comparison and as a tool to re-evaluate the geodynamic conclusions drawn from these results by Blisniuk *et al.* (2006), I added a reference model to each of the 5 samples (panel D in Figures 4.7 and 4.8, panel C in Figure 4.9) mimicking their model setup in terms of placement and size of constraints. I added the AHe data from Guillaume *et al.* (2013) and used the updated fission track annealing model of Ketcham *et al.* (2007b) (compared to the annealing model of Ketcham *et al.* (1999) used by Blisniuk *et al.* (2006)). Because of the addition of more data (AHe) I doubled the number of iterations (40 000 compared to 20 000 used by Blisniuk *et al.* (2006)).

The reference model results are consistent with those obtained with our model setup and document numerous good-fitting thermal histories of monotonic cooling with protracted passing through the AFT PAZ along with some scenarios with reheating episodes between 10 and 6 Ma. Notably, in this model setup sample CB130 displays a more evenly distributed frequency of both types of thermal paths with many reheating scenarios that support the data as well. The data inversion with the reference model setup for the uppermost sample CB1960 does yield only few acceptable thermal histories (Figure 4.9C); adding another constraint over a larger temperature interval around the very young

onset time for final cooling improves the results, but still yields only a few good-fitting paths. This is likely because, as suggested by the forward model and the preceding data inversions (Figure 4.9A and B), most good-fitting paths need a larger amount of reheating, i.e. the constraints preceding final cooling need to extend over temperatures lower than 40°C.

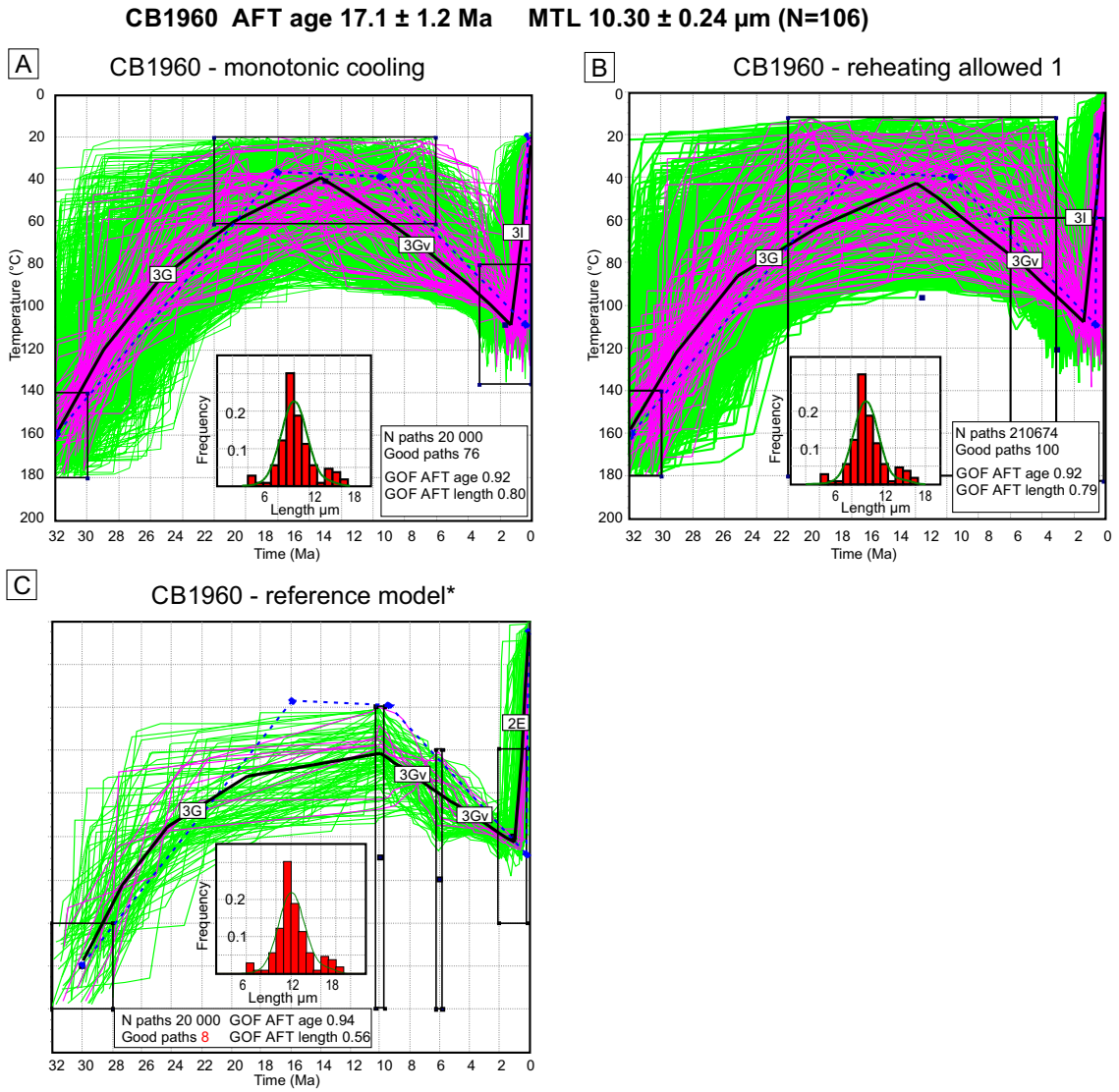

Figure 4.9 – HeFTy model of sample CB1960, Cerro Barrancos with more (A) and less constrained (B) forced-reheating scenario, and a model setup mimicking modeling conditions of Blisniuk *et al.* (2006) as a reference model (C).

Leones samples

Only two samples from the Leones transect provided enough input data in terms of track length measurements for forward and inverse thermal modeling (AFT and AHe age and ~ 50 track length measurements). From the remaining samples no or only a few track length measurements could be performed likely because of the young AFT ages (< 10 Ma, i.e. generally few spontaneous tracks present) and bad quality of some of the apatite grains in the mounted slides. Sample LL11-06 (1351 m a.s.l.) and sample LL11-08 (1005 m a.s.l.) have nearly identical AFT and AHe ages that overlap within error.

However the track length distributions differ with mean track length (MTL) of 14.1±1.5 μm for LL06 (N=67) and 12.7±1.5 μm for LL08 (N=45). Certainly, the limited number of track lengths in these samples might result in distributions that underestimate some of the track length populations, therefore the results are interpreted with caution focusing on the general trends and refraining from over-fitting the data (particularly the track length distributions).

Forward modeling of data from sample LL11-06 (1351 m a.s.l.) indicates onset of rapid exhumation at ~ 8 Ma with apparent stepwise cooling episodes after ~ 4 Ma (Figure 4.10). The unconstrained model (besides initial and present-day constraints) results in only acceptable thermal history paths. The simple monotonic cooling scenario with one intermediate constraint broadly encompassing the onset of final exhumation yields a couple of good paths confirming onset of rapid cooling at ~ 8 Ma with a stepwise course after 4 Ma (Figure 4.10A). Adding two additional constraint boxes in order to force such stepwise course of the later thermal history and matching the forward model more precisely notably increases the effectiveness of the modeling algorithm and the number of good fitting paths (Figure 4.10B). The final scenario that allows for some reheating episode preceding final pulse of exhumation confirms that monotonic cooling is the preferred thermal history matching the data (Figure 4.10C).

Forward modeling of data from sample LL11-08 (1005 m a.s.l.) suggests a later onset of rapid exhumation at ~ 4 Ma preceded by an episode of very minor reheating (~ 20°C) within the AFT PAZ (Figure 4.11). As expected, the monotonic cooling scenarios with no or one intermediate constraint result in no or very few good-fitting paths, respectively (Figure 4.11A). Conversely, the input of additional intermediate constraint boxes closely matching the course of the forward model and therefore forcing minor reheating results in a robust output with a large number of good fitting paths (Figure 4.11B). Changing the shape of these intermediate constraint in order to allow monotonic cooling paths as well (Figure 4.11C) and increase the amount of potential reheating (Figure 4.11D) confirms that the minor-reheating scenario is the preferred one (Figure 4.11), although a larger degree of reheating is not entirely excluded by the data.

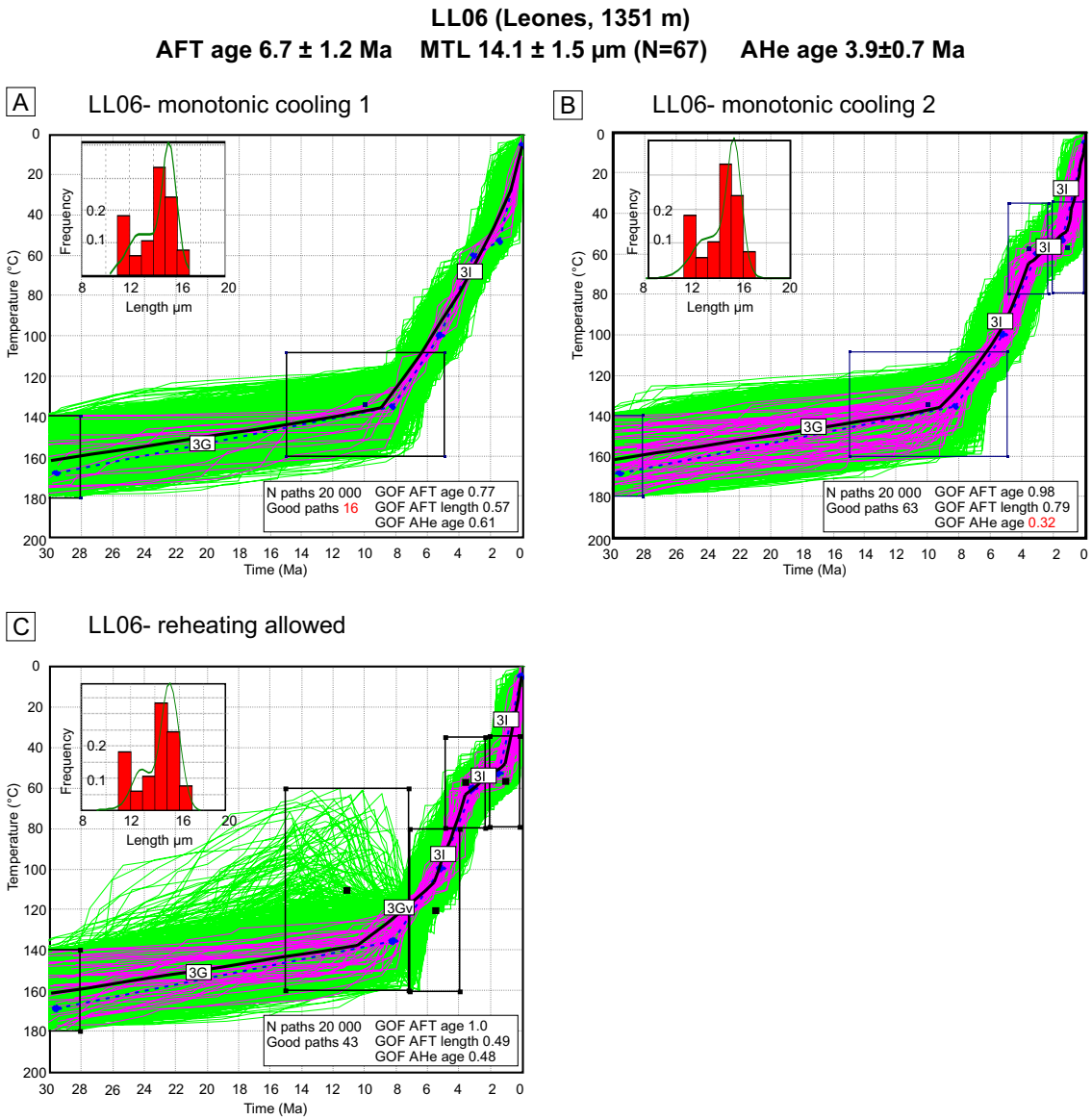

Figure 4.10 – HeFTy model of sample LL06, Leones transect with less (A) and more constrained (B) only-cooing scenario and a setup with allowed reheating (C).

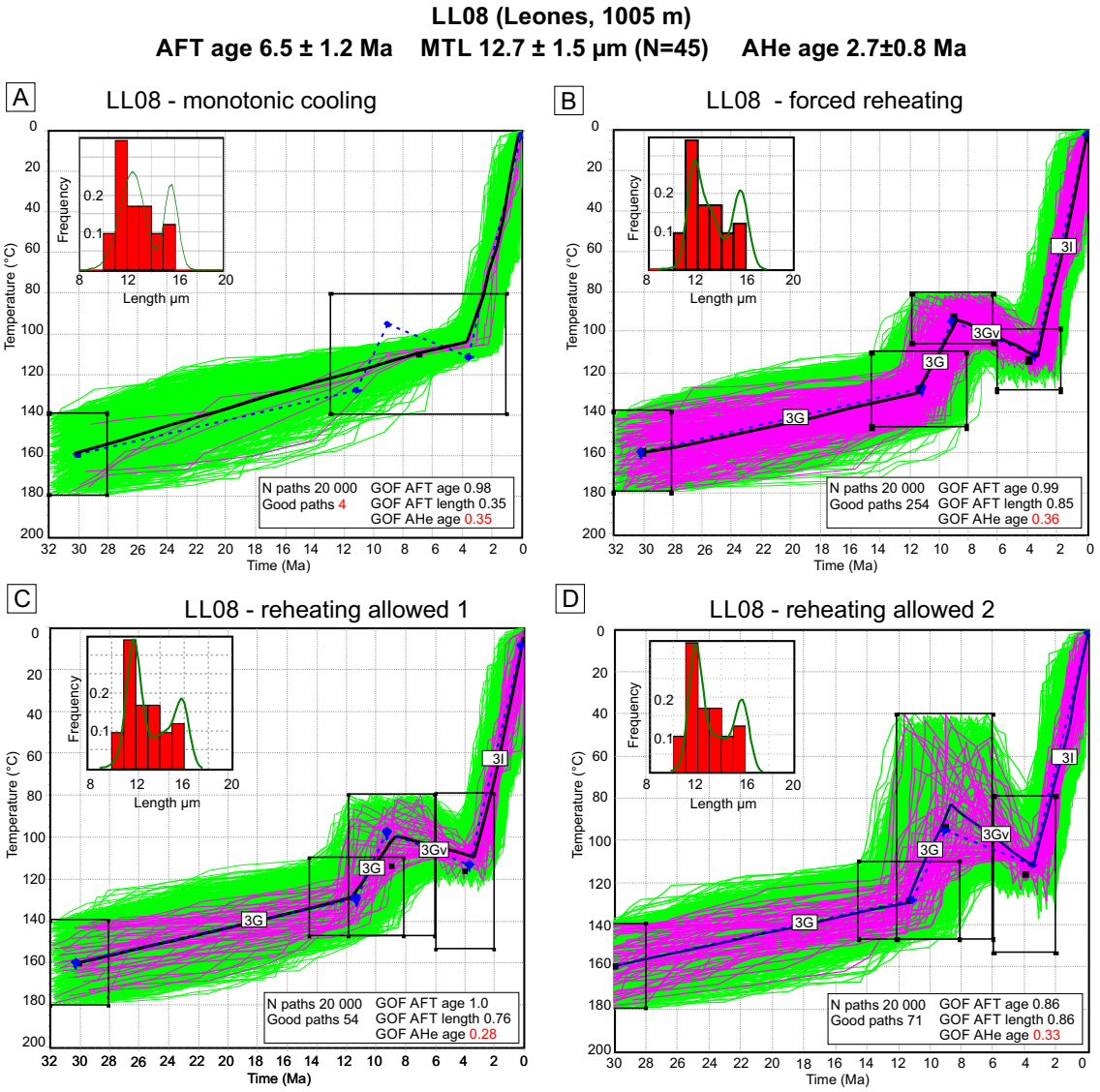

Figure 4.11 – HeFTy model of sample LL08, Leones transect with only-cooling scenario (A), forced and tightly constrained reheating (B) and variable degree of allowed reheating (C, D).

4.6.2 Inverse Thermal Modeling - QTQt

4.6.2.1 Cerro Barrancos - Single Samples

Inverse thermal modeling of data from single samples with QTQt was performed on all five samples from the Cerro Barrancos transect. For three samples (CB130, CB550 and CB930, located at 130, 550 and 930 m a.s.l., respectively) fission track data from the study of Blisniuk *et al.* (2006) were combined with AHe data from Guillaume *et al.* (2013) from samples along the same transect located at 147, 594 and 1019 m a.s.l., respectively. The small variation in elevations is considered irrelevant given the much

larger uncertainty of the dating methods. For samples CB1410 and CB1960 only AFT data was used as input.

All modeling outputs are summarised in Figure 4.12 (thermal histories) and Appendix B6, Figures B.13-B.17 (thermal histories and predicted vs. observed data). Figure 4.12 shows the probability distribution of all thermal histories for the final model runs along with the ensemble of accepted thermal histories (maximum likelihood, maximum posterior and mode models, cf. Gallagher (2012)) and the mean thermal history referred to as the **expected model**. The expected model represents a mean model weighted by the posterior probability of all models and therefore not an actually sampled thermal history. The expected thermal history can be similar to or very different particularly from the maximum likelihood model (best-fit to the data) that tends to have more structure as it is not penalised for its complexity. Figures B.13-B.17 in Appendix B4 also show a summary of the model predictions from the expected model vs. the observed data for each model along with the thermal histories. Note that the symbols indicating observed and predicted AHe ages correspond to the uncorrected ages.

The modeled thermal histories for all samples largely overlap with modeling results achieved with the HeFTy program. Results from the three intermediate samples (CB550, CB930 an CB1410 - Figure 4.11B-D) indicate cooling scenarios with onset of final rapid exhumation between 8 and 6 Ma preceded by a few million years of protracted passage through the PAZ for AFT. The lowermost sample in the transect CB130 indicates a slightly younger onset of final exhumation at around 5 Ma preceded by a minor reheating of 30-40 °C, which is also expressed by the bimodality of the track length distribution.

Model predictions of AHe and AFT data from the expected model fall within error of the observed data for most of the modeled samples (Figures B.13-17). The older AHe single-grain ages from the two lowermost samples with larger single-grain age dispersion (CB130 and CB550, Figure B.13 and B.14) do not match model predictions. In agreement with HeFTy results, the modeled thermal histories seem to favour the younger single-grain age population instead, which I consider representative for the AHe age of these samples. For all samples except CB930 the AFT age predicted by the expected model falls in the upper limit (or outside for CB1960) of the 2-sigma error of the observed data; however, the actually sampled posterior and maximum likelihood models fit the data well and the latter is in all four cases very similar to the mean (expected) model. For sample CB550 (Figure B.12A) the maximum likelihood model might propose some very different scenario (abrupt cooling-reheating) with equally good fit to the data; however, these thermal histories are penalised for their complexity (from a

Bayesian perspective, cf. Gallagher (2012)) since the data is well predicted by a simpler thermal history reflected by the expected model.

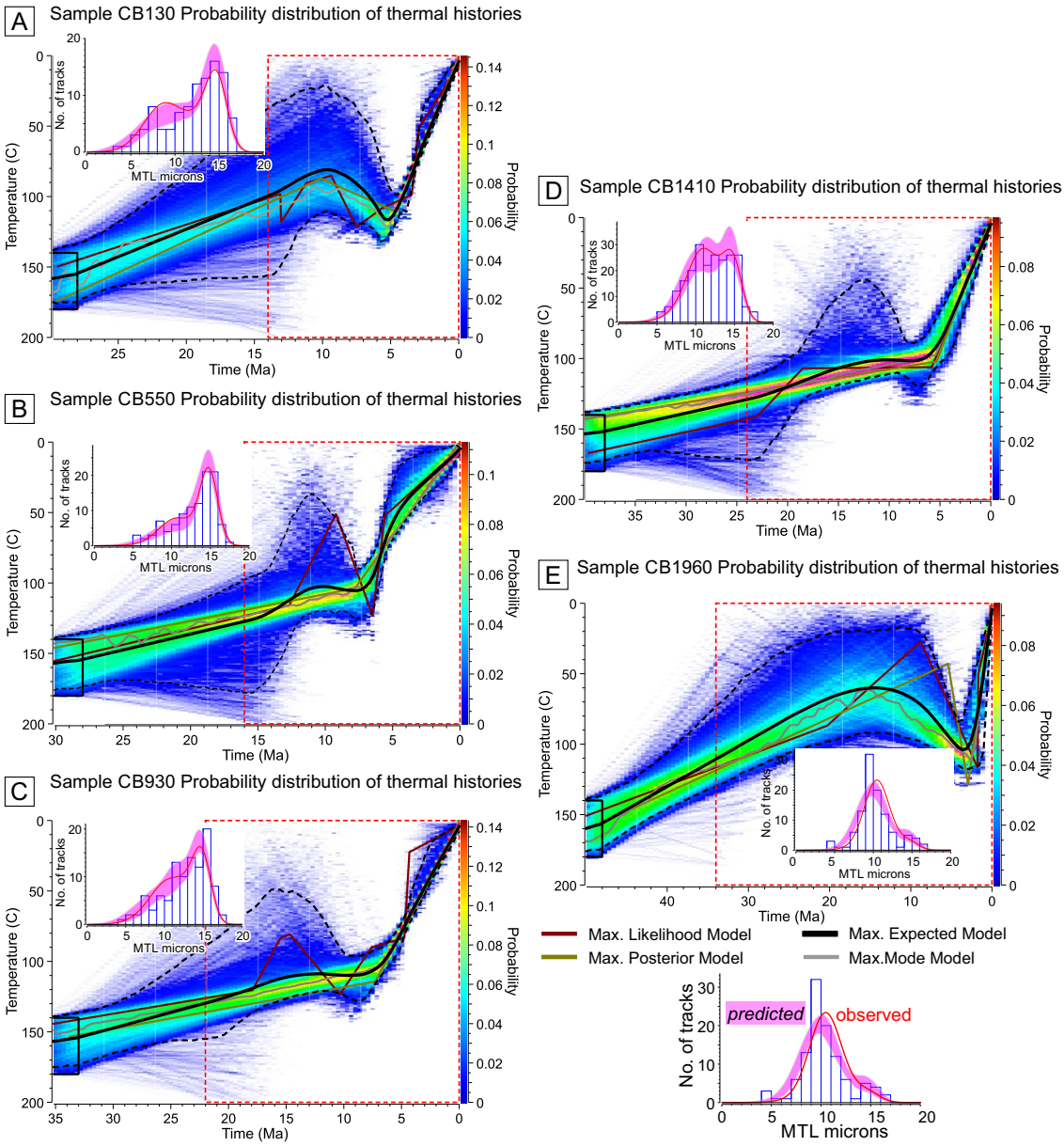

Figure 4.12 – Cerro Barrancos - Summary of results from single-sample model runs with QTQt from samples CB130 (A), CB550 (B), CB930 (C), CB1410 (D), and CB1960 (E).

In agreement with HeFTy results, the QTQt inversion of data from the uppermost sample CB1960 (Figure 4.12E and Figure B.17) constrains a major episode of reheating of 40-80°C with vaguely defined temporal onset and well constrained, very rapid cooling from above ~ 120°C to surface temperatures over a short time interval of < 2 million years. As mentioned above, the mean model here predicts an AFT age that is off-error of the observed data, but the maximum likelihood and posterior models haven an excellent data fit with the reheating-rapid cooling scenario.

For all three samples with AHe data the inversion was run with both standard He diffusion kinetics (Farley, 2000) and the the radiation damage model of Gautheron *et al.* (2009) for comparison (Figure B.13-15, panels A and B, respectively). The objective of considering radiation damage here despite our expectation for its negligible effect on the AHe data is the following discussion of the study of Guillaume *et al.* (2013), who propose that considering radiation damage effects on the AHe data of these samples is a crucial element in deciphering a major reheating event with significant geodynamic implications for this region. In contrast, the data inversion with the radiation damage model of Gautheron *et al.* (2009) for all three samples yields thermal histories analog to the ones resulting from standard diffusion kinetics.

4.6.2.2 Cerro Barrancos - Multiple Samples

Multiple-sample models were run for all AFT (Blisniuk *et al.*, 2006) and AHe (Guillaume *et al.*, 2013) data from the Cerro Barrancos transect excluding AFT data from the uppermost sample CB1960. As observed by Blisniuk *et al.* (2006) and confirmed by the single-sample models with HeFTy and QTQt this sample records a very different and therefore apparently incompatible (with the rest of the data set) thermal history likely because of analytical inconsistencies or local factors that cannot be assessed.

The preferred multiple-sample model setup for Cerro Barrancos includes samples from 130 to 1410 m spanning approximately 1300 m of elevation. The input temperature offset between the uppermost and lowermost sample is set to 45±13°C, which corresponds to a range of geothermal gradients of 25-45°C/km and is allowed to vary over time. We consider a temporal variance of the geothermal gradient in order to allow for (but not force) proposed thermal effects of ridge collision and slab window opening (Guillaume *et al.*, 2013; Braun *et al.*, 2013) and the effects of major erosional events associated with the onset of glaciation (Mercer & Sutter, 1982; Lagabrielle *et al.*, 2010) in this region that both could have potentially altered the thermal structure of the modelled section. The time prior is set to 24 Ma (oldest AFT age is 11.3 Ma) and the temperature prior is set to 200°C. The initial constraint for the uppermost sample is set ~ 15 Ma before

the upper limit of the time prior at 40±2 Ma and 160±20°C. The model was run with both standard (model cbr-11, Figure B.18 in Appendix B6) (Farley, 2000) and modified (model cbr-G02, Figure B.19 in Appendix B6) (Gautheron *et al.*, 2009) He-diffusion parameters for comparison. The mean thermal histories (expected model) and their corresponding predictions (modeled vs. observed data) are summarised in Figure 4.13 and Figures B.18 and B.19 in Appendix B6.

Both models define similar thermal histories with comparable data fit within error of the observed data. The thermal histories are well constrained (see 95% confidence interval for the uppermost and lowermost samples) reflecting similar shape of all three sampled output paths (max. likelihood, max. mode and max. posterior models). The thermal history in both models defines protracted passage through the AFT PAZ and onset of rapid cooling at ~ 6-7 Ma. Using the modified He-diffusion parameters after Gautheron *et al.* (2009) introduces more structure to the final cooling episode implying stepwise exhumation (Figure 4.13B). This model also yields a slightly better fit to the three lower AHe data points, however at the expense of overpredicted corresponding AFT data (Fig. 13B, right panel). Both models predict a rather constant geothermal gradient of ~ 30-35°C/km despite allowed variation. The second model that implies modified He-diffusion parameters predicts a sudden and transient increase up to ~ 40°C/km at the onset time of the final rapid cooling episode. A third model was run with standard diffusion kinetics and constant geothermal gradient (model cbr-16, Figure B.20 in Appendix B6). Here, the geothermal gradient was kept constant over time by letting the search algorithm to select a value for the temperature offset from the same range (45±13°C, corresponding to a range of geothermal gradients of 35±10°C/km). The thermal history is similar to the first two models with a predicted stable geothermal gradient of ~ 30°C/km.

The predicted MTL for the lowermost and uppermost samples with AFT data (CB130 and CB1410) in all models fall just outside or barely inside the error estimates of the observed data, respectively (Figure 4.13, right panels). The original authors of this data set also observed that these two samples behave similarly and differ from the other two (CB550 and CB930) by yielding good-fitting paths, including reheating episodes in their model setup (Blisniuk *et al.*, 2006). Based on this multi-sample simulation, the single-sample HeFTy models of both samples and the single-sample QTQt simulation of CB130 presented above, I conclude that these two samples show some affinity for minor reheating scenarios to explain the data that is also reflected in the relatively shorter observed MTLs. However, as single-sample HeFTy simulations show above,

only-cooling scenarios reproduce the combined AHe and AFT data from both samples equally well. The only-cooling scenario is also the preferred QTQt mean path for all samples (except CB130) reflecting the Bayesian (QTQt) preference for simpler models that explain the data equally well.

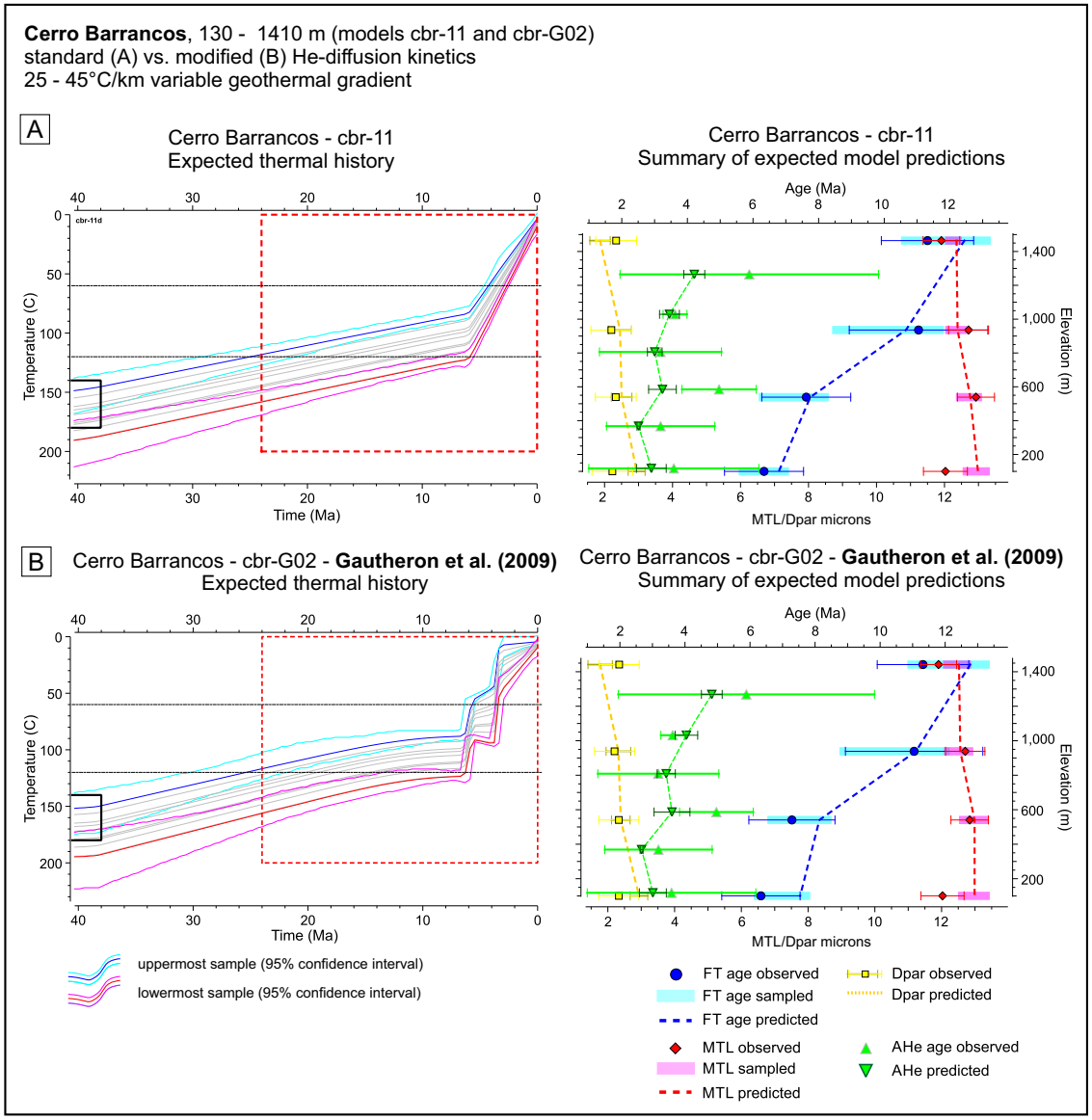

Figure 4.13 – Cerro Barrancos transect - Summary of QTQt results from multiple-sample model runs with standard (A) and modified (after Gautheron *et al.* (2009), B) He-diffusion parameters and variable (25-45°C) geothermal gradient.

Combined, the data inversion of all samples demonstrates some inconsistencies, because the samples with shorter track lengths and apparently stronger tendency for reheating scenarios (CB130 and CB1410) are located at the top and the bottom of the

transect. This is difficult to reconcile in a consistent thermal history for the entire transect and, from a geological perspective, challenging to explain. Local natural processes (e.g. hydrothermal circulation, wild fires, lightning etc) can theoretically alter track length distributions, but such factors are not realistically assessable and considered improper for the data interpretation here. I rather consider minor analytical inconsistencies as a more likely explanation. Notably, the original fission track data set does not contain information for the orientation of the measured tracks with respect to the c-axis (Warkus, 2002; Blisniuk *et al.*, 2006). Using c-axis projected tracks corrects for track-length anisotropy effects and could potentially remove noise from the length data, particularly in the shorter track populations (Ketcham *et al.*, 2007a; Ketcham, 2005b).

4.6.2.3 Leones - Single-Sample Models

Figure 4.14 summarises the modeled thermal histories for samples LL11-06 (1351 m a.s.l.) and LL11-08 (1005 m a.s.l.) from the Leones transect. For both model runs the general priors are set to 14 Ma and 200 °C (observed AFT ages of ~ 6-7 Ma). The younger part of the thermal history is well resolved indicating rapid cooling from 100-120 °C to surface temperatures starting at 4-5 Ma. The preceding cooling path is less well constrained and indicates more protracted passing through the AFT PAZ. The mean model in both simulations indicates minor reheating on the order of ~ 30 °C that is more pronounced for sample LL08 and likely derived from the shorter track lengths in this sample. Notably, the reheating component of the mean model is introduced by the more complex maximum likelihood model that does not coincide with the majority of likely solutions with good fit to the data. Applying modified He diffusion kinetics considering radiation damage effects (Gautheron *et al.*, 2009) was attempted, but yielded coinciding modeling output for these two samples (results not shown here).

4.6.2.4 Leones and Nef - Multiple-Sample Models

Multi-sample inverse thermal modeling is applied for 17 samples from the Leones transect over ~ 2000 m of elevation range (Figure 4.15). All 17 samples yield AHe ages, 9 samples comprise AFT ages and on 2 of them (LL11-06 and LL11-08 presented above) a moderate number of confined track lengths was measured. The general priors were set accordingly to 15 Ma (oldest AFT age ~ 7 Ma) and 200 °C and the temperature offset was allowed to vary over time within a temperature range corresponding to a range of geothermal gradients between 25 and 45 °C/km. The inverse thermal multi-sample modeling of the Nef transect includes 7 samples over ~ 1200 m elevation range, from which all yield AHe ages and 3 comprise AFT ages (Figure 4.16). One sample with 10 measured

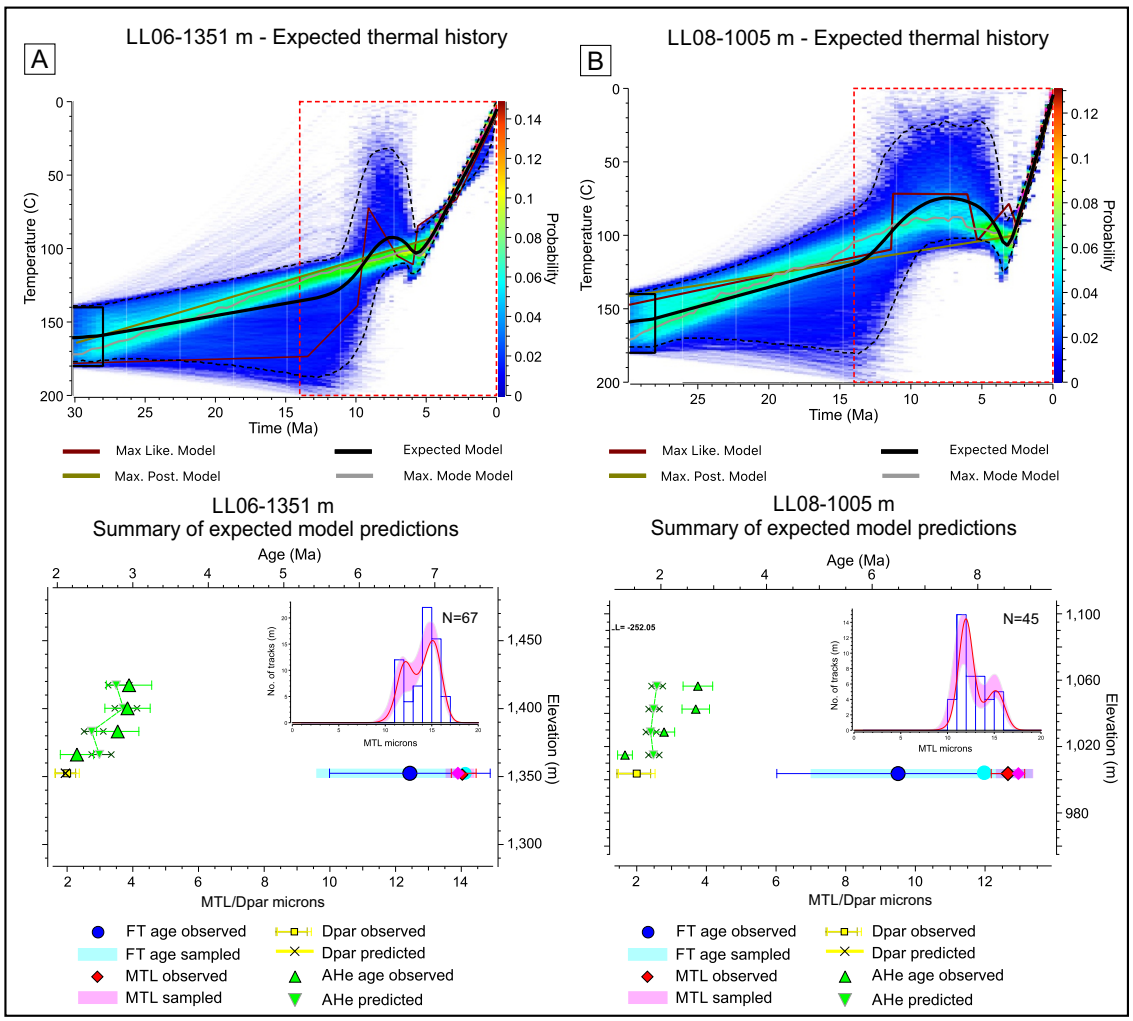

Figure 4.14 – Leones transect- Summary of results from single-sample model runs with QTQt. (A) Sample LL06, 1351 m a.s.l. (B) Sample LL08, 1005 m a.s.l.

track lengths is included here, but not considered for single-sample inversion because of the scarcity of the data. The time prior is set to 20 Ma according to the oldest AFT age of ~ 10 Ma. For both transects the Dpar values (and therefore annealing kinetics) are set to vary within the measurement error. For both simulations an initial constraint for the uppermost sample is set at 30±2 Ma and 160±20°C in order to preclude random thermal inheritance from the AFT PAZ. For the sake of consistency both transects were modelled with standard (Farley, 2000) and modified (Gautheron *et al.*, 2009) diffusion kinetics without signifiant differences in the output. Figures 4.15 (Leones) and 4.16 (Nef) summarise the modeling results for standard He-diffusion kinetics; Figures B.22-25 in Appendix B6 show all results including the modified simulations.

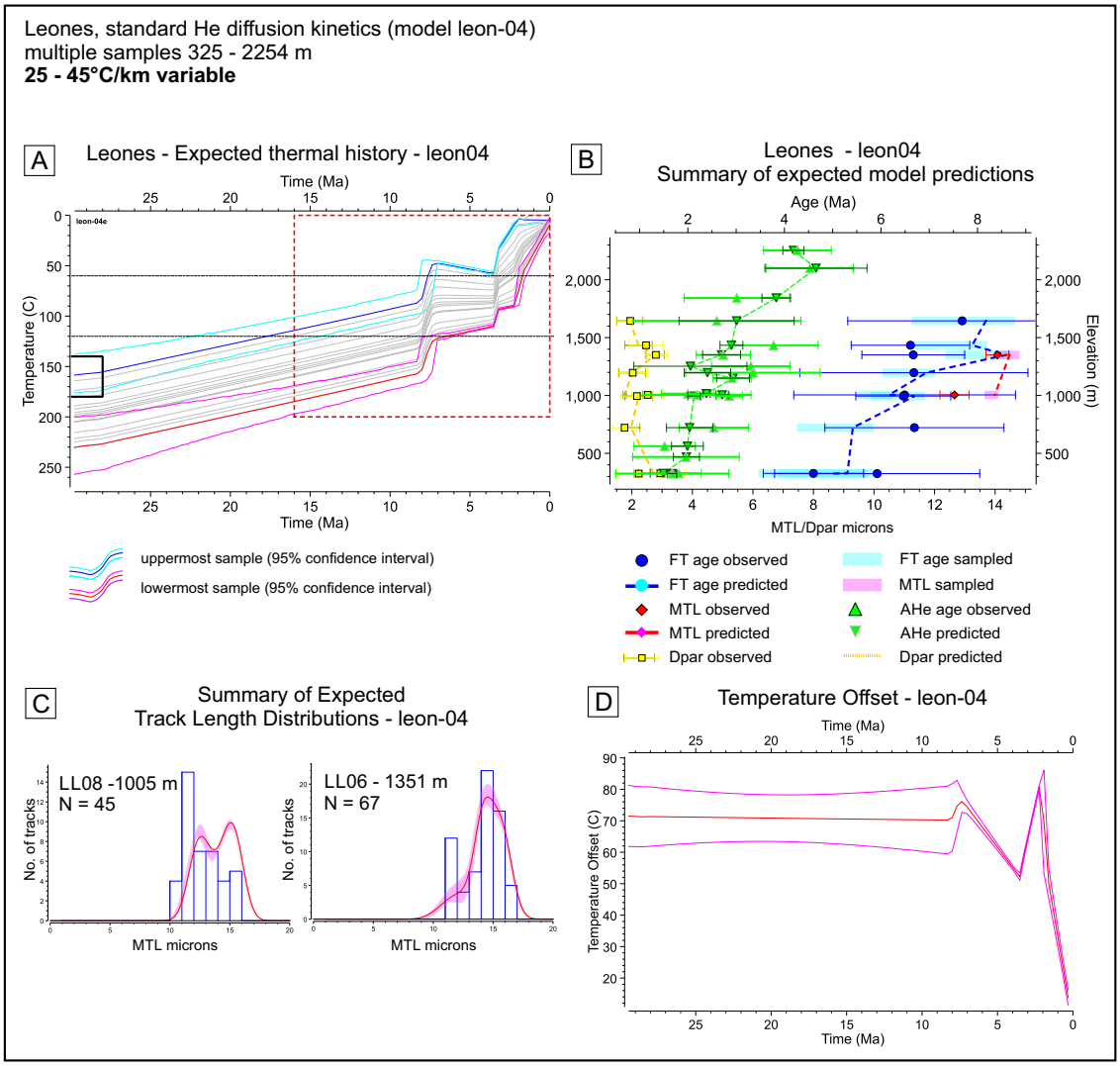

Figure 4.15 – Leones transect - Summary of QTQt results from multiple-sample model runs with standard He-diffusion parameters (Farley, 2000) and variable (25-45°C) geothermal gradient. A: Expected thermal history; B: Summary of expected model predictions vs. observed data; C: Summary of expected vs. observed track length distributions for samples LL06 and LL08; D: Evolution of the temperature offset between the uppermost and lowermost samples over the course of the model.

The data sets from both models define well constrained modelled thermal histories with excellent fit to the observed data. For the Leones transect abrupt pulses of accelerated cooling are predicted at ~ 8 Ma and ~ 3 Ma in a stepwise fashion (Figure 4.15). The AHe, AFT ages and AFT annealing kinetics (Dpar) are well predicted by the mean model except for two samples in the upper part of the transect where AFT ages are over-predicted. Similar to examples described above, for this simulation the

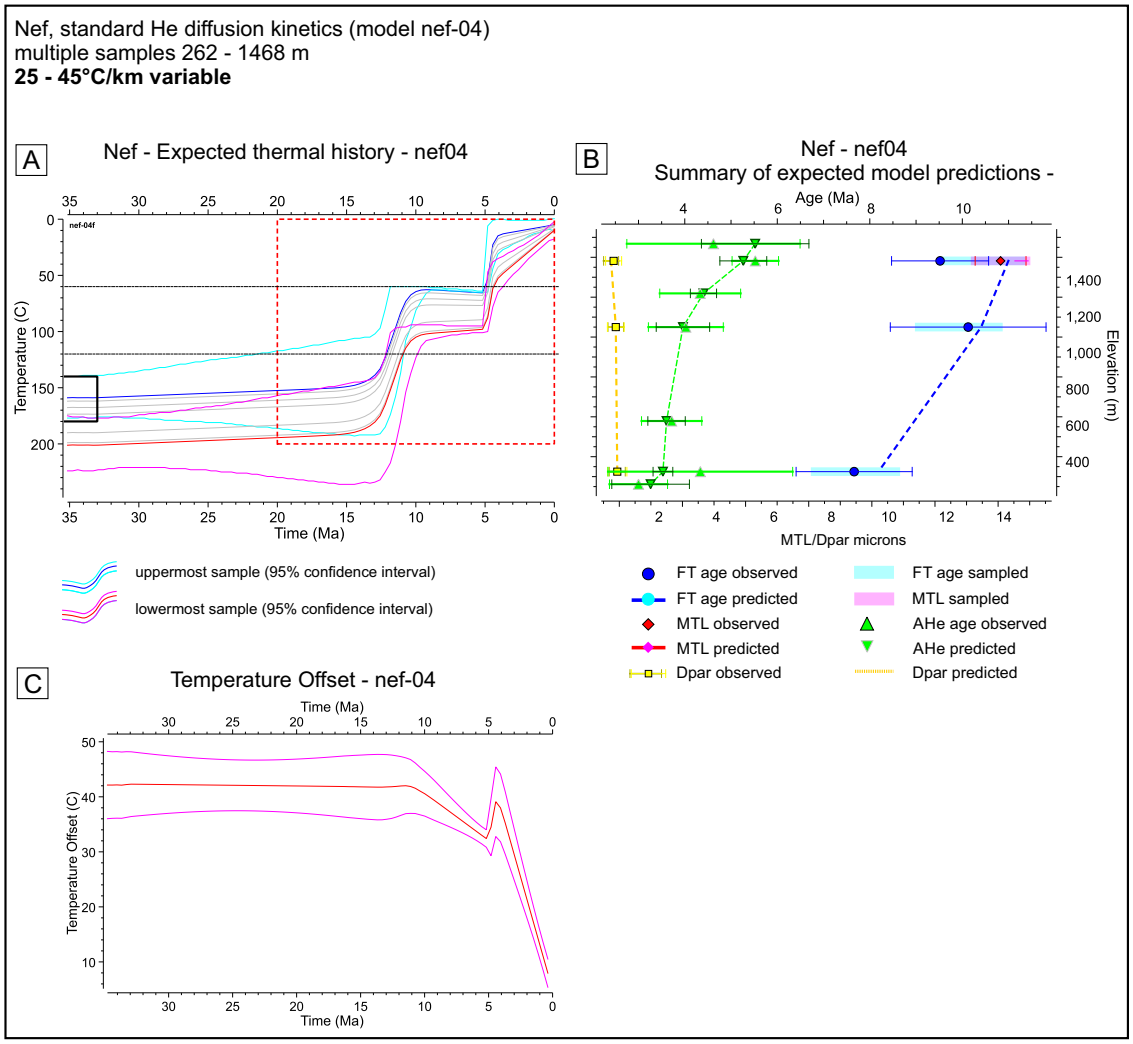

Figure 4.16 – Nef transect - Summary of QTQt results from multiple-sample model runs with standard He-diffusion parameters (Farley, 2000) and variable (25-45°C) geothermal gradient. A: Expected thermal history; B: Summary of expected model predictions vs. observed data; C: Evolution of the temperature offset between the uppermost and lowermost samples over the course of the model.

maximum likelihood and posterior models define similar shape of the cooling path with good predictions for these samples. This again demonstrats that the mean model is not an actually sampled thermal path, but can be justified when it averages similar (but slightly different) solutions with better fit to the data. However, the mean track length for sample LL11-08 (1005 m a.s.l.) is consistently over-predicted by all models (max. likelihood, max. posterior, mode model, expected model), and therefore inconsistent with the general thermal history predicted for the entire transect. For the Nef transect stepwise pulses of rapid cooling are predicted at ~ 10 and 5 Ma with a protracted res-

idence in the AFT PAZ in between (Figure 4.16). The observed data is well predicted except for the uppermost AFT age that is over-predicted, but again well fitted by the max. likelihood and posterior models.

Against the background of the integrated geological, geomorphic, structural and thermochronological observations from the Leones and Nef regions presented in Chapter 3 (Georgieva *et al.*, 2016), a final model was set up mostly as an experiment and in order to 1) potentially verify/falsify the derived thermal histories with a larger data set; and 2) as an independent test for the structural relationship between the Leones and Nef catchments derived from the proposed neotectonic model. As outlined in detail in Chapter 3, fault movement along the reverse Exploradores Fault in the northern foothills of the NPI was likely responsible for ~ 1000 m of vertical offset between the Leones (closer to the fault) and Nef (farther from the fault) transects (Figure 4.17A). The displacement is considered to have occurred after ~ 2 Ma, e.g. after the youngest (and lowermost) samples from the Leones transect had crossed the AHe closure isotherm. The structural implication of this model is that in terms of recorded thermal history before this time (~ 2 Ma), the Nef transect represents a crustal section located 1000 m above the Leones transect (Figure 4.17B). To simulate this structural setting 1000 m were added to the elevation of each sample from the Nef transect and the modified data files together with all Leones data were combined and modelled as a single pseudo-elevation crustal transect. This composite transect mimics the crustal structure before onset of faulting 2 Ma ago and benefits from a larger amount of data to potentially constrain the thermal history given a good data fit is achieved. Obtaining good data fit with a consistent thermal history for this pseudo-transect would also independently confirm the proposed structural model for this region (Chapter 3, section 3.7).

Results from the inverse thermal modeling of the composite transect are summarised in Figure 4.18. The expected (mean) thermal history is very well constrained and confirms onset of faster cooling after 8 Ma in a stepwise fashion. A major pulse of accelerated cooling and entering of the lowermost samples into the AFT PAZ is predicted at ~ 8 Ma followed by a protracted cooling or residence in the AFT PAZ and a renewed pulse of rapid cooling at ~ 3-4 Ma. The predicted vs. observed correlation is very good, particularly given the large amount of data used as input (24 AHe ages, 12 FT ages for ~ 2100 m of pseudo-elevation range). Without exception, all predicted values fall into the 2-sigma error bars and mostly very close to the mean values. Small deviations from the observed values for the AFT ages in the middle part of the transect are characteristic only for the expected (mean) model, whereas the very similar maximum likelihood and

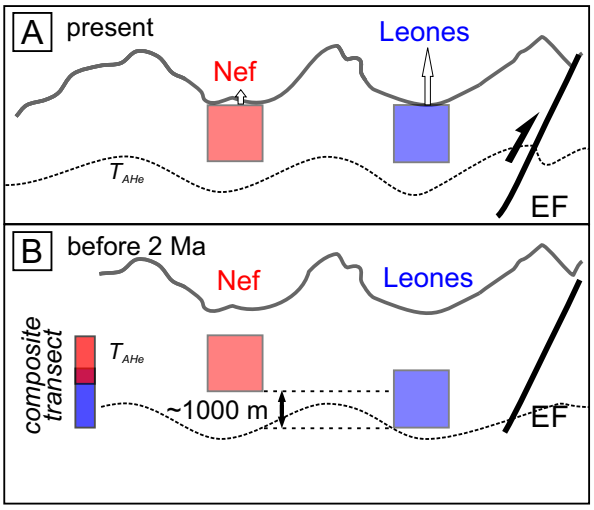

Figure 4.17 – Sketch illustrating the structural position of the Leones and Nef transects at present (A) and and before 2 Ma (B), i.e. before onset of fault movement along the Exploradores Fault (EF). The composite pseudo-elevation transect presented in Figure 4.15 mimics the crustal structure before onset of fault movement (B).

posterior models have better predictions here as well. The mean track length for sample LL11-08 (1005 m a.s.l.) is again largely over-predicted and likely inconsistent with the overall thermal history determined by the rest of the data.

4.7 Discussion

4.7.1 Interpretation of Thermal Modeling Results

Overall the modeling results from single-sample simulations with HeFTy and QTQt and multi-sample simulations of elevation transects with QTQt show consistent results constraining the thermal history of this region based on the input data:

Apatite fission track ages from the Cerro Barrancos transect range between 6 and 11 Ma (excluding the uppermost sample CB1960 as discussed above) and constrain a period of protracted cooling before 6-7 Ma and the onset of a major pulse of rapid cooling starting at at this time. The latter is constrained by the AHe data from this transect that, although spanning an elevation range of ~ 1000 m (147-1245 m a.s.l.), show little variation of cooling ages around 5 Ma. The AHe model predictions for for this transect (HeFTy and QTQt, single- and multiple-sample simulations) rather favor the lower error bound of the observed data. The dispersion and indistinct age-elevation relationship of AHe data from Cerro Barrancos might result from analytical inconsistency and/or other inaccessible factors, such as grain chemistry or zonation.

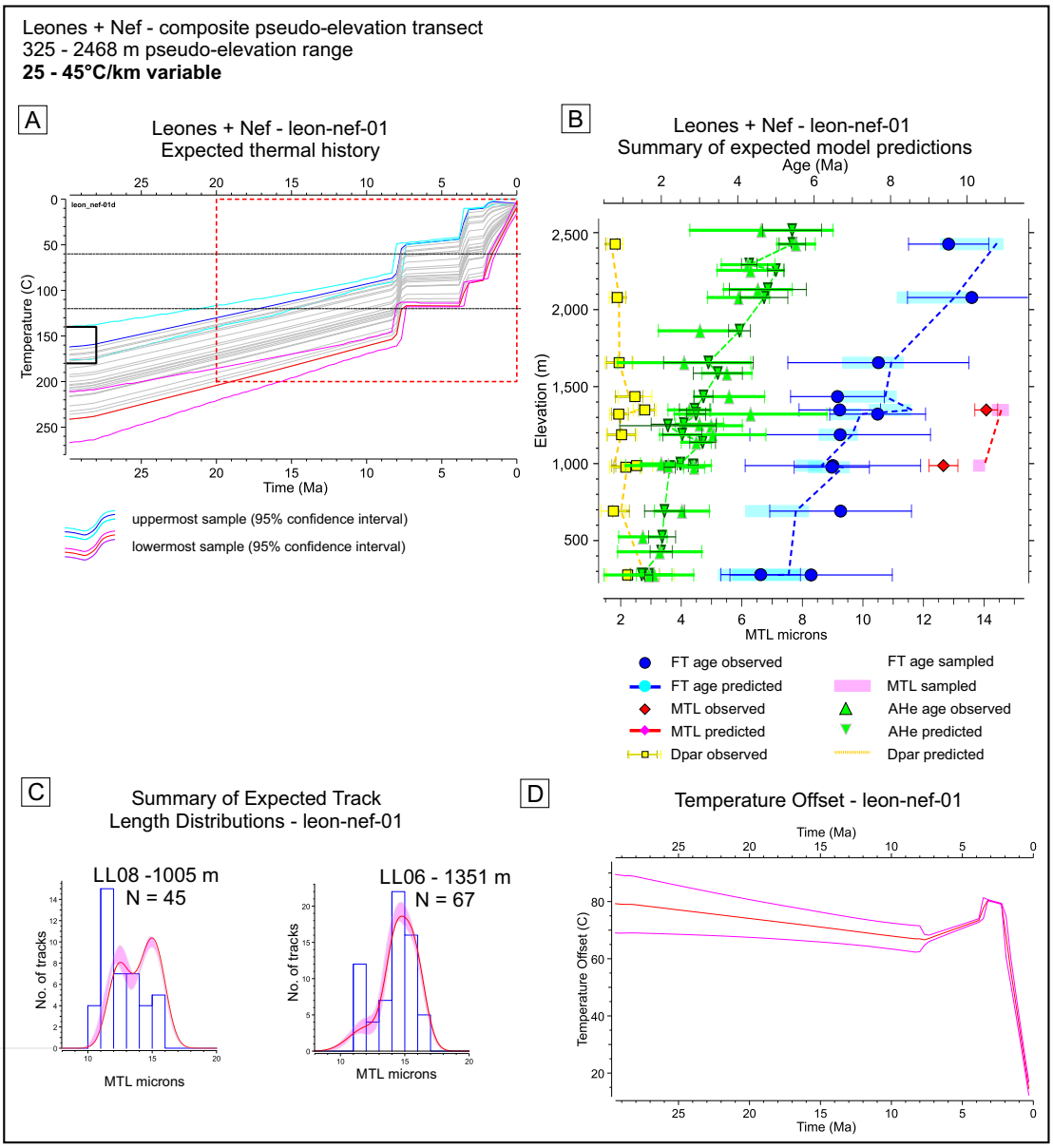

Figure 4.18 – Composite pseudo-elevation transect with data from the Leones and Nef transects. Summary of QTQt results from multiple-sample model runs with standard He-diffusion parameters (Farley, 2000) and variable (25-45°C) geothermal gradient. A: Expected thermal history; B: Summary of expected model predictions vs. observed data; C: Summary of expected vs. observed track length distributions for samples LL06 and LL08; D: Evolution of the temperature offset between the uppermost and lowermost samples over the course of the model.

The modeling results from the Nef and Leones transects confirm and complete this cooling history. Apatite fission track and AHe data from the Nef transect are very similar to those from the Cerro Barrancos transect in terms of both cooling ages and corresponding elevation indicating that both crustal sections might share the same thermal history; however, the Nef dataset lacks track length measurements, which limits the comparison. The AFT ages from the Nef transect range between 7±0.5 Ma and 9±1 Ma (1-sigma error) and define a not well-resolved entrance into the AFT PAZ between 10 and 20 Ma, a well constrained (see 95% confidence interval of the thermal history) protracted cooling and/or residence in the AFT PAZ between 9 and 5 Ma, and onset of rapid exhumation at 5 Ma (Figure 4.16). Modeling results from the Leones transect (Figure 4.15) predict the same cooling pattern, however shifted in time since both AFT and AHe ages from this transect are consistently younger compared to the Nef transect due to a later superimposed episode of differential uplift related to fault movement (cf. Chapter 3). The thermal history indicates an entrance into the AFT PAZ for the uppermost sample at ~ 15±2 Ma, followed by protracted cooling until 8 Ma when a short-lived pulse of rapid cooling is predicted. The last part of the cooling path is characterised by a stepwise course with onset of final more rapid cooling at 3-4 Ma. This thermal history is largely confirmed and even better constrained by the composite pseudo-elevation transect (Figure 4.18). Although the geothermal gradient in all models (including Cerro Barrancos) is allowed to vary between 25 and 45°C, it is predicted to remain stable over time within a range of 30-35 °C, except for transient increases associated with major pulses of cooling (e.g. Mancktelow & Grasemann, 1997).

In summary, all modeling results are compatible with a transient pulse of rapid cooling at ~ 6-8 Ma, followed by protracted or stagnant cooling, and a final episode of rapid cooling starting at 3-4 Ma. Notably, this result also agrees with single-sample HeFTy models, in which different scenarios including reheating that might also generally account for shortened track lengths, are allowed for. In contrast, HeFTy models (not shown here) that force reheating episodes preceding final cooling did not yield good-fitting scenarios for any of the samples with measured track lengths except sample CB1960 (Cerro Barrancos) that records a notably different thermal history (Blisniuk *et al.*, 2006), sample LL11-08 (Leones) that has a very limited number of track lengths (n=45) and sample CB130 (Cerro Barrancos) that shows a somehow stronger affinity with minor cooling scenarios, but originates from the data set that lacks correction for the annealing anisotropy. Based on these arguments and the entity of modeling results, I disagree with the previously proposed reheating scenarios for this region and their implications

discussed below (Guillaume *et al.*, 2013) and favor the more simple stepwise only-cooling scenario exemplified in Figure 4.18 (pseudo-elevation transect).

This scenario is also compatible with the geological, geomorphological and glacio-chronological record of the Northern Patagonian Icefield region. The main episode of shortening, orogenic uplift and denudation in this region is constrained to the time interval between 22 and 14 Ma (Coutand *et al.*, 1999; Suarez *et al.*, 2000; Lagabrielle *et al.*, 2004; Blisniuk *et al.*, 2005, see section 4.2). It likely implies an episode of rapid cooling that is not constrained by the modeled data since the oldest AFT age from the Cerro Barrancos transect is 11.3 Ma, whereas the 17 Ma AFT age of the uppermost sample CB1960 in this transect, should be referred to with caution because of the differing thermal history recorded.

After 14 Ma sedimentation rates east from the NPI dramatically decreased, the scarce younger deposits are not shortened and only minor Pliocene-to recent extensional deformation has been documented within the former Patagonian fold-and-thrust belt. The geological record suggests that after 14 Ma the region of the NPI and its eastern foreland were characterised by a tectonic quiescence, erosion and peneplanation of the former tectonic front and the piedmont surface (Lagabrielle *et al.*, 2004; Suarez *et al.*, 2000) . This is also documented by the deposition of the main basaltic plateau sequence of the Meseta Lago Buenos Aires (MLBA) (Figure 4.2) immediately east of the former tectonic front over a plain surface, gently dipping to the east. This period corresponds to the constrained protracted passage through the AFT PAZ recorded in all samples of the Cerro Barrancos transect (both HeFTy and QTQt models).

The data from the Nef, and particularly the Leones transect, are younger and do not constrain this period, however they introduce more pattern into the younger thermal history. A major pulse of cooling is predicted at ~ 6-8 Ma, followed by a more protracted cooling and final rapid cooling starting at 3-4 Ma. The main denudational event in Southern Patagonia after the deposition of the synorogenic deposits was the onset of episodic extensive glaciations beginning in the Late Miocene (Figure 4.19A). Glacial deposits at the MLBA record the oldest glacial advance at the latitude of the NPI to have occurred between 5 and 7 Ma (Mercer & Sutter, 1982; Ton-That *et al.*, 1999; Lagabrielle *et al.*, 2010). However, ~ 250 km to the south of this location Wenzens (2006) described even older glacial deposits suggesting an age between 9 and 10.5 Ma based on geomorphological mapping, Ar/Ar dating of volcanic flows and correlations with glacio-chronological data from the Antarctic Peninsula. The possibility of a ca. 12 Ma old glaciation has been also tentatively proposed by (Suarez, 2007) in the area of

Baño Nuevo, located ~ 250 km to the north. The age constraints in these two studies are not as robust as in the case of MLBA, where the 5-7 Ma glacial deposits are actually interbedded with basaltic flows dated by Ar/Ar dating (Mercer & Sutter, 1982; Ton-That *et al.*, 1999; Lagabrielle *et al.*, 2010); however the findings of Wenzens (2006) and (Suarez, 2007) provide viable evidence to suggest that glaciation in Southern Patagonia might have started even before 7 Ma. Since the region of the NPI was not tectonically active at this time, I assign the older episode of rapid cooling at ~ 7-8 Ma recorded in the combined Leones-Nef data set (Figure 4.18) to the onset of widespread glaciation in Southern Patagonia in the Late Miocene.

The second pulse of rapid cooling is recorded from 3-4 Ma to the present and its onset coincides with a major episode of a broad regional uplift of the eastern Andean piedmont and a tectonically controlled disruption and dissection of the contiguous surface that that once covered the main relief of the Cordillera, and the upper plateau basalts in the foreland (Lagabrielle *et al.*, 2004) (Figure 4.19B). The tectonic activity at that time was mainly characterised by minor extensional faulting in the foreland and the former fold and-thrust belt and was inferred to have been coeval with a well-documented widespread glacial incision starting at 3-4 Ma in this region (Lagabrielle *et al.*, 2004, 2007; Scalabrino *et al.*, 2011; Suarez, 2007). This Pliocene-Quaternary phase of broad uplift in the foreland, exhumation and isostatic response to erosion is also documented by a series of various granitic plutons dated between 9 and 3 Ma straddling the former fold-and-thrust belt region and the eastern foreland(Suárez & De la Cruz, 2001; Sánchez *et al.*, 2008; Pankhurst *et al.*, 1999).

The tectonic disruption of the former fold-and-thrust belt region and the eastern piedmont of the Patagonian Andes at these latitudes has been correlated with the opening of the Patagonian slab window directly below this region since 3-4 Ma (Breitsprecher & Thorkelson, 2009) introducing hot asthenospheric mantle at the base of the lithosphere (Russo *et al.*, 2010b,a; Gorring *et al.*, 2003; Espinoza *et al.*, 2008; Guivel *et al.*, 2006; Dietrich *et al.*, 2010; Ivins & James, 1999), weakening of the lithosphere and inducing rotation of regional stress tensor allowing local extension (Lagabrielle *et al.*, 2004, 2007; Scalabrino *et al.*, 2011). The internal part of the mountain range, where the Leones and Nef data originate from, is located farther away from the centre of the slab window, but more proximal to the trench and the migrating site of ridge collision. As presented by the integration of observations and data in Chapter 3, this region was at the same time (2-3 Ma to present) rather subjected to strain partitioning, local differential uplifts and transpression related to the closely spaced oblique collision of several ridge segments in

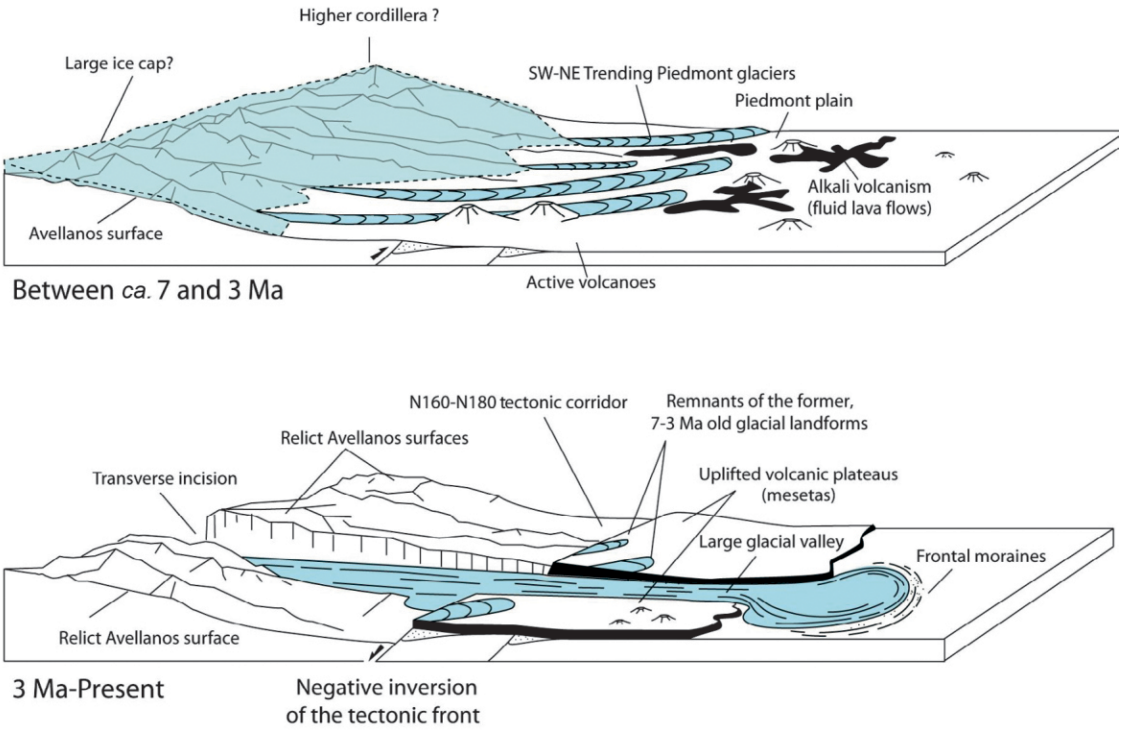

Figure 4.19 – Sketch showing the possible landscape evolution in Southern Patagonia after onset of glaciation ~ 7 Ma ago with emphasis on the 3 Ma tectonic event proposed by Lagabrielle *et al.* (2004). Figure from Lagabrielle *et al.* (2010).

the Golfo de Penas region. The superimposed tectonic contribution to the last episode of rapid cooling cannot be resolved by the data and model predictions, since most of it likely occurred after 2 Ma (youngest ages in the Leones transect, cf. Chapter 3, Section 3.7), but it is evident in the faster cooling rate after 5 Ma recorded in the Leones (Figure 4.15) compared to the Nef transect (Figure 4.16).

In Patagonia, the overall palaeotopography of the mountain range was likely smoother that the current one between 7 and 3 Ma, i.e. even after 3-4 Ma of glaciation, as evidenced by the landform record of closely spaced and not deeply incised 3-Ma old glacial outlets preserved in the eastern foreland, on the top of the now 2000 m surface of the MLBA (Malagnino, 1995), Lagabrielle2010 (Figure 4.19A). Certainly, the following period of rapid cooling, deep incision and exhumation after 3-4 Ma (Figure 4.19B) also overlaps with the global increase in the frequency of glacial conditions and overall intensification of glaciation in the Quaternary (Haug *et al.*, 1999; Ravelo *et al.*, 2004; Clark *et al.*, 2006) that has likely played a major role for more efficient glacial erosion, stronger incision and exhumation after 2 Ma. The relative impact of both processes (tectonic disruption vs. climatically forced intensification of glaciation and incision)

cannot be resolved here. More sophisticated numerical simulations in combination with e.g. $^{4}He/^{3}He$ data could potentially resolve the youngest thermal history with more detail and allow comparison between the three transects. Notably, episodic cooling concurrent with glaciation has been recorded also in regions with negligible tectonic effects such as the European Alps (Valla *et al.*, 2011a, 2012, 2016; Van Der Beek *et al.*, 2010; Glotzbach *et al.*, 2011) and has been assigned to climatically controlled changes in glacial dynamics and pulses of incision and increase in relief (Valla *et al.*, 2010; Glotzbach *et al.*, 2011). Nevertheless, the geodynamic background and the integration of geological, structural, geomorphic and thermochronologal data from the NPI region and its foreland suggest a more complex suite of factors that influenced the thermal histories, including climatic, but also geodynamic and tectonic factors related to ridge collision and slab window opening.

4.7.2 Comparison to Previous Models

4.7.2.1 Cerro Barrancos AFT single-sample inverse thermal modeling (AFTSolve) (Blisniuk et al., 2006)

As mentioned at the beginning of this chapter, the thermochronological data from the Cerro Barrancos transect has already been implemented into inverse thermal modeling techniques partly overlapping with the methods applied here (Blisniuk *et al.*, 2006; Guillaume *et al.*, 2013). The results from these studies are in disagreement with the reassessment of the Cerro Barrancos data and also with the predicted thermal histories for the Leones and Nef data presented in this thesis. In this section we will compare the different outputs with more detail and discuss possible sources for this inconsistency.

Blisniuk *et al.* (2006) performed single-sample inverse thermal modeling of the AFT data from the Cerro Barrancos transect using the modeling software AFTSolve, a forerunner software of HeFTy described by Ketcham *et al.* (2000). The software has similar functionalities, but it is no longer available, hence it was imposible to reassess the modeling on an identical platform. Nevertheless, AFTSolve and HeFTy are based on the same search algorithm and the proposed thermal histories are subjected to the same statistical criteria regarding their fit to the observed data. Therefore, it is not expected major differences in the modeling output to result solely from the application of the different softwares.

Predicted thermal histories from the study of Blisniuk *et al.* (2006) from AFT data for all five samples from the Cerro Barrancos transect indicate a 60±30°C reheating episode preceding final rapid cooling (original figure presented in Figure B.27, Appendix B6).

The onset of this pulse of reheating is not well constrained, but generally placed in the Miocene and prior to 4-6 Ma. The key feature of this result for the present discussion is that the predicted reheating episode is *constrained*, i.e. all good *and* acceptable paths found by the search algorithm between the constraints bounding the reheating event document some amount reheating (Figure B.27, Appendix B6). Notably, Blisniuk *et al.* (2006) explicitly state that their modeling setup does not force reheating and merely allows for it, i.e. that monotonic cooling paths are also evaluated. The HeFTy model setup presented here has the same objective (see Section 4.4.2) and evidently in all simulations (including the reference model that mimics the setup of Blisniuk *et al.* (2006)) some good and acceptable paths documenting reheating are found, but the majority of the preferred thermal histories predict monotonic cooling with protracted passage through the AFT PAZ that accounts for the observed shortened track lengths (Figures B.6-9, panels B,C and D). One exception is perhaps the lowermost sample CB130 that records a somehow more balanced distribution between monotonic cooling and reheating paths, likely arising from the slightly larger fraction of shortened track lengths in this sample. However, as argued above, this singular finding should not be over interpreted, particularly given the lack of angular data (orientation of tracks to the c-axis) in this data set. Moreover, the HeFTy results presented here are confirmed by the QTQt simulations of the same samples that are generated by a completely different search algorithm and refrain from the use of constraints on the modeling space.

As described in the model setup above (Section 4.4.2), the essential setting that influences whether both types of cooling paths are tried between the corresponding constraints (constraints 2a and 2b in our model setup or the two middle constraints in the reference model) are the properties of the connecting segment. The current HeFTy setup provides the selection between "monotonic consistent" and "monotonic variable". If the second constraint is centred at slightly higher temperatures than the preceding one (constraints 2b and 2a in our model; constraints placed at 6 and 10 Ma in the model of Blisniuk *et al.* (2006)) and "monotonic consistent" property is selected, then the algorithm tries only reheating paths. Conversely, a "monotonic variable" setting (as in all our models) randomly tries both cooling and reheating paths between the corresponding constraints. The study of Blisniuk *et al.* (2006) does not contain such detailed information on the model setup. However, with HeFTy we were able to reproduce their result of constrained reheating only by editing the relevant segment properties in such a way ("monotonic consistent") that monotonic cooling paths are excluded from the search algorithm (results not shown here). The only sample for which our model setup yielded

similar results with Blisniuk *et al.* (2006) is CB1960 - the uppermost sample that records an outlier thermal history not compatible with the rest of the data set (Figure B.10, Appendix B6). The data of this sample can be reproduced exclusively with a thermal history involving a major episode of reheating and extremely fast and very young (~ 1 Ma) final cooling - a scenario which is naturally filtered out in our setup (trying both cooling and reheating) and the setup of Blisniuk *et al.* (2006) that appears to prescribe reheating.

Based on these arguments and the integrity of our results (HeFTy and QTQt, single- and multiple sample approaches) we consider the constrained reheating episode proposed by Blisniuk *et al.* (2006) and its large-scale geodynamic implications as rather not justified.

4.7.2.2 Cerro Barrancos AFT-AHe multiple-sample inverse thermal modeling (QTQt) (Guillaume et al., 2013)

Guillaume *et al.* (2013) performed multiple-sample inverse thermal modeling with QTQt of the combined AFT-AHe dataset from the Cerro Barrancos transect (original figure presented in Figure B.28, Appendix B6). With few exceptions explained below, the data input is identical to the one used in our model, however the modeling results are fundamentally different.

Guillaume *et al.* (2013) applied three different model setups by varying the kinetic parameters for He-diffusion and comparing standard kinetic parameters (Farley, 2000) (Fig. B.28A) with two different diffusion models that take into account the effects of radiation damage on He-diffusion in apatite (Flowers *et al.*, 2009; Gautheron *et al.*, 2009, Figures B.28B and C, respectively). The authors identify a distinctive episode of reheating in the Cerro Barrancos region between 15 and 10 Ma that is particularly well constrained in the simulations with modified He-diffusion kinetics, therefore highlighting the impact of this parameter in this particular dataset. In order to explain this reheating event Guillaume *et al.* (2013) draw large-scale geodynamic implications that involve a far reaching heating pulse originating from the onset of ridge collision and slab window opening ~ 15 Ma ago at 54°S (Breitsprecher & Thorkelson, 2009), i.e. ~ 700 km to the south from Cerro Barrancos. The geodynamic plausibility of this interpretation will be discussed in the following section, whereas here we strictly focus on important differences in the model setup that might explain the discrepancy with our modeling results. The objective of this section is the juxtaposition of the different results, but mostly to provide a methodological contribution that might be helpful for other studies using QTQt.

Unfortunately, the study of Guillaume *et al.* (2013) contains very little information on the QTQt model setup, which hampers a more direct comparison and evaluation of the impact of different parameters *. However, the available information and the graphical output from their models allow for some analysis.

Notably, the models presented by Guillaume *et al.* (2013) were run with a rather limited number of iterations (20 000, as stated in the Supplementary Material attached to the original study). As explained in detail and exemplified on a variety of examples by Gallagher (2012), the Bayesian approach adopted in QTQt usually requires a much larger number of iterations (rather in the order of 200 000 or much more) until a satisfactory convergence of the likelihood chain, i.e. maximum possible fit to the observed data, is reached. This is particularly the case for multiple-sample models implying multiple thermochronometers as in the case of Cerro Barrancos. Indeed, there is no strict prescription on the number of iterations implied in a QTQt model; however 20 000 model runs are considered as exploratory chains, a number of which is recommended to be performed at the beginning of each model run as a sole tuning tool for the the MCMC modeling parameters (proposal scales) (Gallagher, 2012). Final model runs of multi-sample transects with satisfactory convergence are commonly performed with a n x 10^5 iterations as demonstrated on a variety of examples (e.g. Gallagher, 2012; Wildman *et al.*, 2016; Valla *et al.*, 2016; Cogné *et al.*, 2014, to name a few).

One of the potential problems of insufficient number of iterations is the lack of tuning of the proposal scales, e.g. the steps with which each parameter is perturbed when new thermal paths are proposed during the search algorithm. As summarised in Section 4.4.3 above and explained in detail by (Gallagher, 2012), the adequate proposal scales ensure efficient sampling of the modeling space by the MCMC chain and therefore, a representative modeling results. Many times the intermediary results from the exploratory (20 000 iterations) chains yield overly complex and not well constrained thermal paths that lack fit with the observed data, precisely because the MCMC parameters have still not been adjusted. The study of Guillaume *et al.* (2013) does not present a comparison of the predicted vs. observed data neither, which is an essential information for justifying any modeling output from QTQt in general (Gallagher, 2012, 2016).

In contrast to our model setup, Guillaume *et al.* (2013) do not implement an initial constraint at the beginning of the model that would ensure complete resetting of all thermochronometers at the beginning of the thermal path. Given a sufficient number

*Communication on this matter with the authors was attempted, but unsuccessful until the time of submission of this thesis.

of iterations is implemented, the lack of initial constraint itself might not necessarily be a problem, since the data (provided it records a consistent thermal history) will define alone which preferably simple thermal history predicts the observations best. This is one of the main characteristics of the Bayesian approach, namely to leave the modeling space free of constraints and let the data and its uncertainty define the most likely solution (even if it is a not very good fitting one, see Vermeesch & Tian (2014)). However, the implementation of an initial constraint at resetting temperatures is a recommendable modeling approach in order to exclude inherited thermal history.

This concept is exemplified in Figure B.29 (Appendix B6) summarising results from a single-sample model of the lowermost sample CB130 without initial constraint. Figure B.29A shows the modeling output after the initial (20 000 iterations, 10 000 burn-in, 10 000 post burn-in) and it proposes a higher amount of reheating defined (but badly constrained) within the older (> 6-7 Ma) part of the time prior. Figure B.29B presents the final results after ~ 200 000 iterations - the the expected model is better converged after 7 Ma and defines a protracted residence in the AFT PAZ or very minor reheating followed by final rapid cooling. Notably, in this particular case the predicted data fits well the observations in both simulations (right panels in Figure B.29A and B), because the younger part of the thermal history (after 6 Ma) is very similar. However, the reheating pattern in the exploratory model (Figure B.29A) can be very misleading, particularly if the default color scale for the probability distribution is not maintained, as it seems to be the case for the results of Guillaume *et al.* (2013) presented in Figure B.28. The color scale for the probability distribution is a direct indicator of how well a model is resolved at a given time. For example, the thermal path of the exploratory model in Figure B.29A at e.g. 10 Ma, is clearly not well constrained. However, decreasing the color scale for the probability distribution by an order of magnitude (from 0.15 to 0.02 used by Guillaume *et al.* (2013)) results in a (visually) very different thermal history that masks the actual degree of resolution (Figure B.29C).

In the case of Guillaume *et al.* (2013)'s model the combined impact of limited number of iterations with the lack of initial constraint are further augmented by the fact that sample CB1960 is included in the model. As noted by the original authors (Blisniuk *et al.*, 2006) and confirmed by HeFTy and QTQt results here, this sample records a thermal history that is incompatible with the rest of the data set. A model setup without initial constraint at higher temperatures and including a singular sample that clearly requires reheating, might potentially yield some reheating scenarios, particularly during the initial exploratory-tuning state of the model run. However, they do not

necessarily predict the data set well and likely are not well constrained. Such is the case for all three models presented by Guillaume *et al.* (2013) - notably, the 95% confidence intervals for the upper- and lowermost samples preceding ~ 12 Ma largely overlap and do not constrain the thermal path (Fig. B.28). The expected model in QTQt is an average model of all thermal paths and it is representative where it is well constrained (Gallagher, 2012), i.e. the final cooling episode in Guillaume *et al.* (2013)'s models. Again, a longer sampling chain will naturally discard a singular outlying sample and fail to predict its data in favor of a thermal history and data predictions of the remaining data that does not require reheating.

A final point will be discussed here, mainly because of its geodynamic implication and significance for the last section of this discussion. Guillaume *et al.* (2013) describe their interpretation of the modeling output as slow cooling between 25 and 15 Ma at a geothermal gradient of 30°C followed by a reheating phase between ~ 15 and 10 Ma and increase of the geothermal gradient up to 60°C, and slow cooling between 10 and 5 Ma and final rapid cooling after 5 Ma "in a hot crust context". Notably, the multiple-sample model of Guillaume *et al.* (2013) spans ~ 1800 m of elevation (130-1930 m a.s.l.), but the temperature offset between the upper- and lowermost sample in all three predicted thermal histories is 20°C, which corresponds to a constant geothermal gradient of 10°C/km over the entire modelled time span (Figure B.28). Such low geothermal gradient is iinconsistent with the proposed interpretation and geologically unreasonable.

As suggested by the results in this study, the data from the Cerro Barrancos transect can be predicted considering a geothermal gradient of ~ 30-35°C, which is also a geologically justifiable value for this region (discussed in the next section). Stacking the set of samples within a tight temperature range instead, naturally invites for more complexity in the model since it attempts to converge thermal histories from crustal levels that lie farther apart. This is demonstrated by the model presented in Figure B.30 (Appendix B6) that mimics precisely our preferred model (Figure B.18) except for the temperature offset parameter, which has been decreased corresponding to a geothermal gradient of 10°C/km and kept stable over time. The first exploratory model run (Figure B.30A) introduces a lot of structure with a marginal fit to the data, particularly to the obsereved AFT ages. In the final model run (~ 450 000 iterations, 100 000 as burn-in) some of this structure (particularly the reheating episode) is smoothed out, the data fit is slightly better but the overall thermal history is poorly constrained except for the final cooling event (see overlapping confidence intervals compared to the preferred model in Figure B.18).

Two final model runs were performed mimicking the setup of Guillaume *et al.* (2013) as close as possible, i.e. the temperature offset is stable and corresponds to a geothermal gradient of 10 °C/km, sample CB1960 is included, there is no initial constraint at resetting temperatures and the He-diffusion setting for standard (Farley, 2000) (Figure B.31) and modified (Gautheron *et al.*, 2009) (Figure B.32) kinetics are compared. The exploratory (panel A in both figures, 20 000 iterations) and final model runs (panel B in both figures) are presented. For both model runs the exploratory runs introduce more structure indicating reheating that is mostly smoothed out in the final model. It is evident that after sufficient number of iterations (both models were run until a converged sampling chain was obtained) both models converge toward the overall thermal history predicted by our preferred model, indicating a protracted passage through the AFT PAZ followed by rapid cooling after 6 Ma. However, the thermal histories for the upper- and lowermost samples are less well constrained and the fit of the predicted to the observed data is less pronounced, likely as a result of the unreasonable assumption of very low temperature offset.

In summary, the insufficient number of iterations appears to be the most important factor for the lack of reliability in Guillaume *et al.* (2013)'s modeling approach; however, against the background of this shortcoming, other, improperly selected parameters also play a role for the presented output. Based on the critical re-evaluation of both Blisniuk *et al.* (2006)'s and Guillaume *et al.* (2013)'s modeling approaches we confidently rely on the modeling results and interpretation presented in this thesis. The discussion of the geodynamic impacts related to both differing scenarios is provided in the following section.

4.7.3 Implications for the Geodynamic and Cooling History Evolution in Southern Patagonia (47°S)

In the previous chapter I challenged the numerical approach used to back up the proposed far-reaching northward propagation of crustal heating triggered by ridge collision and slab window opening in Southern Patagonia that is argued to be recorded in low-temperature cooling ages (AFT, AHe). Apart from the modeling inconsistencies described in detail above, there are also some important geodynamic and geological aspects of such scenario that may have to be reconsidered.

Several modeling and field studies have addressed the spatial and/or temporal scales of thermal effects related to ridge collision and slab window opening on the thermal structure and overprint of the overriding lithosphere. For example, Groome & Thorkelson (2009) presented a series of 3D numerical models investigating possible thermal

and mechanical effects of ridge collision and slab window opening and migration. Their study demonstrates that many of the geologic effects of slab window migration (e.g., anomalously high-T metamorphism in the fore-arc, non-arc-like magmatism in the volcanic arc) are linked to the introduction of a region of hot, upwelling asthenospheric mantle in the subduction zone environment.

The model of Groome & Thorkelson (2009) uses idealised geometries (e.g. orthogonal ridge collision) and end-member boundary conditions (e.g. very slow trench-parallel migration of the triple junction resulting in more protracted heating, constant asthenospheric-mantle temperature of 1300°C within the entire slab window) aiming to reproduce not so much the magnitude, but rather the pattern of related effects. In terms of the thermal impact on the overriding lithosphere, Groome & Thorkelson (2009) predict abrupt and significant increase in temperatures close to the site of ridge collision (50 km inboard from the trench) that reaches into crustal levels as shallow as 5-10 km depth. Farther inboard in the overriding plate the thermal impact dissipates into longer duration (more protracted passage over a widened slab window) and decreasing magnitude that is almost negligible at 5-10 km crustal depth and at a distance of 250 km from the trench. Importantly, these effects are predicted for a region located directly above the slab window, i.e. aligned with the site of ridge collision. The thermal effect on the overriding plate in a direction parallel to the trench, i.e. preceding/following onset/cessation of ridge collision, is predicted to be rather limited at 40 km and non-existent at 60 km trench-parallel distance from the triple junction.

Notably, there is an order of magnitude discrepancy between the spatial reach of thermal effects proposed by Groome & Thorkelson (2009) (a couple of tens of km) and Guillaume *et al.* (2013) (several hundreds of km). However, the former model (Groome & Thorkelson, 2009) is rather in agreement with a number of combined field-based and numerical studies, e.g. from Japan (Underwood *et al.*, 1993; Brown, 1998; Sakaguchi, 1996) and Southern Alaska (Sisson *et al.*, 2003b, 1989; Hudson & Plafker, 1982; Haeussler *et al.*, 1995, 2003; Dickinson & Snyder, 1979) that report a variety of thermal imprints related to ridge collision and slab window opening from the forearc region in the immediate vicinity to the site of the triple junction. The overview studies of Thorkelson (1996) and Sisson *et al.* (2003b) also highlight that the thermal anomalies will tend to be most pronounced where subduction is shallow and the overlying mantle wedge is thin, i.e. particularly at the base of the fore-arc region and certainly not into upper crustal levels of the arc region, as corresponding to the Cerro Barrancos region.

Currently, there appear no other studies directly linking such distal thermal imprints to slab window formation.

The geodynamic interpretation of Guillaume *et al.* (2013) is largely backed-up by an analog modeling study by the same authors (Guillaume *et al.*, 2010) that documents lateral (trench-parallel) mantle flow induced by the opening of the slab window. The authors propose that such far-reaching lateral mantle flow can bring sub-slab asthenospheric material hundreds of kilometres north from the northernmost extent of the slab window, trigger magmatism and heat transport by advection, and explain the reheating apparently recorded in the thermochronological data. Both studies (Guillaume *et al.*, 2010, 2013) further back up these findings with the occurrence and temporal constraints of back-arc volcanism in Southern Patagonia, which they link partly to the distal reach of lateral sub-slab asthenospheric mantle flow.

It is far outside the scope of this thesis to re-evaluate the laboratory model setup and associated assumptions of the study by Guillaume *et al.* (2010) (based on model setup presented in Funiciello *et al.* (2004, 2006). This analog approach certainly provides important and meaningful insights into how subducting slabs and slab window formation might influence the subduction process in general, and particularly the slab-induced 3-D mantle circulation and lateral flow. However, as any other model, including the thermo-mechanical models of Groome & Thorkelson (2009) discussed above, it implies a number of assumptions and resulting limitations. For instance, the sinking of the subducting slab in these models is driven by a negative buoyancy set to - 60 kg/m^3 - a value rather corresponding and exceeding the one of oceanic plates older than 80 Ma (- 40 kg/m^3, Cloos (1993)). This setup is likely incompatible with subduction dynamics directly preceding slab window formation, which are characterised by the subduction of 0-to-10 m.y.-old hot and buoyant oceanic lithosphere. As it is valid for the model of Groome & Thorkelson (2009), the general predicted mantle flow patterns might be representative, however the magnitude could be significantly amplified.

It is considered important to keep such considerations in mind, especially when an attempt to up-scale modeling results into nature is being made. Matching the geological record in the study region is certainly a strong argument for such an attempt irrespectively of the type of model being used. However, it has been demonstrated by the new results presented here and the re-evaluation of Guillaume *et al.* (2013)'s and (Blisniuk *et al.*, 2006)' models that the thermochronology data in the NPI region (Cerro Barrancos, Leones, and Nef) do not record a reheating event. Guillaume *et al.* (2013) claim to document the anticipation of the reheating pulse also farther north, at $\sim$ 5 Ma and

250 km to the north from Cerro Barrancos, i.e. in a region that is still located north of the present day extension of the slab widow. This conclusion is based on the observed partial opening of the apatite (U-Th)/He isotope system and progressive partial resetting of cooling ages from an elevation transect of the Cerro MacKay dacitic porphyry, to which the authors erroneously assign a superficial emplacement with expected invariant AHe ages equal to the crystallisation age of 63±2 Ma (De la Cruz *et al.*, 2003). However, the Cerro MacKay dacitic porphyry has actually been described as a very shallow intrusive body (subvolcanic stock) with intrusive contacts to Lower Cretaceous volcanosedimentary host rocks (De la Cruz *et al.*, 2003). The partial resetting of AHe ages in the lower levels of the elevation transect can be easily explained by an intrusion depth with the upper 0-3 km (typical for porphyry rocks) and protracted residence of parts of the intrusive body within the AHe partial retention zone. This interpretation also agrees with regional studies documenting very slow exhumation rates since the Upper Cretaceous recorded in Upper Cretaceous - Early Paleogene zircon and apatite fission track ages, respectively (Thomson *et al.*, 2001).

Furthermore, the geochemical signature, as well as the spatiotemporal characteristics of the back-arc volcanism in Southern Patagonia do not necessarily require, or constrain the reach of such lateral mantle flow (albeit they do not completely exclude it neither) and numerous studies have already proposed different scenarios for their origin. Between 12 and 3 Ma voluminous and extensive alkaline-to-transitional basalts were emplaced in the Patagonian backarc region (e.g. Gorring *et al.*, 1997; Gorring & Kay, 2001; Guivel *et al.*, 2006; Espinoza *et al.*, 2008; Boutonnet *et al.*, 2010) over a smooth paleotopography derived from the erosion of the 16-m.y.-old tectonic front of the Patagonian Andes at 47°southern latitude; these form the main body of the preserved Meseta Lago Buenos Aires and Meseta Chile Chico volcanic plateaus at 47°S (Lagabrielle *et al.*, 2007; Boutonnet *et al.*, 2010; Suárez & De la Cruz, 2001). These main-plateau basalts display a geochemical signature with variable OIB- and subduction-related components and would be generated by the variable degrees of partial melting of OIB-type mantle sources involving the deep subslab asthenosphere and the subcontinental mantle (Gorring *et al.*, 2003; Guivel *et al.*, 2006; Espinoza *et al.*, 2008; Boutonnet *et al.*, 2010). In contrast, Pliocene-to-Quaternary (3 Ma to 110 ka) post-plateau OIB-like basalts display clear geochemical similarities to basalts at the active Chile Ridge and the Chile Triple Junction and are considered to have formed by partial melting of large-scale upwelling of asthenospheric mantle immediately above the Patagonian slab window that was fully

opened below this region at that time (after 3-4 Ma) (Guivel *et al.*, 2006; Breitsprecher & Thorkelson, 2009).

Indeed, at the time of onset of the main-plateau forming volcanic event (~ 12 Ma) the centre of the Patagonian slab window was located 300-500 km to the south from the volcanic mesetas at 47°S, which led Guivel *et al.* (2006) to propose a large-scale northward propagating slab-tearing event parallel to the trench that would provide the source for the necessary subslab-asthenospheric-mantle imprint observed in these rocks. The need of such a tear is supported by the compilation of the volcanic chronology in the Patagonian back-arc and the lack of along-trench correlation between volcanic ages and the timing of opening of the slab window observed by Guillaume *et al.* (2010) (Figure 4.20). Particularly north of 49°S numerous volcanic manifestations with OIB-like signature predate arrival of the main Patagonian slab window. Guillaume *et al.* (2010) and Guillaume *et al.* (2013) do not discard such slab-tearing event, but propose an alternative scenario, in which lateral mantle flow at the edges of the slab window and associated heat wave propagated to the north and triggered OIB-like volcanism way ahead of the slab window .

As a matter of fact, Guillaume *et al.* (2013) rightfully note that it is difficult to explain the interpreted lithospheric heating ~ 15 Ma ago at Cerro Barrancos and ~ 5 Ma ago at Cerro Mackay with a single slab-tearing event starting at 15 Ma, as proposed by Guivel *et al.* (2006). This criticism is important with respect to the volcanics with OIB-signature in the back-arc. For example, between 12 and 3 Ma the Meseta Lago Buenos Aires records volcanic activity with variable, but ever emerging OIB-signature, which is indeed incompatible with a single slab-tearing event. Because of the fast convergence between the Nazca and South American plates, a 15-m.y.-old slab tear of the subducting plate would be now located more that 1000 km east of the study area (Guillaume *et al.*, 2013) (cf. Figure 4.1A). Given the lack of evidence for crustal heating as a trigger for volcanism, I favor the slab tearing event proposed by Guivel *et al.* (2006) to reconcile the timing and occurrence of OIB-related volcanism in the back-arc,

Rosenbaum *et al.* (2008) review conceptual models of different types of slab tearing, including horizontal tear propagation as proposed by Guivel *et al.* (2006) (Figure 4.1A, Figure 4.21A) and vertical tear propagation (illustrated as downward propagating slab tear, cf.Figure 4.21B). Three-dimensional models of slab detachment (Burkett & Billen, 2010) further identify previously unrecognised mechanisms of slab tearing, such as vertical downward tearing along a thermally offset and transform-weakened boundary between slab segments (Figure 4.21B). The presence of the transform weak zone facili-

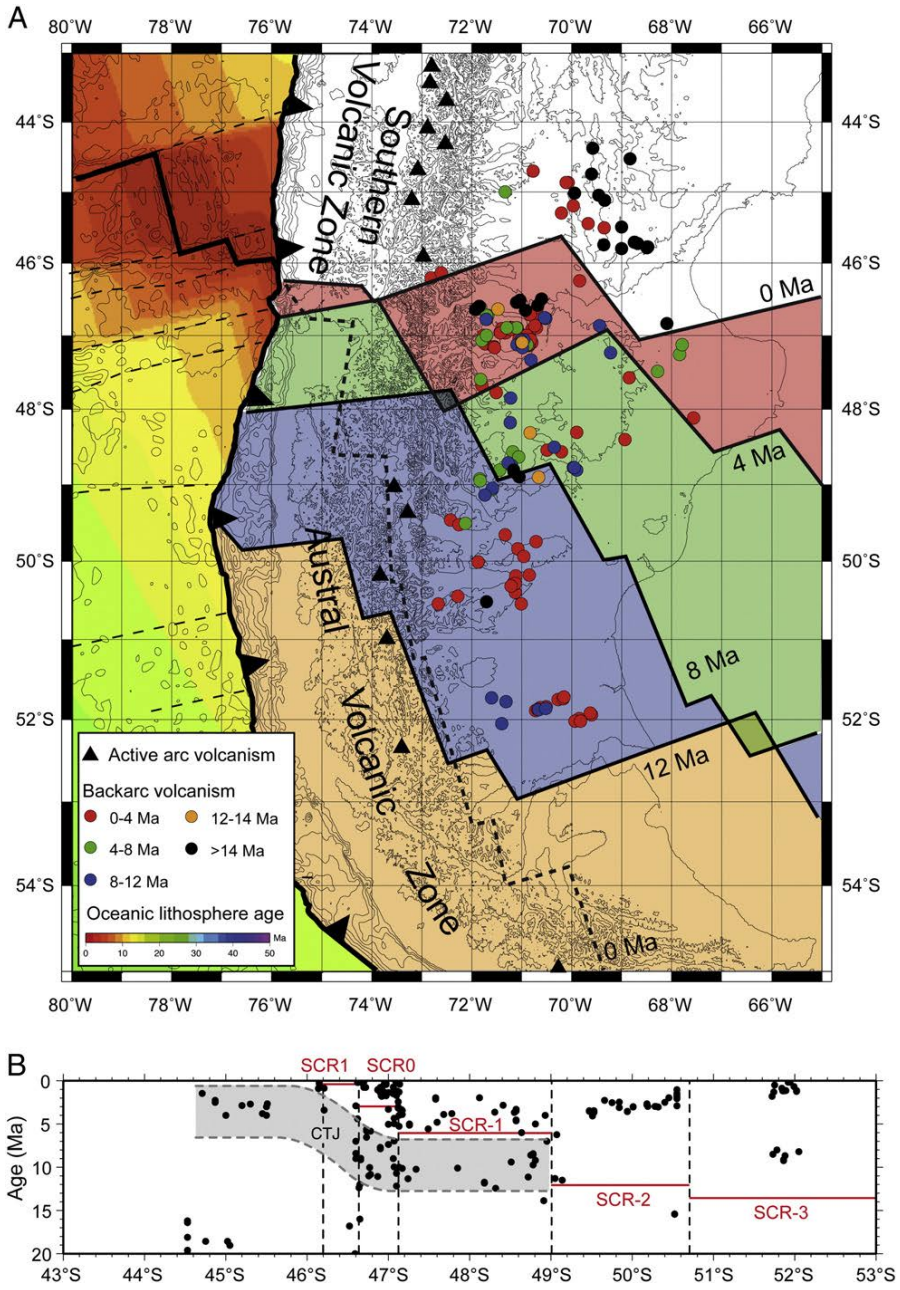

Figure 4.20 – (A) Compilation of available K/Ar and $^{40}Ar/^{39}Ar$ ages of Patagonian back-arc magmatism. Black triangles denote sites of active arc volcanism, and colored circles indicate the back-arc volcanism (prior to 14 Ma in black, between 14 and 12 Ma in yellow, between 12 and 8 Ma in blue, between 8 and 4 Ma in green, and between 4 Ma and today in red). Also displayed on the map is the kinematically reconstructed edge of the Nazca slab, defining the easternmost extension of the slab window, at 12, 8, 4 and 0 Ma (black solid line) and the present-day kinematically reconstructed edge of the Antarctic slab (black dotted line). (B) Along-trench direction plot of the K/Ar and $^{40}Ar/^{39}Ar$ ages of the Patagonian back-arc lavas since the Early Miocene. The latitude and time at which the different segments of the Chile Ridge (SCR) entered the trench are indicated in red. The gray area underlines the areas where back-arc volcanism occurred prior to the subduction of the Chile Ridge segments at the same latitude. Figure from Guillaume *et al.* (2010).

tates the opening of the vertical slab gap by allowing more thinning of the lithosphere by thermal erosion within the weakened zone (Burkett & Billen, 2010). Vertical tear propagation might initiate from a lateral difference in thermal structure and strength within a subducting slab, possibly arising from the presence of a transform fault or fracture zone. Transform faults are part of a subducting ridge-transform-trench configuration and represent characteristic features of the downgoing slab with differing thermal, mechanical and buoyancy properties and play a significant role for the geometry and kinematics of a growing slab window (e.g. Thorkelson, 1996).

Considering vertical, downward-propagating tears in the Nazca slab south of the latitude of the Chile Triple Junction might be an alternative explanation for the temporal and spatial occurrences of OIB-related back-arc volcanism in Southern Patagonia. The ridge-trench-transform geometry in Southern Patagonia displays several right-stepping transform faults offsetting ridge segments that collided with the margin over the last 16 Ma (Breitsprecher & Thorkelson, 2009) (Figure 4.1, Figure 4.20A). Transform faults are large-scale plate features that extend laterally far outside the ridge-transform configuration, and their ENE-continuation in Southern Patagonia aligns with the spatial occurrence of back-arc volcanism in the overriding South American plate (Figure 4.1, Figure 4.20A).

Interestingly, south of 49°S the compilation of volcanic ages from the backarc region documents only one site of volcanism that is older than the successive slab window formation below this region (Figure 4.20B). In contrast, north of this latitude (and south from the CTJ) numerous volcanic rocks with OIB-signature predate the arrival of the main gap between the Antarctic and Nazca plates. Notably, the region south of 49°S coincides with the collision sites of three longitudinally closely spaced ridge segments that were offset by relatively short transform boundaries (Breitsprecher & Thorkelson, 2009) (Figure 4.1, Figure 4.20A). North of this latitude the ridge segments that collided with the subduction margin at 10, 6 and 3 Ma were apparently offset by longer transform faults that were possibly more mature. These transform faults might have represented more pronounced zones of weakness in the downgoing slab with higher potential to develop downward propagating fissures that could occasionally provide paths for sub-slab asthenospheric mantle below the overriding continental lithosphere.

4.7.4 The Near-Surface Geothermal Gradient in Southern Patagonia

A final argument will be made here regarding the large-scale heat flow and geothermal gradient conditions in Southern Patagonia. Certainly, ongoing ridge collision and slab window formation intuitively suggest elevated thermal conditions below and within the

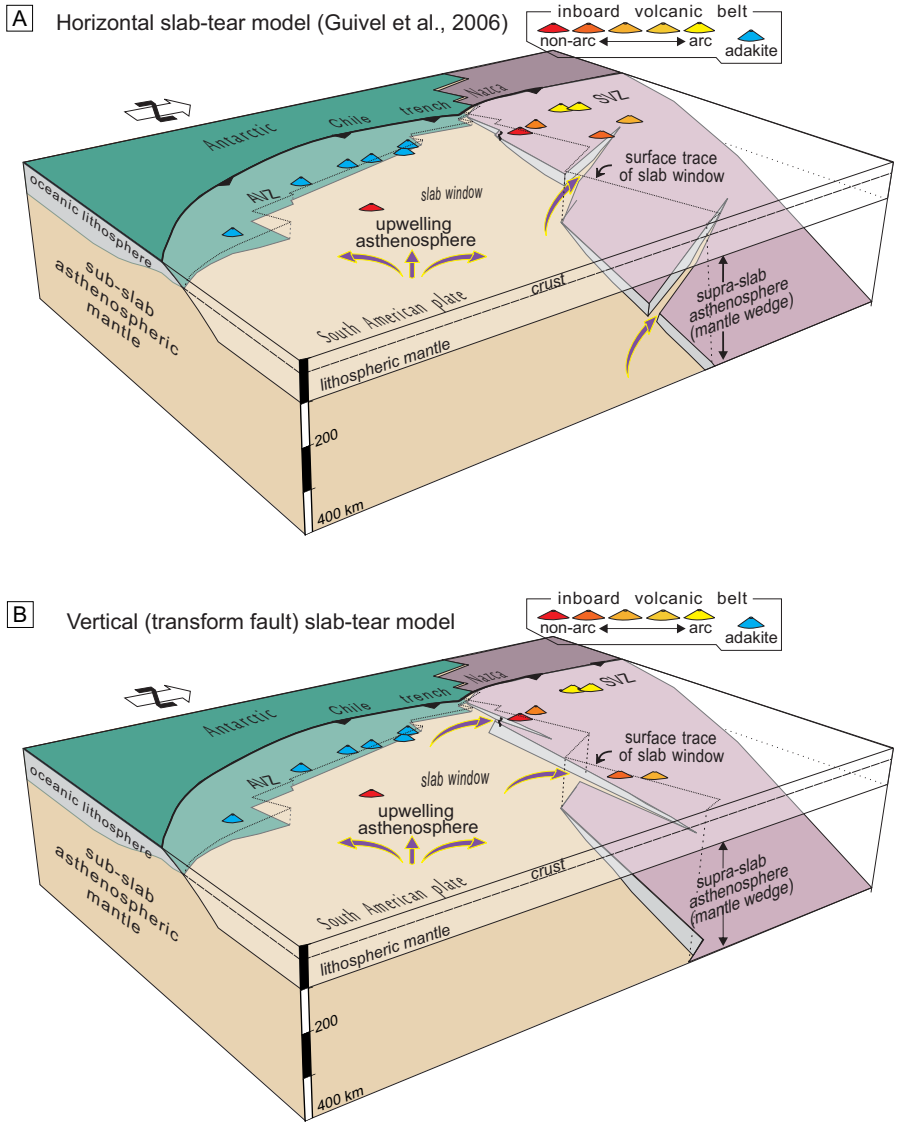

Figure 4.21 – Block diagram of the Patagonian slab window with two different slab-tear scenarios. This simplified view is projected towards the northwest from a bird's-eye perspective. The volcanic centres are color-coded corresponding to their genesis, from yellow (subduction-related arc volcanism, typical for the Southern Volcanic Zone north of the CTJ) to orange and red (transitional-to-alkaline, related to slab-tearing and successive slab window formation). (A) and (B) present different geometries of slab-tearing of the trailing edge of the Nazca slab corresponding to horizontal (A) and vertical (along transform faults) slab-tear propagation. (B) Figure modified from Breitsprecher & Thorkelson (2009).

overriding plate. As argued above, such conditions are most likely to be expected and detected in the immediate vicinity of active ridge collision and in the orogens fore-arc. In Southern Patagonia very high heat flow values in the order of 100-350 mW/m^2 have been effectively measured offshore of the Taitao Peninsula (Cande *et al.*, 1987; Bangs & Brown, 1995), where ridge collision is taking place since ~ 3 Ma (Breitsprecher & Thorkelson, 2009). In the back-arc region at the latitude of the CTJ, approximately 250-300 km east of the trench, Murdie *et al.* (1999) performed eight heat flow measurements in lake sediments of Lake General Carreras. The study was designed as a testing ground for a newly developed lightweight, portable equipment dedicated to measuring thermal gradients in shallow water sediments (3-5 m ground penetration). The average heat flow value of 103 ± 15 mW/m^2 from these eight measurements is higher than the global average of 62 mW/m^2 (Jessop, 1990) and the average for South America of 63±36 mW/m^2 (Hamza & Muñoz, 1996); however it is within the heat flow range for the entire Andean domain that varies between 78 mW/m^2 and 160 mW/m^2. The upper bound of this range (160 mW/m^2) is reported by Hamza & Muñoz (1996) for "Southern Patagonia" and occasionally referred to with respect to elevated geothermal conditions above the Patagonian slab window (Groome & Thorkelson, 2009; Scalabrino *et al.*, 2010). However, it is important to note that this value constitutes an average from a number of measurements located 700-1000 km to the north of the CTJ from the active Southern Volcanic Zone and along the active Liquiñe-Ofqui Fault Zone; it is clearly not representative for the ridge-collision and slab-window setting in Southern Patagonia.

A recent study by Sachse *et al.* (2016) presented vitrinite reflectance data from several wells in the Austral Basin located at 50-53°S and 250-300 km to the east of the trench - a region that has been above the slab window since the Late Miocene (Breitsprecher & Thorkelson, 2009). Sachse *et al.* (2016) report comparable paleo and present-day heat flow values between 65 and 78 mW/m^2 with locally increased values due to magmatism. Assuming an average crustal conductivity of 2.5-3 W/m*K (Turcotte & Schubert, 2014) these heat flow values correspond to a rather normal geothermal gradient of 25-35°C/km. In summary, the testing approach and the limited number of measurements in the study of Murdie *et al.* (1999) and the scarcity of other data should be kept in mind, particularly when speculating about elevated geothermal conditions above the entire arc and back-arc domains in the slab window region (Guillaume *et al.*, 2013; Groome & Thorkelson, 2009; Breitsprecher & Thorkelson, 2009; Thorkelson, 1996). So far, there is no field evidence to support such an interpretation.

4.8 Summary and Conclusions

1. This study combines new and already published apatite fission track and (U-Th)/He data from the region of the Northern Patagonian Icefield located inboard of the Chile Triple Junction where the active Chile Ridge collides with the South American margin. The data was implemented in single-samples and multiple-samples (elevation transects) thermal modeling with HeFTy and QTQt. The results are discussed against the background and re-evaluation of studies with a similar approach under the critical consideration of methodological, geological and geodynamical aspects.

2. The numerical modeling results from the Leones, Nef and Cerro Barrancos transects presented here indicate stepwise cooling of samples through the upper 3-5 km of the crust since the Upper Miocene (10 Ma). The episodic character of the thermal history is particularly well constrained by the density of data for the last 5 Ma and likely caused by a combination of pulses of neotectonic activity triggered by oblique ridge collision at these latitudes and superposed repeated glacial advances and valley incision.

3. Previously published thermal modeling results proposed a far-reaching Late Miocene reheating episode for this region related to ridge collision and slab window formation. These findings are contradictory to this study and the discrepancy is likely to be found in important shortcomings of the used model setups that are evaluated in detail here. It is concluded that in the event that such reheatingaffected the lregional thermal regime of the arc- and back-arc region south of the CTJ, then it is not recorded in the available low-temperature (AFT and AHe) data.

4. From the geodynamic perspective the plausibility of such a pulse of Late Miocene reheating is also considered to be rather ambiguous. A review of modeling and field-based studies suggests that such reheating episodes are more likely to be limited to the forearc region in the close vicinity of the site of ridge collision where the contact to the sub-slab asthenosphere is relatively shallow.

5. Regarding the spatial and temporal distribution of volcanism with sub-slab signature in the Patagonian back-arc, I favor the slab-tear model (Guivel *et al.*, 2006) in stead of the lateral-mantle-flow model (Guillaume *et al.*, 2013) to explain the introduction of sub-slab asthenospheric material below the upper plate prior to arrival of the main slab window. Here, a vertical, downward-propagating, instead

of horizontal (Guivel *et al.*, 2006), slab tear is favored; however, a combination of both geometries is also possible.

6. Finally, based on a review of available heat flow data from Southern Patagonia, we conclude that there is no strong evidence for an elevated near-surface geothermal gradient above the Patagonian slab window.

Supplementary Material

See Appendix B.

Chapter 5

General Discussion & Conclusions

The principal aim of this thesis was to address neotectonic activity and late Cenozoic cooling histories of the Patagonian Andes at the latitude of the Chile Triple Junction (CTJ, 46°S) and evaluate these observations in a regional context of geodynamics and landscape evolution. Particular emphasis was focused on the coeval Miocene-to-recent oceanic ridge collision and slab window formation in this unique setting where protracted tectonic and climatic processes have impacted the evolution of the Andean orogen until the present day. The primary regional focus of this investigation was the high massif capped by the Northern Patagonian Icefield (NPI, 47°S) and its eastern foreland, located immediately inboard of the present-day location of the CTJ. The rationale for selecting this study area: First, the NPI region coincides with the closely spaced, and most recent oblique collision of three successive oceanic ridge segments with the subduction margin at 6, 3 and 0.3 Ma, and overlies the most recent extent of the Patagonian slab window that has been forming there since 4 Myr (e.g. Breitsprecher & Thorkelson, 2009, Figure 3.1, 4.1 and 5.1). Therefore, this region was considered to have a higher potential to preserve possible structural and exhumational imprints of these processes compared with other sectors of the orogen that had experienced the collision with oceanic ridge segments earlier during the Miocene. (farther south) where they could be obscured by subsequent deformation and the effects of multiple glacigenic processes. Secondly, the NPI massif marks the abrupt increase of summit elevations and relief in the Southern Patagonian Andes (south from the CTJ) that has been controversially addressed in recent studies. This has resulted resulting in interpretations that either consider purely geodynamic or exclusively climatic controlling factors. However, although climate-driven processes undoubtedly have had a major impact on the Patagonian Andes, the short wavelength of this major topographic changes appears to be inconsistent with gradual climate gradients or large-scale geodynamic processes that govern this region. Furthermore, the fact that the morphologic changes and variations in the timing and the degree of exhumation

occur precisely at the latitude of the Chile Triple Junction suggests a greater structural control than previously thought. This complex and controversially interpreted region of the orogen was thus the main motivation for the field-based approach adopted in this study.

The two principal research chapters in this thesis thus attempt to address some aspects of the structural (Chapter 3) and geodynamic (Chapter 4) evolution of the Southern Patagonian Andes and provide new insights and a solid basis for re-evaluation of existing models explaining the geodynamic impact of ridge collision and slab window formation on the overriding plate. Here, I briefly summarise and integrate the main conclusions of the two research chapters and discuss them in light of the compiled record of late Cenozoic exhumation data in Southern Patagonia as recored by low-temperature thermochronometers (AHe and AFT).

5.1 Tectonic and Cooling Records of Oceanic Ridge Collision in Southern Patagonia

The integration of geomorphic, structural and thermochronological data presented in Chapter 3 supports my initial hypothesis that the closely spaced collision of oceanic ridge segments in the Golfo de Penas area since 6 Ma has enhanced strain partitioning in the overriding plate, promoting margin-parallel strike-slip faulting and the decoupling and coeval northward motion of the NPI block. The localised uplift of this crustal sliver along the likely reactivated Exploradores Fault Zone is strongly supported by the offset of cooling ages from both AHe and AFT thermochronometers between more proximal (Leones) and more distal (Nef) regions with respect to the fault.

At the time of publication of Chapter 3 only AHe data from these two profiles were available. Since this thermochronometer records cooling below very low temperatures of 40-70°C, and therefore exhumation across the upper 1-3 km of the crust, an important part of the discussion in the corresponding part of the study is dedicated to the evaluation of variable surface processes (glacial erosion in particular) that have been hypothesized to significantly impact cooling age patterns (Thomson *et al.*, 2010). However, such significant variations in erosional efficiency over relatively short spatial scales has been discarded based on the lack of geomorphic, climatic and glacial characteristics that could unambiguously support it. Moreover, the addition of new AFT data from the two elevation transects mimic precisely the same offset in cooling ages (by 2 Ma younger cooling ages in Leones compared to Nef) and strongly supports my conclusion

that it was tectonic forcing rather than variable climate-driven impact on exhumation processes that best explains the observed cooling patterns.

This conclusion and the observed regional pattern of cooling ages in the region of the NPI (Figure 3.8E) gave rise to the hypothesis that coeval normal faulting along the southern foothills of the NPI might explain the abrupt decrease in summit elevations immediately south from the NPI. Hence, the more subdued topography and drowned fjord landscape in this region might be the result of recent or ongoing extension along the trailing edge of the NPI block. Documenting the proposed extensional structures in the fjord landscape south of the NPI has proven challenging because of the lack of structural markers in the granitic lithologies and the difficult accessibility of this region. However, first indications for recent localised normal faulting in the southeastern foothills of the NPI massif (El Salton Fault) might support this hypothesis. Such large-scale structural pattern would mimic extensional structures in the Golfo de Penas region farther west resulting from an analogous northward movement of the adjacent crustal sliver, the Chiloé Block, triggered by the same processes of oblique ridge collision and strain partitioning the upper plate. Ongoing work based on results from this thesis is focused on extensive low-elevation (sea-level) sampling across proposed extensional structures in the fjord region that might possibly track differential uplift patterns and complete the cooling pattern presented in Figure 3.8E.

The deeply dissected landscape of the Southern Patagonian Andes (south of the CTJ) with abrupt variations in summit elevations and highly variable relief (Figure 3.1) might record several million years of regional exhumation by fluvial (before 7-8 Ma) and glacial (prior 7-8 Ma) superimposed by occasional and localised tectonic disruption and differential uplift triggered by sustained northward migrating oblique ridge collision. Certainly, in the region of the NPI these impacts on the upper plate are expected to be more recent and pronounced and consequently detectable in the low-temperature thermochronometry record and the landscape.

The second research focus (Chapter 4) addresses the late Cenozoic thermal history of the NPI region based on inverse thermal modelling of samples taken along elevational transects across this area. The results of the thorough modelling procedure suggests a stepwise cooling of the upper 4-5 km of the crust over the last 10 Ma. This relatively simple cooling scenario is consistently supported by both single-sample and multiple-sample numerical simulations; ; these results are furthermore compatible with the regional geological record thus reconciling the effects of several (glacial) erosional and tectonic events since the Late Miocene.

Importantly, the inverse thermal modelling of new data and a reassessment of published thermochronometric data could not reproduce previously proposed scenarios, such as important reheating episodes in this region (Blisniuk *et al.*, 2006; Guillaume *et al.*, 2013). Such reheating had been related to the approaching slab window in general (Blisniuk *et al.*, 2006) and lateral, i.e. (trench-parallel), mantle flow during slab-window formation in particular, that may have transported heat through advection over large distances (Guillaume *et al.*, 2013). The reason for this inconsistency between this study and previous results lies most likely in major differences between the modelling setups (addressed in detail in Section 4.7.2). Nevertheless, this null-hypothesis invites for some re-consideration regarding two general questions: 1) To what extent can thermal pulses related to slab-window formation plausibly affect the overriding plate, particularly the distant upper-crustal levels of the arc region far from the site of ridge collision?; and, 2) is such a reheating event indeed recorded in the low-temperature thermochronological and geological record of Southern Patagonia?

Certainly, the first of question is more general and can be assessed only indirectly and in light of the existence or lack of evidence for reheating in similar geodynamic settings elsewhere. A synopsis of existing field-based, modelling and review studies combined with my findings does not support the notion of such spatially far-reaching pulses of heating associated with the formation of a slab window - neither in Southern Patagonia nor elsewhere. The available data to data rather constrain possible thermal effects to the on- and offshore sectors of the forearc and the immediate vicinity of the active site of ridge collision. Regarding the second question, with particular focus on Southern Patagonia, it has been demonstrated that the thermal history recorded in the available low-temperature thermochronological data (AHe and AFT) from the NPI area does not record Late Miocene reheating episodes. Furthermore, the existence of anomalous alkaline volcanism in the back-arc region, originally used as an argument to support heat-wave propagation(Guillaume *et al.*, 2013), can be alternatively explained by the horizontal, i.e. (trench-parallel), slab tearing model proposed by Guivel *et al.* (2006) or a modified scenario, which might include successive formation of subvertical, i.e. (orthogonal to the trench), tears in the downgoing slab along existing transform faults.

Importantly, the null-hypothesis regarding Late Miocene reheating episodes in the NPI region, does not per se contradict the existence of lateral mantle flow patterns predicted by analog models (Guillaume *et al.*, 2010), even if the proposed spatial reach and the effects of such heat transport could be questioned, given the simplified setup

conditioned by the used models. However, the null-hypothesis does explicitly contradict the argument that such potential reheating events are recorded in the existing low-temperature thermochronological dataset (AHe and AFT) used as modelling input.

5.2 Exhumation and Dynamic Topography in Southern Patagonia

Several of the recent studies addressing the large-scale landscape (Thomson *et al.*, 2010; Herman & Brandon, 2015) and geodynamic (Guillaume *et al.*, 2013; Braun *et al.*, 2013) evolution of the Patagonian Andes base their conclusions to a large extent on an extensive data set of AHe and AFT cooling ages. However, even though the number of data points is significant, given the large extent of the entire Patagonian Andes (38°to 54°S, < 2000 km), the variability of tectonic styles north and south of the Chile Triple Junction, and the selective spatial distribution sampling locations in this region (die to limited access), care should be taken when interpreting regional trends. A close inspection of the spatial distribution of cooling ages should thus accompany any interpretation of the cooling record and trends to avoid potential spatial bias with respect to the structural or climatic conditions of sampled locations. For an updated synopsis of all currently available AHe and AFT ages from the Patagonian Andes (south from 40°S) I plotted cooling trends south of the CTJ, i.e. in the region that has been affected by ridge collision and slab window formation over the last 16 Myr.

Figure 5.1 portrays the topography of the Patagonian Andes south from 40°S superposed by the locations of all available AHe (green) and AFT (blue) cooling ages. All AHe ages correspond to single-grain ages. The three coloured boxes correspond to the swath profiles indicated in Figures 5.2, 5.3, and 5.4, along which all corresponding data points (the data points enclosed by each box) were projected. The yellow swath box (Swath 1, Figure 5.2) encompasses the entire available data set south of 40°S. The southernmost data points were excluded because they originate from the close vicinity of the Magallanes Fault and the transition towards the Scotia Plate, which thus represents an entirely different structural setting (Figure 3.1). The pink box (Swath 2, Figure 5.3) encompasses all data points located east of the main divide and south of the CTJ, including more arc-proximal regions (such as Leones, Cerro Barrancos or data from Fosdick *et al.* (2013) at 51°S) and some scattered data from the eastern foreland (back-arc) domain. The red box (Swath 3, Figure 5.4) encompasses all data points located south of the CTJ and west from the main divide, i.e. the area that broadly corresponds to the onshore sector of the fore-arc.

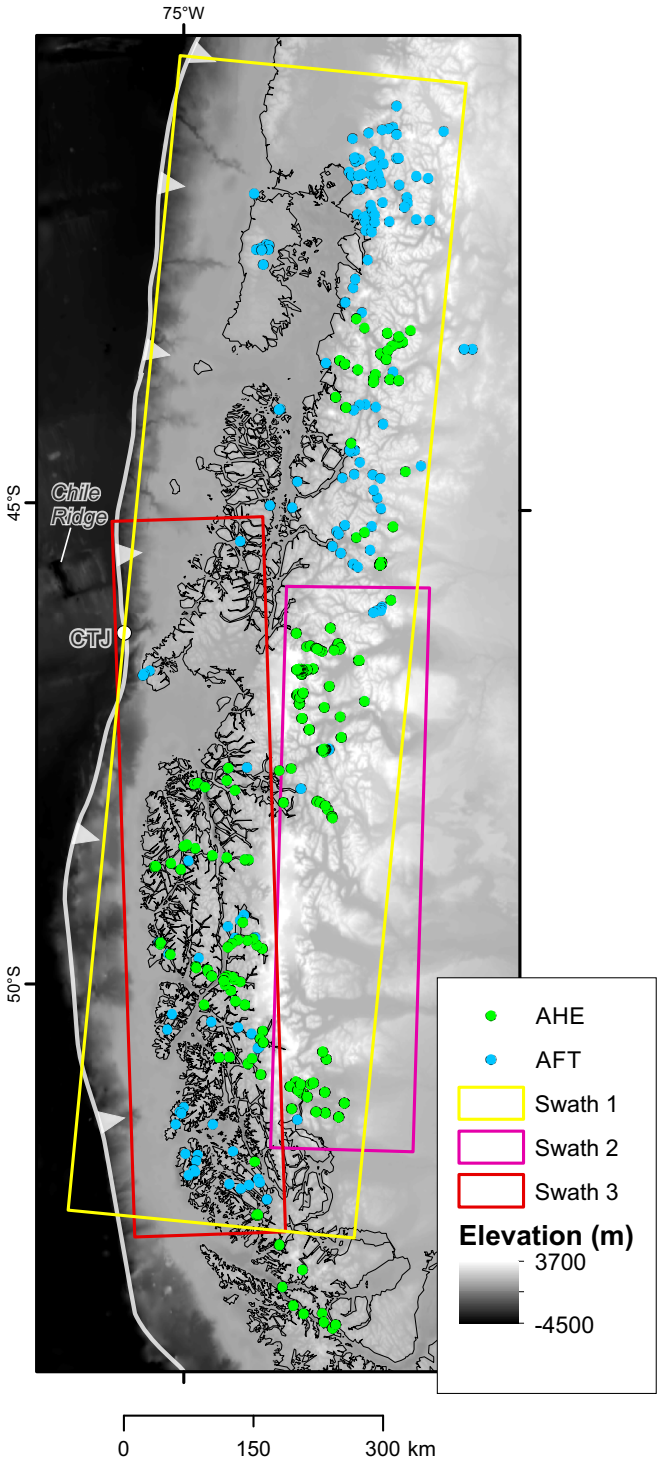

Figure 5.1 – Compilation of available apatite (U-Th)/He and fission track cooling ages from the Southern Patagonian Andes. Data from Thomson *et al.* (2001); Thomson (2002); Adriasola *et al.* (2006); Blisniuk *et al.* (2006); Thomson *et al.* (2010); Fosdick *et al.* (2013); Guillaume *et al.* (2013); Georgieva *et al.* (2016). Apatite (U-Th)/He (AHe) indicated by green circles, apatite fission track (AFT) indicated by blue circles. The yellow (Swath 1), pink (Swath2) and red (Swath 3) rectangles correspond to swath areas presented Figures 5.2, 5.3, and 5.4, respectively. The AHe and AFT data plotted in each of these figures corresponds to all samples within each corresponding swath area.

At a first glance the projection of all available data along-strike of the Patagonian Andes south of 40°S displays an interesting trend that was recognised and interpreted in very differing ways (Figure 5.2). As first noted by Thomson *et al.* (2010), both AFT and AHe cooling ages north of 46°S are rather young and mostly < 5 Ma (AHe) and <10 Ma (AFT), respectively. In contrast, south of this latitude an apparently southward-increasing trend in both minimum AHe and AFT cooling ages can be detected. However, disregarding the fact that the onset of this increasing trend coincides with the present-day location of the CTJ, Thomson *et al.* (2010) interpreted this phenomenom as the cumulative record of a southward-decreasing efficiency of glacial erosion towards higher latitudes arisinf from colder climate and decreased ice-sliding velocities (and therefore glacial erosion efficiency). This interpretation of the cooling record is also in agreement with a recent study by Herman & Brandon (2015) who proposed that the cluster of relatively young cooling ages at 44°S is a climatically conditioned "erosional hotspot" compared to slower erosion rates farther south. Conversely, Guillaume *et al.* (2013) and Braun *et al.* (2013) highlighted the coincidence between the position of the CTJ within this correlation and interpreted the northward-decreasing trend in AHe and AFT ages south from the CTJ as the imprint of a northward-migrating pulse of crustal heating and accompanying dynamic uplift related to slab window formation (Guillaume *et al.*, 2009, 2013) and balanced by erosion (Braun *et al.*, 2013). These latter studies focused specifically on the back-arc domain, i.e the region located east of the main divide, where numerical (Guillaume *et al.*, 2009, 2013) and analog (Guillaume *et al.*, 2010) modeling predicts the highest gradient in dynamic uplift.

A closer inspection of the along-strike data projection presented here might invite an alternative view of the proposed scenarios. The data set presented in Figure 5.2 has been extended (compared to the compilation of Thomson *et al.* (2010)) by the new data presented in this study (AHe and AFT from Leones and Nef transects) and AHe data from Cerro Barrancos (47°S) and Cerro MacKay (45°S) (Guillaume *et al.*, 2013) and Lago Torro (51°S) (Fosdick *et al.*, 2013). The newly added AHe data clearly disturb the proposed trend and document similar levels of exhumation between the far south (Lago Torro) and the immediate proximity of the CTJ (Cerro Barrancos, Nef, Leones) from comparable locations in the eastern foothills and proximal to the glaciated orogen's interior. As shown in Chapter 3, the even younger ages in the Leones transect result from localised differential uplifts due to neotectonic activity at the CTJ. It is expected that AFT cooling ages from the Lago Torro area would confirm this disturbance of trend

and be rather comparable with ages from the Cerro Barrancos and Nef transects (6-12 Ma old).

Extracting only the cooling ages from samples collected **east** from the main divide, Guillaume *et al.* (2013) and Braun *et al.* (2013) observed an increasing trend in minimum cooling ages across the latitude of the CTJ towards the region that has still not been affected by the predicted pulse of dynamic uplift, which had been inferred to be balanced by erosion. However, this abrupt increase in trend arises from the consideration of the evidently partially reset samples from the Cerro MacKay (5-100 Ma) and very few scattered data points from the far eastern, very dry foreland region away from the icefield region (Fig. 5.2). Hence, it appears not to be feasible to compare cooling ages from the proximity of the repeatedly and extensively glaciated, eroded orogen interior with the distal foreland regions in the north.

By focusing only on the data located south of the CTJ and east of the main divide, i.e. the region with the largest gradient in predicted dynamic uplift and associated erosion, the proposed trend is not evident (Figure 5.3). AHe ages in the very south (51°S) coincide with the range of ages close to the CTJ and notably located at very similar elevations. The slight northward decreasing trend of both AFT and AHe ages between 48°S and 46°S is mainly determined by the very young ages (including high elevations, note color-coding) from the Leones transect. This trend appears to be augmented in the data representations by previous publications due to the adoption of a logarithmic age-scale (e.g. Braun *et al.*, 2013, their Figure 3), which is rather questionable given the relatively large error range of the AHe and AFT dating methods.

As noted above and expanded in the discussion in the previous chapters, the thermal and mechanical transient effects of ridge collision and slab window formation on the upper plate are expected to be largest and most likely to be recorded in the trench-proximal domain of the overriding plate. A significant number of data points south of the CTJ originates west of the main divide and corresponds to samples collected at or close to sea level in the fjord landscape, spanning the western flank of the Southern Patagonian Icefield (Figure 5.1). This part of the data set is considered to be particularly suitable for tracking the proposed imprint of dynamic topography based on two considerations: First, the distribution of data points overlaps with the numerically predicted northward increasing gradient of cumulative dynamic uplift (Guillaume *et al.*, 2009, 2013). Second, all samples from this region were collected at very similar elevations close to sea level, which eliminates potential bias that might result from the expected age-elevation rela-

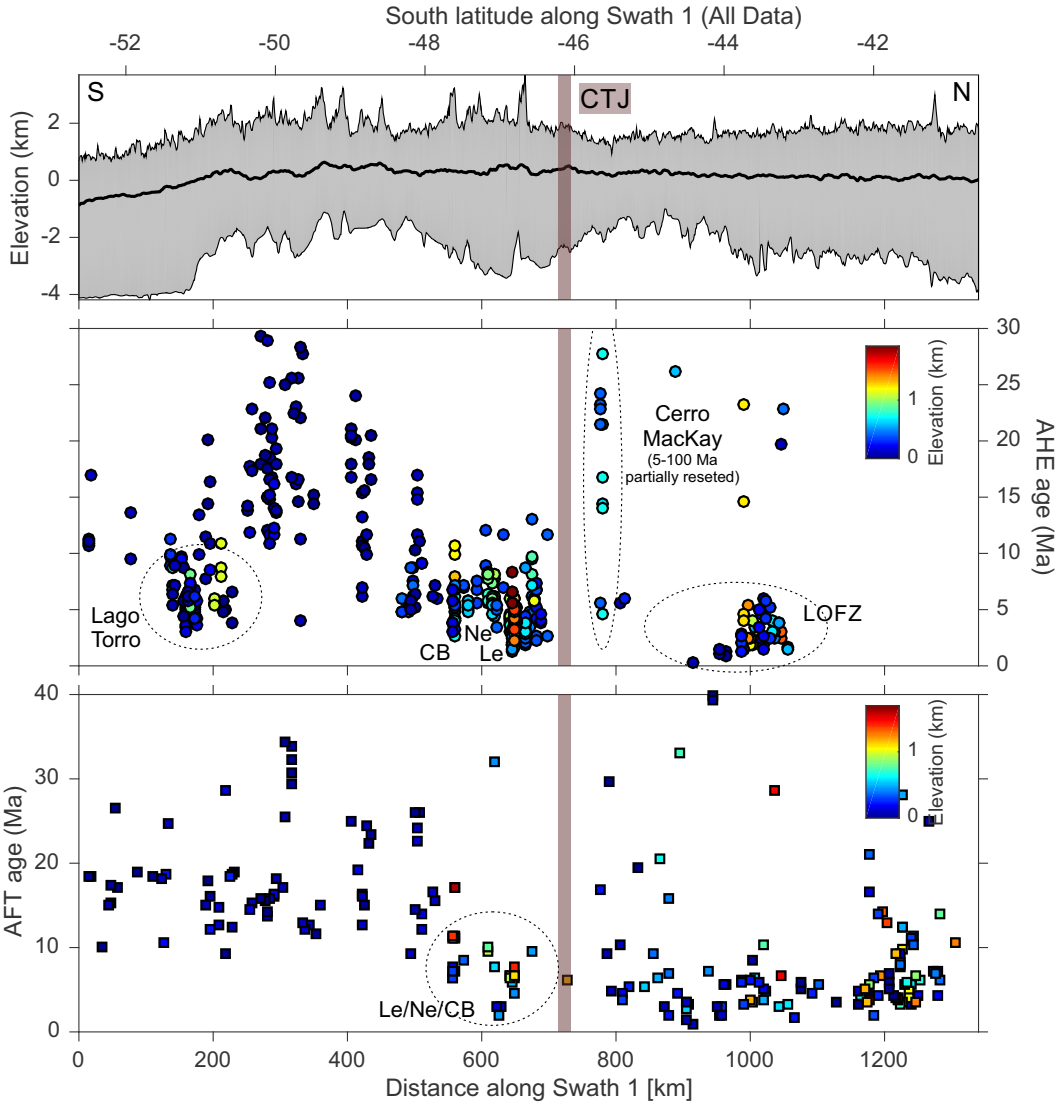

Figure 5.2 – Swath profile (Swath1) and compilation of all available (U-Th)/He (single grain) and AFT cooling ages from the Patagonian Andes south of 44°S. Data from Thomson *et al.* (2001); Thomson (2002); Adriasola *et al.* (2006); Blisniuk *et al.* (2006); Thomson *et al.* (2010); Fosdick *et al.* (2013); Guillaume *et al.* (2013); Georgieva *et al.* (2016). Brown stripe marks the present-day location of the Chile Triple Junction (CTJ). AHe single grain and AFT cooling ages are plotted against distance along swath and latitude and are color-coded by sampling elevation. CB: Cerro Barrancos,; Ne: Nef; Le: Leones; LOFZ: Liquiñe-Ofqui Fault Zone.

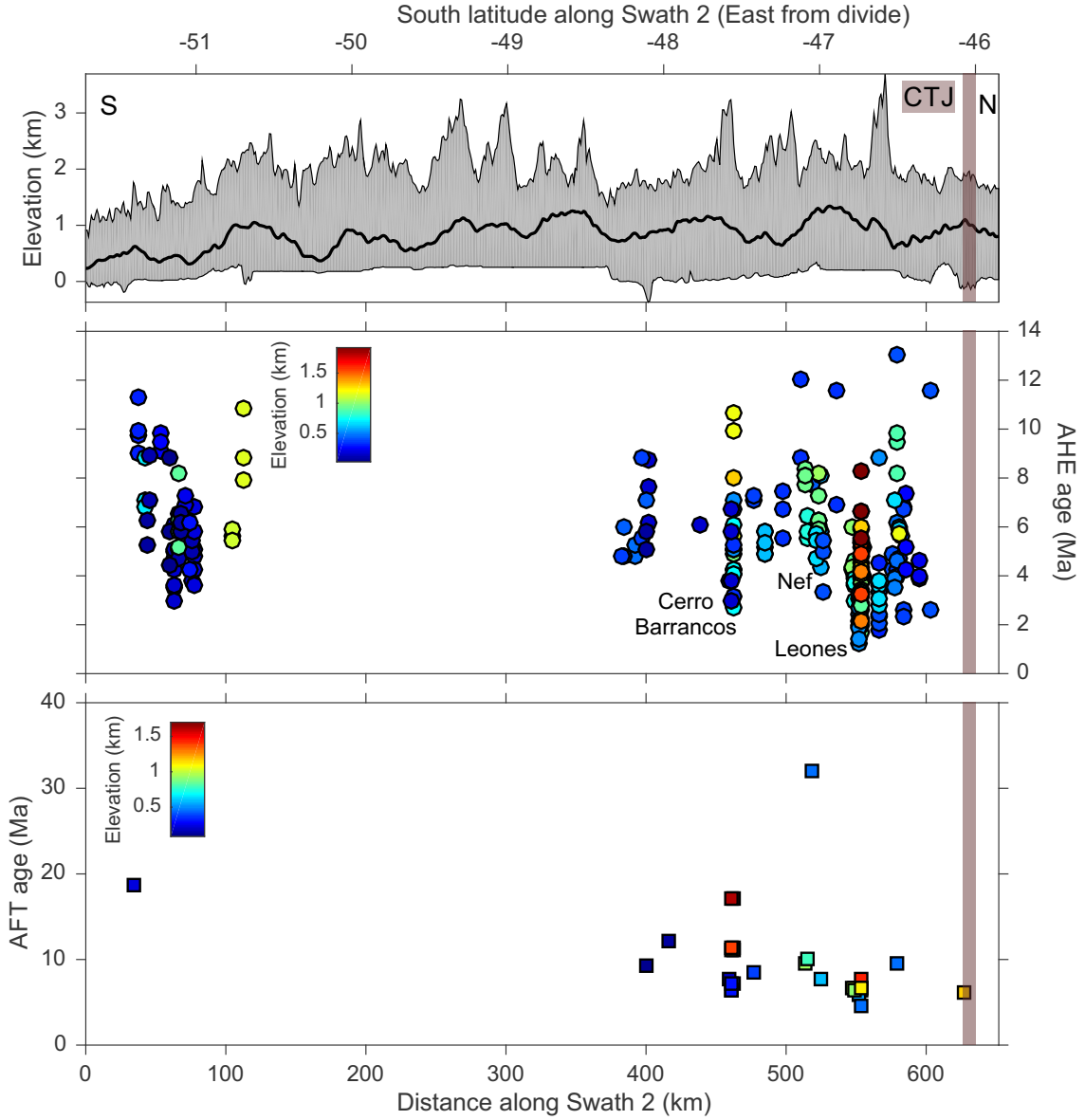

Figure 5.3 – Swath profile (Swath2) and compilation of all available (U-Th)/He (single grain) and AFT cooling ages **east** of the main divide of the Southern Patagonian Andes (south of 46°S). Data from Thomson *et al.* (2001); Thomson (2002); Blisniuk *et al.* (2006); Thomson *et al.* (2010); Fosdick *et al.* (2013); Guillaume *et al.* (2013); Georgieva *et al.* (2016). Brown stripe marks the present-day location of the Chile Triple Junction (CTJ). AHe single grain and AFT cooling ages are plotted against distance along swath and latitude and color-coded by sampling elevation.

tionship of cooling ages, and provides an ideal sampling distribution for tracking spatial trends.

Nevertheless, projecting this data set along strike of the forearc region does not reveal any particular N-S trend in the distribution of AHe and AFT cooling ages either (Figure 5.4). The majority of both AHe and AFT ages fall within the range of 20±5 Ma (AHe) and 20±10 Ma (AFT) and likely document the proposed onset of mejor deformation in this region around 25 Ma ago coincident with the onset of deposition of the continental synorogenic sediments in the eastern foreland (Blisniuk *et al.*, 2005). The onset of regional deformation and accelerated erosion and foreland deposition was likely triggered by an increase in convergence velocities between the Nazca and South American plates between 28 and 26 Ma (Pardo-Casas & Molnar, 1987; Somoza, 1998; Thomson *et al.*, 2001) that induced the main episode of mountain building and surface uplift (Blisniuk *et al.*, 2005) at these latitudes associated with a significant successive eastward propagation of the deformation front (Thomson *et al.*, 2001). The uniform topographic characteristics in this region imply that any subsequent passive (i.e. after closure of the isotope systems) wave of dynamic uplift should have been balanced by an equal amount of erosion that must be recorded in a pulse of differential exhumation, which, however, is not recorded in the data.

A closer examination of the color-coded elevations of the cooling ages in Figure 5.4, and particularly in the AHe data set, surprisingly reveals that samples located at lower elevations (dark-blue colors) appear to have older cooling ages. This observation has a simple explanation and discloses the only trend actually recorded in this data set that becomes evident when the data is plotted across-strike of the orogen (Figure 5.5). A gradual eastward decrease in minimum and maximum cooling ages can be observed from the westernmost Pacific coastlines of the fjord region towards the foothills of the Southern Patagonian Icefield to the east. This trend is not obscured by the fact that slightly higher elevations were apparently sampled preferentially in the east, close to the glacial outlets and the rising mountain front. The observation of this trend might not be relevant for the discussion of dynamic topography and its record, but it is very exemplary for the need to critically evaluate the spatial distribution of this extensive dataset before drawing conclusions about large-scale climatically- or tectonically-driven trends and processes.

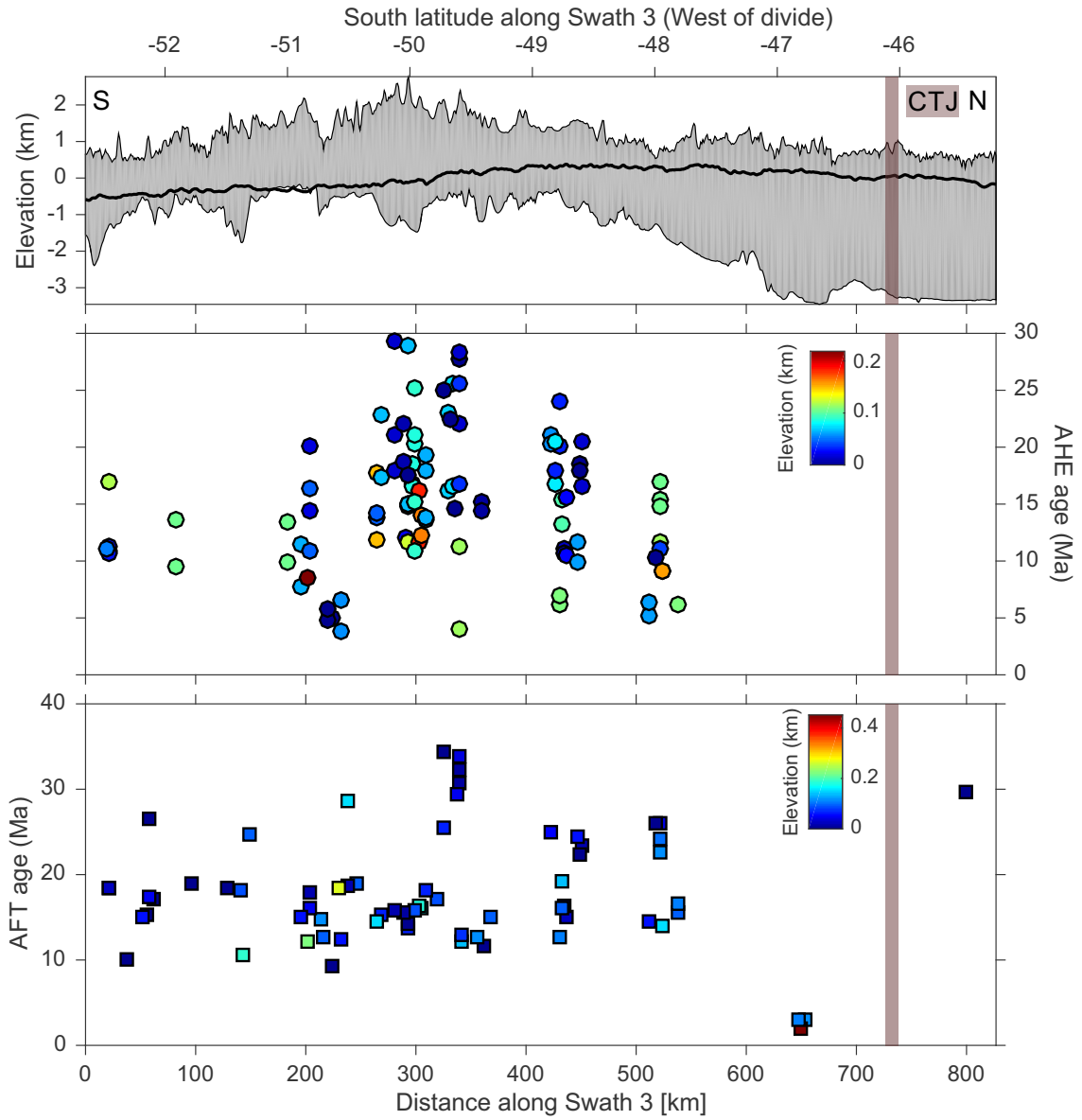

Figure 5.4 – Swath profile (Swath3) and compilation of all available (U-Th)/He (single grain) and AFT cooling ages **west** of the main divide of the Southern Patagonian Andes (south of 46°S). Data from Thomson *et al.* (2001); Thomson (2002); Blisniuk *et al.* (2006); Thomson *et al.* (2010); Guillaume *et al.* (2013); Georgieva *et al.* (2016). Brown stripe marks the present-day location of the Chile Triple Junction (CTJ). AHe single grain and AFT cooling ages are plotted against distance along swath and latitude and color-coded by sampling elevation.

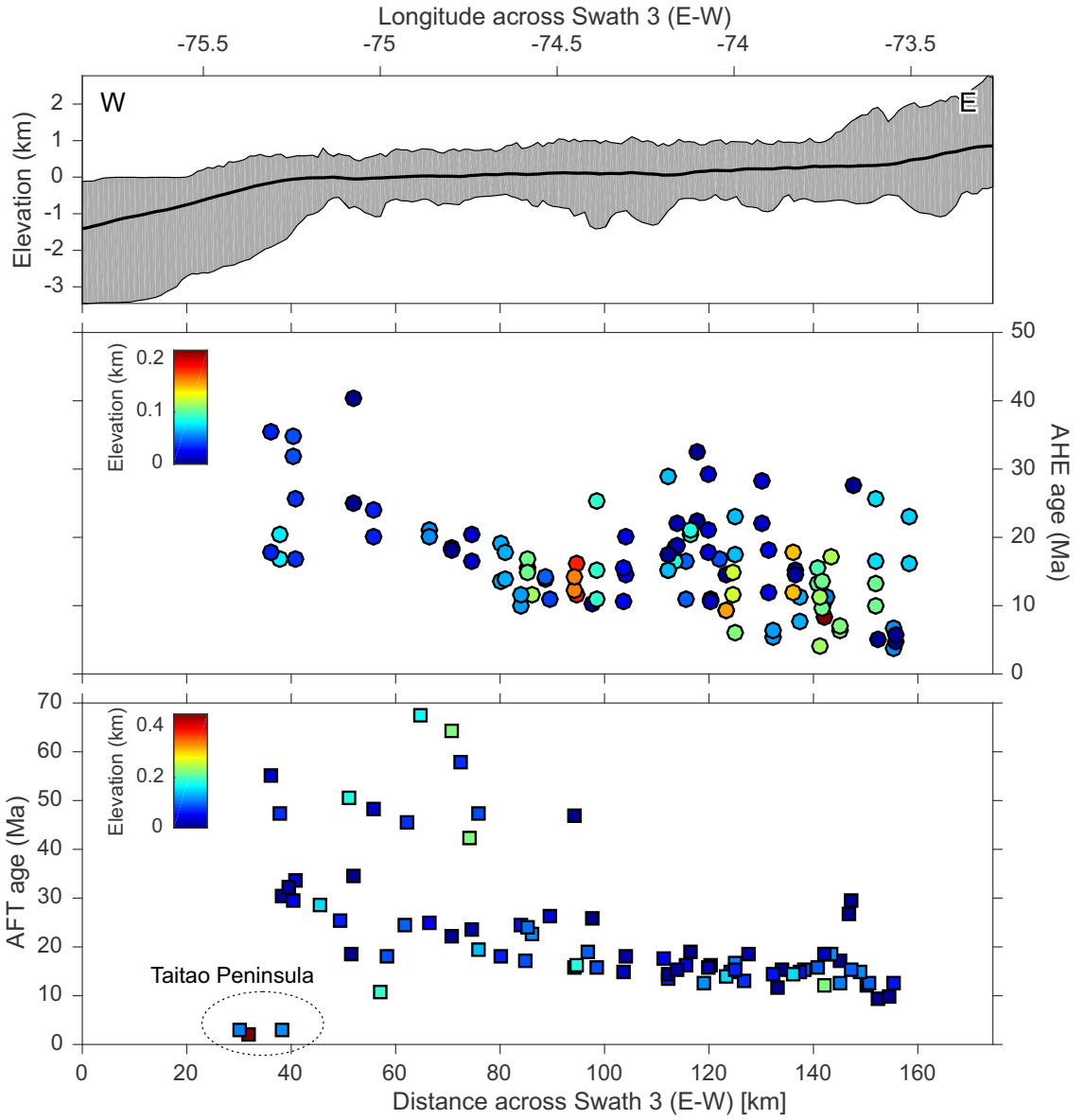

Figure 5.5 – Swath profile (Swath4) and compilation of all available (U-Th)/He (single grain) and AFT cooling ages **west** of the main divide of the Southern Patagonian Andes (south of 46°S). Data from Thomson *et al.* (2001, 2010). Brown stripe marks the present-day location of the Chile Triple Junction (CTJ). AHe single grain and AFT cooling ages are plotted against distance along swath and longitude and color-coded by sampling elevation.

The dynamic topography signal in Southern Patagonia predicted by numerical (Guillaume *et al.*, 2009, 2013) and analog (Guillaume *et al.*, 2010) models mainly results from the cancellation of the downward force exerted on the overriding plate when a slab window forms (e.g. Hynes, 2005; Husson, 2006). However, for example Hynes (2005) demonstrated how factors such as the age or slab dip angle of the subducting plate, both determining its negative buoyancy, or the amount of convergence, can significantly affect this downward force and the resulting dynamic subsidence (or uplift when the force is cancelled). As noted in the previous chapter, the buoyancy characteristics for the downgoing plate in the above models appear significantly exaggerated and incompatible with the subduction of hot, young and hence very buoyant oceanic lithosphere in Patagonia immediately preceding slab window formation. This model setup might result in an amplification of the predicted dynamic signal and explain why it does not seem to be recorded in the low-temperature thermochronometry record as expected.

On the other hand, detailed morphometic studies on river terraces (Guillaume *et al.*, 2009) and catchment characteristics (Jeandet, 2014) were carried out in the distal dry eastern foreland of the Southern Patagonian Andes at and south from the present-day location of the CTJ. These studies reveal gentle tilting patterns of river terraces or variations in catchment morphometrics that were explained by a very long-wavelength (i.e. hundreds of kilometres) and transient uplift of this area related to slab window formation immediately below this region. It is noteworthy, that the above conclusions, drawn from the low-temperature-thermochronometry cooling record, do not contradict these findings or the existence of dynamic topography in Southern Patagonian. The thermochronometric merely emphasise the fact, that the previously proposed magnitude of such uplift might be overestimated and that it is apparently not recorded in the low-temperature thermochronology record, as previously suggested.

5.3 The Role of Glaciation

Finally, I will comment on the role of glaciation for landscape evolution and particularly the low-temperature cooling record in the Patagonian Andes. The studies by Thomson *et al.* (2010) and Herman & Brandon (2015) infer a significant impact of climatically controlled (glacial) erosion gradients on the exhumational record (AHe, AFT) and the topographic characteristics of the Patagonian Andes. The interpretation of the data set was focused on a climatically conditioned decrease of glacial erosion towards higher latitudes (Thomson *et al.*, 2010) and the inference of an "erosional hotspot" at 44°S coincident with the latitudinal shifts in Southern Hemisphere Westerlies during glacial

maxima (Herman & Brandon, 2015). The former interpretation particularly linked the proposed variability in glacial erosion efficiency to the observed southward increase of summit elevations and a missing "glacial buzzsaw" topography in the Southern Patagonian Andes (Thomson *et al.*, 2001).

Both interpretations of particularly effective glacial erosion north of 46°S are based on a large concentration of very young AHe and AFT cooling ages from the orogen's interior distributed along strands of the active transpressional Liquiñe-Ofqui Fault Zone (LOFZ). The LOFZ is genetically linked to the oblique collision of the Nazca Plate, and the Chile Ridge along its trailing edge, and has contributed to large amounts of differential uplift and exhumation since the Mid-Miocene (e.g. Nelson *et al.*, 1994; Thomson, 2002; Adriasola *et al.*, 2006; Rosenau *et al.*, 2006; Cembrano *et al.*, 2002; Lange *et al.*, 2008; Agurto-Detzel *et al.*, 2012). South from the CTJ, such tectonic contribution to exhumation is missing and generally the sampling in the intra-arc region is much more limited. Even though glaciation has certainly played a major role for exhumation in the Patagonian Andes since the Late Miocene, it seems that the "erosional hotspot" identified by Herman & Brandon (2015) rather represents a "sampling and tectonic hotspot" where a dense dataset records several million years of tectonic uplift continuously balanced by glacial erosion.

The balanced interplay between tectonic uplift and glacial erosion has been suggested to be the key factor for the formation of "glacial buzzsaw" topography characterised by mean and summit elevations that closely follow trends in the equilibrium line altitude of glaciers (Pedersen *et al.*, 2010). Such topographic characteristics were identified in the Northern Patagonian Andes (Thomson *et al.*, 2010) and in other active orogens (e.g. Brozoviç *et al.*, 1997; Mitchell & Montgomery, 2006; Egholm *et al.*, 2009; Pedersen *et al.*, 2010, and references therein). In the Southern Patagonian Andes (south from the CTJ) this correlation does not exist and large surface area is preserved above the equilibrium line altitude. The new thermochronometry data presented in this thesis, combined with data from Fosdick *et al.* (2013) and Guillaume *et al.* (2013), clearly document that glacial erosion in the Southern Patagonian Andes has been equally effective, at least on the scale of single catchments. However, the overall modification and exhumation of the landscape by glacial erosion processes has not been continuously balanced by widespread tectonic exhumation, compared to latitudes north of the CTJ. Additionally, the regional exhumational pattern south of the CTJ might have been episodically and locally disrupted by superimposed differential rock uplift resulting from oblique collision of oceanic ridge segments, enhanced plate coupling, and ultimately the spatiotemporal partition-

ing of upper crustal deformation. Last but not least, the progressive replacement of cold subduction-related mantle overlying the Nazca slab with hot asthenospheric low-viscosity mantle from the slab window below Southern Patagonia over the last 16 Myrs might have significantly influenced the transient isostatic responses of the upper plate to erosion linked to fluvio-glacial dynamics (Dietrich *et al.*, 2010) and left its cumulative imprint on the overall present-day topography.

In conclusion, it is challenging to disentangle and rank the impacts of all these very different processes on the overall landscape evolution of the Southern Patagonian Andes. This study emphasizes, that the complex geodynamic setting of the Southern Patagonian Andes has to be considered as first tectonic processes set the pace at which topography is being built and contemporaneously modified by climate-driven processes. It is therefore important that integrative approaches, as shown here, should be encouraged, as the combination of structural, geomorphological, geophysical and thermochronometric data will help to more efficiently design models of these complex issues, predict how the tectonic and surface-process system is coupled and to reconcile observations from different data sources and multiple timescales towards more objective conclusions.

References

Abratis, M., Wörner, G., 2011. Ridge collision, slab-window formation, and the flux of pacific asthenosphere into the caribbean realm. Geology 29 (2), 127–130.

Adriasola, A. C., Thomson, S. N., Brix, M. R., Herve, F., Stockhert, B., 2006. Postmagmatic cooling and late cenozoic denudation of the north patagonian batholith in the los lagos region of chile, 41 degrees-42 degrees 15's. International Journal of Earth Sciences 95 (3), 504–528.

Agurto-Detzel, H., Rietbrock, A., Barrientos, S., Bataille, K., Legrand, D., Jul 2012. Seismo-tectonic structure of the aysen region, southern chile, inferred from the 2007 mw=6.2 aysen earthquake sequence. Geophysical Journal International 190 (1), 116–130, times Cited: 0.

Agurto-Detzel, H., Rietbrock, A., Bataille, K., Miller, M., Iwamori, H., Priestley, K., 2014. Seismicity distribution in the vicinity of the chile triple junction, aysén region, southern chile. Journal of South American Earth Sciences 51, 1–11.

Amundson, J. M., Truffer, M., Lüthi, M. P., Fahnestock, M., West, M., Motyka, R. J., Nov 18 2008. Glacier, fjord, and seismic response to recent large calving events, jakobshavn isbræ, greenland. Geophys. Res. Lett. 35 (22), L22501.

Anderson, R. S., Molnar, P., Kessler, M. A., 2006. Features of glacial valley profiles simply explained. Journal of Geophysical Research 111 (F1), F01004.

Angermann, D., Klotz, J., Reigber, C., Sep 1999. Space-geodetic estimation of the nazca-south america euler vector. Earth and Planetary Science Letters 171 (3), 329–334.

Bangs, N. L., Brown, K. M., 1995. 19. regional heat flow in the vicinity of the chile triple junction constrained by the depth of the bottom-simulating reflection. In: Lewis, S. D., Behrmann, J. H., Musgrave, R. J., Cande, S. C. (Eds.), Proceedings of the Ocean Drilling Program, Scientific ResultS. Vol. 141 of Proceedings of the Ocean Drilling Program, Scientific Results.

Barbarand, J., Hurford, T., Carter, A., 2003. Variation in apatite fission-track length measurement: implications for thermal history modelling. Chemical Geology 198 (1), 77–106.

Blisniuk, P. M., Stern, L. A., Chamberlain, C. P., Idleman, B., Zeitler, P. K., 2005. Climatic and ecologic changes during miocene surface uplift in the southern patagonian andes. Earth and Planetary Science Letters 230 (1-2), 125–142, times Cited: 34.

Blisniuk, P. M., Stern, L. A., Chamberlain, C. P., Zeitler, P. K., Ramos, V. A., Sobel, E. R., Haschke, M., Strecker, M. R., Warkus, F., 2006. Links between mountain uplift, climate, and surface processes in the southern patagonian andes. In: The Andes. Springer, pp. 429–440.

Bourgois, J., Martin, H., Lagabrielle, Y., Le Moigne, J., Jara, J. F., Aug 01 1996. Subduction erosion related to spreading-ridge subduction: Taitao peninsula (chile margin triple junction area). Geology 24 (8), 723–726.

Boutonnet, E., Arnaud, N., Guivel, C., Lagabrielle, Y., Scalabrino, B., Espinoza, F., 2010. Subduction of the south chile active spreading ridge: A 17 ma to 3 ma magmatic record in central patagonia (western edge of meseta del lago buenos aires, argentina). Journal of Volcanology and Geothermal Research 189 (3-4), 319–339.

Braun, J., Nov 28 2010. The many surface expressions of mantle dynamics. Nature Geoscience 3 (12), 825–833.

Braun, J., Robert, X., Simon-Labric, T., May 23 2013. Eroding dynamic topography. Geophys. Res. Lett. 40 (8), 1494–1499.

Breitsprecher, K., Thorkelson, D., Groome, W., Dostal, J., 2003. Geochemical confirmation of the kula-farallon slab window beneath the pacific northwest in eocene time. Geology 31 (4), 351–354.

Breitsprecher, K., Thorkelson, D. J., 2009. Neogene kinematic history of nazca-antarctic-phoenix slab windows beneath patagonia and the antarctic peninsula. Tectonophysics 464 (1-4), 10–20.

Brocard, G., Teyssier, C., Dunlap, W. J., Authemayou, C., Simon-Labric, T., Cacao Chiquín, E. N., Gutiérrez Orrego, A., Morán Ical, S., 2011. Reorganization of a deeply incised drainage: role of deformation, sedimentation and groundwater flow. Basin Research 23 (6), 631–651.

Brocklehurst, S. H., Whipple, K. X., 2004. Hypsometry of glaciated landscapes. Earth Surface Processes and Landforms 29 (7), 907–926.

Brown, M., 1998. Ridge-trench interactions and high-t-low-p metamorphism, with particular reference to the cretaceous evolution of the japanese islands. Geological Society, London, Special Publications 138 (1), 137–169.

Brozoviç, N., Burbank, D. W., Meigs, A. J., 1997. Climatic limits on landscape development in the northwestern himalaya. Science 276 (5312), 571–574.

Buiter, S. J., Govers, R., Wortel, M., 2002. Two-dimensional simulations of surface deformation caused by slab detachment. Tectonophysics 354 (3), 195–210.

Burkett, E. R., Billen, M. I., 2010. Three-dimensionality of slab detachment due to ridge-trench collision: Laterally simultaneous boudinage versus tear propagation. Geochemistry, Geophysics, Geosystems 11 (11).

Burtner, R. L., Nigrini, A., Donelick, R. A., 1994. Thermochronology of lower cretaceous source rocks in the idaho-wyoming thrust belt. AAPG bulletin 78 (10), 1613–1636.

Cande, S. C., Leslie, R. B., Jan 10 1986. Late cenozoic tectonics of the southern chile trench. Journal of Geophysical Research-Solid Earth and Planets 91 (B1), 471–496, times Cited: 226.

Cande, S. C., Leslie, R. B., Parra, J. C., Hobart, M., 1987. Interaction between the chile ridge and chile trench: Geophysical and geothermal evidence. Journal of Geophysical Research: Solid Earth (1978–2012) 92 (B1), 495–520.

Carlson, W. D., Donelick, R. A., Ketcham, R. A., 1999. Variability of apatite fission-track annealing kinetics: I. experimental results. American mineralogist 84 (9), 1213–1223.

Cembrano, J., Herve, F., Lavenu, A., 1996. The liquine ofqui fault zone; a long-lived intra-arc fault system in southern chile. Tectonophysics 259, 55–66, second international symposium on Andean geodynamics, Oxford, United Kingdom, Sept. 21-23, 1993 References: 53; illus. incl. geol. sketch maps English 19960630.

Cembrano, J., Hervé, F., 1993. The liquine ofqui fault zone : a major cenozoic strike slip duplex in the southern andes. In: ISAG. ORSTOM Editions, Paris, Oxford, U.K., pp. 175–178.

Cembrano, J., Lavenu, A., Reynolds, P., Arancibia, G., Lopez, G., Sanhueza, A., 2002. Late cenozoic transpressional ductile deformation north of the nazca–south america–antarctica triple junction. Tectonophysics 354, 289–314.

Centro de Estudios Cientificos, 2012. Variaciones recientes de glaciares en respuesta al cambio climático: Características glaciológicas de los glaciares san rafael, nef y colonia, campo de hielo norte. Tech. rep., República De Chile Ministerio De Obras Públicas Dirección General De Aguas Unidad De Glaciología Y Nieves.
URL `http://documentos.dga.cl/GLA5500.pdf`

Clark, P. U., Archer, D., Pollard, D., Blum, J. D., Rial, J. A., Brovkin, V., Mix, A. C., Pisias, N. G., Roy, M., 2006. The middle pleistocene transition: characteristics, mechanisms, and implications for long-term changes in atmospheric pco2. Quaternary Science Reviews 25 (23-24), 3150–3184.

Cloos, M., 1993. Lithospheric buoyancy and collisional orogenesis: Subduction of oceanic plateaus, continental margins, island arcs, spreading ridges, and seamounts. Geological Society of America Bulletin 105 (6), 715–737.

Cogné, N., Chew, D., Stuart, F. M., 2014. The thermal history of the western irish onshore. Journal of the Geological Society 171 (6), 779–792.

Cogné, N., Gallagher, K., Cobbold, P. R., 2012. Coupled inverse and forward modelling to assess the range of acceptable thermal histories, a case study from se brazil. In: EGU General Assembly Conference Abstracts. Vol. 14. p. 5860.

Collins, L. S., Coates, A. G., Jackson, J. B. C., Obando, J. A., 1995. Timing and rates of emergence of the limon and bocas del toro basins: Caribbean effects of cocos ridge subduction? In: Mann, P. (Ed.), Geologic and Tectonic Development of the Caribbean Plate Boundary in Southern Central America. Vol. 295. Geological Society of America Special Papers, Boulder, Colorado, U.S.

Coutand, I., Diraison, M., Cobbold, P. R., Gapais, D., Rossello, E. A., Miller, M., 1999. Structure and kinematics of a foothills transect, lago viedma, southern andes (49 30 s). Journal of South American Earth Sciences 12, 1–15.

Cuffey, K. M., Paterson, W., 2010. The Physics of Glaciers, 4th Edition. Butterworth-Heinemann, Elsevier.

Darwin, C., 1846. Geological observations on South America. Being the third part of the geology of the voyage of the Beagle, under the command of Capt. Fitzroy, R.N. during the years 1832 to 1836. Smith Elder and Co., London.

De la Cruz, R., Suarez, M., Belmar, M., Quiroz, D., Bell, M., 2003. Area Coihaique- Balmaceda, Regoin Aisen del General Carlos Ibañez del Campo, Carta Geologica de Chile, Serie Geología Basíca 80, escala :100 000. Servicio Nacional de Geologia y Mineria.

DeLong, S. E., Schwarz, W., Anderson, R. N., 1979. Thermal effects of ridge subduction. Earth and Planetary Science Letters 44 (2), 239–246.

DeMets, C., Gordon, R. G., Argus, D. F., May 01 2010. Geologically current plate motions. Geophysical Journal International 181 (1), 1–80.

Dickinson, W. R., Snyder, W. S., 1979. Geometry of subducted slabs related to san andreas transform. The Journal of Geology, 609–627.

Dietrich, R., Ivins, E., Casassa, G., Lange, H., Wendt, J., Fritsche, M., 2010. Rapid crustal uplift in patagonia due to enhanced ice loss. Earth and Planetary Science Letters 289 (1), 22–29.

Donelick, R. A., Ketcham, R. A., Carlson, W. D., 1999. Variability of apatite fission-track annealing kinetics: Ii. crystallographic orientation effects. American Mineralogist 84 (9), 1224–1234.

Donelick, R. A., OSullivan, P. B., Ketcham, R. A., 2005. Apatite fission-track analysis. Reviews in Mineralogy and Geochemistry 58 (1), 49–94.

Dunkl, I., 2002. Trackkey: a windows program for calculation and graphical presentation of fission track data. Computers & Geosciences 28 (1), 3–12.

Egholm, D. L., Nielsen, S. B., Pedersen, V. K., Lesemann, J. E., 2009. Glacial effects limiting mountain height. Nature 460 (7257), 884–U120.

Ehlers, T. A., Farley, K. A., Jan 30 2003. Apatite (u-th)/he thermochronometry: methods and applications to problems in tectonic and surface processes. Earth and Planetary Science Letters 206 (1-2), 1–14.

Ehlers, T. A., Farley, K. A., Rusmore, M. E., Woodsworth, G. J., 2006. Apatite (u-th)/he signal of large-magnitude accelerated glacial erosion, southwest british columbia. Geology 34 (9), 765–768, times Cited: 16.

Ekström, G., Nettles, M., Abers, G. A., Oct 23 2003. Glacial earthquakes. Science 302 (5645), 622–624.

Escobar, F., 1992. Water balance in the patagonia icefield. In: Naruse, R., Aniya, M. (Eds.), Glaciological Researches in Patagonia. Japanese Society of Snow and Ice, pp. 109–119.

Espinoza, F., Morata, D., Pelleter, E., Maury, R. C., Suárez, M., Lagabrielle, Y., Polvé, M., Bellon, H., Cotten, J., De la Cruz, R., Guivel, C., Jul 2005. Petrogenesis of the eocene and mio–pliocene alkaline basaltic magmatism in meseta chile chico, southern patagonia, chile: Evidence for the participation of two slab windows. Lithos 82 (3-4), 315–343.

Espinoza, F., Morata, D., Polve, M., Lagabrielle, Y., Maury, R., de la Rupelle, A., Guivel, C., Cotten, J., Bellon, H., Suarez, M., 2010. Middle miocene calc-alkaline volcanism in central patagonia (47°s): petrogenesis and implications for slab dynamics. Andean Geology 37 (2), 300–328.

Espinoza, F., Morata, D., Polvé, M., Lagabrielle, Y., Maury, R. C., Guivel, C., Cotten, J., Bellon, H., Suárez, M., 2008. Bimodal back-arc alkaline magmatism after ridge subduction: Pliocene felsic rocks from central patagonia (47 s). Lithos 101 (3), 191–217.

Faccenna, C., Becker, T. W., Miller, M. S., Serpelloni, E., Willet, S. D., 2014. Isostasy, dynamic topography, and the elevation of the apennines of italy. Earth and Planetary Science Letters 407, 163–174.

Farley, K., Wolf, R., Silver, L., 1996. The effects of long alpha-stopping distances on (u-th)/he ages. Geochimica et Cosmochimica Acta 60 (21), 4223–4229.

Farley, K. A., 2000. Helium diffusion from apatite: General behavior as illustrated by durango fluorapatite. Journal of Geophysical Research: Solid Earth (1978–2012) 105 (B2), 2903–2914.

Flowers, R. M., Ketcham, R. A., Shuster, D. L., Farley, K. A., 2009. Apatite (u–th)/he thermochronometry using a radiation damage accumulation and annealing model. Geochimica et Cosmochimica Acta 73 (8), 2347–2365.

Forsythe, R., Nelson, E., 1985 1985. Geological manifestation of ridge collision - evidence from the golfo de penas-taitao basin, southern chile. Tectonics 4 (5), 477–495, times Cited: 112.

Forsythe, R. D., Nelson, E. P., Carr, M. J., Kaeding, M. E., Herve, M., Mpodozis, C., Soffia, J. M., Harambour, S., Jan 1986. Pliocene near-trench magmatism in southern chile - a possible manifestation of ridge collision. Geology 14, 23–27, times Cited: 100.

Fosdick, J. C., Grove, M., Hourigan, J. K., Calderon, M., Jan 2013. Retroarc deformation and exhumation near the end of the andes, southern patagonia. Earth and Planetary Science Letters 361, 504–517.

Funiciello, F., Faccenna, C., Giardini, D., 2004. Role of lateral mantle flow in the evolution of subduction systems: insights from laboratory experiments. Geophysical Journal International 157 (3), 1393–1406.

Funiciello, F., Moroni, M., Piromallo, C., Faccenna, C., Cenedese, A., Bui, H. A., 2006. Mapping mantle flow during retreating subduction: Laboratory models analyzed by feature tracking. Journal of Geophysical Research: Solid Earth 111 (B3).

Gallagher, K., 2012. Transdimensional inverse thermal history modeling for quantitative thermochronology. Journal of Geophysical Research: Solid Earth 117 (B2).

Gallagher, K., 2016. Comment on'a reporting protocol for thermochronologic modeling illustrated with data from the grand canyon'by flowers, farley and ketcham. Earth and Planetary Science Letters 441, 211–212.

Gallagher, K., Brown, R., Johnson, C., 1998. Fission track analysis and its applications to geological problems. Annual Review of Earth and Planetary Sciences 26 (1), 519–572.

Gallagher, K., Charvin, K., Nielsen, S., Sambridge, M., Stephenson, J., 2009. Markov chain monte carlo (mcmc) sampling methods to determine optimal models, model resolution and model choice for earth science problems. Marine and Petroleum Geology 26 (4), 525–535.

Gardner, T. W., Verdonck, D., Pinter, N. M., Slingerland, R., Furlong, K. P., Bullard, T. F., Wells, S. G., 1992. Quaternary uplift astride the aseismic cocos ridge, pacific coast, costa rica. Geological Society of America Bulletin 104 (2), 219–232.

Gautheron, C., Tassan-Got, L., Barbarand, J., Pagel, M., Aug 30 2009. Effect of alpha-damage annealing on apatite (u–th)/he thermochronology. Chemical Geology 266 (3-4), 157–170.

Georgieva, V., Melnick, D., Schildgen, T. F., Ehlers, T. A., Lagabrielle, Y., Enkelmann, E., Strecker, M. R., 2016. Tectonic control on rock uplift, exhumation and topography above an oceanic-ridge collision – southern patagonian andes (47°s), chile. Tectonics, n/a–n/a2016TC004120.

Gleadow, A., 1981. Fission-track dating methods: what are the real alternatives? Nuclear Tracks 5 (1), 3–14.

Gleadow, A., Duddy, I., Green, P. F., Lovering, J., 1986. Confined fission track lengths in apatite: a diagnostic tool for thermal history analysis. Contributions to Mineralogy and Petrology 94 (4), 405–415.

Glodny, J., Gräfe, K., Echtler, H., Rosenau, M., Jul 16 2008. Mesozoic to quaternary continental margin dynamics in south-central chile (36–42°s): the apatite and zircon fission track perspective. International Journal of Earth Sciences 97, 1271–1291.

Glotzbach, C., Van Der Beek, P. A., Spiegel, C., 2011. Episodic exhumation and relief growth in the mont blanc massif, western alps from numerical modelling of thermochronology data. Earth and Planetary Science Letters 304 (3), 417–430.

Gorring, M., Singer, B., Gowers, J., Kay, S. M., 2003. Plio–pleistocene basalts from the meseta del lago buenos aires, argentina: evidence for asthenosphere–lithosphere interactions during slab window magmatism. Chemical Geology 193 (3), 215–235.

Gorring, M. L., Kay, S. M., 2001. Mantle processes and sources of neogene slab window magmas from southern patagonia, argentina. Journal of Petrology 42 (6), 1067–1094.

Gorring, M. L., Kay, S. M., Zeitler, P. K., Ramos, V. A., Rubiolo, D., Fernandez, M. I., Panza, J. L., Feb 1997. Neogene patagonian plateau lavas: Continental magmas associated with ridge collision at the chile triple junction. Tectonics 16 (1), 1–17.

Green, P., Duddy, I., Gleadow, A., Tingate, P., Laslett, G., 1986. Thermal annealing of fission tracks in apatite: 1. a qualitative description. Chemical Geology: Isotope Geoscience section 59, 237–253.

Green, P., Durrani, S., 1977. Annealing studies of tracks in crystals. Nuclear Track Detection 1 (1), 33–39.

Green, P. J., 2003. Trans-dimensional markov chain monte carlo. Oxford Statistical Science Series, 179–198.

Groome, W. G., Thorkelson, D. J., 2009. The three-dimensional thermo-mechanical signature of ridge subduction and slab window migration. Tectonophysics 464 (1-4), 70–83.

Groome, W. G., Thorkelson, D. J., Friedman, R. M., Mortensen, J. K., Massey, N. W., Marshall, D. D., Layer, P. W., 2003. Magmatic and tectonic history of the leech river complex, vancouver island, british columbia: Evidence for ridge-trench intersection and accretion of the crescent terrane. Special Papers-Geological Society of America, 327–354.

Gräfe, K., Frisch, W., Villa, I. M., Meschede, M., 4/29/ 2002. Geodynamic evolution of southern costa rica related to low-angle subduction of the cocos ridge: constraints from thermochronology. Tectonophysics 348 (4), 187–204.

Guenthner, W. R., Barbeau, D. L., Reiners, P. W., Thomson, S. N., 2010. Slab window migration and terrane accretion preserved by low-temperature thermochronology of a magmatic arc, northern antarctic peninsula. Geochemistry Geophysics Geosystems 11 (3), times Cited: 0.

Guillaume, B., Gautheron, C., Simon-Labric, T., Martinod, J., Roddaz, M., Douville, E., Mar 2013. Dynamic topography control on patagonian relief evolution as inferred from low temperature thermochronology. Earth and Planetary Science Letters 364, 157–167.

Guillaume, B., Martinod, J., Husson, L., Roddaz, M., Riquelme, R., 2009. Neogene uplift of central eastern patagonia: Dynamic response to active spreading ridge subduction? Tectonics 28 (TC2009).

Guillaume, B., Moroni, M., Funiciello, F., Martinod, J., Faccenna, C., Dec 13 2010. Mantle flow and dynamic topography associated with slab window opening: Insights from laboratory models. Tectonophysics 496 (1-4), 83–98, times Cited: 2.

Guivel, C., Morata, D., Pelleter, E., Espinoza, F., Maury, R. C., Lagabrielle, Y., Polve, M., Bellon, H., Cotten, J., Benoit, M., Suarez, M., de la Cruz, R., 2006. Miocene to late quaternary patagonian basalts (46-47 degrees s): Geochronometric and geochemical evidence for slab tearing due to active spreading ridge subduction. Journal of Volcanology and Geothermal Research 149 (3-4), 346–370.

Gutscher, M.-A., Malavieille, J., Lallemand, S., Collot, J.-Y., 1999. Tectonic segmentation of the north andean margin: impact of the carnegie ridge collision. Earth and Planetary Science Letters 168 (3), 255–270.

Haeussler, P. J., Bradley, D., Goldfarb, R., Snee, L., Taylor, C., 1995. Link between ridge subduction and gold mineralization in southern alaska. Geology 23 (11), 995–998.

Haeussler, P. J., Bradley, D. C., Goldfarb, R. J., 2003. Brittle deformation along the gulf of alaska margin in response to paleocene-eocene triple junction migration. Special Papers-Geological Society of America, 119–140.

Hager, B. H., Clayton, R. W., Richards, M. A., Comer, R. P., 1985. Lower mantle heterogeneity, dynamic topography and the geoid. Nature 313, 541–545.

Hallet, B., 1979. A theoretical model of glacial abrasion. Journal of Glaciology 23 (89), 39–50.

Hamza, V. M., Muñoz, M., 1996. Heat flow map of south america. Geothermics 25 (6), 599–646.

Harrison, S., Glasser, N. F., Winchester, V., Haresign, E., Warren, C., Duller, G. A. T., Bailey, R., Ivy-Ochs, S., Jansson, K., Kubik, P., Jun 2008. Glaciar leon, chilean patagonia: late-holocene chronology and geomorphology. Holocene 18 (4), 643–652.
URL <GotoISI>://WOS:000256882300012

Haschke, M., Sobel, E. R., Blisniuk, P., Strecker, M. R., Warkus, F., 2006. Continental response to active ridge subduction. Geophysical Research Letters 33 (L15315).

Haug, G. H., Sigman, D. M., Tiedemann, R., Pedersen, T. F., Sarnthein, M., 1999. Onset of permanent stratification in the subarctic pacific ocean. Nature 401 (6755), 779–782.

Hein, A. S., Hulton, N. R. J., Dunai, T. J., Schnabel, C., Kaplan, M. R., Naylor, M., Xu, S., Aug 30 2009. Middle pleistocene glaciation in patagonia dated by cosmogenic-nuclide measurements on outwash gravels. Earth and Planetary Science Letters 286 (1-2), 184–197, times Cited: 11.

Herman, F., Beyssac, O., Brughelli, M., Lane, S. N., Leprince, S., Adatte, T., Lin, J. Y. Y., Avouac, J.-P., Cox, S. C., Oct 9 2015. Erosion by an alpine glacier. Science 350 (6257), 193–195.

Herman, F., Brandon, M., 2015. Mid-latitude glacial erosion hotspot related to equatorial shifts in southern westerlies. Geology 43 (11), 987–990.

Herman, F., Seward, D., Valla, P. G., Carter, A., Kohn, B., Willett, S. D., Ehlers, T. A., 2013. Worldwide acceleration of mountain erosion under a cooling climate. Nature 504 (7480), 423–426.

Hernandez Moreno, C., Speranza, F., Di Chiara, A., 2014. Understanding kinematics of intraarc transcurrent deformation: Paleomagnetic evidence from the liquiñeofqui fault zone (chile, 38–41°s). Tectonics 33.

Herve, F., Aguirre, L., Sepulveda, V., Morata, D., Jul 1999. Contrasting geochemistry and metamorphism of pillow basalts in metamorphic complexes from aysen, s-chile. Journal of South American Earth Sciences 12 (4), 379–388.

Hervé, F., Pankhurst, R. J., Fanning, C. M., Calderon, M., Yaxley, G. M., Sep 2007. The south patagonian batholith: 150 my of granite magmatism on a plate margin. Lithos 97 (3-4), 373–394.

Hsu, J. T., 1992. Quaternary uplift of the peruvian coast related to the subduction of the nazca ridge: 13.5 to 15.6 degrees south latitude. Quaternary International 15/16, 87–97.

Hubbard, A., Hein, A. S., Kaplan, M. R., Hulton, N. R. J., Glasser, N., 2005. A modelling reconstruction of the last glacial maximum ice sheet and its deglaciation in the vicinity of the northern patagonian icefield, south america. Geografiska Annaler: Series A, Physical Geography 87 (2), 375–391.

Hudson, T., Plafker, G., 1982. Paleogene metamorphism of an accretionary flysch terrane, eastern gulf of alaska. Geological Society of America Bulletin 93 (12), 1280–1290.

Hulton, N., Purves, R. S., Bentley, M. J., Hulton, N., Purves, R. S., Bentley, M. J., 2002. The last glacial maximum and deglaciation in southern south america. Quaternary Science Reviews 21 (1), 233–241, 10.1016/S0277-3791(01)00103-2.

Humphrey, N. F., Raymond, C. F., 1994. Hydrology, erosion and sediment production in a surging glacier: Variegated glacier, alaska, 1982-83. Journal of Glaciology.

Hurford, A. J., Green, P. F., 1983. The zeta age calibration of fission-track dating. Chemical Geology 41, 285–317.

Husson, L., 2006. Dynamic topography above retreating subduction zones. Geology 34 (9), 741–744.

Hynes, A., 2005. Buoyancy of the oceanic lithosphere and subduction initiation. International Geology Review 47 (9), 938–951.

Iverson, N. R., 2012. A theory of glacial quarrying for landscape evolution models. Geology 40 (8), 679–682.

Ivins, E. R., James, T. S., 1999. Simple models for late holocene and present-day patagonian glacier fluctuations and predictions of a geodetically detectable isostatic response. Geophysical Journal International 138 (3), 601–624.

Jeandet, L., June 4, 2014 2014. Assessing dynamic topography from river characteristics in patagonia forelands. Master, Université Joseph Fourier, Grenoble.

Jessop, A., 1990. Developments in solid earth geophysics.

Johnston, S. T., Thorkelson, D. J., 1997. Cocos-nazca slab window beneath central america. Earth and Planetary Science Letters 146 (3), 465–474.

Kaplan, M. R., Douglass, D. C., Singer, B. S., Caffee, M. W., 2005. Cosmogenic nuclide chronology of pre-last glacial maximum moraines at lago buenos aires, 46 degrees s, argentina. Quaternary Research 63 (3), 301–315, times Cited: 37.

Kay, S. M., Ramos, V. A., Marquez, M., Nov 1993. Evidence in cerro pampa volcanic rocks for slab melting prior to ridge-trench collision in southern south america. Journal of Geology 101 (6), 703–714, times Cited: 245.

Kendrick, E., Bevis, M., Smalley Jr., R., Brooks, B., Vargas, R. B., Lauria, E., Fortes, L. P. S., Jul 2003. The nazca–south america euler vector and its rate of change. Journal of South American Earth Sciences 16 (2), 125–131.

Ketcham, R. A., 2005a. Forward and inverse modeling of low-temperature thermochronometry data. Reviews in mineralogy and geochemistry 58 (1), 275–314.

Ketcham, R. A., 2005b. The role of crystallographic angle in characterizing and modeling apatite fission-track length data. Radiation measurements 39 (6), 595–601.

Ketcham, R. A., Carter, A., Donelick, R. A., Barbarand, J., Hurford, A. J., 2007a. Improved measurement of fission-track annealing in apatite using c-axis projection. American Mineralogist 92 (5-6), 789–798.

Ketcham, R. A., Carter, A., Donelick, R. A., Barbarand, J., Hurford, A. J., 2007b. Improved modeling of fission-track annealing in apatite. American Mineralogist 92 (5-6), 799–810.

Ketcham, R. A., Donelick, R. A., Balestrieri, M. L., Zattin, M., 2009. Reproducibility of apatite fission-track length data and thermal history reconstruction. Earth and Planetary Science Letters 284 (3), 504–515.

Ketcham, R. A., Donelick, R. A., Carlson, W. D., 1999. Variability of apatite fission-track annealing kinetics: Iii. extrapolation to geological time scales. American Mineralogist 84 (9), 1235–1255.

Ketcham, R. A., Donelick, R. A., Donelick, M. B., 2000. Aftsolve: A program for multi-kinetic modeling of apatite fission-track data. Geological Materials Research 2 (1), 1–32.

LaFemina, P., Dixon, T. H., Govers, R., 2009. Forearc motion and cocos ridge collision in central america. Geochemistry, Geophysics, Geosystems 10 (5).

Lagabrielle, Y., Guivel, C., Maury, R. C., Bourgois, J., 2000. Magmatic–tectonic effects of high thermal regime at the site of active ridge subduction: the chile triple junction model. Tectonophysics 326 (3-4), 255–268.

Lagabrielle, Y., Le Moigne, J., Maury, R., Cotten, J., Bourgois, J., 1994. Volcanic record of the subduction of an active spreading ridge, taitao peninsula (southern chile). Geology 22 (6), 515–518.

Lagabrielle, Y., Scalabrino, B., Suarez, M., Ritz, J. F., 2010. Mio-pliocene glaciations of central patagonia: New evidence and tectonic implications. Andean Geology 37 (2), 276–299.

Lagabrielle, Y., Suarez, M., Malavieille, J., Morata, D., Espinoza, F., Maury, R. C., Scalabrino, B., Barbero, L., de la Cruz, R., Rossello, E., Bellon, H., 2007. Pliocene extensional tectonics in the eastern central patagonian cordillera: geochronological constraints and new field evidence. Terra Nova 19, 413–424.

Lagabrielle, Y., Suarez, M., Rossello, E. A., Herail, G., Martinod, J., Regnier, M., de la Cruz, R., 2004. Neogene to quaternary tectonic evolution of the patagonian andes at the latitude of the chile triple junction. Tectonophysics 385 (1-4), 211–241.

Lange, D., Cembrano, J., Rietbrock, A., Haberland, C., Dahm, T., Bataille, K., Jul 18 2008. First seismic record for intra-arc strike-slip tectonics along the liquine-ofqui fault zone at the obliquely convergent plate margin of the southern andes. Tectonophysics 455 (1-4), 14–24.

Laslett, G., Gleadow, A., Duddy, I., 1984. The relationship between fission track length and track density in apatite. Nuclear Tracks and Radiation Measurements (1982) 9 (1), 29–38.

Lindvall, S. C., Rockwell, T. K., Hudnut, K. W., Apr 1989. Evidence for prehistoric earthquakes on the superstition hills fault from offset geomorphic features. Bulletin of the Seismological Society of America 79 (2), 342–361.

MacGregor, K. R., Anderson, R. S., Waddington, E. D., 2009. Numerical modeling of glacial erosion and headwall processes in alpine valleys. Geomorphology.

Maeda, J., Kagami, H., 1996. Interaction of a spreading ridge and an accretionary prism: Implications from morb magmatism in the hidaka magmatic zone, hokkaido, japan. Geology 24 (1), 31–34.

Maksymowicz, A., Contreras-Reyes, E., Grevemeyer, I., Flueh, E. R., Sep 2012. Structure and geodynamics of the post-collision zone between the nazca–antarctic spreading center and south america. Earth and Planetary Science Letters 345-348, 27–37.

Malagnino, E., 1995. The discovery of the oldest extra-andean glaciation in lago buenos aires basin, argentina. In: Rabassa, J., Salemme, M. (Eds.), Quaternary of South America and Antarctic Península. Balkema, Rotterdam, pp. 69–83.

Manaker, D. M., Calais, E., Freed, A. M., Ali, S. T., Przybylski, P., Mattioli, G., Jansma, P., Prépetit, C., de Chabalier, J. B., Sep 01 2008. Interseismic plate coupling and strain partitioning in the northeastern caribbean. Geophysical Journal International 174 (3), 889–903.

Mancktelow, N., Grasemann, B., Mar 15 1997 1997. Time-dependent effects of heat advection and topography on cooling histories during erosion. Tectonophysics 270 (3-4), 167–195.

Margirier, A., Robert, X., Audin, L., Gautheron, C., Bernet, M., Hall, S., Simon-Labric, T., 2015. Slab flattening, magmatism, and surface uplift in the cordillera occidental (northern peru). Geology 43 (11), 1031–1034.

Melnick, D., Bookhagen, B., Strecker, M. R., 2009a. Segmentation of megathrust rupture zones from forearc deformation patterns over hundreds to millions of years, arauco peninsula, chile. Journal of Geophysical Research: Solid Earth 114 (B1), B01407.

Melnick, D., Charlet, F., Echtler, H., De Batist, M., Oct 4 2006. Incipient axial collapse of the main cordillera and strain partitioning gradient between the central and patagonian andes, lago laja, chile. Tectonics 25 (5).

Melnick, D., Georgieva, V., Lagabrielle, Y., Jara, Scalabrino, B., Leidich, J., 2009b. Neotectonics along the eastern flank of the north patagonian icefield, southern chile: Cachet and exploradores fault zones. In: XII Congreso Geológico Chileno, 22 - 26 de Noviembre 2009, Santiago, Chile.

Mercer, J. H., Sutter, J. F., 1982. Late miocene earliest pliocene glaciation in southern argentina - implications for global icesheet history. Palaeogeography Palaeoclimatology Palaeoecology 38 (3-4), 185–206.

Merritts, D., Bull, W. B., Nov. 1989. Interpreting Quaternary uplift rates at the Mendocino triple junction, northern California, from uplifted marine terraces. Geology 17 (11), 1020–1024.

Michaud, F., Witt, C., Royer, J.-Y., Jul 01 2009. Influence of the subduction of the carnegie volcanic ridge on ecuadorian geology: Reality and fiction. Geological Society of America Memoirs 204 (0), 217–228.

Miller, M., Bataille, K., Priestley, K., Iwamori, H., Calisto, I., Dec 01 2005. Seismic imaging of a subducted ridge, southern chile. In: AGU Fall Meeting. San Francisco, U.S., p. 0982.

Mitchell, S. G., Montgomery, D. R., 2006. Influence of a glacial buzzsaw on the height and morphology of the cascade range in central washington state, usa. Quaternary Research 65 (1), 96–107.

Mitrovica, J. X., Beaumont, C., Jarvis, G. T., 1989. Tilting of continental interiors by the dynamical effects of subduction. Tectonics 8 (5), 1079–1094.

Murdie, R., Pugh, D., Styles, P., 1999. A lightweight, portable, digital probe for measuring the thermal gradient in shallow water sediments, with examples from patagonia. Geo-Marine Letters 18 (4), 315–320.

Murdie, R. E., Prior, D. J., Styles, P., Flint, S. S., Pearce, R. G., Agar, S. M., Dec 01 1993. Seismic responses to ridge-transform subduction:chile triple junction. Geology 21 (12), 1095–1098.

Nelson, E., Forsythe, R., Arit, I., Jul 1994. Ridge collision tectonics in terrane development. Journal of South American Earth Sciences 7 (3-4), 271–278.

Osozawa, S., 1997. The cessation of igneous activity and uplift when an actively spreading ridge is subducted beneath an island arc. Island Arc 6 (4), 361–371.

Pankhurst, R. J., Herve, F., Rojas, L., Cembrano, J., Apr 30 1992. Magmatism and tectonics in continental chiloe, chile (42°-42°30's). Tectonophysics 205 (1-3), 283–294.

Pankhurst, R. J., Weaver, S. D., Herve, F., Larrondo, P., Jul 1999. Mesozoic-cenozoic evolution of the north patagonian batholith in aysen, southern chile. Journal of the Geological Society 156, 673–694.

Pardo-Casas, F., Molnar, P., 1987. Relative motion of the nazca (farallon) and south american plates since late cretaceous time. Tectonics 6 (3), 233–248.

Pedersen, V. K., Egholm, D., Nielsen, S., 2010. Alpine glacial topography and the rate of rock column uplift: a global perspective. Geomorphology 122 (1), 129–139.

Pedoja, K., Regard, V., Husson, L., Martinod, J., Guillaume, B., Fucks, E., Iglesias, M., Weill, P., May 15 2011. Uplift of quaternary shorelines in eastern patagonia: Darwin revisited. Geomorphology 127 (3-4), 121–142.

Piromallo, C., Becker, T., Funiciello, F., Faccenna, C., 2006. Three-dimensional instantaneous mantle flow induced by subduction. Geophysical Research Letters 33 (8).

Ramos, V. A., 1989. Andean foothills structures in northern magallanes basin, argentina. AAPG Bulletin 73 (7), 887–903.

Ramos, V. A., Apr 2005. Seismic ridge subduction and topography: Foreland deformation in the patagonian andes. Tectonophysics 399 (1-4), 73–86.

Ramos, V. A., Kay, S. M., Apr 1992. Southern patagonian plateau basalts and deformation - backarc testimony of ridge collisions. Tectonophysics 205 (1-3), 261–282.

Ravelo, A. C., Andreasen, D. H., Lyle, M., Lyle, A. O., Wara, M. W., 2004. Regional climate shifts caused by gradual global cooling in the pliocene epoch. Nature.

Reiners, P. W., Brandon, M. T., 2006. Using thermochronology to understand orogenic erosion. Annu. Rev. Earth Planet. Sci. 34, 419–466.

Ricard, Y., Richards, M. A., Lithgow-Bertelloni, C., Le Stunff, Y., 1993. A geodynamic model of mantle density heterogeneity. Journal of Geophysical Research: Solid Earth 98 (B12), 21895–21909.

Rivera, A., Benham, T., Casassa, G., Bamber, J., Dowdeswell, J. A., Oct 2007. Ice elevation and areal changes of glaciers from the northern patagonia icefield, chile. Global and Planetary Change 59 (1-4), 126–137.

Rivera, a., Zamora, R., Andres Uribe, J., Oberreuter, J., Gacitua, G., Rignot, E., 2014. Recent ice thickness helicopter borne radar surveys in patagonia. In: EGU General Assembly Conference Abstracts. Vol. 16. Vienna, Austria, p. 15392.

Rogers, R. D., Kárason, H., van der Hilst, R. D., 2002. Epeirogenic uplift above a detached slab in northern central america. Geology 30 (11), 1031.

Rosenau, M., Melnick, D., Echtler, H., 2006. Kinematic constraints on intra-arc shear and strain partitioning in the southern andes between 38 degrees s and 42 degrees s latitude. Tectonics 25 (TC4013).

Rosenbaum, G., Gasparon, M., Lucente, F. P., Peccerillo, A., Miller, M. S., 2008. Kinematics of slab tear faults during subduction segmentation and implications for italian magmatism. Tectonics 27 (2).

Russo, R. M., Gallego, A., Comte, D., Mocanu, V. I., Murdie, R. E., VanDecar, J. C., Aug 01 2010a. Source-side shear wave splitting and upper mantle flow in the chile ridge subduction region. Geololy 38, 707–710.

Russo, R. M., VanDecar, J. C., Comte, D., Mocanu, V. I., Gallego, A., Murdie, R. E., 2010b. Subduction of the chile ridge: Upper mantle structure and flow. GSA Today 20 (9), 4–10.

Sachse, V., Anka, Z., Littke, R., Rodriguez, J., Horsfield, B., di Primio, R., 2016. Burial, temperature and maturation history of the austral and western malvinas basins, southern argentina, based on 3d basin modelling. Journal of Petroleum Geology 39 (2), 169–191.

Sak, P. B., Fisher, D. M., Gardner, T. W., Marshall, J. S., LaFemina, P. C., 2009. Rough crust subduction, forearc kinematics, and quaternary uplift rates, costa rican segment of the middle american trench. Geological Society of America Bulletin 121 (7-8), 992–1012.

Sakaguchi, A., 1996. High paleogeothermal gradient with ridge subduction beneath the cretaceous shimanto accretionary prism, southwest japan. Geology 24 (9), 795–798.

Sambridge, M., Gallagher, K., Jackson, A., Rickwood, P., 2006. Trans-dimensional inverse problems, model comparison and the evidence. Geophysical Journal International 167 (2), 528–542.

Sánchez, A., Hervé, F., de Saint-Blanquat, M., 2008. Relations between plutonism in the back-arc region in southern patagonia and chile rise subduction: A geochronological review. In: International Symposium on Andean Geodynamics. pp. 485–488.

Scalabrino, B., Lagabrielle, Y., Malavieille, J., Dominguez, S., Melnick, D., Espinoza, F., Suarez, M., Rossello, E., 2010. A morphotectonic analysis of central patagonian cordillera: Negative inversion of the andean belt over a buried spreading center? Tectonics 29 (TC2010).

Scalabrino, B., Ritz, J.-F., Lagabrielle, Y., Apr 2011. Relief inversion triggered by subduction of an active spreading ridge: evidence from glacial morphology in central patagonia. Terra Nova 23 (2), 63–69.

Scholz, C. H., Small, C., Jul 01 1997. The effect of seamount subduction on seismic coupling. Geology 25 (6), 487–490.

Seifert, W., Rosenau, M., Echtler, H., May 2005. Crystallization depths of granitoids of south central chile estimated by al-in-hornblende geobarometry: implications for mass transfer processes along the active continental margin. Neues Jahrbuch Fur Geologie Und Palaontologie-Abhandlungen 236 (1-2), 115–127.

Shuster, D. L., Ehlers, T. A., Rusmore, M. E., Farley, K. A., 2005. Rapid glacial erosion at 1.8 ma revealed by he-4/he-3 thermochronometry. Science 310 (5754), 1668–1670.

Shuster, D. L., Flowers, R. M., Farley, K. A., Sep 30 2006. The influence of natural radiation damage on helium diffusion kinetics in apatite. Earth and Planetary Science Letters 249 (3-4), 148–161.

Sieh, K. E., Jahns, R. H., 1984 1984. Holocene activity of the san andreas fault at wallace creek , california. Geological Society of America Bulletin 95 (8), 883–896.

Simon, J. L., Perez-Cueva, A. J., Calvo-Cases, A., May 8 2013. Tectonic beheading of fluvial valleys in the maestrat grabens (eastern spain): Insights into slip rates of pleistocene extensional faults. Tectonophysics 593, 73–84.

Singer, B. S., Ackert, R. P., Guillou, H., 2004. Ar-40/ar-19 and k-ar chronology of pleistocene glaciations in patagonia. Geological Society of America Bulletin 116 (3-4), 434–450.

Sisson, V., Hollister, L., Onstott, T., 1989. Petrologic and age constraints on the origin of a low-pressure/high-temperature metamorphic complex, southern alaska. Journal of Geophysical Research: Solid Earth 94 (B4), 4392–4410.

Sisson, V., Pavlis, T. L., Roeske, S. M., Thorkelson, D., 2003a. Introduction: An overview of ridge-trench interactions in modern and ancient settings. Geological Society of America Special Paper 371.

Sisson, V. B., Pavlis, T. L., 1993. Geologic consequences of plate reorganization: An example from the eocene southern alaska fore arc. Geology 21 (10), 913–916.

Sisson, V. B., Poole, A. R., Harris, N. R., Burner, H. C., Pavlis, T. L., Copeland, P., Donelick, R. A., McLelland, W. C., 2003b. Geochemical and geochronologic constraints for genesis of a tonalite-trondhjemite suite and associated mafic intrusive rocks in the eastern chugach mountains, alaska: A record of ridge-transform subduction. Special Papers-Geological Society of America, 293–326.

Somoza, R., 1998. Updated nazca (farallon) - south america relative motions during the last 40 my: implications for mountain building in the central andean region. Journal of South American Earth Sciences 11 (3), 211–215.

Stern, C. R., Kilian, R., Apr 1996. Role of the subducted slab, mantle wedge and continental crust in the generation of adakites from the andean austral volcanic zone. Contributions to Mineralogy and Petrology 123 (3), 263–281.

Sternai, P., Herman, F., Fox, M. R., Castelltort, S., 2011. Hypsometric analysis to identify spatially variable glacial erosion. Journal of Geophysical Research: Solid Earth (1978–2012) 116 (F3), F03001.

Suárez, M., De la Cruz, R., 2001. Jurassic to miocene k–ar dates from eastern central patagonian cordillera plutons, chile(45°–48° s). Geological Magazine 138 (1), 53–66.

Suarez, M., de la Cruz, R., Bell, C. M., 2000. Timing and origin of deformation along the patagonian fold and thrust belt. Geological Magazine 137 (4), 345–353.

Suarez, M. De la Cruz, R. B. M., 2007. Geologia del Area Ñireguao-Baño Nuevo, Region Aisen del General Carlos Ibañez del Campo. Servicio Nacional de Geologia y Mineria, Carta Geologica de Chile, Serie Geologia Basica 1:100 000. Santiago de Chile.

Taylor, F. W., Frohlich, C., Lecolle, J., Strecker, M., May 10 1987. Analysis of partially emerged corals and reef terraces in the central vanuatu arc - comparison of contemporary coseismic and nonseismic with quaternary vertical movements. Journal of Geophysical Research-Solid Earth and Planets 92 (B6), 4905–4933.

Taylor, F. W., Mann, P., Bevis, M. G., Edwards, R. L., Cheng, H., Cutler, K. B., Gray, S. C., Burr, G. S., Beck, J. W., Phillips, D. A., Cabioch, G., Recy, J., 2005. Rapid forearc uplift and subsidence caused by impinging bathymetric features: Examples from the new hebrides and solomon arcs. Tectonics 24 (6).

Thomson, S. N., 2002. Late cenozoic geomorphic and tectonic evolution of the patagonian andes between latitudes 42 degrees s and 46 degrees s: An appraisal based on fission-track results from the transpressional intra-arc liquine-ofqui fault zone. Geological Society of America Bulletin 114 (9), 1159–1173.

Thomson, S. N., Brandon, M. T., Reiners, P. W., Tomkin, J. H., V · squez, C., Wilson, N. J., 2010. Glaciation as both destructive and constructive long-term control on mountain building. Nature 467, 313–317.

Thomson, S. N., Hervé, F., Stöckhert, B., 2001. Mesozoic-cenozoic denudation history of the patagonian andes (southern chile) and its correlation to different subduction processes. Tectonics 20 (5), 693–711.

Thorkelson, D. J., 1996. Subduction of diverging plates and the principles of slab window formation. Tectonophysics 255 (1-2), 47–63.

Thorkelson, D. J., Taylor, R. P., 1989. Cordilleran slab windows. Geology 17 (9), 833–836.

Tomkin, J. H., Roe, G. H., 2007. Climate and tectonic controls on glaciated critical-taper orogens. Earth and Planetary Science Letters 262 (3-4), 385–397.

Ton-That, T., Singer, B. S., Mörner, N. A., 1999. Datación de lavas basálticas por 40 ar/39 ar y geología glacial de la región del lago buenos aires, provincia de santa cruz, argentina. Revista de la Asociación Geologica Argentica 54 (4), 333–352.

Turcotte, D. L., Schubert, G., 2014. Geodynamics. Cambridge University Press.

Turner, K. J., Fogwill, C. J., McCulloch, R. D., 2005. Deglaciation of the eastern flank of the north patagonian icefied and associated continental-scale lake diversions. Geografiska Annaler: Series A, Physical Geography 87 (2), 363–374.

Underwood, M. B., Byrne, T., Hibbard, J., DiTullio, L., Laughland, M. M., 1993. The effects of ridge subduction on the thermal structure of accretionary prisms: a tertiary example from the shimanto belt of japan. Geological Society of America Special Papers 273, 151–168.

Valla, P. G., Beek, P. A., Shuster, D. L., Braun, J., Herman, F., Tassan-Got, L., Gautheron, C., 2012. Late neogene exhumation and relief development of the aar and aiguilles rouges massifs (swiss alps) from low-temperature thermochronology modeling and 4he/3he thermochronometry. Journal of Geophysical Research: Earth Surface 117 (F1).

Valla, P. G., Herman, F., Van Der Beek, P. A., Braun, J., 2010. Inversion of thermochronological age-elevation profiles to extract independent estimates of denudation and relief historyi: Theory and conceptual model. Earth and Planetary Science Letters 295 (3), 511–522.

Valla, P. G., Rahn, M., Shuster, D. L., van der Beek, P. A., 2016. Multi-phase late-neogene exhumation history of the aar massif, swiss central alps. Terra Nova.

Valla, P. G., Shuster, D. L., van der Beek, P. A., 2011a. Significant increase in relief of the european alps during mid-pleistocene glaciations. Nature Geoscience 4 (10), 688–692.

Valla, P. G., van der Beek, P. A., Braun, J., Jul 15 2011b. Rethinking low-temperature thermochronology data sampling strategies for quantification of denudation and relief histories: A case study in the french western alps. Earth and Planetary Science Letters 307 (3-4), 309–322.

Van Der Beek, P. A., Valla, P. G., Herman, F., Braun, J., Persano, C., Dobson, K. J., Labrin, E., 2010. Inversion of thermochronological age–elevation profiles to extract independent estimates of denudation and relief historyii: Application to the french western alps. Earth and Planetary Science Letters 296 (1), 9–22.

Vermeesch, P., Tian, Y., 2014. Thermal history modelling: Hefty vs. qtqt. Earth-Science Reviews 139, 279–290.

Wang, K., Hu, Y., Bevis, M., Kendrick, E., Smalley, R., Lauria, E., 2007. Crustal motion in the zone of the 1960 chile earthquake: Detangling earthquake-cycle deformation and forearc-sliver translation. Geochemistry Geophysics Geosystems 8 (10).

Warkus, F., 2002. Die neogene hebungsgeschichte der patagonischen anden im kontext der subduktion eines aktiven spreizungszentrum. Phd thesis, Institut für Geowissenschaften, Universität Potsdam.

Wenzens, G., 2006. Terminal moraines, outwash plains, and lake terraces in the vicinity of lago cardiel (49°s; patagonia, argentina)—evidence for miocene andean foreland glaciations. Arctic, Antarctic, and Alpine Research 38-2, 276–291.

West, M. E., Larsen, C. F., Truffer, M., O'Neel, S., LeBlanc, L., Apr 24 2010. Glacier microseismicity. Geology 38 (4), 319–322.

Whipple, K. X., Meade, B. J., 2006. Orogen response to changes in climatic and tectonic forcing. Earth and Planetary Science Letters.

Wildman, M., Brown, R., Beucher, R., Persano, C., Stuart, F., Gallagher, K., Schwanethal, J., Carter, A., 2016. The chronology and tectonic style of landscape evolution along the elevated atlantic continental margin of south africa resolved by joint apatite fission track and (u-th-sm)/he thermochronology. Tectonics.

Willett, S. D., Brandon, M. T., 2013. Some analytical methods for converting thermochronometric age to erosion rate. Geochemistry, Geophysics, Geosystems 14 (1), 209–222.

Witt, C., Bourgois, J., Michaud, F., Ordoñez, M., Jiménez, N., Sosson, M., 2006. Development of the gulf of guayaquil (ecuador) during the quaternary as an effect of the north andean block tectonic escape. Tectonics 25 (3).

Wolf, R., Farley, K., Kass, D., 1998. Modeling of the temperature sensitivity of the apatite (u–th)/he thermochronometer. Chemical Geology 148 (1), 105–114.

Wolf, R. A., Farley, K. A., Silver, L. T., Nov 1996 1996. Helium diffusion and low-temperature thermochronometry of apatite. Geochimica et Cosmochimica Acta 60 (21), 4231–4240.

Yanites, B. J., Ehlers, T. A., 2012. Global climate and tectonic controls on the denudation of glaciated mountains. Earth and Planetary Science Letters 325-326, 63–75.

Zandt, G., Humphreys, E., 2008. Toroidal mantle flow through the western U.S. slab window. Geology 36 (4), 295–4.

Appendix A

Supplementary Material for Chapter 3

A.1 Sample Preparation and Analytical Procedure for Apatite (U-Th)/He dating

The granitic bedrock samples (3 kg each) were prepared following standard mineral separation procedures (jaw crushing, sieving, magnetic separation, heavy liquids SPT and DI) for the extraction of apatite grains for (U-Th)/He (AHe) and fission track (AFT) dating. Most samples yielded good quality apatite grains (entire, clear, euhedral crystals with diameter > 70 micrometers), and almost half of them a sufficient quantity of for the preparation of mounts for fission track analysis (see A2 below).

For AHe dating clear apatite grains without inclusions or any other impurities or cracks were selected using a binocular microscope at the University of Tübingen and University of Potsdam. The grain dimensions were measured for the calculation of the alpha-correction factor after [Farley et al., 1996]. Single grains were packed in Nb-tubes for (U-Th)/He analysis. In general, we analysed 3-5 aliquots per sample. Helium was measured in the Patterson Helium-extraction line at the University of Tübingen, which is equipped with a 960 nm diode laser. Apatite grains were heated for 5 min at 11 A and zircon grains for 10 min at 20 A. Each grain was re-heated and analysed to make sure that the grain was degassed entirely in the first step. The re-extracts generally showed <1% of the first signal. After Helium analysis the grain packages were sent to the University of Arizona at Tucson for U and Th measurements using an ICP-MS. U, Th and Sm analysis for the following aliquots were performed at the University of Tübingen: *Ex0808-5, AG0808-5, LL04-4, LL04-6, CM03-4, CM03-5, 12VGEx11-1, 12VGEx11-2, 12VGEx11-3*.

Concentrations of U, Th and Sm for these aliquots were determined by isotope dilution using the Thermo Fisher iCAP ICP-MS at University Tübingen equipped with an all-PFA sample introduction system. Apatite samples together with the Nb-tubes were spiked with a calibrated mixed spike of ^{233}U + ^{230}Th + ^{149}Sm, and dissolved over night in 2 ml 5% HNO $_3$ + 0.1% HF at 65 °C. The grain mass of each sample was estimated from measured 43Ca concentrations assuming 39.4 wt-% Ca in apatite (497,664 ppm Zr in zircon).

For all aliquots the analytical error of the mass spectrometer measurements are generally very low and do not exceed 2%. In contrast, the reproducibility of the sample age constitutes a much larger error. We therefore report the mean U-Th/He age and the standard deviation of the measured aliquots as the sample error. For single grain ages we apply a 5% 2-sigma error based on the reproducibility of standard measurements in the lab. New apatite (U-Th/He) data from bedrock samples related to this study are presented in Figure A.1 below. All single-grain aliquot measurements are listed separately. Aliquots from the same sample are grouped following the naming convention SampleName-aliquot1, SampleName-aliquot2...etc. (e.g. *12VGEx11-1, 12VGEx11-2...*) and delimited by thicker lines. The samples marked grey were not included in the data interpretation due to lack of reproducibility between sample aliquots. The single aliquots marked grey were considered as outliers.

A.2 New Apatite (U-Th)/He Data

Figure A.1 – New Apatite (U-Th)/He Data

Sample	Lat	Lon	Elevation	4-He	U	232-Th	147-Sm	eU	ucorr. Age	Ft corr.	corr. Age	mean age	error
			(m)	(mol)	(ppm)	(ppm)	(ppm)		Ma		Ma	Ma	Ma
AG08_33_1	-47.00	-73.27	323	3.8E-15	39.51	61.78	43.27	54.03	**4.08**	**0.699**	**5.83**		
AG08_33_2	-47.00	-73.27	323	1.6E-14	82.52	317.16	167.88	157.05	**5.61**	**0.693**	**8.09**	**6.09**	**1.88**
AG08_33_3	-47.00	-73.27	323	2.8E-15	21.97	44.40	71.46	32.41	**3.21**	**0.735**	**4.36**		
AG08_08_1	-46.99	-73.12	231	1.0E-15	21.82	23.02	70.81	27.23	**4.83**	**0.621**	**7.76**		
AG08_08_2	-46.99	-73.12	231	3.9E-15	12.98	29.19	50.39	19.84	**12.64**	**0.684**	**18.48**		
AG08_08_3	-46.99	-73.12	231	1.2E-15	15.82	15.92	61.59	19.56	**5.94**	**0.650**	**9.14**		
AG08-08_4	-46.99	-73.12	231	1.8E-15	10.17	10.77	40.75	12.70	**7.75**	**0.706**	**10.98**		
AG08-08_5	-46.99	-73.12	231	9.4E-15	10.20	17.30	41.41	14.27	**12.19**	**0.787**	**15.49**		
AG08_18_1	-47.09	-73.24	1050	2.5E-15	34.14	18.03	49.43	38.38	**3.78**	**0.681**	**5.56**		
AG08_18_2	-47.09	-73.24	1050	4.9E-15	44.18	31.93	63.54	51.69	**4.56**	**0.709**	**6.42**	**5.92**	**0.45**
AG08_18_3	-47.09	-73.24	1050	2.1E-15	59.94	26.29	55.74	66.12	**3.64**	**0.629**	**5.78**		
AG08_13_1	-47.01	-73.28	1468	7.8E-16	11.84	44.86	67.62	22.38	**3.79**	**0.626**	**6.06**		
AG08_13_2	-47.01	-73.28	1468	2.5E-15	12.84	34.02	73.34	20.84	**5.81**	**0.711**	**8.17**	**6.83**	**1.16**
AG08_13_3	-47.01	-73.28	1468	1.0E-15	15.23	45.27	76.29	25.87	**3.97**	**0.634**	**6.26**		
AG08_13_4	-47.01	-73.28	1468	1.6E-15	16.49	53.72	69.25	29.11	**7.83**	**0.599**	**13.07**		
AG08_12_1	-47.02	-73.27	1219	1.6E-15	23.73	67.26	85.84	39.53	**4.00**	**0.641**	**6.24**		
AG08_12_2	-47.02	-73.27	1219	5.4E-15	44.95	154.35	154.85	81.23	**4.89**	**0.668**	**7.32**	**6.49**	**0.74**
AG08_12_3	-47.02	-73.27	1219	3.2E-15	34.18	95.31	106.71	56.57	**3.93**	**0.667**	**5.90**		
AG08_17_1	-47.10	-73.24	1382	3.1E-15	43.40	2.34	48.42	43.95	**5.63**	**0.672**	**8.38**		
AG08_17_2	-47.10	-73.24	1382	8.7E-15	75.95	4.72	47.18	77.06	**5.71**	**0.705**	**8.10**		
AG08_17_3	-47.10	-73.24	1382	5.0E-15	91.79	6.20	46.76	93.25	**5.08**	**0.657**	**7.72**	**8.07**	**0.27**
AG08_17_4	-47.10	-73.24	1382	1.2E-14	156.50	9.71	56.77	158.79	**5.58**	**0.691**	**8.08**		

Fig. A.1 New Apatite (U-Th)/He Data, cont.

Sample	Lat	Lon	Elevation	4-He	U	232-Th	147-Sm	eU	ucorr. Age	Ft corr.	corr. Age	mean age	error
			(m)	(mol)	(ppm)	(ppm)	(ppm)		Ma		Ma	Ma	Ma
AG08_10_1	-47.03	-73.23	579	2.5E-15	18.38	56.28	67.77	31.60	**3.38**	**0.721**	**4.68**		
AG08_10_2	-47.03	-73.23	579	1.4E-15	6.89	25.73	29.71	12.93	**4.11**	**0.723**	**5.68**	**5.25**	**0.51**
AG08_10_3	-47.03	-73.23	579	4.7E-16	7.91	17.67	33.09	12.06	**3.50**	**0.648**	**5.40**		
AG08-34_2	-46.98	-73.19	262	4.5E-15	95.15	95.64	68.74	117.62	**3.29**	**0.661**	**4.98**		
AG08-34_3	-46.98	-73.19	262	7.6E-16	41.48	33.96	46.26	49.46	**3.10**	**0.570**	**5.44**	**4.59**	**1.10**
AG08-34_4	-46.98	-73.19	262	8.5E-15	71.35	71.30	64.71	88.11	**2.56**	**0.765**	**3.34**		
LE08_02_1	-46.73	-73.04	283	1.7E-15	36.07	26.00	34.89	42.18	**2.74**	**0.689**	**3.98**		
LE08_02_2	-46.73	-73.04	283	2.2E-15	51.44	28.00	59.59	58.02	**3.39**	**0.660**	**5.13**	**4.33**	**0.70**
LE08_02_3	-46.73	-73.04	283	1.6E-15	33.43	31.03	41.36	40.72	**2.67**	**0.689**	**3.87**		
11-LL-03_1	-46.79	-73.22	995	4.1E-15	117.29	43.69	33.64	127.55	**2.81**	**0.668**	**4.21**		
11-LL-03_2	-46.79	-73.22	995	5.7E-15	142.75	41.14	28.56	152.42	**3.03**	**0.677**	**4.47**	**4.32**	**0.26**
11-LL-03_3	-46.79	-73.22	995	2.9E-15	108.12	31.41	39.00	115.50	**2.93**	**0.638**	**4.58**		
11-LL-03_4	-46.79	-73.22	995	3.9E-15	103.79	57.78	27.97	117.36	**2.66**	**0.665**	**4.00**		
11-LL-04_1	-46.79	-73.22	1197	1.6E-15	226.53	77.95	123.49	244.85	**0.63**	**0.657**	**0.95**		
11-LL-04_2	-46.79	-73.22	1197	1.6E-15	3.34	0.84	0.23	3.53	**29.38**	**0.694**	**42.26**		
11-LL-04_3	-46.79	-73.22	1197	2.2E-15	20.72	54.83	71.79	33.60	**3.05**	**0.713**	**4.27**		
11-LL-04_4	-46.79	-73.22	1197	9.8E-16	25.71	93.24	126.21	47.62	**2.61**	**0.603**	**4.33**	**4.87**	**0.99**
11-LL-04_6	-46.79	-73.22	1197	5.6E-16	5.70	6.37	12.62	7.20	**4.25**	**0.706**	**6.02**		
11-LL-05_1	-46.78	-73.22	722	1.2E-15	27.70	16.92	62.17	31.68	**2.09**	**0.709**	**2.95**		
11-LL-05_2	-46.78	-73.22	722	4.8E-15	24.98	21.17	46.51	29.96	**3.03**	**0.788**	**3.85**	**3.52**	**0.39**
11-LL-05_3	-46.78	-73.22	722	7.8E-16	33.17	20.02	77.57	37.88	**2.28**	**0.635**	**3.60**		
11-LL-05_4	-46.78	-73.22	722	1.6E-15	26.89	13.12	58.11	29.97	**2.64**	**0.717**	**3.68**		

Fig. A.1 New Apatite (U-Th)/He Data, cont.

Sample	Lat	Lon	Elevation	4-He	U	232-Th	147-Sm	eU	ucorr. Age	Ft corr.	corr. Age	mean age	error
			(m)	(mol)	(ppm)	(ppm)	(ppm)		Ma		Ma	Ma	Ma
11-LL-06_1	-46.74	-73.24	1351	2.6E-15	32.22	53.97	16.28	44.90	**2.95**	**0.712**	**4.15**		
11-LL-06_2	-46.74	-73.24	1351	2.4E-15	21.76	40.01	14.34	31.16	**2.92**	**0.734**	**3.98**	**3.95**	**0.40**
11-LL-06_3	-46.74	-73.24	1351	9.4E-16	24.29	34.17	11.26	32.32	**2.79**	**0.652**	**4.28**		
11-LL-06_4	-46.74	-73.24	1351	8.4E-16	23.22	27.76	9.18	29.74	**2.26**	**0.671**	**3.37**		
11-LL-07_1	-46.74	-73.23	1150	2.8E-15	6.47	15.90	17.40	10.21	**3.15**	**0.811**	**3.88**		
11-LL-07_2	-46.74	-73.23	1150	1.1E-15	9.06	14.46	16.16	12.46	**2.79**	**0.748**	**3.72**	**3.68**	**0.22**
11-LL-07_3	-46.74	-73.23	1150	1.7E-15	8.76	13.91	11.25	12.03	**2.71**	**0.787**	**3.45**		
11-LL-08_1	-46.74	-73.22	1005	1.8E-15	7.15	21.37	20.60	12.17	**2.64**	**0.783**	**3.37**		
11-LL-08_2	-46.74	-73.22	1005	1.1E-15	9.13	13.72	24.15	12.35	**2.03**	**0.770**	**2.64**		
11-LL-08_3	-46.74	-73.22	1005	9.9E-16	11.76	11.98	15.19	14.57	**1.31**	**0.785**	**1.68**	**2.76**	**0.80**
11-LL-08_4	-46.74	-73.22	1005	2.1E-15	7.99	15.84	24.63	11.71	**2.67**	**0.798**	**3.35**		
11-LL-09_1	-46.75	-73.21	562	3.5E-16	4.05	6.29	29.87	5.53	**1.82**	**0.755**	**2.41**		
11-LL-09_2	-46.75	-73.21	562	2.9E-16	4.81	30.64	20.99	12.01	**0.87**	**0.728**	**1.20**	**2.24**	**0.96**
11-LL-09_3	-46.75	-73.21	562	5.1E-16	8.49	9.04	26.60	10.61	**2.23**	**0.721**	**3.10**		
11-LL-10_1	-46.74	-73.14	327	1.6E-15	31.96	48.79	22.51	43.42	**2.03**	**0.705**	**2.88**		
11-LL-10_2	-46.74	-73.14	327	1.6E-15	29.21	48.35	17.55	40.57	**1.45**	**0.735**	**1.97**	**2.71**	**0.51**
11-LL-10_3	-46.74	-73.14	327	7.9E-16	39.78	54.63	19.94	52.62	**1.77**	**0.629**	**2.82**		
11-LL-10_4	-46.74	-73.14	327	1.4E-15	59.63	77.40	26.88	77.81	**1.99**	**0.630**	**3.16**		
12-CM-10_1	-46.76	-73.21	469	2.8E-16	5.81	7.36	21.25	7.54	**1.54**	**0.730**	**2.11**		
12-CM-10_2	-46.76	-73.21	469	8.0E-16	3.27	5.75	30.36	4.62	**2.63**	**0.798**	**3.29**	**2.45**	**0.73**
12-CM-10_3	-46.76	-73.21	469	6.1E-16	5.87	5.90	25.43	7.25	**1.55**	**0.789**	**1.96**		

Fig. A.1 New Apatite (U-Th)/He Data, cont.

Sample	Lat	Lon	Elevation	4-He	U	232-Th	147-Sm	eU	ucorr. Age	Ft corr.	corr. Age	mean age	error
			(m)	(mol)	(ppm)	(ppm)	(ppm)		Ma		Ma	Ma	Ma
12-CM-09_1	-46.75	-73.21	562	2.2E-16	4.92	6.76	23.60	6.51	**1.89**	**0.701**	**2.69**		
12-CM-09_2	-46.75	-73.21	562	4.3E-16	6.89	7.21	30.99	8.58	**1.44**	**0.759**	**1.90**	**2.01**	**0.64**
12-CM-09_3	-46.75	-73.21	562	5.4E-16	7.45	4.97	31.87	8.61	**1.14**	**0.791**	**1.44**		
12-CM-08_1	-46.74	-73.22	1016	4.2E-16	9.27	14.11	17.71	12.59	**1.63**	**0.714**	**2.28**		
12-CM-08_2	-46.74	-73.22	1016	9.1E-16	13.40	33.31	22.38	21.23	**2.29**	**0.702**	**3.27**	**2.79**	**0.49**
12-CM-08_3	-46.74	-73.22	1016	5.3E-16	8.28	13.59	12.27	11.47	**2.05**	**0.722**	**2.83**		
12-CM-07_1	-46.74	-73.24	1253	1.8E-15	36.48	115.76	24.63	63.69	**2.89**	**0.634**	**4.55**		
12-CM-07_2	-46.74	-73.24	1253	4.4E-15	33.07	108.77	19.82	58.63	**3.66**	**0.703**	**5.21**	**4.95**	**0.78**
12-CM-07_3	-46.74	-73.24	1253	2.3E-15	34.20	126.71	29.14	63.98	**3.75**	**0.634**	**5.91**		
12-CM-07_4	-46.74	-73.24	1253	2.3E-15	21.22	65.62	17.35	36.64	**2.92**	**0.710**	**4.11**		
12-CM-06_1	-46.74	-73.26	1434	3.4E-15	45.18	8.82	41.98	47.25	**4.25**	**0.707**	**6.00**		
12-CM-06_2	-46.74	-73.26	1434	1.7E-15	35.53	7.04	30.74	37.19	**3.00**	**0.689**	**4.36**	**5.29**	**0.68**
12-CM-06_3	-46.74	-73.26	1434	4.0E-15	50.88	22.48	30.21	56.16	**3.82**	**0.709**	**5.39**		
12-CM-06_4	-46.74	-73.26	1434	3.5E-15	37.03	11.61	37.87	39.75	**3.95**	**0.730**	**5.42**		
12-CM-05_1	-46.74	-73.27	1645	4.7E-16	46.94	34.26	57.00	54.99	**1.32**	**0.603**	**2.19**		
12-CM-05_2	-46.74	-73.27	1645	8.8E-16	20.13	46.59	61.28	31.08	**3.02**	**0.635**	**4.76**	**3.96**	**1.23**
12-CM-05_3	-46.74	-73.27	1645	4.0E-16	23.42	43.37	54.87	33.61	**2.33**	**0.566**	**4.12**		
12-CM-05_4	-46.74	-73.27	1645	8.5E-16	4.35	11.14	20.56	6.97	**3.58**	**0.748**	**4.79**		
12-CM-04_1	-46.74	-73.27	1843	1.2E-15	30.24	22.23	43.89	35.46	**2.25**	**0.686**	**3.28**		
12-CM-04_2	-46.74	-73.27	1843	1.4E-15	29.06	30.40	56.29	36.20	**3.52**	**0.662**	**5.32**	**4.51**	**1.08**
12-CM-04_3	-46.74	-73.27	1843	1.0E-15	24.27	29.23	28.11	31.14	**3.20**	**0.649**	**4.93**		

Fig. A.1 New Apatite (U-Th)/He Data, cont.

Sample	Lat	Lon	Elevation	4-He	U	232-Th	147-Sm	eU	ucorr. Age	Ft corr.	corr. Age	mean age	error
			(m)	(mol)	(ppm)	(ppm)	(ppm)		Ma		Ma	Ma	Ma
12-CM-03_1	-46.75	-73.29	2100	1.5E-15	34.47	97.92	149.01	57.48	**4.72**	**0.572**	**8.26**		
12-CM-03_2	-46.75	-73.29	2100	2.5E-15	35.11	62.48	99.62	49.79	**3.71**	**0.670**	**5.53**	**6.77**	**1.12**
12-CM-03_3	-46.75	-73.29	2100	6.3E-16	156.16	28.13	13.53	162.77	**0.27**	**0.693**	**0.39**		
12-CM-03_4	-46.75	-73.29	2100	1.1E-15	8.58	16.15	53.56	12.38	**4.68**	**0.705**	**6.64**		
12-CM-03_5	-46.75	-73.29	2100	2.9E-15	19.06	49.70	47.81	30.74	**4.70**	**0.706**	**6.66**		
AG08_31_1	-47.25	-73.20	316	2.6E-15	37.62	26.08	135.88	43.74	**4.52**	**0.671**	**6.74**		
AG08_31_2	-47.25	-73.20	316	1.2E-15	62.22	24.69	122.26	68.02	**3.22**	**0.578**	**5.57**	**6.60**	**0.97**
AG08_31_3	-47.25	-73.20	316	2.6E-15	62.30	19.03	97.82	66.77	**4.75**	**0.633**	**7.50**		
11-SM-13_1	-47.36	-73.08	879	1.3E-15	16.23	17.41	20.96	20.32	**3.48**	**0.705**	**4.94**		
11-SM-13_2	-47.36	-73.08	879	6.0E-16	9.02	4.83	21.25	10.15	**3.61**	**0.700**	**5.16**	**5.29**	**0.43**
11-SM-13_3	-47.36	-73.08	879	2.0E-15	12.38	10.10	20.57	14.75	**4.34**	**0.752**	**5.77**		
11-SM-13_4	-47.36	-73.08	879	1.6E-15	20.65	19.57	37.18	25.25	**6.38**	**0.640**	**9.97**		
11-SM-14_1	-47.36	-73.08	690	6.1E-16	19.91	25.15	44.04	25.82	**3.04**	**0.621**	**4.90**		
11-SM-14_2	-47.36	-73.08	690	5.4E-16	20.81	20.03	36.44	25.52	**3.46**	**0.593**	**5.82**	**5.35**	**0.46**
11-SM-14_3	-47.36	-73.08	690	4.1E-15	10.41	7.92	16.14	12.27	**4.34**	**0.813**	**5.34**		
12-Ex-11-1	-46.36	-73.31	35	1.3E-15	17.34	54.02	78.18	30.03	**2.61**	**0.677**	**3.85**		
12-Ex-11-2	-46.36	-73.31	35	2.7E-15	68.01	107.02	93.54	93.16	**2.61**	**0.653**	**3.99**	**4.16**	**0.42**
12-Ex-11-3	-46.36	-73.31	35	1.6E-15	21.47	77.54	81.27	39.69	**3.07**	**0.662**	**4.63**		
EX08_08_2	-46.51	-73.06	160	5.2E-15	27.01	103.26	191.37	51.27	**7.35**	**0.668**	**11.00**		
EX08_08_3	-46.51	-73.06	160	2.0E-15	11.28	51.19	131.18	23.31	**4.72**	**0.685**	**6.89**		
EX08_08_4	-46.51	-73.06	160	6.5E-16	25.99	27.61	77.10	32.48	**2.84**	**0.610**	**4.66**		
EX08_08_5	-46.51	-73.06	160	1.5E-15	9.78	52.87	126.27	22.20	**5.85**	**0.643**	**9.09**		

A.3 Additional Supplementary Material to Chapter 3

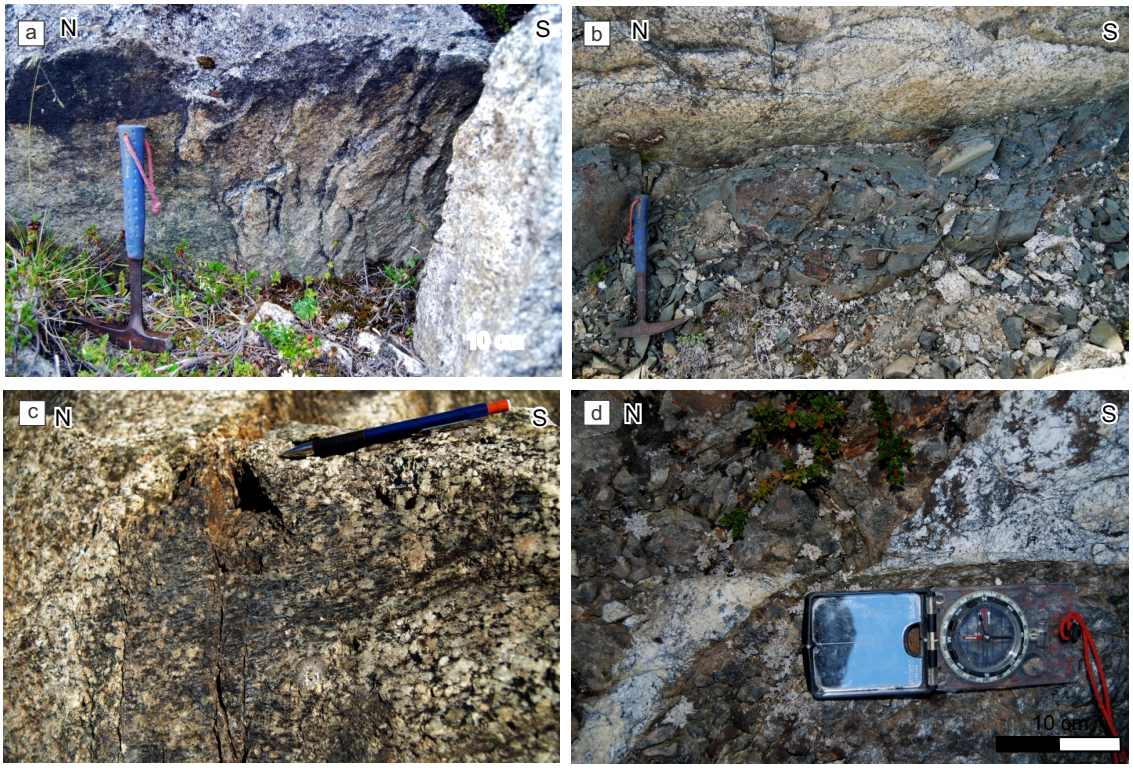

Figure A.2 – Cachet Fault field – field photographs. (A) and (B) N-S striking nearly vertical fault planes along the trace of the Cachet Fault. Subhorizontal lineation records right-lateral sense of shear. (C) Sub-horizontal lineation on nearly vertical N-S striking fault plane from (B) along the Cachet Fault. The orientation of the pencil is parallel to the lineation. (D) Right-lateral dm-scale offset of pegmatitic dyke along discreet fault plane associated with the Cachet Fault.

CACHET FAULT OFFSET MEASUREMENTS

	Distance along profile [km]	Mean offset [km]	Offset error [km]
Pared Norte/Sur MIN	4.3	10.0	4.2
Pared Norte/Sur MAX	4.3	16.6	3.3
Beheaded valley 3	26.4	5.7	1.6
Colonia	36.9	5.7	2.3
Beheaded valley 2	45.8	4.1	1.0
Nef	54.8	3.6	1.9
Beheaded valley 1	61.3	2.7	1.2

Figure A.3 – Cachet Fault - Offset measurements on displaced valleys.

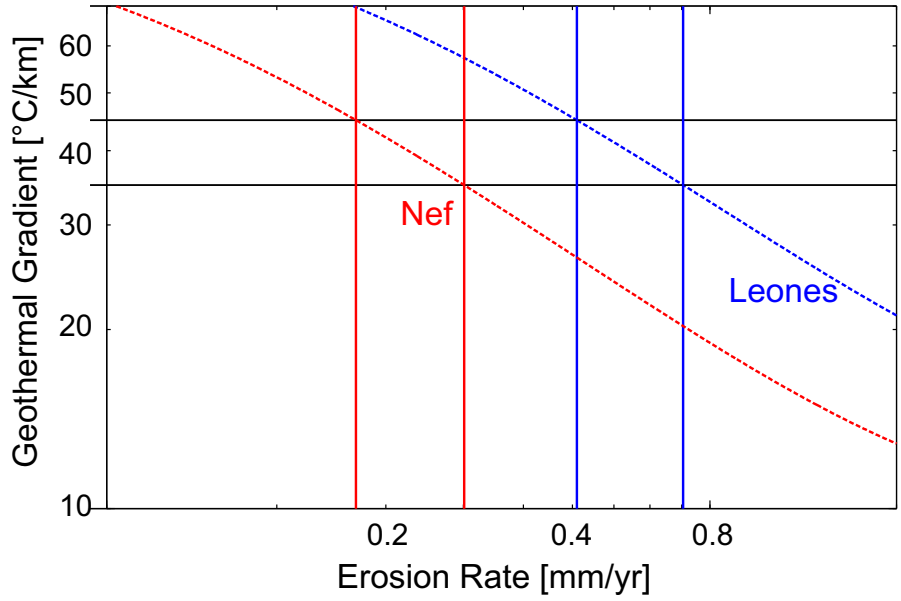

Figure A.4 – Parametric determination of erosion rate by plotting a thermochronometric age as a function of geothermal gradient and erosion rate using the MATLAB scrip AGE2EDOT from the study by Willett & Brandon (2013). A range of geothermal gradients between 35 and 45°C for the lowermost samples from both AERs located at 300 m elevation a.s.l. and AHe ages of 2 Ma for the Leones region and 4 Ma for the Nef region. See main text and attached MATLAB script for explanations and interpretation of results.

PARAMETERS USED IN CALCULATION OF EXHUMATION RATES USING AGE2EDOT

Activation energy for closure temperature	138 [kJ/mol]
Normalized frequency factor Ω	7.64E+07 [s^{-1}]
Closure temperature for apatite -(U-Th)/He for 15°C/Ma cooling rate	70 [°C]
Surfacetemperature at mean elevation	0 [°C]
Range of geothermal gradients	35 - 45 [°C/km]

Figure A.5 – Parameters used in calculation with AGE2EDOT (Farley, 2000; Groome & Thorkelson, 2009; Willett & Brandon, 2013)

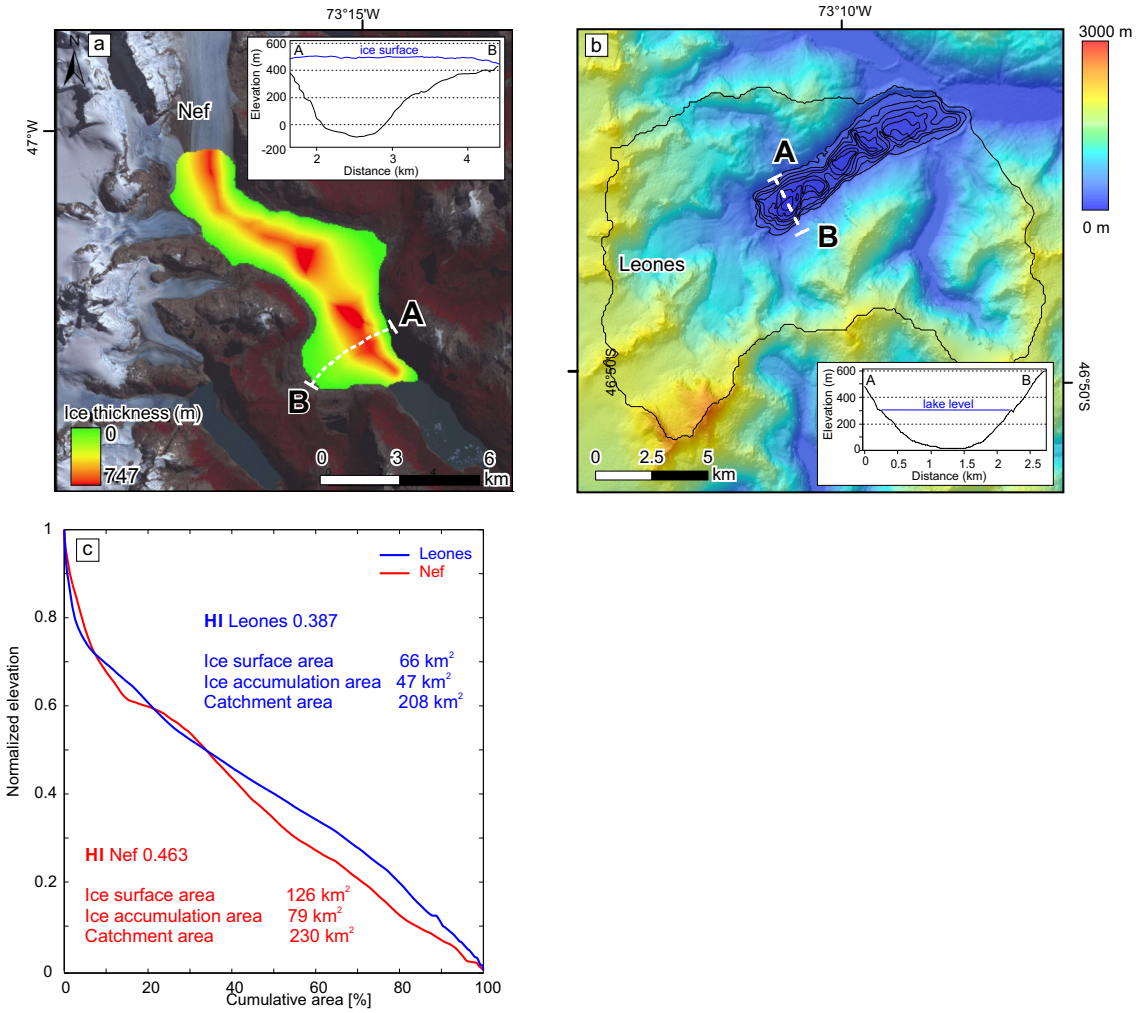

Figure A.6 – (A) Ice thickness map of the lower Nef glacier and valley cross-section with inferred subglacial topography (inset). Data from Ministry of Public Affaires of the republic of Chile, Main Water Department (Centro de Estudios Cientificos, 2012). (B) Topography in the catchment of Glaciar Leones including bathymetry of Lake Leones (bathymetry data from Harrison *et al.* (2008) . (C) Hypsometric integrals of Leones and Nef catchments with values for ice surface, ice accumulation and catchment areas. Areas from GLIMS (http://www.glims.org), Rivera *et al.* (2007) and SRTM-1 30m.

Figure A.7 – Locations of outcrops and associated structural measurements documented in this study (Fig. 3.4, Fig. 3.6, Fig.3.7). Structural measurements are documented following the Dip Direction/Dip convention. Shear sense was inferred from mineral growth fabrics along lineations recording fault motion.

Cachet Fault								
E	N	elevation	dip dir	dip	L dip dir	L dip	shear sense	outcrop ID
660646	4792326	206	114	80				cach-1
646050	4793991	238	90	10	300	10	dextral	cach-2
634721	4790250	571	78	70	10	10	dextral	cach-3
631724	4793575	387	70	70				cach-4
631724	4793575	387	86	90	32	15	dextral	cach-4
637453	4795651	217	103	60				cach-5
632523	4782702	668	115	85	15	10	dextral	cach-6
Exploradores Fault Zone								
656643	4844699	236	20	40				ex-1
656643	4844699	236	45	30				ex-1
651900	4845980	214	65	60	135	35		ex-2
648876	4847096	214	220	60				ex-3
648876	4847096	214	255	30				ex-3
648876	4847096	214	178	82	245	75		ex-3
630073	4864330	35	132	60				ex-4
631505	4861006	56	260	48	294	42	inv	ex-5
631505	4861006	56	145	68	56	22		ex-5
631505	4861006	56	244	34	251	33	inv	ex-5
631505	4861006	56	292	80	220	67	inv	ex-5
631505	4861006	56	294	89	207	58	inv	ex-5
631505	4861006	56	298	78	228	80	inv	ex-5
631505	4861006	56	286	89	192	44	inv	ex-5
631505	4861006	56	280	84	200	68	inv	ex-5
631505	4861006	56	323	32	274	20		ex-5
631505	4861006	56	144	70	62	6	dx	ex-5
631505	4861006	56	232	42	242	47	inv	ex-5
631505	4861006	56	232	38	270	29	inv	ex-5
631505	4861006	56	240	61	265	65	inv	ex-5
631505	4861006	56	198	34	237	25		ex-5
631505	4861006	56	294	65	255	60	inv	ex-5
631505	4861006	56	288	48	274	44	inv	ex-5
631505	4861006	56	257	56	255	65	inv	ex-5
631505	4861006	56	235	20	235	20		ex-5
631505	4861006	56	233	52	245	50	inv	ex-5
631505	4861006	56	252	42	265	40		ex-5
631505	4861006	56	120	48	134	48	inv	ex-5
643473	4849181	158	180	68				ex-6
643473	4849181	158	167	89				ex-6
656115	4844831	230	238	80				ex-7
656115	4844831	230	218	78				ex-7
656115	4844831	230	232	76	154	35	inv	ex-7

Fig. A.7 Locations of Outcrops and Structural Data, cont.

El Salton Fault								
E	N	elevation	dip dir	dip	L dip dir	L dip	shear sense	outcrop ID
648259	4734984	139	243	85				sal-1
648259	4734984	139	65	75				sal-1
648259	4734984	139	40	80				sal-1
647970	4734977	195	230	86				sal-2
647970	4734977	195	44	85				sal-2
647889	4735041	189	355	74	310	60	norm	sal-3
647889	4735041	189	13	83				sal-3
647889	4735041	189	5	75				sal-3
647678	4735474	199	205	88				sal-4
647678	4735474	199	205	90				sal-4
647678	4735474	199	165	74	100	30		sal-4
648655	4734731	77	195	76				sal-5
648655	4734731	77	203	63	158	56	norm	sal-5
648655	4734731	77	188	79	120	68	norm	sal-5
648655	4734731	77	182	80	108	78	norm	sal-5
648655	4734731	77	193	80				sal-5
648655	4734731	77	192	76				sal-5
648655	4734731	77	196	80	120	48	norm	sal-5
648655	4734731	77	198	62	184	56	norm	sal-5
648655	4734731	77	188	76				sal-5
648655	4734731	77	183	83				sal-5
648655	4734731	77	210	83	146	85	norm	sal-5
648216	4734525	76	176	78				sal-6
648216	4734525	76	168	76	110	62	norm	sal-6
648216	4734525	76	146	80	95	62	norm	sal-6
648216	4734525	76	168	84	88	67	norm	sal-6
648216	4734525	76	182	82	110	63	norm	sal-6
647836	4734335	126	176	73	100	55		sal-7
647836	4734335	126	172	83				sal-7
647836	4734335	126	150	86	260	70		sal-7
647836	4734335	126	178	88				sal-7
647836	4734335	126	155	72				sal-7
647836	4734335	126	148	88	68	85		sal-7
647836	4734335	126	178	72				sal-7

Appendix B

Supplementary Material for Chapter 4

B.1 Apatite (U-Th)/He Data Cerro Barrancos

Figure B.1 – Apatite (U-Th)/He Data from the Cerro Barrancos transect from the study of Guillaume *et al.* (2013). Details of the sample preparation and analytical procedure related to AHe data from the Cerro Barrancos transect can be found in the supplementary information of the study by (Guillaume *et al.*, 2013). Grey-shaded single-grain ages have been dismissed as outliers by the original authors of the data set.

AHe data Cerro Barrancos (Guillaume et al., 2013)

Sample	Latitude	Longitude	Elevation [m]	4He [nmol/g]	U [ppm]	Th [ppm]	uncorr. Age [Ma]	FT	corr. Age [Ma]	error [Ma]	mean age [Ma]
DES16-C26	-47.5633	-72.8219	1436	1.36	27.8	56.6	6.1	0.77	8	2.6	8.0
DES17-A	-47.5635	-72.826	1245	0.49	18.2	37.4	3.4	0.83	4.1	1.2	7.6
DES17-B26	-47.5635	-72.826		0.48	10.6	37	4.6	0.82	5.6	1.7	
DES17-C26	-47.5635	-72.826		1.01	16.6	33	7.7	0.78	9.9	2.9	
DES17-D	-47.5635	-72.826		1.74	28.2	52.2	8	0.75	10.7	1.2	
DES18-A	-47.5625	-72.8325	1019	0.66	21.4	45.9	3.8	0.77	4.9	0.6	4.8
DES18-B	-47.5625	-72.8325		0.66	24.7	48.8	3.4	0.79	4.3	0.5	
DES18-C	-47.5625	-72.8325		0.99	31.4	75.9	3.7	0.73	5.1	0.6	
DES19-A	-47.5625	-72.8392	806	1.23	37.4	52.8	4.6	0.75	6.1	0.7	4.3
DES19-B	-47.5625	-72.8392		0.67	30.5	41.4	3.1	0.72	4.3	0.5	
DES19-C	-47.5625	-72.8392		0.85	37	56.6	3.1	0.76	4.1	0.5	
DES19-D	-47.5625	-72.8392		0.67	46.6	71.8	2	0.72	2.7	0.4	
DES20-A	-47.5638	-72.8462	594	0.2	5.7	6.5	5.1	0.77	6.7	1.2	6.3
DES20-B	-47.5638	-72.8462		0.67	4.5	45.6	8.1	0.79	10.4	0.6	
DES20-C	-47.5638	-72.8462		0.62	16	47.6	4.2	0.84	5.1	0.4	
DES20-D	-47.5638	-72.8462		0.37	9.7	11	5.6	0.79	7.1	0.4	
DES21-C	-47.5645	-72.8532	386	0.79	23.8	53.7	4	0.75	5.3	0.7	4.3
DES21-D	-47.5645	-72.8532		6.99	23.6	50.9	36.4	0.73	49.8	0.8	
DES21-B	-47.5645	-72.8532		0.65	35	67.8	2.4	0.73	3.2	0.2	
DES22-A	-47.5711	-72.8652	147	0.24	4.7	14.6	5.5	0.83	6.7	0.8	4.8
DES22-B	-47.5711	-72.8652		1.04	38.9	33.8	4.1	0.71	5.8	0.7	
DES22-C	-47.5711	-72.8652		0.43	16.2	55.1	2.7	0.72	3.8	0.2	
DES22-D	-47.5711	-72.8652		0.36	19.5	52.2	2.1	0.69	3	0.2	

B.2 Apatite Fission Track Data Cerro Barrancos

Figure B.2 – Apatite Fission Track Data from the Cerro Barrancos transect from the studies of Blisniuk *et al.* (2006) and Warkus (2002). Details of the sample preparation and analytical procedure related to AFT data from the Cerro Barrancos transect can be found in the the studies by (Blisniuk *et al.*, 2006) and (Warkus, 2002).

AFT data Cerro Barrancos (Blisniuk et al., 2005; Warkus, 2002)

N - number of dated apatite crystals; ρs (ρi) - spontaneous (induced) track densities (x105 tracks/cm2); Ns (Ni) - number of counted spontaneous (induced) tracks; pd - dosimeter track density (x10E+05 tracks/cm2); Nd - number of tracks counted on dosimeter; P(χ2) - probability obtaining Chi-square value (χ2) for n degree of freedom (where n = No. of crystals - 1); Age ± 1σ - central age ± 1 standard error [Galbraith and Laslett. 1993]; MTL - mean track length; SD - standard deviation of track length distribution; N (L) - number of horizontal confined tracks measured; Dpar - average etch pit diameter of fission tracks. Ages were calculated using zeta calibration method [Hurford and Green. 1983]. Glass dosimeter CN-5 and zeta value of 370.06± 6.1 year/cm2.

Sample	Latitude	Longitude	Elevation [m]	N	ρ_s	N_s	ρ_i	N_i	ρ_d	N_d	P(χ2) [%]	Age [Ma]	± 1σ [Ma]	Dpar [µm]	SD [µm]	MTL [µm]	SD [µm]	N (L)
CB130	-47.57	-72.88	130	29	0.550	117	18.724	3985	11.67	4226	99	6.3	0.6	2.33	0.16	12.1	0.33	101
CB550	-47.57	-72.88	550	26	0.534	129	15.890	3842	11.744	4226	100	7.3	0.7	0.33	0.17	12.88	0.29	106
CB930	-47.57	-72.83	930	6	1.073	118	21.224	2334	11.819	4226	99	11	1.1	2.2	0.2	12.74	0.3	104
CB1410	-47.57	-72.82	1410	27	1.699	290	32.986	5631	11.893	4226	92	11.3	0.7	2.34	0.15	11.94	0.29	111
CB1960	-47.57	-72.77	1960	28	1.397	240	18.040	3099	11.967	4226	99	17.1	1.2	2.35	0.2	10.3	0.24	106

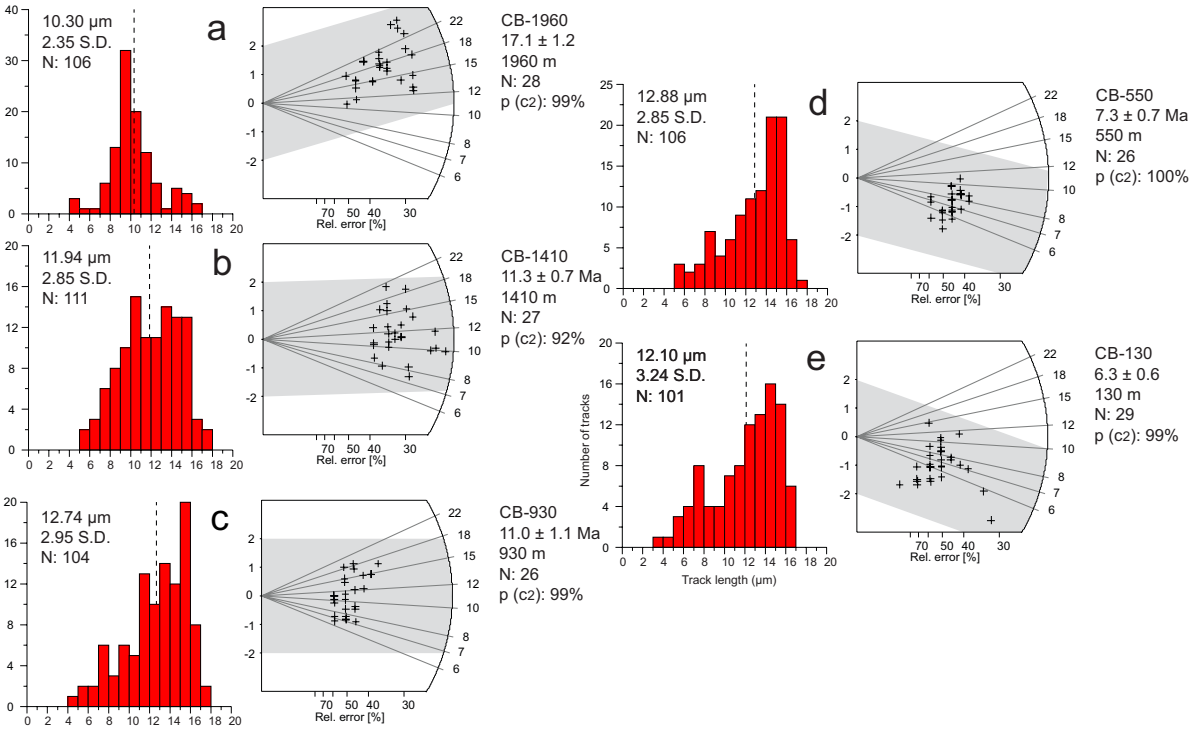

Figure B.3 – Radial Plots and Track Length Distributions of Apatite Fission Track Data from Cerro Barrancos, from the studies of Blisniuk *et al.* (2006) and Warkus (2002)

B.3 New Apatite Fission Track Data (Leones and Nef transects) - Analytical Procedure

The formation of a fission track is described by the ion-spike explosion model (Fleischer et al., 1975). According to this model an unstable ^{238}U isotope build in the crystal structure decays by spontaneous fission splitting into two highly charged particles. Those new particles travel very fast in an opposite direction, damaging the crystal lattice on their way and leaving a trace named as fission track (FT). Main materials used for fission-track dating are U-rich minerals as apatite, zircon, sphene and more rarely obsidian, epidote or mica (see Wagner and Van den haute, 1992). For age calculation spontaneous (produced from ^{238}U) and induced (produced from ^{235}U in the reactor) tracks quantity in the same mineral grain is obligatory with a known neutron flux ratio applied. The analytical procedure employs external detector method (Gleadow and Duddy, 1981) where tracks are counted simultaneously for the same mineral grain and mica detector.

Ages were calculated with the equation (Price and Walker, 1963; Naeser, 1967):

$t = 1/\lambda d \ln [(\lambda d)(\rho s / \rho i)\rho d\, \zeta g + 1]$ where:

t – sample age;

ζ – zeta calibration factor;

ρs – spontaneous tracks density ^{238}U (track/cm^2);

ρi – induced tracks density ^{235}U (track/cm^2)

Fission-tracks represent metastable products highly temperature dependent, fading in the process known as fission-track annealing (Wagner Van den haute, 1992). Annealing process occurs only in a certain temperature range which is known as partial annealing zone (PAZ). Above this range tracks totally disappear and this range is called total annealing zone (TAZ), below they are stable. This phenomenon has a fundamental meaning for FT method, where track length plays a key role in thermal history reconstructions. Usually, PAZ zone upper limit is set up for apatite as 120°C and the zircon 240°C. The chemical composition of mineral and track orientation in relation to crystal

c-axis are indicated to be other factors which influence annealing style. Tracks annealing kinetics is characterised by "Dpar" parameter describing the diameter of track parallel to crystal c-axis (Crowley et al., 1991; Burtner et al., 1994). This factor fairly good illustrates the influence of chemical composition on track annealing (Ketcham, 2005; Ketcham et al., 2007). This issue has been discussed by O'Sullivan and Parrish (1995) for plutonic rocks, who reported that single-grain ages may significantly vary between chlorine-rich and fluorine-rich apatites, resulting in older and younger single grain ages respectively. Dpar values have been measured by two operators (A. Sobczyk, E. Sobel)) following correction procedure proposed by Sobel Seward (2004) to constrain analytical reliability. For fission track dating of apatite the external detector method was adopted (Gleadow, 1981), and etching protocol of Donelick et al. (1999). Apatite separation followed standard magnetic (Frantz) and density (SPT, DI) methods to retrieve mineral concentrates. Then, apatite grains were mounted on glass slides with Araldite® epoxy, grinded and polished to expose minerals' internal structure. Next, 5.5 mol HNO_3 etchant has been applied for 20 seconds at 21°C to reveal spontaneous fission tracks. Samples were irradiated at Triga reactor of Oregon State University (USA) to produce induced fission tracks. Following irradiation, mica external detectors were etched with 21C, 40% HF acid for 45 minutes. The pooled and central ages are reported (tab.xx) for samples, which pass or fail $\chi 2$ test respectively, resulting in a P($\chi 2$) value greater than (less than) 5%. Age errors are presented as one sigma, calculated with zeta calibration method (Hurford and Green, 1983), a ζ value of 347.6 $\pm$ 6.3 (A. Sobczyk) and Durango age standard (31.3$\pm$0.3 Ma, Naeser Fleischer, 1975). AFT ages were calculated by TrackKey 4.2 g software (Dunkl, 2002). All tracks densities in mounts and micas were measured with a Leica DMRM microscope with drawing tube located above a digitising tablet and a Kinetek computer-controlled automated stage driven by the FT Stage software (Dumitru, 1993). The analysis was performed with reflected and transmitted light at 1250x magnification. To reconstruct thermal history, as many horizontal confined tracks-in-tracks (TINTs) as possible were measured. Measurements have been performed both for standard irradiated samples (Triga reactor, US), and heavy ions slides irradiated at the Materials Research Department of the GSI Helmholtzzentrum, Darmstadt, Germany made to increase the number of all recorded horizontal tracks-in-tracks. To avoid length distribution bias in thermal modeling resulted from heavy ions irradiation, c-axis projected lengths have been used (Ketcham et al., 1999). The length histograms are included in Figure B.5.

B.4 New Apatite Fission Track Data (Leones and Nef transects) - Summary

Figure B.4 – New Apatite Fission Track Data (Leones and Nef transects) - Summary

a N - number of dated apatite crystals; ρs (ρi) - spontaneous (induced) track densities (x105 tracks/cm2); Ns (Ni) - number of counted spontaneous (induced) tracks; ρd - dosimeter track density (x105 tracks/cm2); Nd - number of tracks counted on dosimeter; P(χ2) - probability obtaining Chi-square value (χ2) for n degree of freedom (where n = No. of crystals - 1); Age ± 1σ - central age ± 1 standard error (Galbraith and Laslett. 1993); MTL - mean track length; SD - standard deviation of track length distribution; N (L) - number of horizontal confined tracks measured; Dpar - average etch pit diameter of fission tracks. Ages were calculated using zeta calibration method (Hurford and Green. 1983); glass dosimeter CN-5. and zeta value of 347.6± 6.3 year/cm2.

Sample	Lon.	Lat.	Elevation [m]	N	ρ_s	N_s	ρ_i	N_i	ρ_d	N_d	P(χ2) (%)	Age [Ma]	± 1σ	Dpar[a]	SD[a]	Dpar[b]	SD[b]	MTL	SD	N (L)
12-CM-05	-73.2666	-46.738	1645	15	0.887	44	23.28	1155	11.63	4587	100	7.7	1.2	1.75	0.26	2.09	0.3	9.73	3.69	20
12-CM-06	-73.2551	-46.741	1434	18	1.735	123	52.67	3733	11.57	4587	80	6.6	0.6	2.47	0.28	-	-	-	-	-
11-LL-08	-73.2221	-46.739	1005	18	0.36	33	13.51	1229	13.94	5665	100	6.5	1.2	2.38	0.34	2.59	0.31	9.29	3.31	45
08-AG-17	-73.2404	-47.099	1382	20	3.114	364	76.68	8963	13.52	5665	91	9.5	0.6	1.82	0.18	2.18	0.28	12.8	1.54	8
08-AG-18	-73.2418	-47.092	1050	20	2.16	155	49.74	3569	13.45	5665	99	10.1	0.9	1.89	0.24	-	-	-	-	-
08-AG-33	-73.2662	-46.998	325	20	1.75	160	46.33	4232	11.69	4587	100	7.7	0.6	1.93	0.20	-	-	-	-	-
11-LL-09	-73.2074	-46.755	325	19	0.231	32	9.38	1300	13.87	5665	100	5.9	1.1	2.23	0.35	-	-	-	-	-
11-LL-05	-73.2158	-46.784	722	15	1.065	54	39.24	1989	14.22	5665	100	6.7	0.9	1.76	0.20	-	-	-	-	-
11-LL-04	-73.2163	-46.793	1197	12	0.722	33	26.77	1224	14.29	5665	100	6.7	1.2	2.03	0.25	-	-	-	-	-
11-LL-03	-73.2214	-46.789	995	20	2.499	183	96.27	7046	14.35	5665	83	6.5	0.5	2.17	0.27	-	-	14	1.27	3*
11-LL-06	-73.2357	-46.742	1351	23	0.918	166	33.62	6077	14.08	5665	100	6.7	0.5	2.39	0.27	2.81	0.33	12	3.24	67
11-LL-10	-73.1351	-46.744	327	20	0.746	81	38.84	4214	13.80	5665	100	4.6	0.5	2.94	0.41	2.95	0.32	12.6	2.33	13

[a] Dpar and SD data from AFT grain-age sample

[b] Dpar and SD data from ^{252}Cf-derived fission fragments sample

* Lengths data from AFT grain-age sample

Dpar data for count data from grain-age file, averaged per grain. For grains without Dpar measurement the averaged Dpar value from the entire set of grain-Dpars has been used.

Dpar data for lengths from 252Cf-derived fission fragments sample, averaged per grain, in which the length has been measured.

Figure B.5 – New Apatite Fission Track Data - Radial Plots Summary

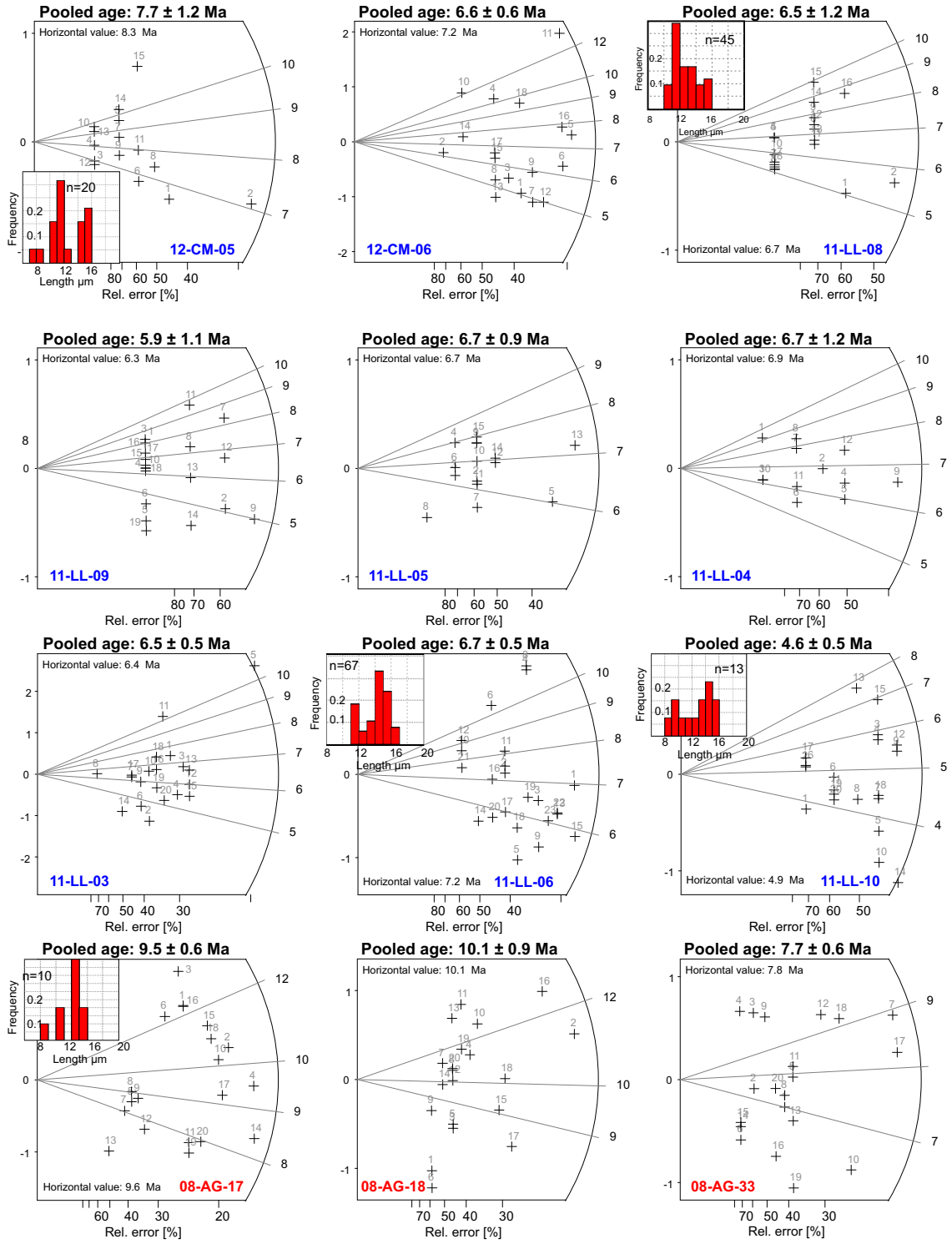

B.5 Inverse thermal modeling - HeFTy

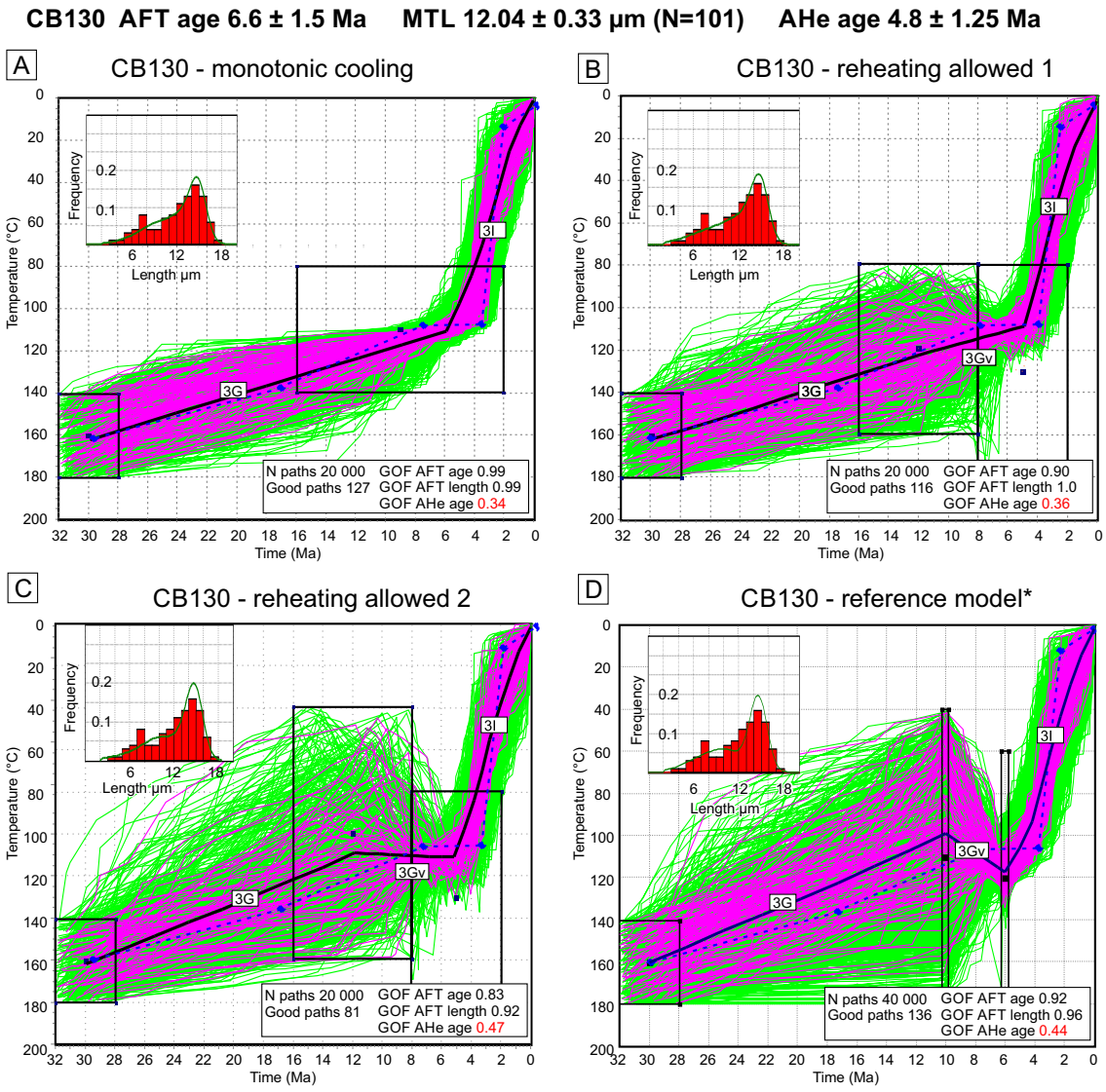

Figure B.6 – HeFTy model of sample CB130, Cerro Barrancos with cooling-only scenario (A), minor (B) and major (B) degree of reheating allowed, and a model setup mimicking modeling conditions of Blisniuk *et al.* (2006) as a reference model (D).

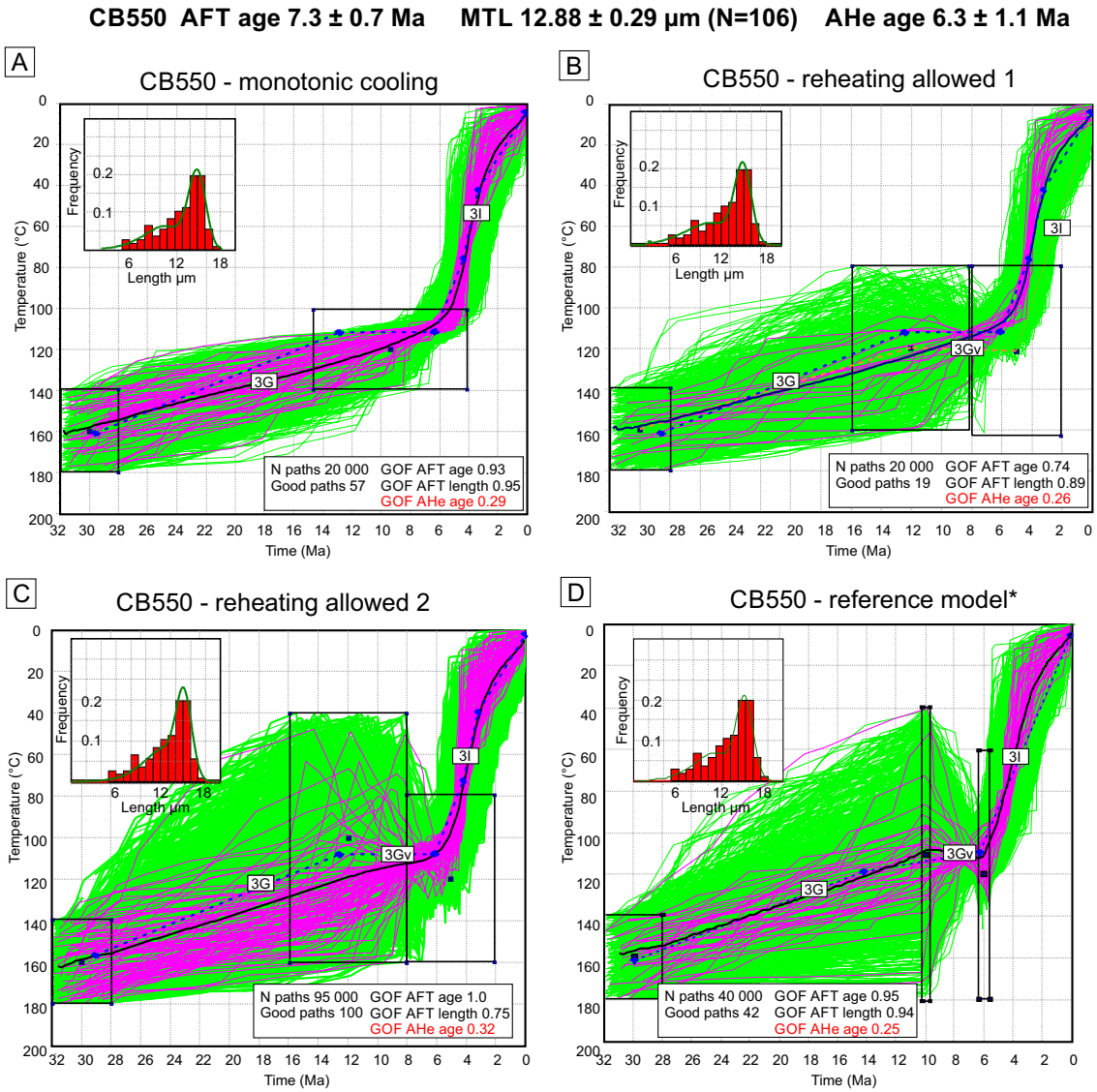

Figure B.7 – HeFTy model of sample CB550, Cerro Barrancos with cooling-only scenario (A), minor (B) and major (B) degree of reheating allowed, and a model setup mimicking modeling conditions of Blisniuk *et al.* (2006) as a reference model (D).

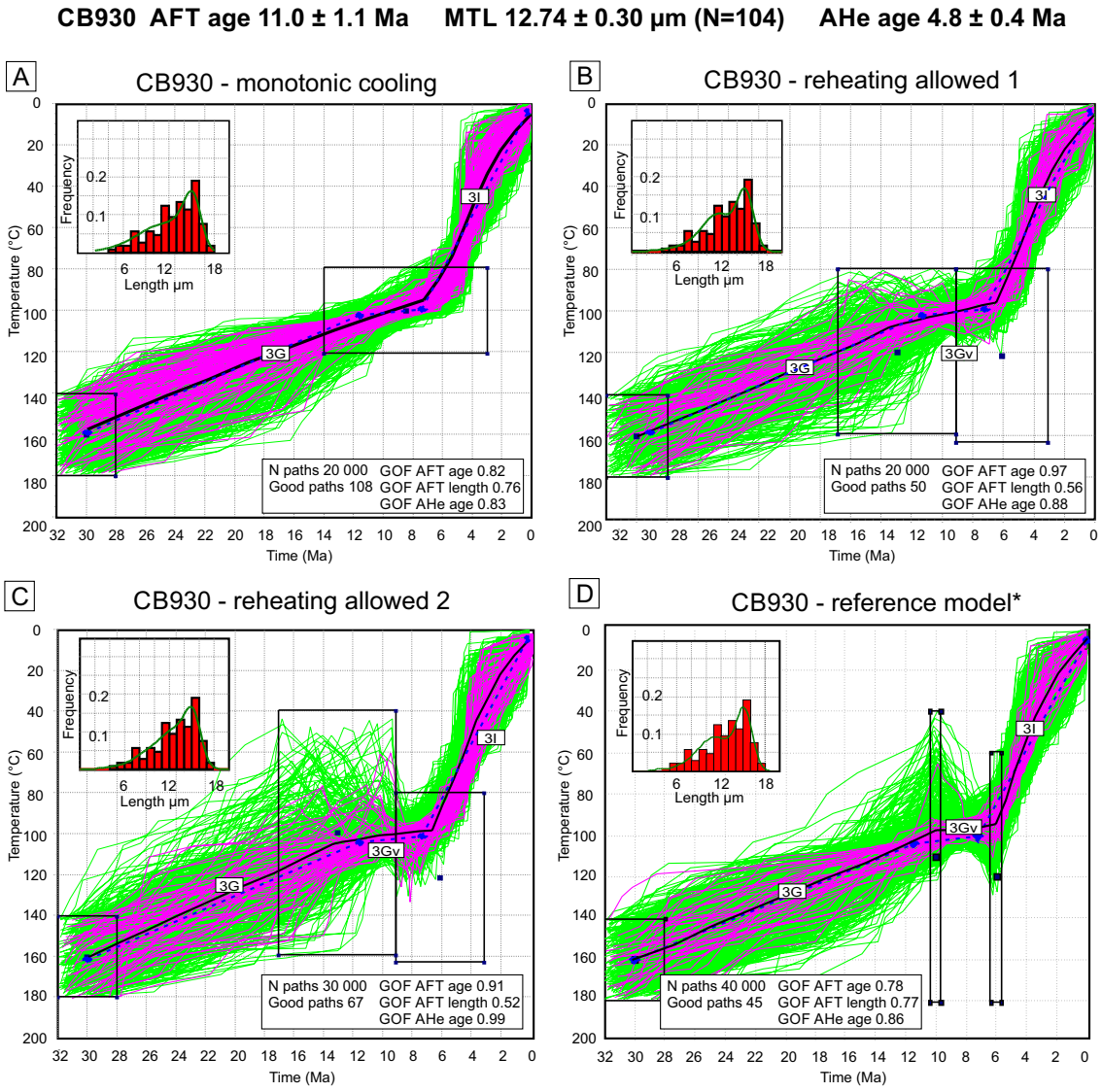

Figure B.8 – HeFTy model of sample CB930, Cerro Barrancos with cooling-only scenario (A), minor (B) and major (B) degree of reheating allowed, and a model setup mimicking modeling conditions of Blisniuk *et al.* (2006) as a reference model (D).

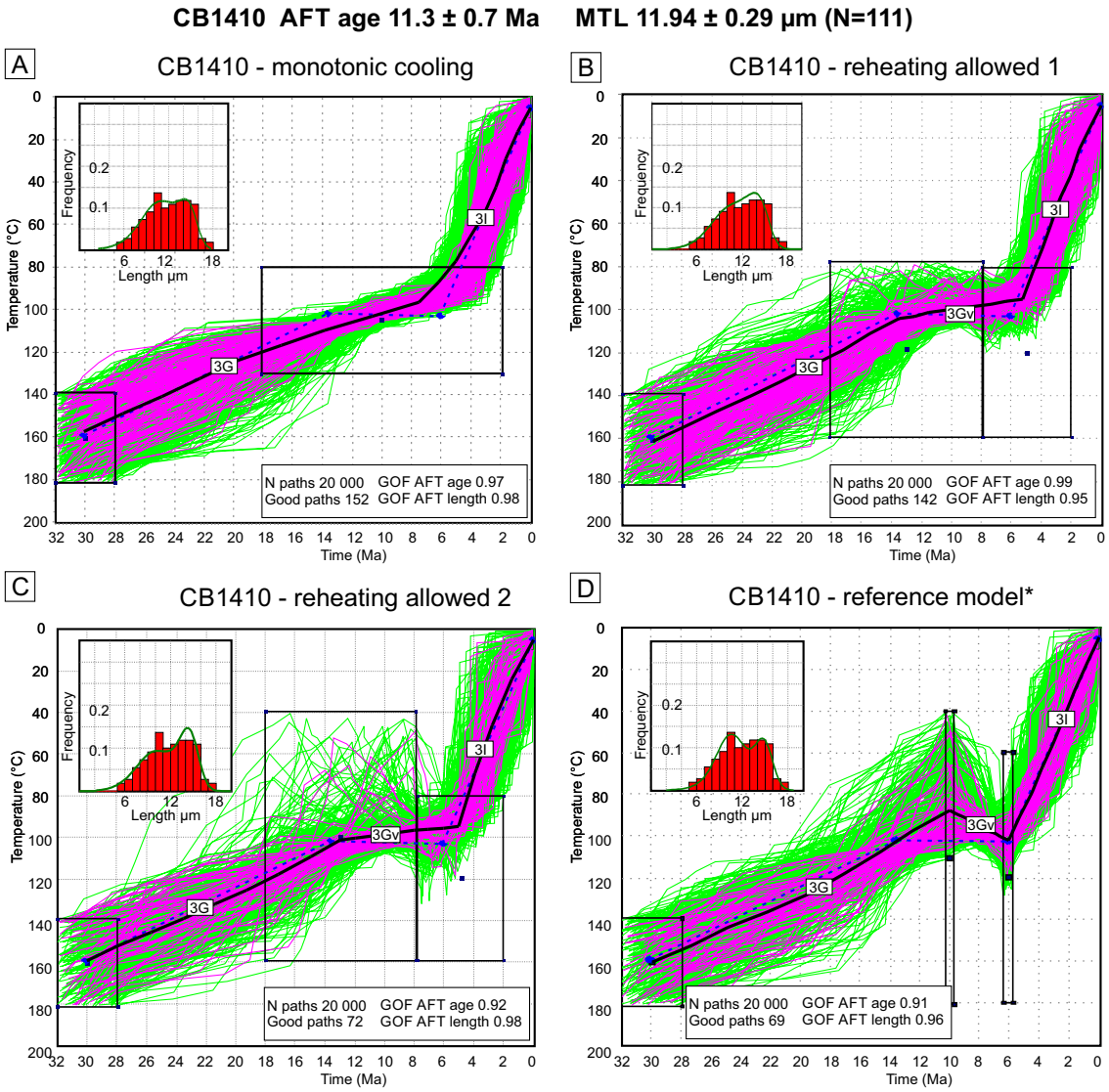

Figure B.9 – HeFTy model of sample CB1410, Cerro Barrancos with cooling-only scenario (A), minor (B) and major (B) degree of reheating allowed, and a model setup mimicking modeling conditions of Blisniuk *et al.* (2006) as a reference model (D).

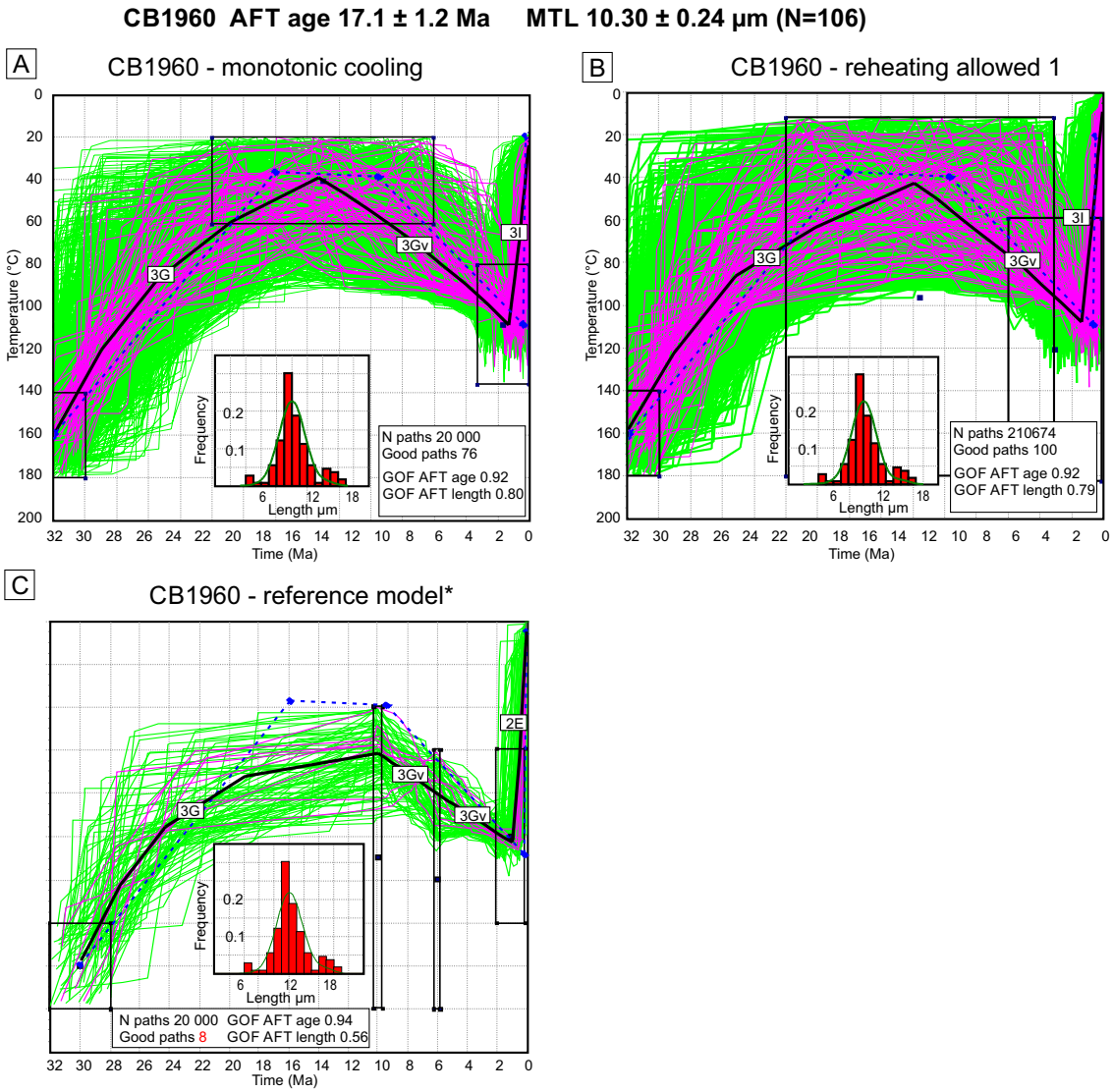

Figure B.10 – HeFTy model of sample CB1960, Cerro Barrancos with more (A) and less constrained (B) forced-reheating scenario, and a model setup mimicking modeling conditions of Blisniuk *et al.* (2006) as a reference model (C).

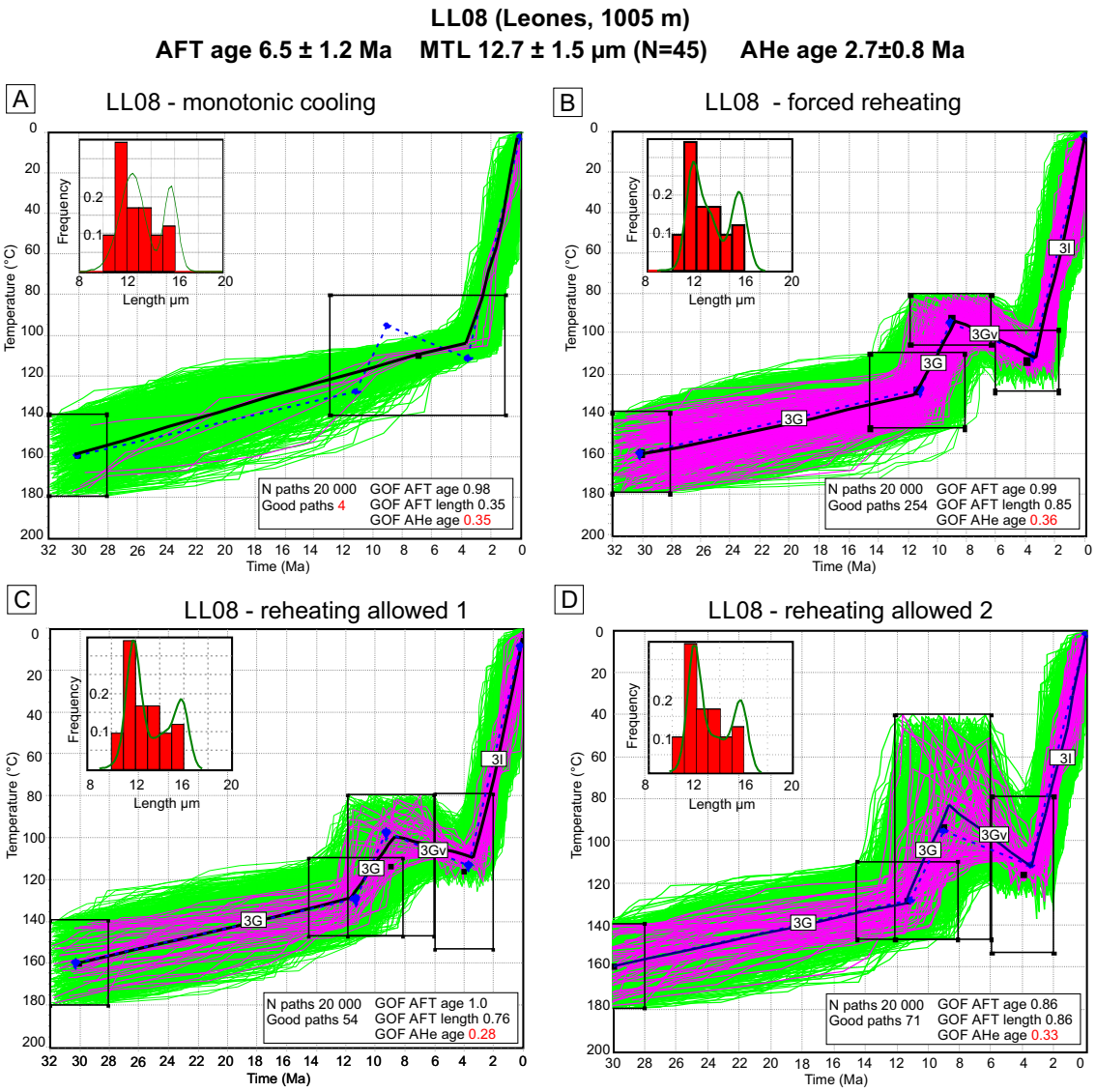

Figure B.11 – HeFTy model of sample LL08, Leones transect with only-cooling scenario (A), forced and tightly constrained reheating (B) and variable degree of allowed reheating (C, D).

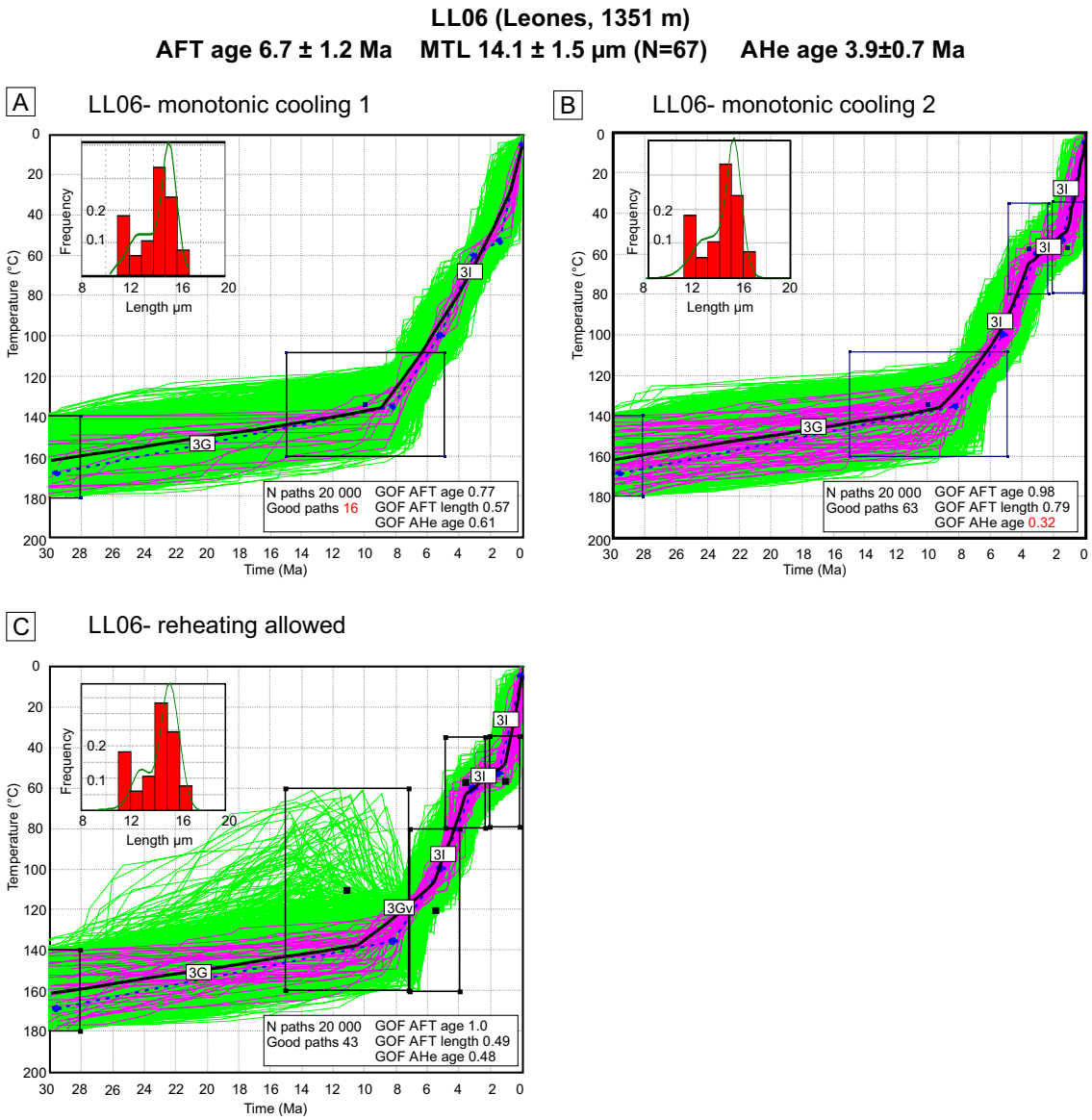

Figure B.12 – HeFTy model of sample LL06, Leones transect with less (A) and more constrained (B) only-cooing scenario and a setup with allowed reheating (C).

B.6 Inverse thermal modeling - QTQt

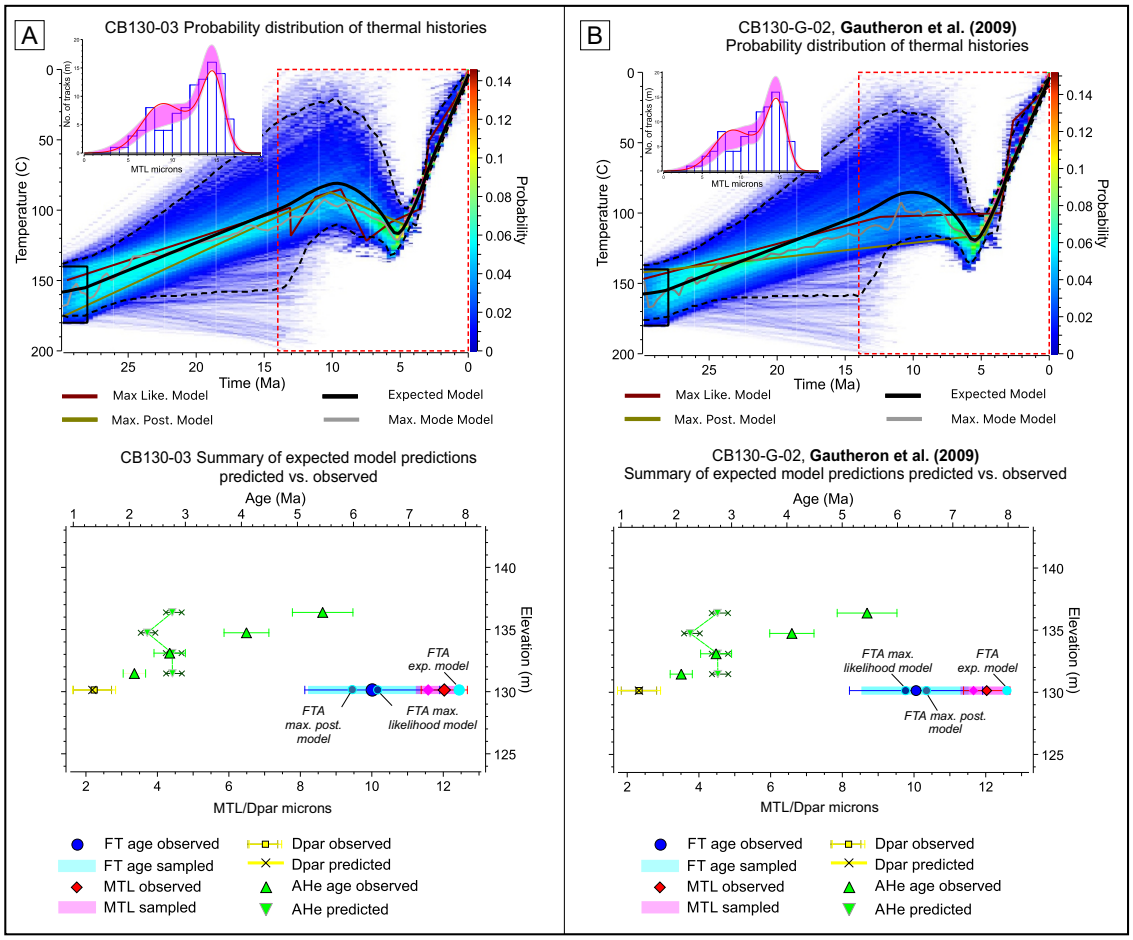

Figure B.13 – QTQt Model - Cerro Barrancos transect, Sample CB130 with standard (A) and modified (B) (after Gautheron *et al.* (2009) He-diffusion kinetics. The upper panels show the probability distribution of expected thermal histories. The lower panels show the summary of expected model predictions vs. the observed data.

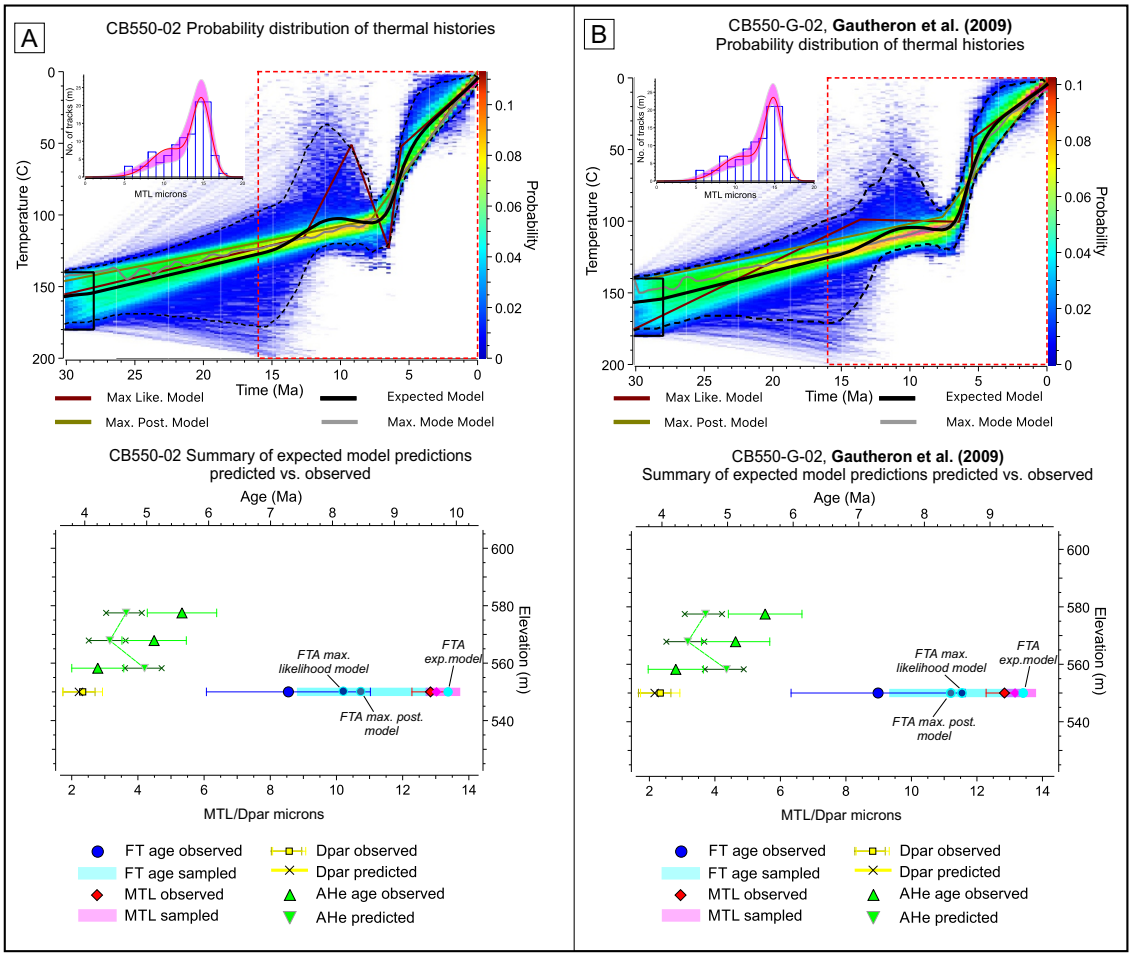

Figure B.14 – QTQt Model - Cerro Barrancos transect, Sample CB550 with standard (A) and modified (B) (after Gautheron *et al.* (2009) He-diffusion kinetics. The upper panels show the probability distribution of expected thermal histories. The lower panels show the summary of expected model predictions vs. the observed data.

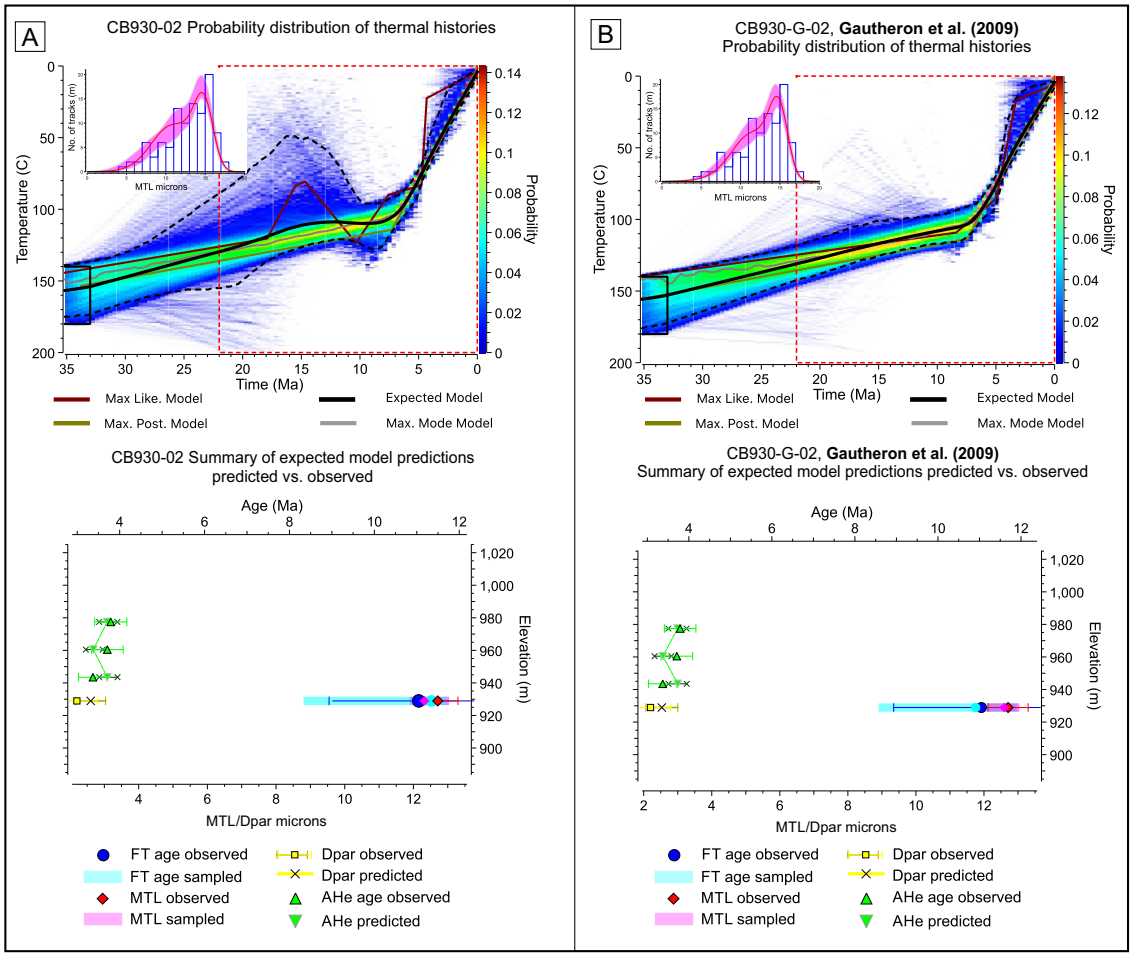

Figure B.15 – QTQt Model - Cerro Barrancos transect, Sample CB930 with standard (A) and modified (B) (after Gautheron *et al.* (2009) He-diffusion kinetics. The upper panels show the probability distribution of expected thermal histories. The lower panels show the summary of expected model predictions vs. the observed data.

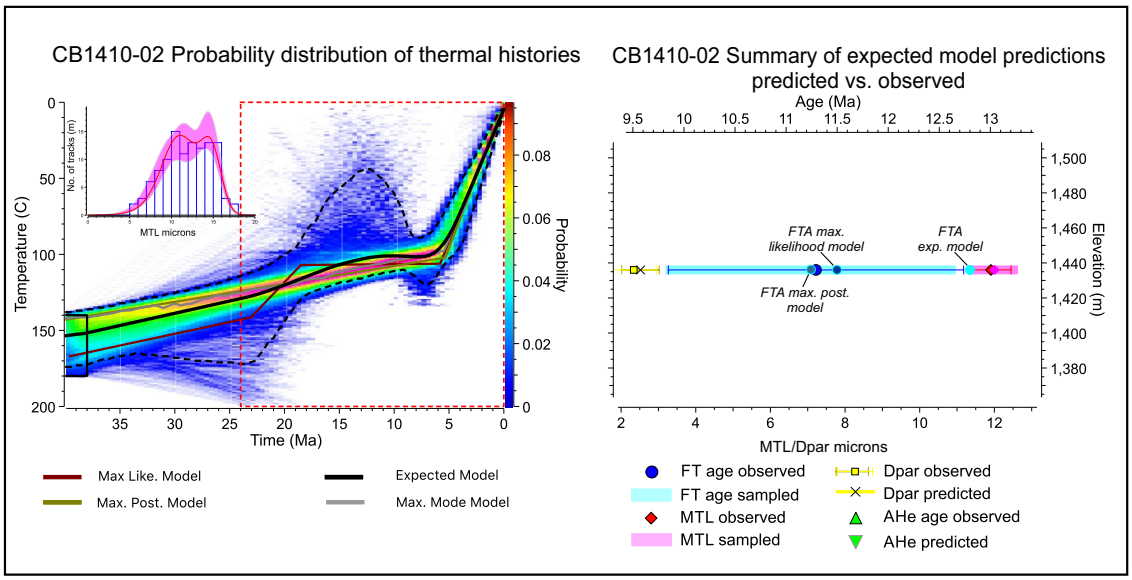

Figure B.16 – QTQt Model - Cerro Barrancos transect, Sample CB1410. The left panels show the probability distribution of expected thermal histories. The right panels show the summary of expected model predictions vs. the observed data.

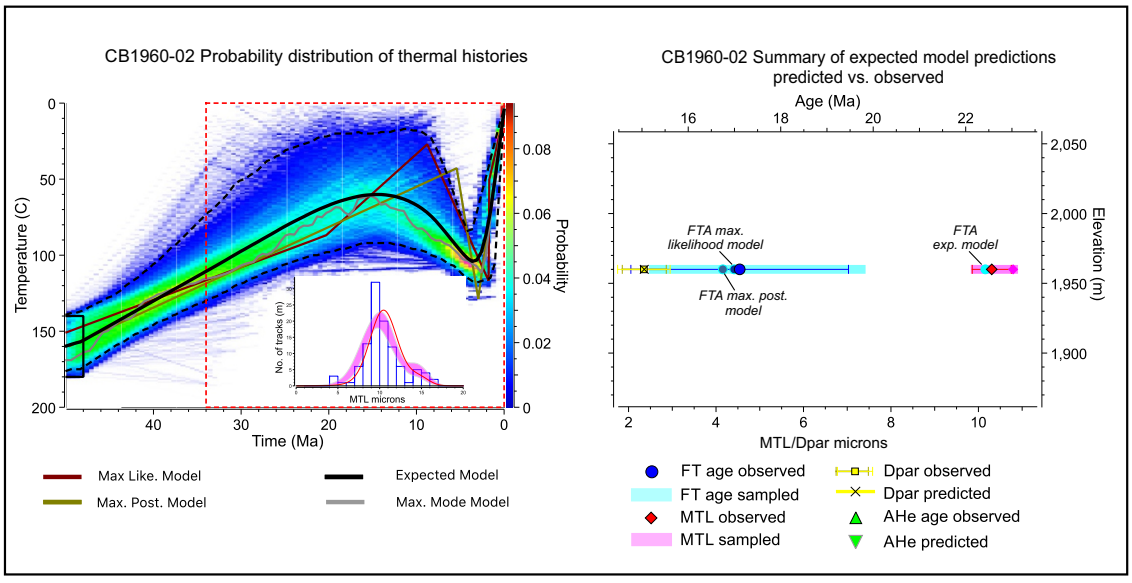

Figure B.17 – QTQt Model - Cerro Barrancos transect, Sample CB1960. The left panels show the probability distribution of expected thermal histories. The right panels show the summary of expected model predictions vs. the observed data.

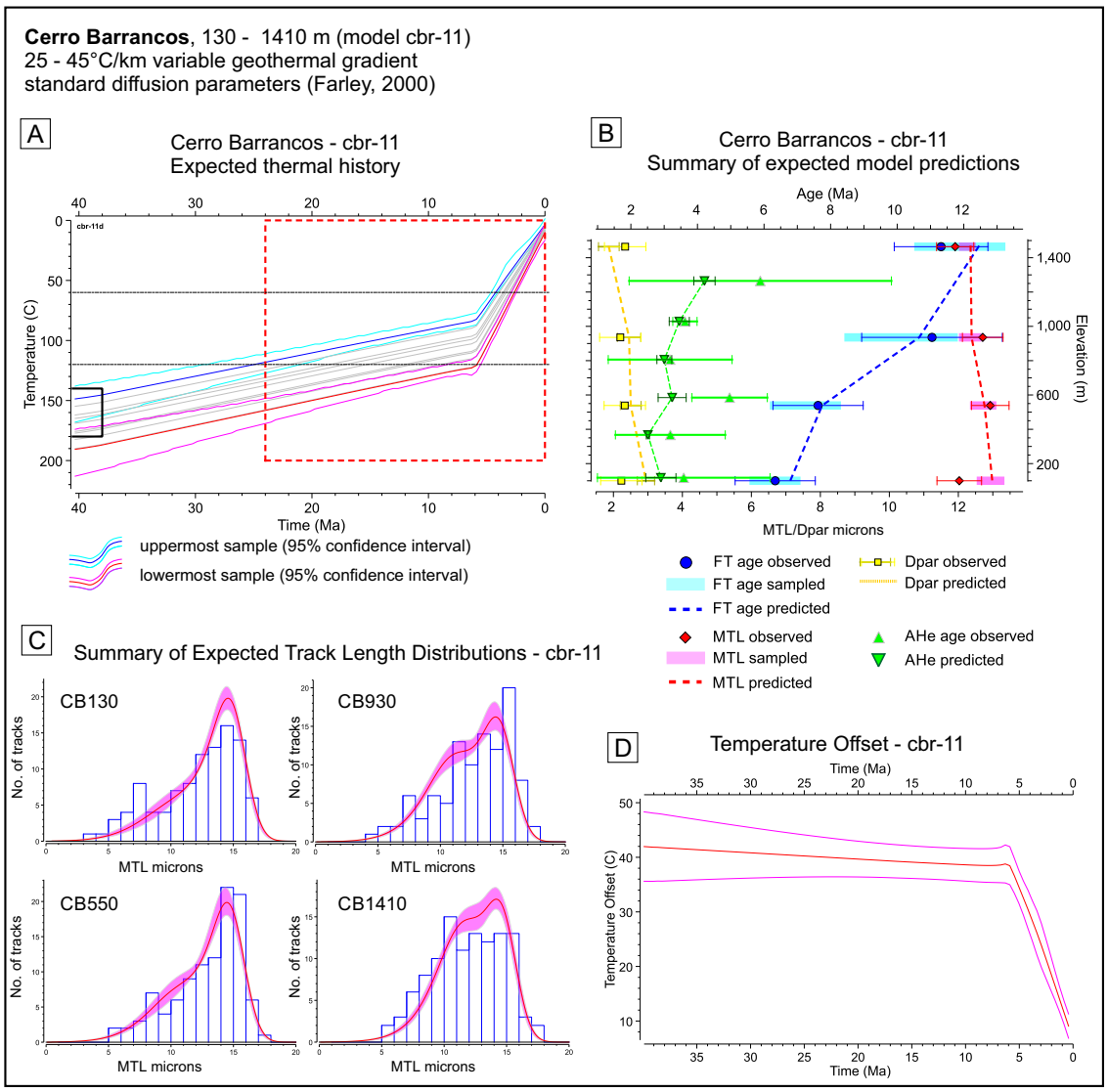

Figure B.18 – Cerro Barrancos transect - Summary of QTQt results from multiple-sample model runs with standard He-diffusion parameters (Farley, 2000) and variable (25-45°C) geothermal gradient. A: Expected thermal history; B: Summary of expected model predictions vs. observed data; C: Summary of expected vs. observed track length distributions; D: Evolution of the temperature offset between the uppermost and lowermost samples over the course of the model.

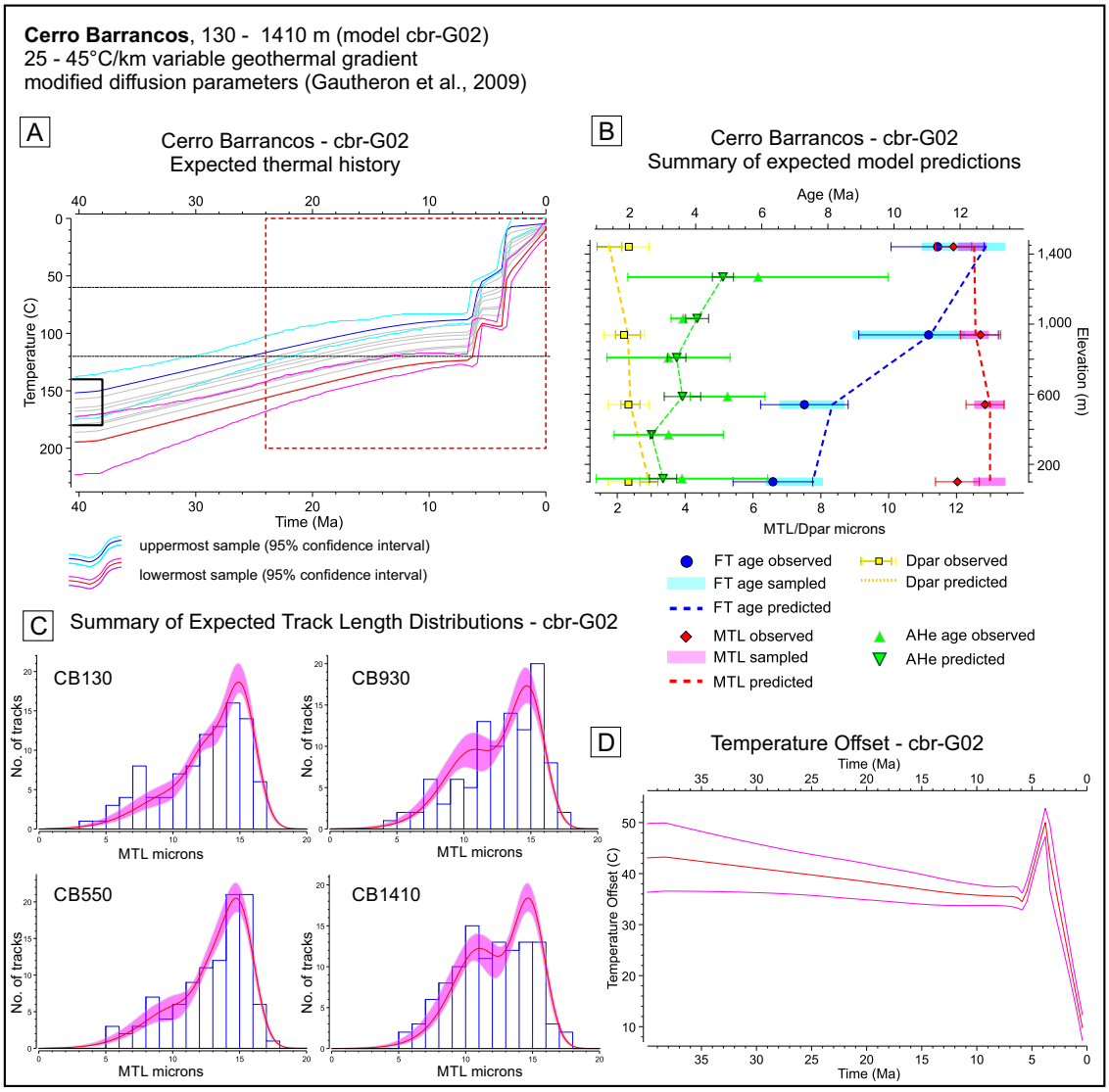

Figure B.19 – Cerro Barrancos transect - Summary of QTQt results from multiple-sample model runs with modified He-diffusion parameters (Gautheron *et al.*, 2009) and variable (25-45°C) geothermal gradient. A: Expected thermal history; B: Summary of expected model predictions vs. observed data; C: Summary of expected vs. observed track length distributions; D: Evolution of the temperature offset between the uppermost and lowermost samples over the course of the model.

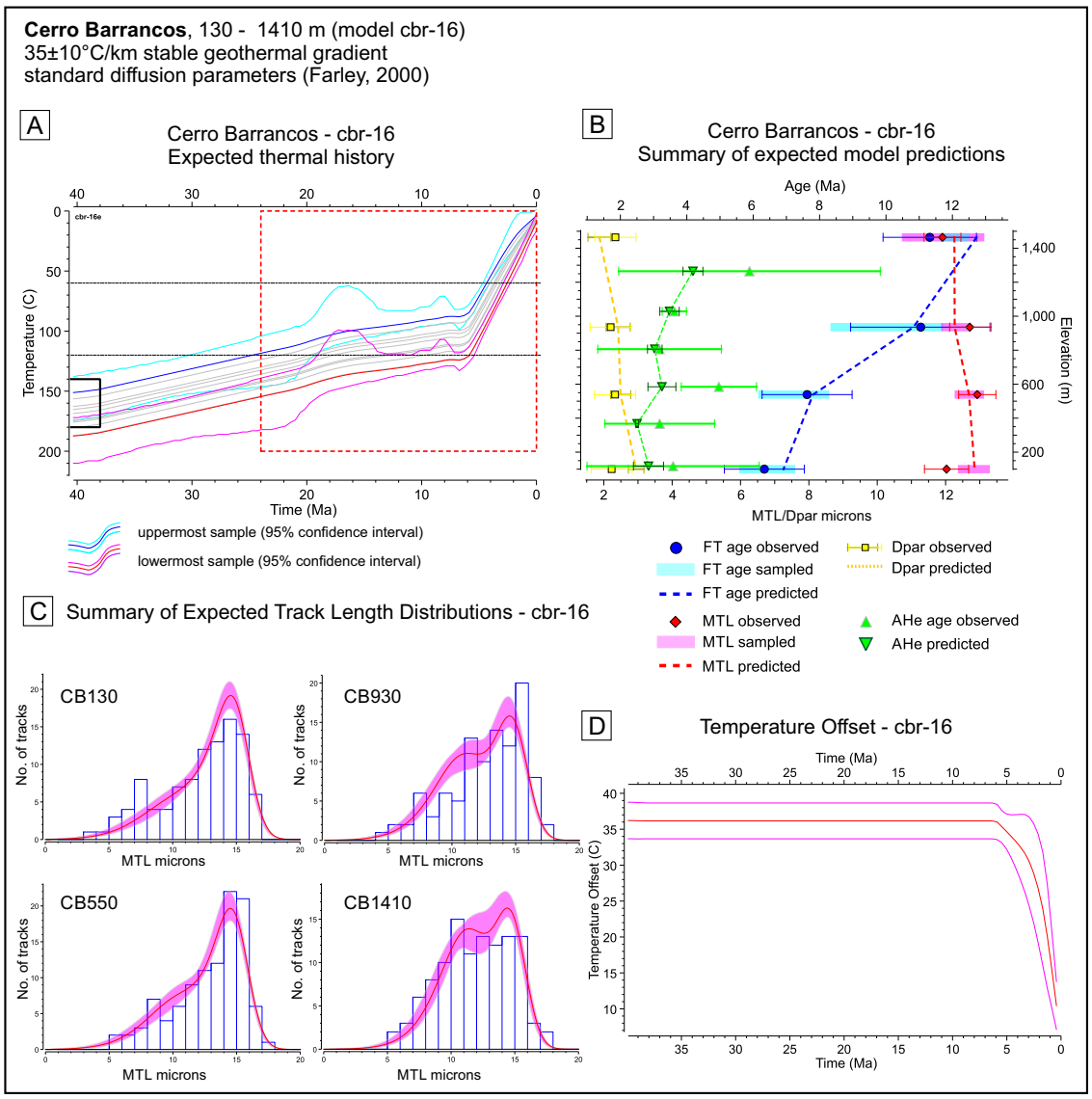

Figure B.20 – Cerro Barrancos transect - Summary of QTQt results from multiple-sample model runs with standard He-diffusion parameters (Farley, 2000) and stable (35°C) geothermal gradient. A: Expected thermal history; B: Summary of expected model predictions vs. observed data; C: Summary of expected vs. observed track length distributions; D: Evolution of the temperature offset between the uppermost and lowermost samples over the course of the model.

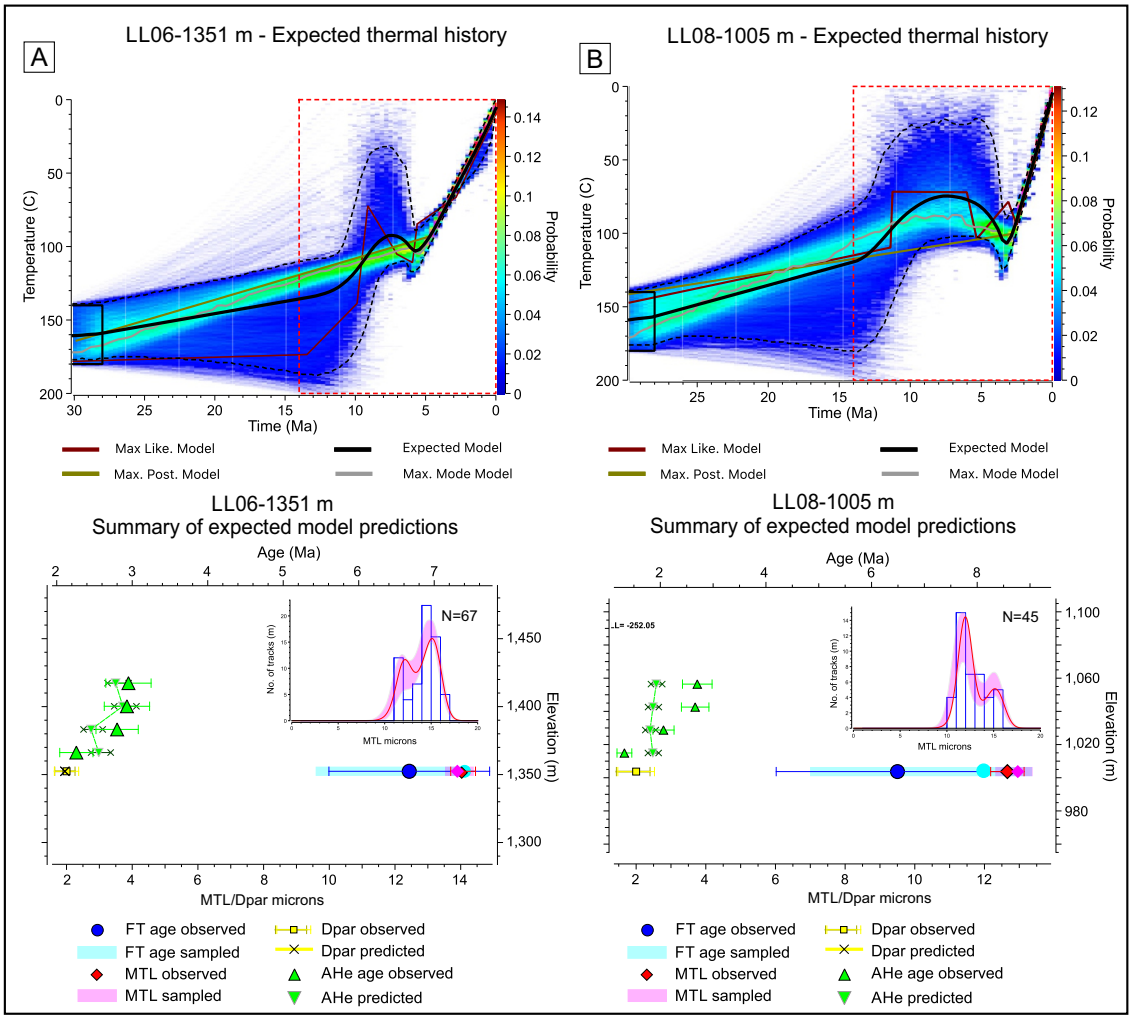

Figure B.21 – Leones transect- Summary of results from single-sample model runs with QTQt. (A) Sample LL06, 1351 m a.s.l. (B) Sample LL08, 1005 m a.s.l. The upper panels show the probability distribution of expected thermal histories. The lower panels show the summary of expected model predictions vs. the observed data.

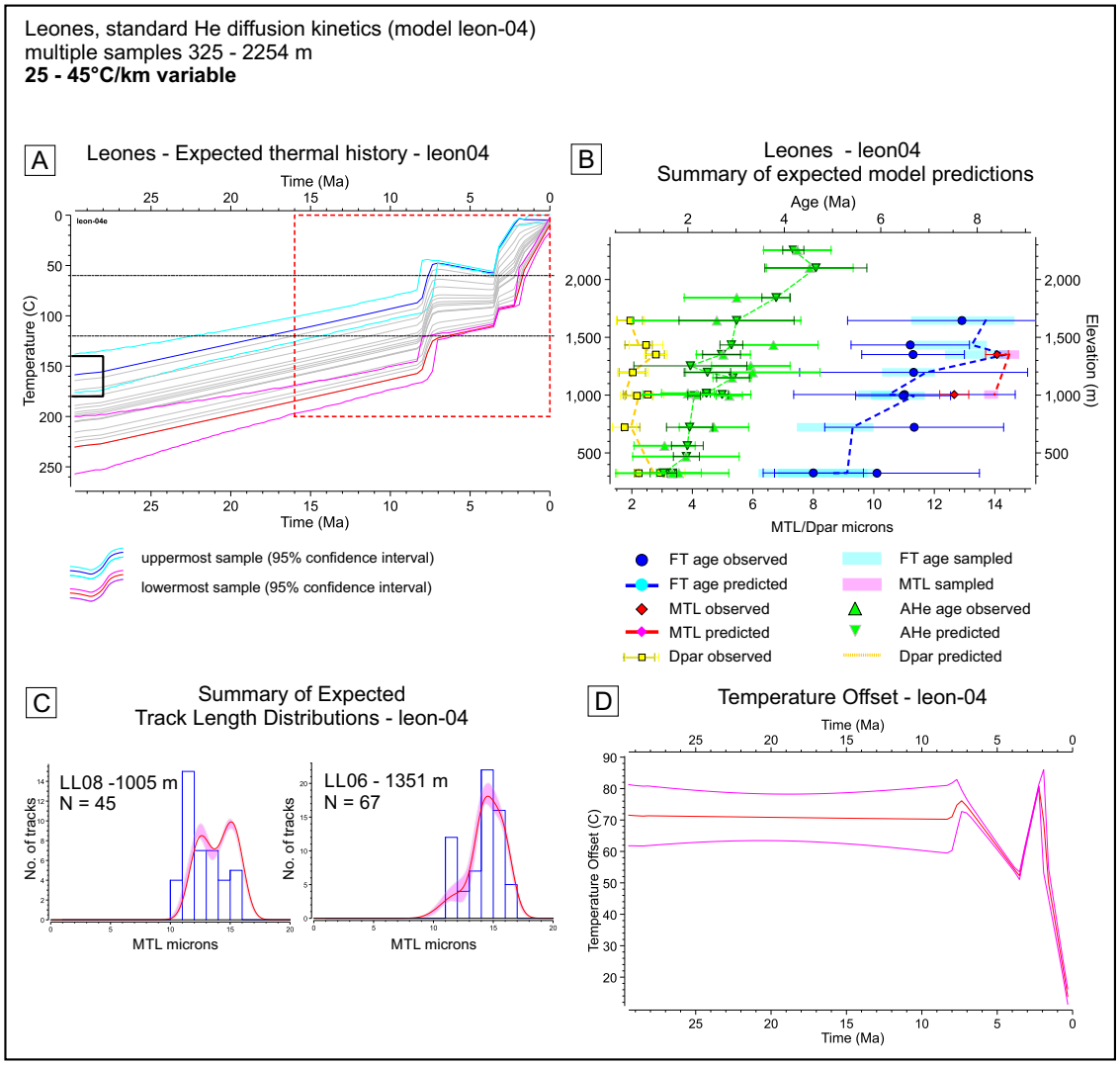

Figure B.22 – Leones transect - Summary of QTQt results from multiple-sample model runs with standard He-diffusion parameters (Farley, 2000) and variable (25-45°C) geothermal gradient. A: Expected thermal history; B: Summary of expected model predictions vs. observed data; C: Summary of expected vs. observed track length distributions for samples LL06 and LL08; D: Evolution of the temperature offset between the uppermost and lowermost samples over the course of the model.

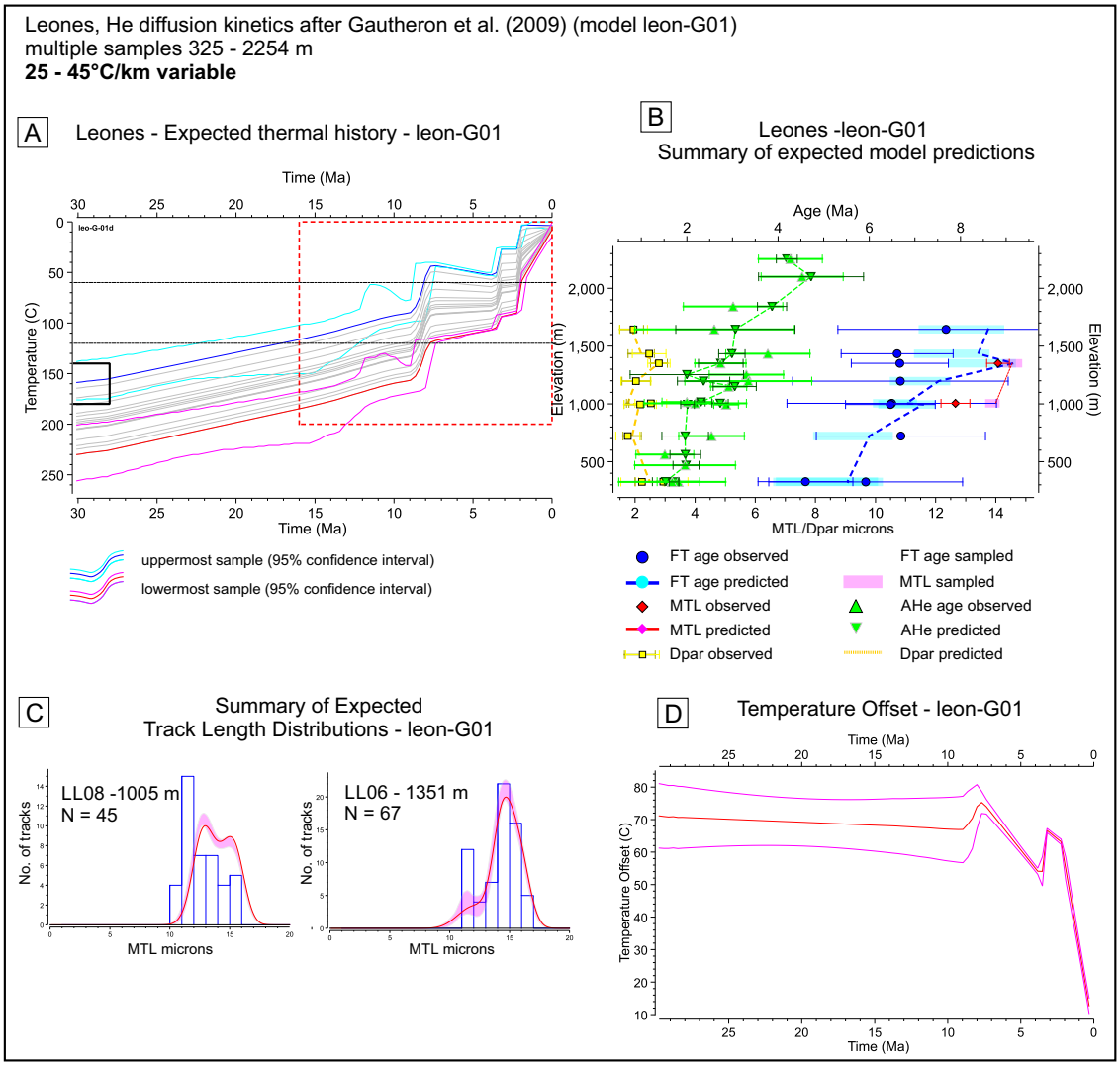

Figure B.23 – Leones transect - Summary of QTQt results from multiple-sample model runs with modified He-diffusion parameters (Gautheron *et al.*, 2009) and variable (25-45°C) geothermal gradient. A: Expected thermal history; B: Summary of expected model predictions vs. observed data; C: Summary of expected vs. observed track length distributions for samples LL06 and LL08; D: Evolution of the temperature offset between the uppermost and lowermost samples over the course of the model.

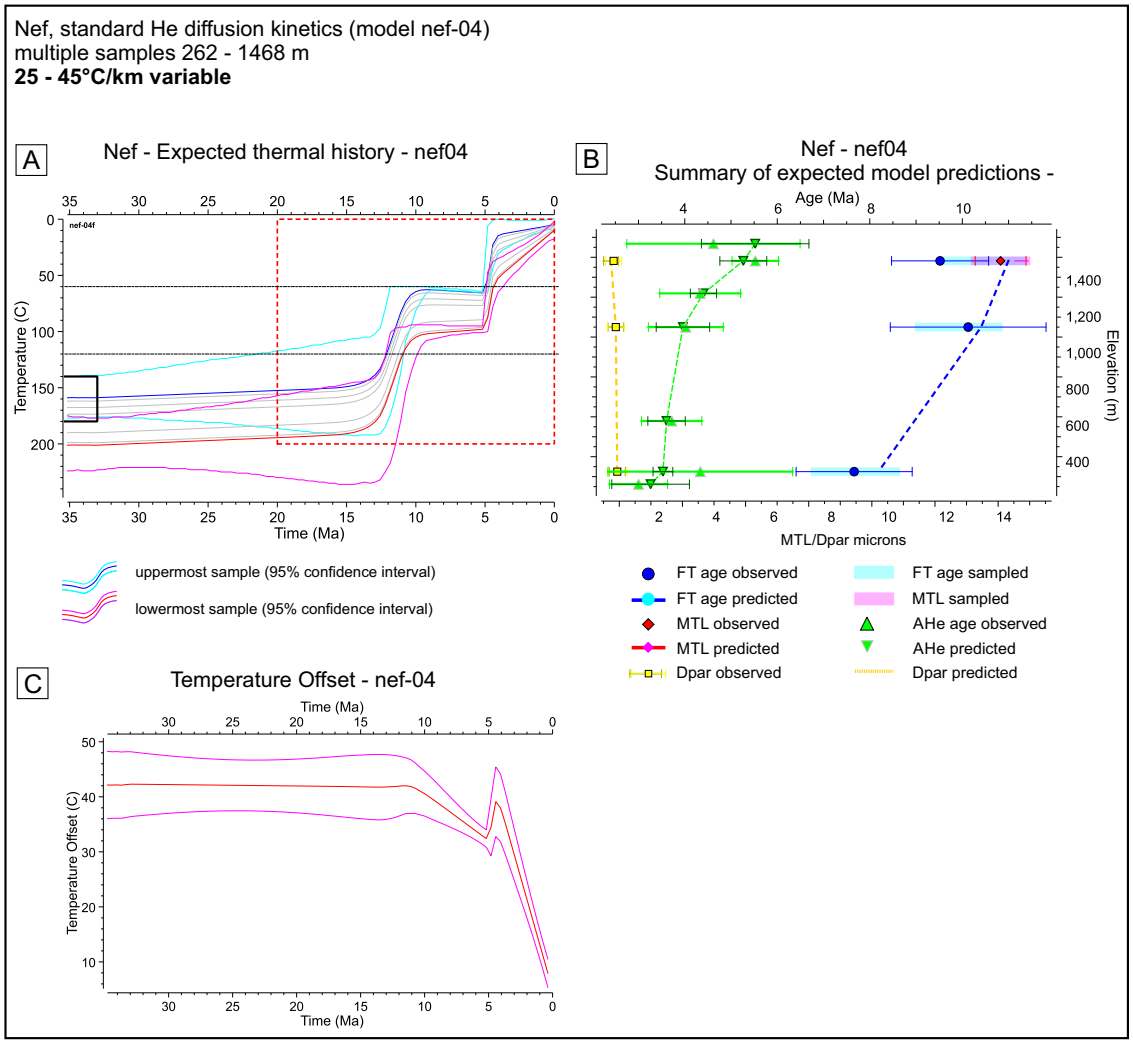

Figure B.24 – Nef transect - Summary of QTQt results from multiple-sample model runs with standard He-diffusion parameters (Farley, 2000) and variable (25-45°C) geothermal gradient. A: Expected thermal history; B: Summary of expected model predictions vs. observed data; C: Evolution of the temperature offset between the uppermost and lowermost samples over the course of the model.

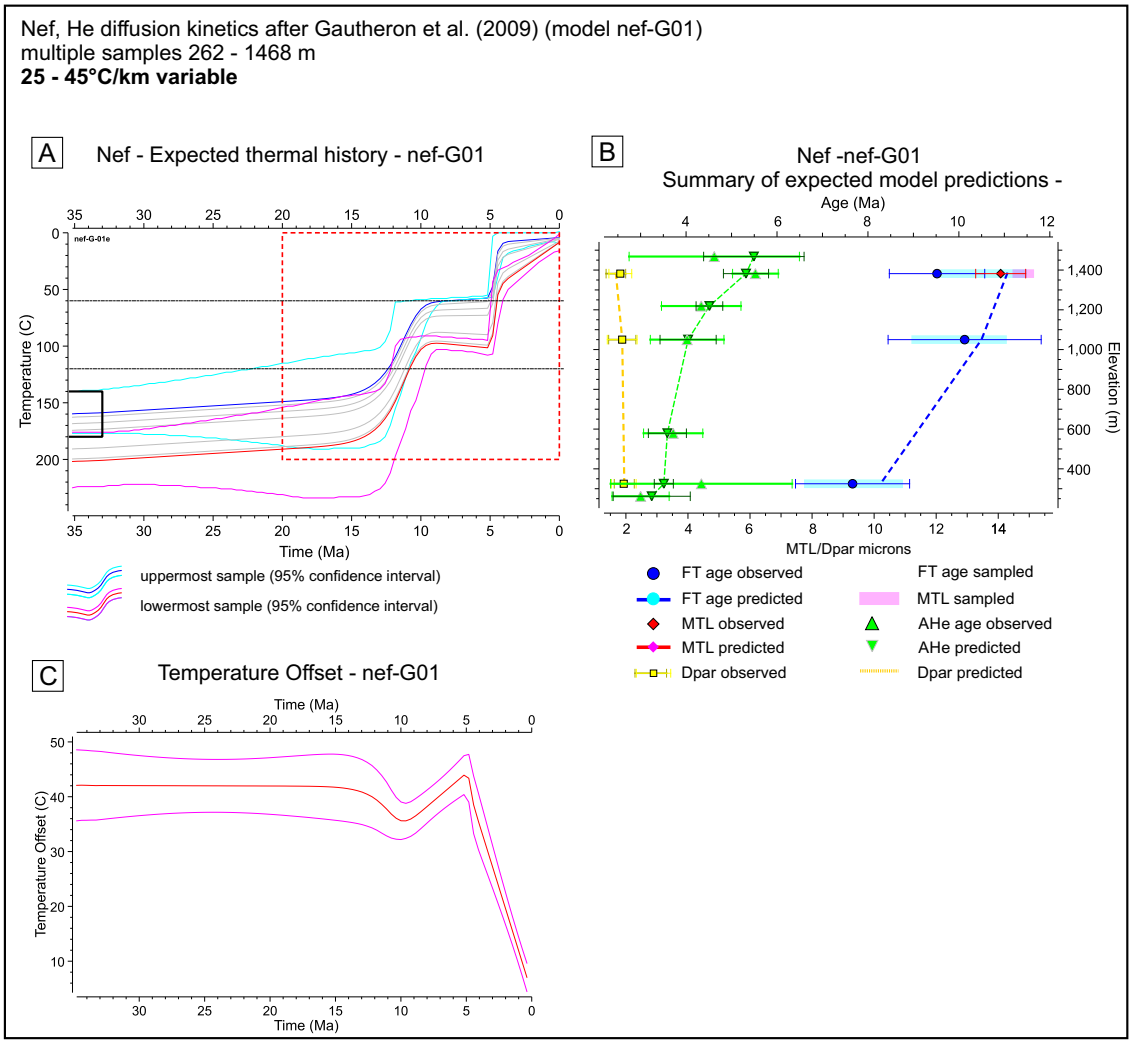

Figure B.25 – Nef transect - Summary of QTQt results from multiple-sample model runs with standard He-diffusion parameters (Gautheron *et al.*, 2009) and variable (25-45°C) geothermal gradient. A: Expected thermal history; B: Summary of expected model predictions vs. observed data; C: Evolution of the temperature offset between the uppermost and lowermost samples over the course of the model.

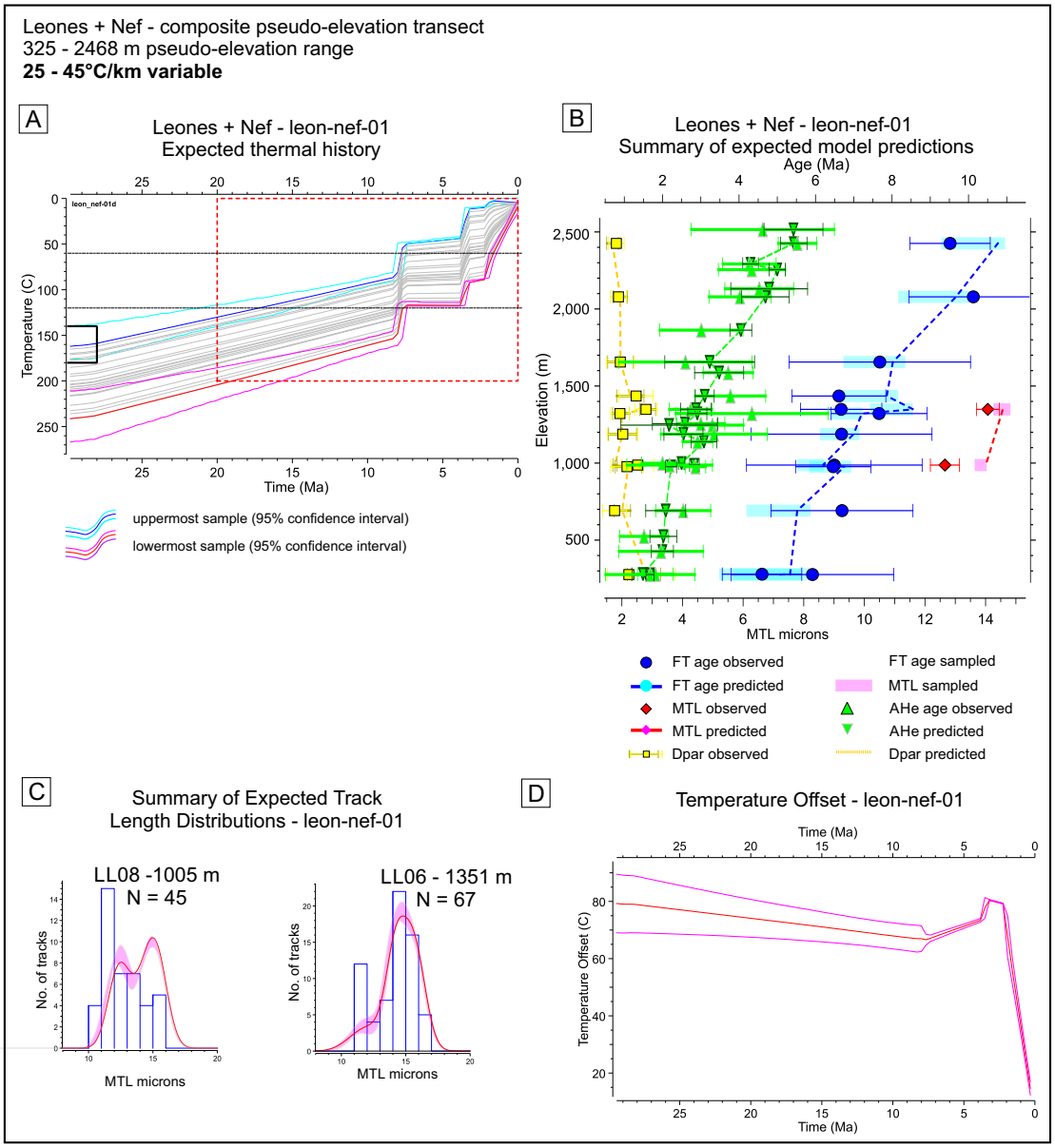

Figure B.26 – Composite pseudo-elevation transect with data from the Leones and Nef transects. Summary of QTQt results from multiple-sample model runs with standard He-diffusion parameters (Farley, 2000) and variable (25-45°C) geothermal gradient. A: Expected thermal history; B: Summary of expected model predictions vs. observed data; C: Summary of expected vs. observed track length distributions for samples LL06 and LL08; D: Evolution of the temperature offset between the uppermost and lowermost samples over the course of the model.

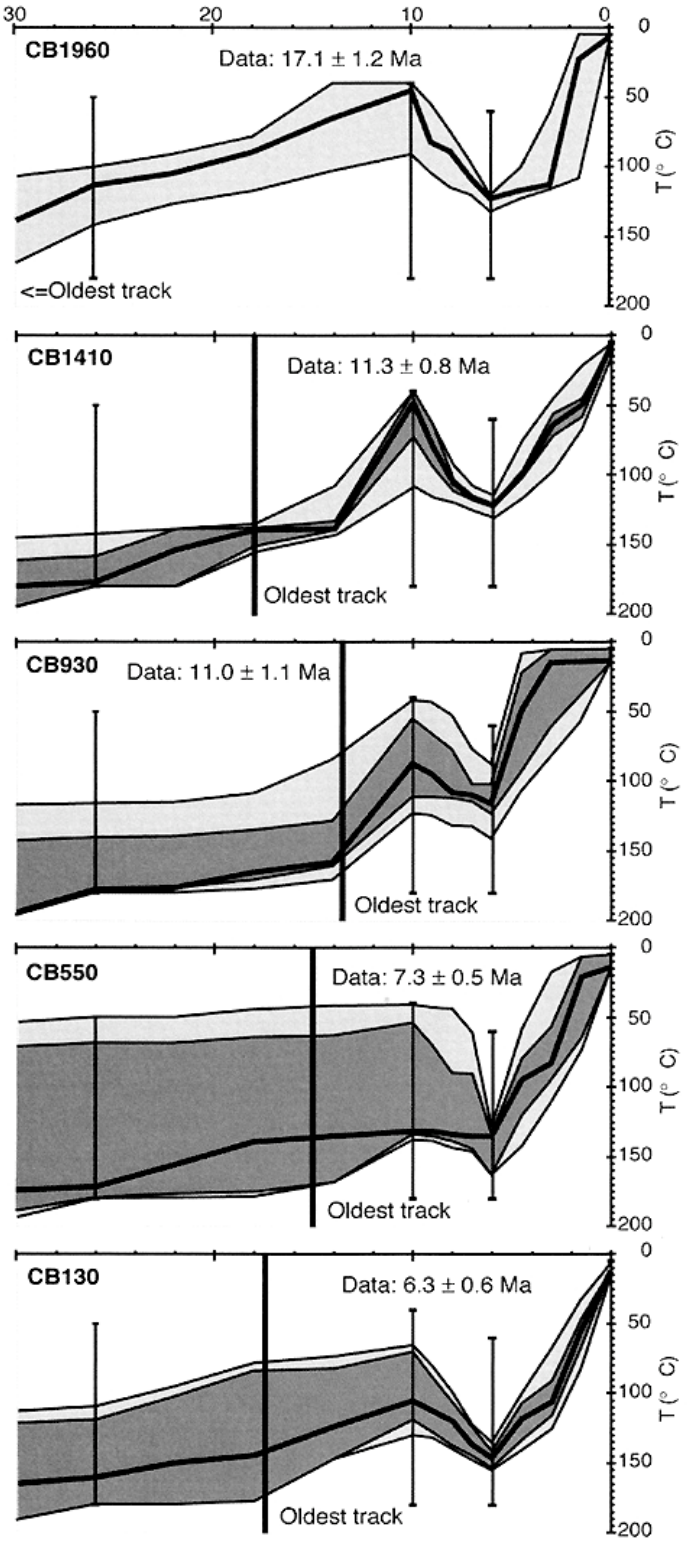

Figure B.27 – Results from AFTSolve modelling from Blisniuk *et al.* (2006) with AFT data from the Cerro Barrancos transect.

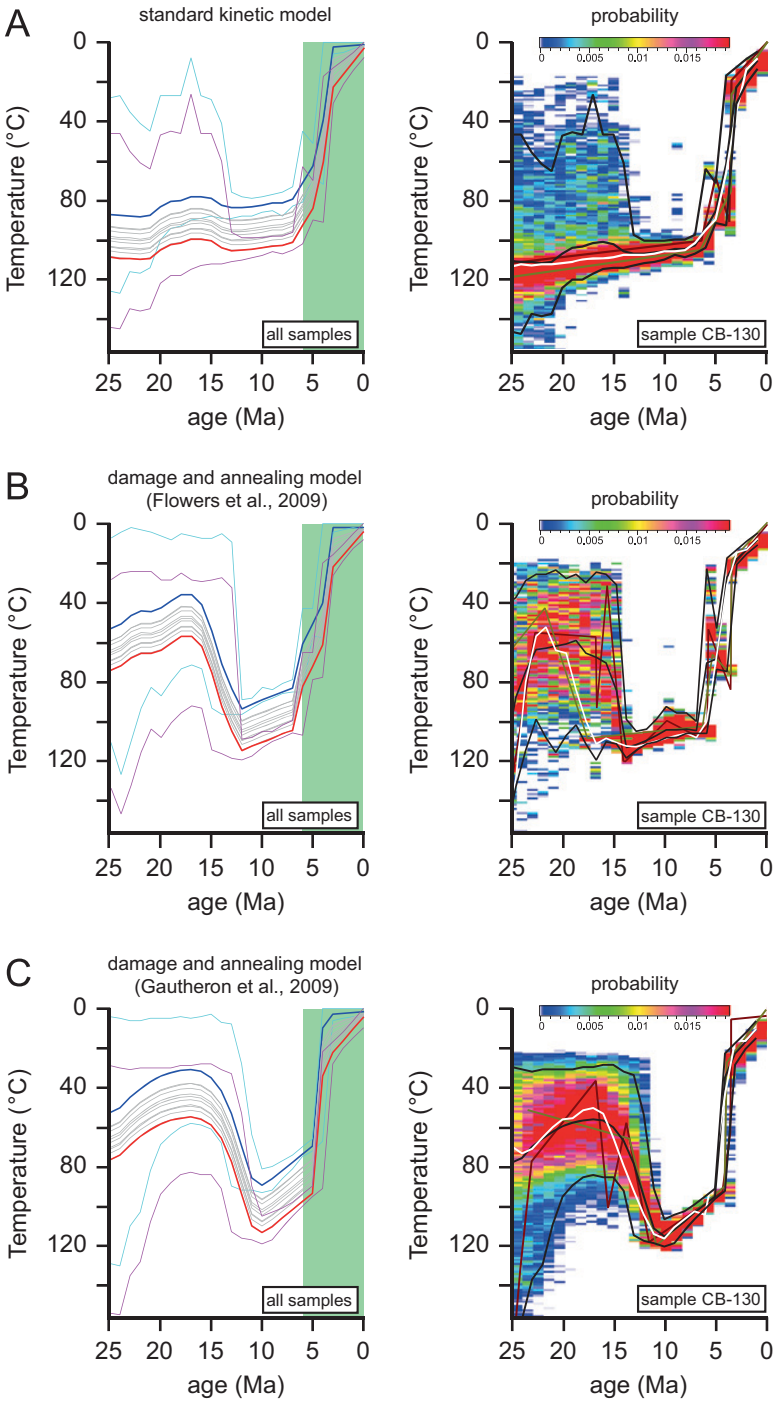

Figure B.28 – Results from QTQt modelling from Guillaume *et al.* (2013) with AHe and AFT data from the Cerro Barrancos transect.

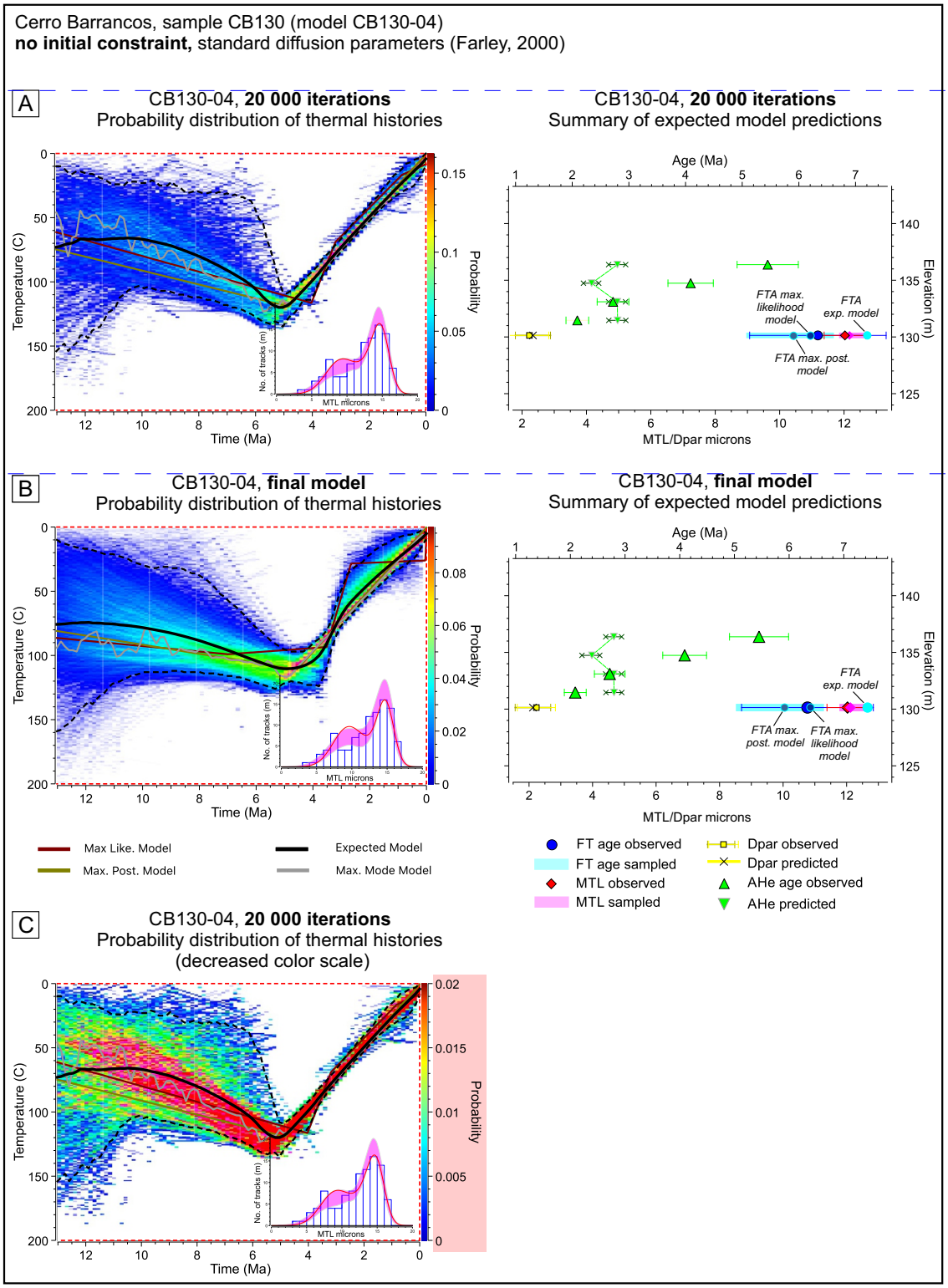

Figure B.29 – QTQt model - Cerro Barrancos transect, Sample CB130 model simulation without initial constraint. Panels (A) and (B) represent the initial (after 20 000 iterations) and final modeling output. Panel (C) illustrates the importance of the imbedded color scale for the visual interpretation of the data, particularly when the initial (still not converged) modeling output is selected (cf. Guillaume *et al.* (2013)

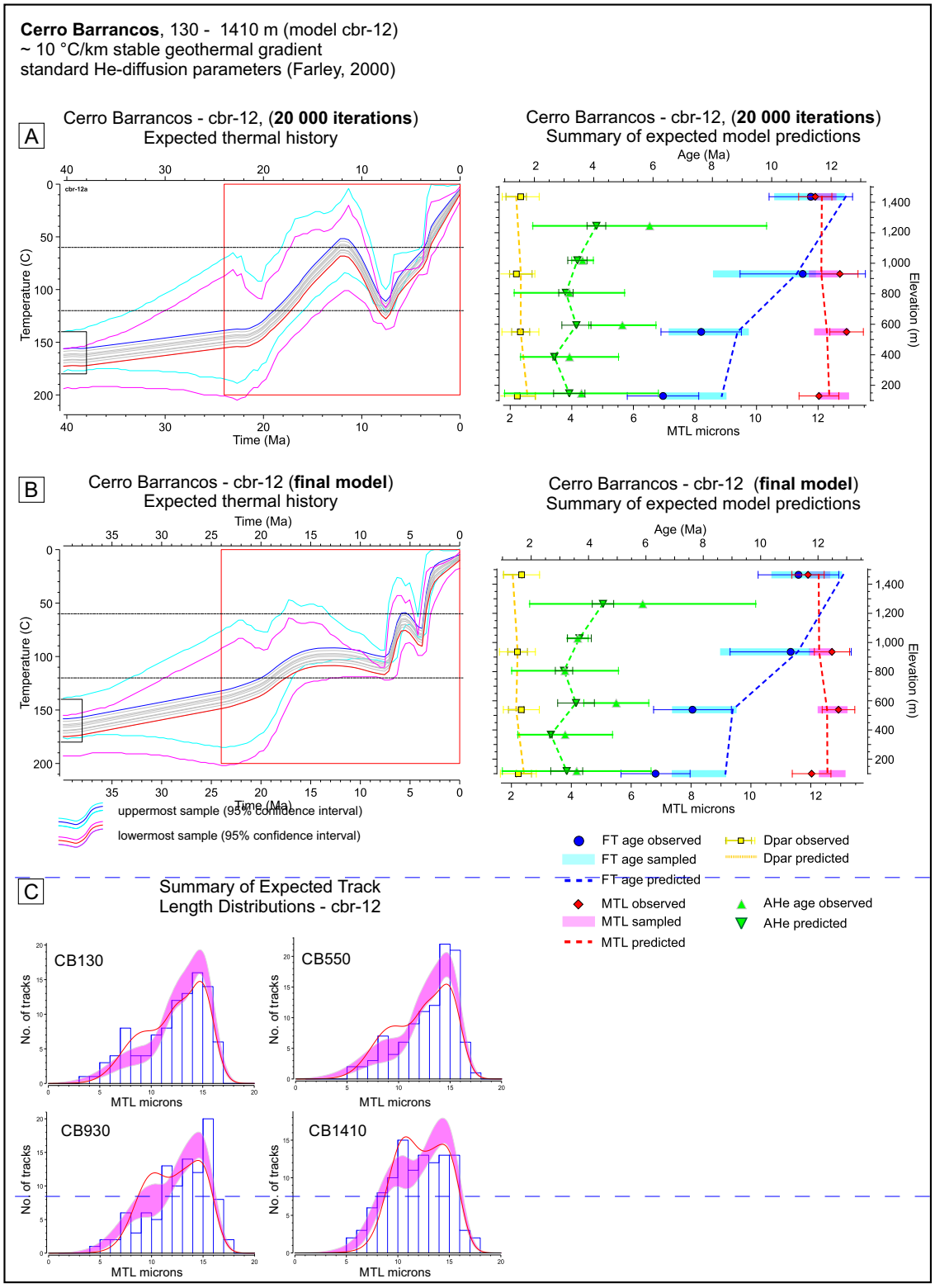

Figure B.30 – QTQt model - Cerro Barrancos transect, multiple-samples model simulation with decreased stable (10°C) geothermal gradient. Panels (A) and (B) represent the initial (after 20 000 iterations) and final modeling output. Panel (C) illustrates the distribution of predicted vs. observed track length distributions.

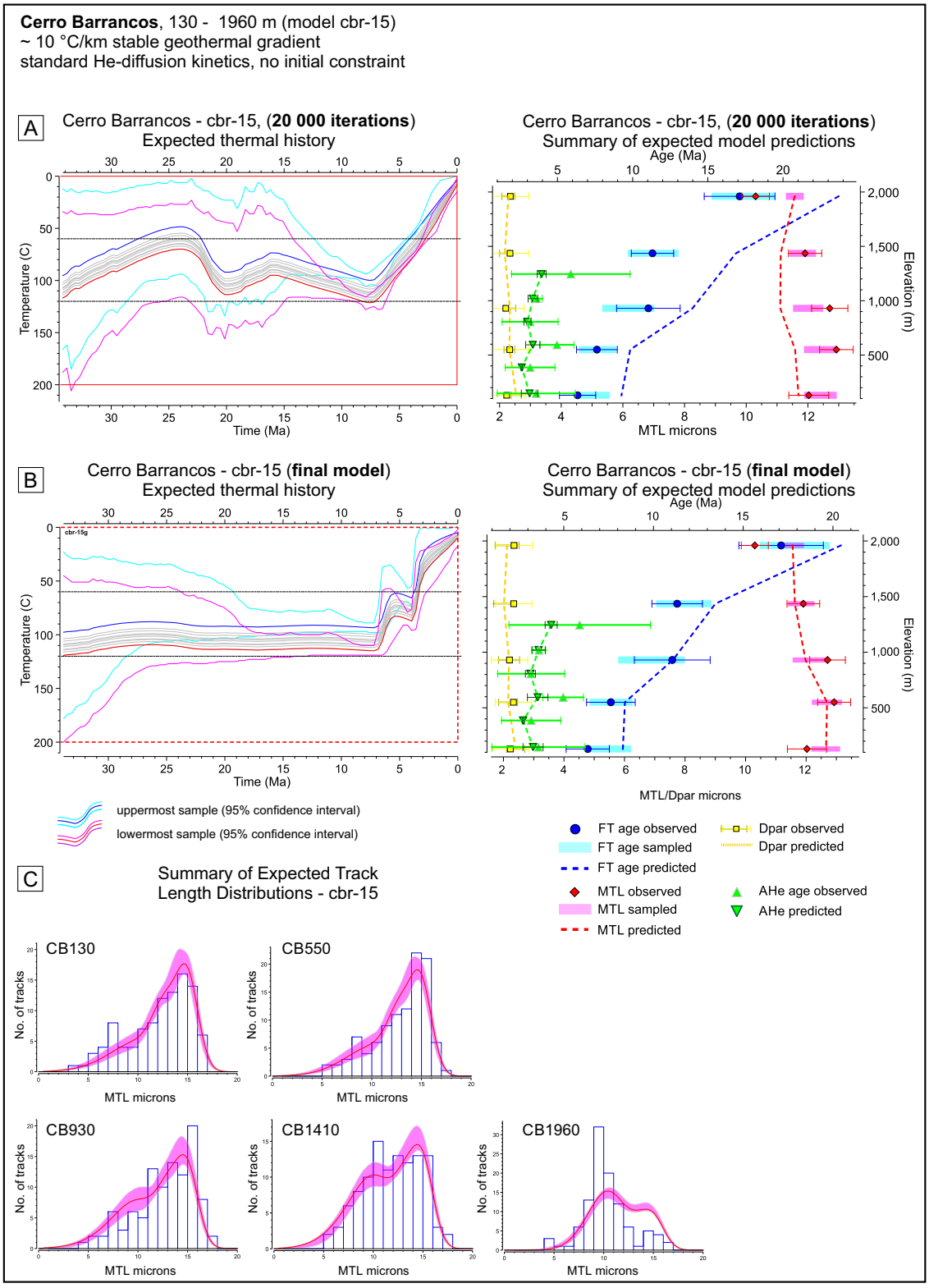

Figure B.31 – QTQt model - Cerro Barrancos transect with reference model setup from Guillaume *et al.* (2013) and standard He-diffusion kinetics (Farley, 2000)

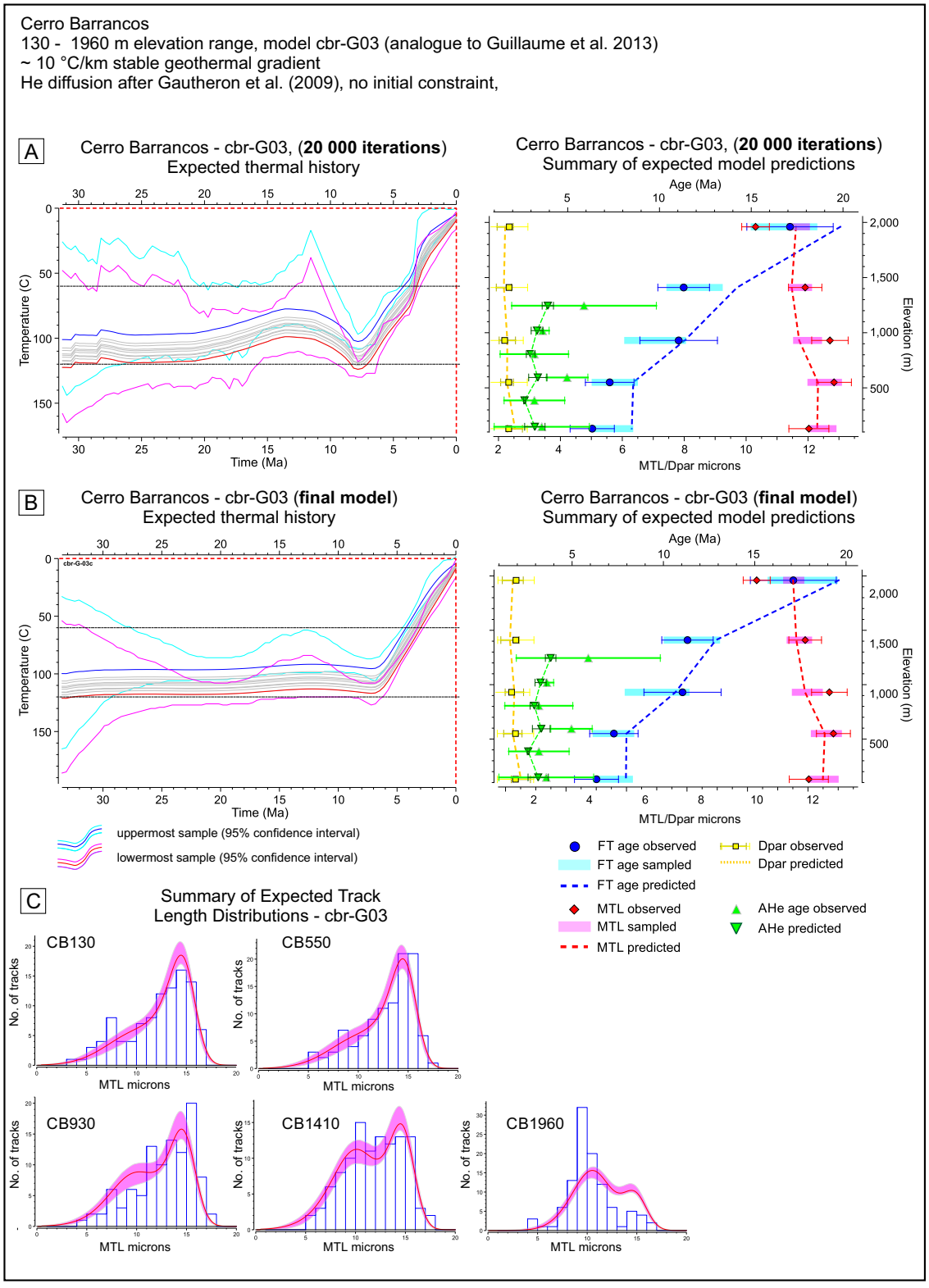

Figure B.32 – QTQt model - Cerro Barrancos transect with reference model setup from Guillaume *et al.* (2013) and modified He-diffusion kinetics (Gautheron *et al.*, 2009)

B.7 QTQt Model Runs and Parameters

Figure B.33 – QTQt Model Runs and Parameters

Model ID	N constraints	1. Time constraint [Ma]	1. T-constraint [°C]	Prior Time [Ma]	Prior T [°C]	Prior Offset	Prior T at 0 Ma [°C]	N iterations burn-in/post burn-in (x 10^3)	Data	Prior Geothermal
LEONES - single samples, standard He-diffusion kinetics (Farley, 2000)										
leo1351_01a	1	30	160	14	200		0-10	10 10	AHe, AFT	
leo1351_01b	1	30	160	14	200		0-10	100 100		
leo1005_01a	1	30	160	14	200		0-10	10 10	AHe, AFT	
leo1005_01b	1	30	160	14	200		0-10	100 100		
leo1005_01c	1	30	160		200		0-10	20 100		
leo995_01a	1	30	160	14	200		0-10	10 10	AHe, AFT	
leo995_01b	1	30	160	14	200		0-10	10 10		
leo995_01c	1	30	160	14	200		0-10	50 100		
LEONES - multiple samples, standard He-diffusion kinetics (Farley, 2000)										
										25±10 C/km
leon-01a	*1*	*30*	*160*	*16*	*200*	*50±20*	*0-10*	*10 10*	*AHe, AFT*	*stable*
leon-01b	*1*	*30*	*160*	*16*	*200*	*50±20*	*0-10*	*10 10*		
leon-01c	*1*	*30*	*160*	*16*	*200*	*50±20*	*0-10*	*50 200*		
										35±10 C/km
leon-02a	*1*	*30*	*160*	*16*	*200*	*70±20*	*0-10*	*10 10*	*AHe, AFT*	*stable*
leon-02b	*1*	*30*	*160*	*16*	*200*	*70±20*	*0-10*	*10 10*		
leon-02c	*1*	*30*	*160*	*16*	*200*	*70±20*	*0-10*	*50 200*		
leon-02d	*1*	*30*	*160*	*16*	*200*	*70±20*	*0-10*	*50 100*		
										45±10 C/km
leon-03a	*1*	*30*	*160*	*16*	*200*	*90±20*	*0-10*	*10 10*	*AHe, AFT*	*stable*
leon-03b	*1*	*30*	*160*	*16*	*200*	*90±20*	*0-10*	*50 200*		
										25 - 45 C/km
leon-04a	1	30	160	16	200	70±20	0-10	10 10	AHe, AFT	variable
leon-04b	1	30	160	16	200	70±20	0-10	10 10		
leon-04c	1	30	160	16	200	70±20	0-10	10 10		
leon-04d	1	30	160	16	200	70±20	0-10	50 200		
leon-04e	1	30	160	16	200	70±20	0-10	50 100		
LEONES -single samples, modified He-diffusion kinetics (Gautheron, 2009)										
leo1351-G-01a	1	30	160	14	200		0-10	10 10	AHeG, AFT	
leo1351-G-01b	1	30	160	14	200		0-10	10 10		
leo1351-G-01c	1	30	160	14	200		0-10	50 100		
leo1351-G-01d	1	30	160	14	200		0-10	50 100		
leo1005-G-01a	1	30	160	14	200		0-10	10 10	AHeG, AFT	
leo1005-G-01b	1	30	160	14	200		0-10	10 10		
leo1005-G-01c	1	30	160	14	200		0-10	10 10		
leo1005-G-01d	1	30	160	14	200		0-10	50 100		
leo995-G-01a	1	30	160	14	200		0-10	10 10	AHeG, AFT	
leo995-G-01b	1	30	160	14	200		0-10	10 10		
leo995-G-01c	1	30	160	14	200		0-10	50 100		
LEONES - multiple samples, modified He-diffusion kinetics (Gautheron, 2009)										
										25 - 45 C/km
leon-G-01a	1	30	160	16	200	70±20	0-10	10 10	AHeG, AFT	variable
leon-G-01b	1	30	160	16	200	70±20	0-10	10 10		
leon-G-01c	1	30	160	16	200	70±20	0-10	50 100		
leon-G-01d	1	30	160	16	200	70±20	0-10	50 100		

Fig. B.33 QTQt Model Runs and Parameters, cont.

Model ID	N constraints	1. Time constraint [Ma]	1. T-constraint [°C]	Prior Time [Ma]	Prior T [°C]	Prior Offset	Prior T at 0 Ma [°C]	N iterations burn-in/post burn-in (x 10^3)	Data	Prior Geothermal
Nef - multiple samples, standard He-diffusion kinetics (Farley, 2000)										
										25±10 C/km
nef-01a	*1*	*35*	*160*	*20*	*200*	*30±12*	*0-10*	*10 10*	*AHe, AFT*	*stable*
nef-01b	*1*	*35*	*160*	*20*	*200*	*30±12*	*0-10*	*10 10*		
nef-01c	*1*	*35*	*160*	*20*	*200*	*30±12*	*0-10*	*50 200*		
										35±10 C/km
nef-02a	*1*	*35*	*160*	*20*	*200*	*42±12*	*0-10*	*10 10*	*AHe, AFT*	*stable*
nef-02b	*1*	*35*	*160*	*20*	*200*	*42±12*	*0-10*	*50 200*		
nef-02c	*1*	*35*	*160*	*20*	*200*	*42±12*	*0-10*	*20 100*		
										45±10 C/km,
nef-03a	*1*	*35*	*160*	*20*	*200*	*12±12*	*0-10*	*10 10*	*AHe, AFT*	*stable*
nef-03b	*1*	*35*	*160*	*20*	*200*	*12±12*	*0-10*	*10 10*		
nef-03c	*1*	*35*	*160*	*20*	*200*	*12±12*	*0-10*	*50 200*		
										25 - 45 C/km
nef-04a	1	35	160	20	200	42±12	0-10	10 10	AHe, AFT	variable
nef-04b	1	35	160	20	200	42±12	0-10	10 10		
nef-04c	1	35	160	20	200	42±12	0-10	50 200		
nef-04d	1	35	160	20	200	42±12	0-10	20 100		
nef-04e	1	35	160	20	200	42±12	0-10	50 200		
nef-04f	1	35	160	20	200	42±12	0-10	20 50		
										10 C/km
nef-05a	*1*	*35*	*160*	*20*	*200*	*20±2*	*0-10*	*10 10*	*AHe, AFT*	*stable*
nef-05b	*1*	*35*	*160*	*20*	*200*	*20±2*	*0-10*	*50 200*		
										10 C/km
nef-06a	*1*	*35*	*160*	*20*	*200*	*20±10*	*0-10*	*10 10*	*AHe, AFT*	*stable*
nef-06b	*1*	*35*	*160*	*20*	*200*	*20±10*	*0-10*	*10 10*		
nef-06c	*1*	*35*	*160*	*20*	*200*	*20±10*	*0-10*	*10 10*		
nef-06d	*1*	*35*	*160*	*20*	*200*	*20±10*	*0-10*	*50 200*		
Nef - multiple samples, modified He-diffusion kinetics (Gautheron, 2009)										
										25 - 45 C/km
nef-G-01a	1	35	160	20	200	42±12	0-10	10 10	AHeG, AFT	variable
nef-G-01b	1	35	160	20	200	42±12	0-10	10 10		
nef-G-01c	1	35	160	20	200	42±12	0-10	10 10		
nef-G-01d	1	35	160	20	200	42±12	0-10	10 10		
nef-G-01e	1	35	160	20	200	42±12	0-10	50 200		
Leones-Nef pseudo-elevation transect, standard He-diffusion kinetics Farley, 2000)										
										25 - 45 C/km
leon-nef-01a	1	30	160	16	200	80±20	0-10	10 10	AHe, AFT	variable
leon-nef-01b	1	30	160	16	200	80±20	0-10	10 10		
leon-nef-01c	1	30	160	16	200	80±20	0-10	10 10		
leon-nef-01d	1	30	160	16	200	80±20	0-10	50 200		

Fig. B.33 QTQt Model Runs and Parameters, cont.

Model ID	N constraints	1. Time constraint [Ma]	1. T-constraint [°C]	Prior Time [Ma]	Prior T [°C]	Prior Offset	Prior T at 0 Ma [°C]	N iterations burn-in/post burn-in (x 10^3)	Data	Prior Geothermal
Cerro Barrancos - single samples (Dpar variable), standard He-diffusion kinetics (Farley, 2000)										
cb130_03a	1	30	160	14	200		0-10	10 10	AHe, AFT	
cb130_03b	1	30	160	14	200		0-10	10 10		
cb130_03c	1	30	160	14	200		0-10	10 10		
cb130_03d	1	30	160	14	200		0-10	50 100		
cb130_04a	-	-	-	14	200		0-10	10 10	AHe, AFT	
cb130_04b	-	-	-	14	200		0-10	10 10		
cb130_04c	-	-	-	14	200		0-10	10 10		
cb130_04d	-	-	-	14	200		0-10	10 10		
cb130_04e	-	-	-	14	200		0-10	50 100		
cb550_02a	1	30	160	16	200		0-10	10 10	AHe, AFT	
cb550_02b	1	30	160	16	200		0-10	10 10		
cb550_02c	1	30	160	16	200		0-10	10 10		
cb550_02d	1	30	160	16	200		0-10	50 100		
cb550_02e	1	30	160	16	200		0-10	50 100		
cb930_02a	1	35	160	22	200		0-10	10 10	AHe, AFT	
cb930_02b	1	35	160	22	200		0-10	10 10		
cb930_02c	1	35	160	22	200		0-10	10 10		
cb930_02d	1	35	160	22	200		0-10	50 100		
cb1410_02a	1	40	160	24	200		0-10	10 10	AFT	
cb1410_02b	1	40	160	24	200		0-10	10 10		
cb1410_02c	1	40	160	24	200		0-10	50 100		
cb1960_02a	1	50	160	34	200		0-10	10 10	AFT	
cb1960_02b	1	50	160	34	200		0-10	10 10		
cb1960_02c	1	50	160	34	200		0-10	50 100		
Cerro Barrancos - single samples (Dpar variable), modified He-diffusion kinetics (Gautheron, 2009)										
cb130_G_02a	1	30	160	14	200		0-10	10 10	AHeG, AFT	
cb130_G_02b	1	30	160	14	200		0-10	10 10		
cb130_G_02c	1	30	160	14	200		0-10	50 100		
cb550_G_02a	1	30	160	16	200		0-10	10 10	AHeG, AFT	
cb550_G_02b	1	30	160	16	200		0-10	10 10		
cb550_G_02c	1	30	160	16	200		0-10	50 100		
cb930_G_02a	1	35	160	22	200		0-10	10 10	AHeG, AFT	
cb930_G_02b	1	35	160	22	200		0-10	10 10		
cb930_G_02c	1	35	160	22	200		0-10	10 10		
cb930_G_02d	1	35	160	22	200		0-10	10 10		
cb930_G_02e	1	35	160	22	200		0-10	50 100		

Fig. B.33 QTQt Model Runs and Parameters, cont.

Model ID	N constraints	1. Time constraint [Ma]	1. T-constraint [°C]	Prior Time [Ma]	Prior T [°C]	Prior Offset	Prior T at 0 Ma [°C]	N iterations burn-in/post burn-in (x 10^3)	Data	Geothermal Gradient
Cerro Barrancos - multiple samples (Dpar variable), standard He-diffusion kinetics (Farley, 2000)										
									AHe, AFT	25 - 45 C/km
cbr-11a	1	40	160	24	200	45.5±13	0-10	10 10	130-1410 m	variable
cbr-11b	1	40	160	24	200	45.5±13	0-10	10 10		
cbr-11c	1	40	160	24	200	45.5±13	0-10	10 10		
cbr-11d	1	40	160	24	200	45.5±13	0-10	50 200		
									AHe, AFT	10 C/km
	1	40	160	24	200	15±2	0-10	10 10	130-1410 m	stable
cbr-12b	1	40	160	24	200	15±2	0-10	10 10		
cbr-12c	1	40	160	24	200	15±2	0-10	10 10		
cbr-12d	1	40	160	24	200	15±2	0-10	10 10		
cbr-12e	1	40	160	24	200	15±2	0-10	50 200		
cbr-12f	1	40	160	24	200	15±2	0-10	20 100		
									AHe, AFT	*25 - 45 C/km*
cbr-13a	*1*	*40*	*160*	*36*	*200*	*64±18*	*0-10*	*10 10*	*130-1960 m*	*variable*
cbr-13b	*1*	*40*	*160*	*36*	*200*	*64±18*	*0-10*	*10 10*		
cbr-13c	*1*	*40*	*160*	*36*	*200*	*64±18*	*0-10*	*10 10*		
cbr-13d	*1*	*40*	*160*	*36*	*200*	*64±18*	*0-10*	*10 10*		
cbr-13e	*1*	*40*	*160*	*36*	*200*	*64±18*	*0-10*	*50 200*		
cbr-13f	*1*	*40*	*160*	*36*	*200*	*64±18*	*0-10*	*50 100*		
									AHe, AFT	*20 C/km*
cbr-14a	*1*	*40*	*160*	*36*	*200*	*20±2*	*0-10*	*10 10*	*130-1960 m*	*stable*
cbr-14b	*1*	*40*	*160*	*36*	*200*	*20±2*	*0-10*	*10 10*		
cbr-14c	*1*	*40*	*160*	*36*	*200*	*20±2*	*0-10*	*10 10*		
cbr-14d	*1*	*40*	*160*	*36*	*200*	*20±2*	*0-10*	*50 200*		
									AHe, AFT	10 C/km
cbr-15a	-	-	-	36	200	20±2	0-10	10 10	130-1960 m	stable
cbr-15b	-	-	-	36	200	20±2	0-10	10 10		
cbr-15c	-	-	-	36	200	20±2	0-10	10 10		
cbr-15d	-	-	-	36	200	20±2	0-10	50 200		
cbr-15e	-	-	-	36	200	20±2	0-10	50 100		
cbr-15f	-	-	-	36	200	20±2	0-10	50 100		
cbr-15g	-	-	-	36	200	20±2	0-10	50 100		
cbr-15h	-	-	-	36	200	20±2	0-10	50 100		
									AHe, AFT	35±10 C/km
cbr-16a	1	40	160	24	200	45.5±13	0-10	10 10	130-1410 m	stable
cbr-16b	1	40	160	24	200	45.5±13	0-10	10 10		
cbr-16c	1	40	160	24	200	45.5±13	0-10	10 10		
cbr-16d	1	40	160	24	200	45.5±13	0-10	50 200		
cbr-16e	1	40	160	24	200	45.5±13	0-10	50 200		
Cerro Barrancos - multiple samples (Dpar variable), modified He-diffusion kinetics (Gautheron, 2009)										
									AHeG, AFT	25 - 45 C/km
cbr-G-02a	1	40	160	24	200	45.5±13	0-10	10 10	130-1410 m	variable
cbr-G-02b	1	40	160	24	200	45.5±13	0-10	10 10		
cbr-G-02c	1	40	160	24	200	45.5±13	0-10	50 200		
cbr-G-02d	1	40	160	24	200	45.5±13	0-10	50 100		
									AHeG, AFT	10 C/km
cbr-G-03a	-	-	-	36	200	20± 2	0-10	10 10	130-1960 m	stable
cbr-G-03b	-	-	-	36	200	20± 2	0-10	10 10		
cbr-G-03c	-	-	-	36	200	20± 2	0-10	50 200		

Autorenerklärung

Hiermit erkläre ich, dass ich die vorliegende Doktorarbeit selbständig verfasst und keine anderen als die angegebenen Hilfsmittel benutzt habe. Die Stellen der Doktorarbeit, die anderen Quellen im Wortlaut oder dem Sinn nach entnommen wurden, sind durch Angaben der Herkunft kenntlich gemacht. Des Weiteren bestätige ich, dass die Arbeit an keiner anderen Hochschule eingereicht worden ist.

Potsdam, den 05. Oktober, 2016
Viktoria Georgieva